Impact of the land biosphere on global biogeochemical cycling and climate through the Phanerozoic

Khushboo Gurung

Submitted in accordance with the requirements for the degree of
Doctor of Philosophy

The University of Leeds

School of Biological Sciences

January 2022

The candidate confirms that the work submitted is her own, except where work which has formed part of jointly-authored publications has been included. The contribution of the candidate and the other authors to this work has been explicitly indicated below. The candidate confirms that appropriate credit has been given within the thesis where reference has been made to the work of others.

The contents of Chapter 2 and Chapter 3 are submitted as:

Gurung, K., Field, K. J., Batterman, S. A., Goddéris, Y., Donnadieu, Y., Porada, P., Taylor, L. L., Mills, B. J. W. Climate windows of opportunity for plant expansion during the Phanerozoic, *In review at Nature Communications.*

K.G, K.F and B.J.W.M designed the research and developed the model. All authors contributed towards the manuscript.

Acknowledgements

During this PhD, I faced many unexpected challenges. I doubted myself, my work and especially, my motivation. Along these challenges however, I also found support. I would firstly like to thank my supervisors: Dr Benjamin Mills, Professor Katie Field and Dr Sarah Batterman for their unrelenting support throughout the years. They have continuously motivated me and helped me in every situation that not only academia, but life threw at me. Their patience, kindness and friendliness always surprise me. I would also like to extend my gratitude towards my parents, who have gently nudged me in the direction of academia since very young. I truly would not be here without their help and advice.

Finally, thank you to everyone that I have worked with and met on this journey. There is no doubt in my mind that every conversation we have had continued to push me to do better and to complete what I started.

This PhD started with a wrong email address, a different PhD interview (thank you for pointing me in the right direction Professor Stefan Kepinski) and a nervous skype call. As bizarrely as it started, it is bittersweet to see it end. I am grateful to have seen this through and to stand triumphant is truly a unique feeling.

Abstract

Land plants and their impact on Earth's climate has been an area of scientific interest for many decades. Global vegetation and climate are linked: climate change induces vegetation change, and as vegetation changes, climate follows suit. While the general trajectory of plant evolution is relatively well understood, it remains difficult to estimate global plant biomass and productivity over geological time: a key consideration in determining the magnitude of any climate or biogeochemical effects. Previous works have relied either on box models, with no consideration of global hydrology and the impact of water availability on key plant physiological processes, or on complex spatial vegetation models which are set up for specific time periods and are not easily extended across Phanerozoic time.

In this thesis, I present a simplified deep-time dynamic global vegetation model called FLORA (Fast Land Occupancy and Reaction Algorithm). The model was built from scratch but is largely based on processes in the LPJ-DGVM. FLORA shows that key windows during the Ordovician and Jurassic-Paleogene periods are compatible with higher plant biomass due to their paleogeography and hydrology. These times coincide with the colonisation of land by embryophytes and the angiosperm radiation, respectively. FLORA is further incorporated into a larger climate-chemical model (SCION - Spatial Continuous Integration) to assess the impact of plants on biogeochemical cycles. A more accurate plant-carbon representation improves model predictions of atmospheric CO_2 and temperature over the Mesozoic and Cenozoic – specifically the aridity of Pangaea results in low Triassic-Jurassic biomass and the enhanced hydrology of the Cretaceous results in high biomass, relative to box model approaches. These changes result in a better fit to the geological record. Overall, this thesis highlights the need for better plant-climate interaction in global biogeochemical models and begins to work towards this.

Table of Contents

List of Tables

List of Figures

Chapter 1. Introduction and literature review

Plants shape and influence global environmental conditions. Since the dawn of their terrestrialisation on land during the Ordovician period (Waters, 2003), plants, both large and small, have had a cumulative impact on the global carbon cycle. Over the Phanerozoic (541 – 0 million years; Figure 1.1.1), plants have evolved from small, cryptogamic covers like mosses into colossal trees such as the redwoods. Along the way, physiological innovations such as strengthening of their cells, creating water systems to provide long distance water transport, has increased the ability of plants to ground themselves on land and dominate it. Their gradual ascendancy to modern day plants has been a journey of efficiency, adaptation and innovation. Although plants are widely recognised as a major players in driving climate change, plants and their role(s) in long-term climate change and global biogeochemical models which reconstruct long-term climate has been greatly simplified.

This thesis explores the potential plant influence on paleoclimate and the carbon cycle in a 2-D setting. Chapter 1 provides a background on how Earth and plants have evolved over the Phanerozoic along with their roles in the shaping of biogeochemical cycles. Chapter 2 describes the simple vegetation model I have developed to explore potential biomass under ancient climates and continental configurations. The model, dubbed FLORA (Fast Land Occupancy and Reaction Algorithm) is used to assess Earth's ability to host plant life throughout the Phanerozoic over Chapter 3. Chapter 4 takes FLORA and integrates it dynamically into the larger climate-chemical model SCION (Spatial Continuous Integration, Mills et al., 2021). Introducing a spatial vegetation map creates regional differences in rates of weathering and carbon sequestration within SCION, which are controlled by regional climate and hydrology. The linked model is assessed in its ability to reproduce atmospheric CO_2 and O_2 levels, temperature and various other environmental and geochemical proxy records over Phanerozoic time. Chapter 5 discusses what is still missing in the FLORA model, such as the potential role of mycorrhizal fungi on nutrient cycling and plant productivity, and how FLORA can be improved going forward. This thesis provides the starting framework for a vegetation model for long-term climate change.

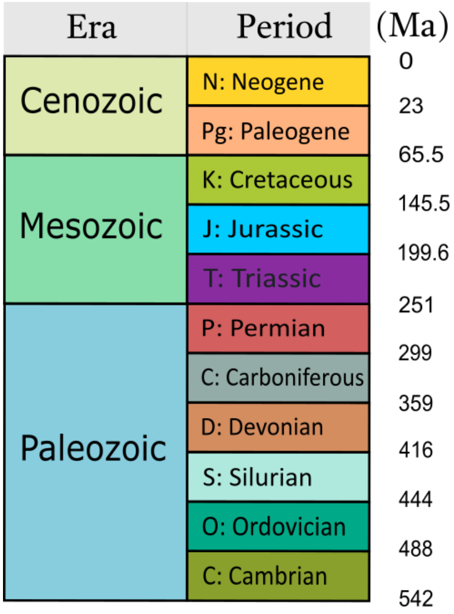

Figure 1.1.1. Phanerozoic timeline. *The Phanerozoic is divided into 3 eras and 11 periods. Dates indicate the start of a new era or period where Ma: million years ago. The following abbreviations are used throughout the thesis figures. Era: Ce, Cenozoic; Mesozoic and Paleozoic. Period: N, Neogene; Pg, Paleogene; K, Cretaceous; J, Jurassic; T, Triassic; P, Permian; C, Carboniferous; D, Devonian; S, Silurian; O, Ordovician; C, Cambrian.*

1.1 Plant evolution

The terrestrial environment was a novel environment for early land plants with simple architecture and minimal physiological and morphological strategies for land-induced challenges including nutrient acquisition, desiccation and photo-oxidative damage to the cells (de Vries and Archibald, 2018). The common ancestor of modern land plants was likely to have been from a single algal clade within Streptophyta estimated at 962-870 Ma (Jones and Dolan, 2012) however the transition to land happened independently among various algae and is also speculated to have occurred in Rhodophyta (red algae) (de Vries and Archibald, 2018). The small body size, height and thalloid organisation (growth close to the ground) made mechanical challenges less of a problem for algal transition to land compared to biophysical challenges such as exposure to high levels of radiation (Bateman et al., 1998). Before the evolution of arborescent plants, early vascular plants faced full sunlight and drying of early skeletal soils with limited water-holding capacity due lack of shading together with limited root or rhizoid systems (Ruszala et al., 2011). The heavily debated subject of the timings of plant evolution (Gitzendanner et al., 2018) creates uncertainty in the order of evolution. This chapter uses the molecular clock analysis timings (Morris et al., 2018) to create order in the following sub-section by using one possible version of stepwise evolution (Figure 1.1.2). Challenges associated with the phylogeny debate is further explored in Chapter 6.2.2.

Over the Phanerozoic, continental configuration and associated environmental changes (regional and global) have posed selective pressures on land plants such as changes in seasonality and water availability (Zeppel et al., 2014). Innovative adaptations for terrestrial colonisation therefore have evolved to reflect environmental conditions. For example, leaf structure varies depending on water availability; dry conditions require leaves to sustain moderate photosynthetic rates without a large evaporation rate, hence the innovation of needles (Brodribb et al., 2010). Co-evolution with mycorrhizal fungi (see Chapter 1.3), and with the evolution of a variety of traits, such as stomata and vasculature, plants made the successful transition from an aquatic environment to a fully terrestrial one. A summary of plant and fungi evolution illustrates the interconnected relationship and the immense difference in plant physiology from the onset to present-day (Figure 1.1.3). The following section explores plant evolution as a product of environmental forcings and their impact on biogeochemical cycles.

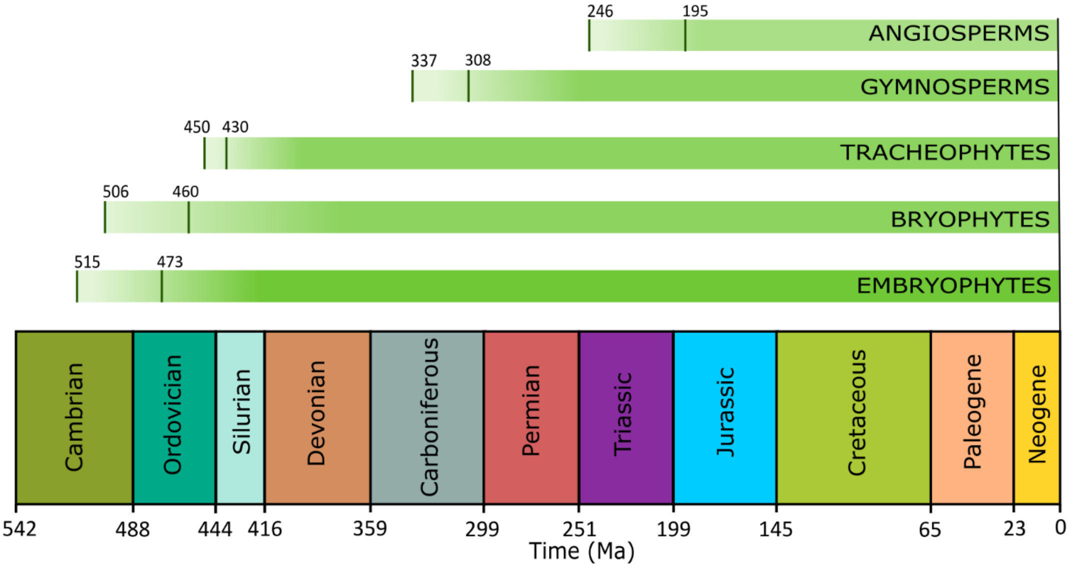

Figure 1.1.2. Approximate estimations of plant evolution and Phanerozoic time periods. *The earliest and latest origin estimates of embryophytes, bryophytes, tracheophytes, gymnosperms and angiosperms according to molecular clock analysis (Morris et al., 2018). Numbers indicate the start of each Phanerozoic period on the timeline; Ma: million years ago.*

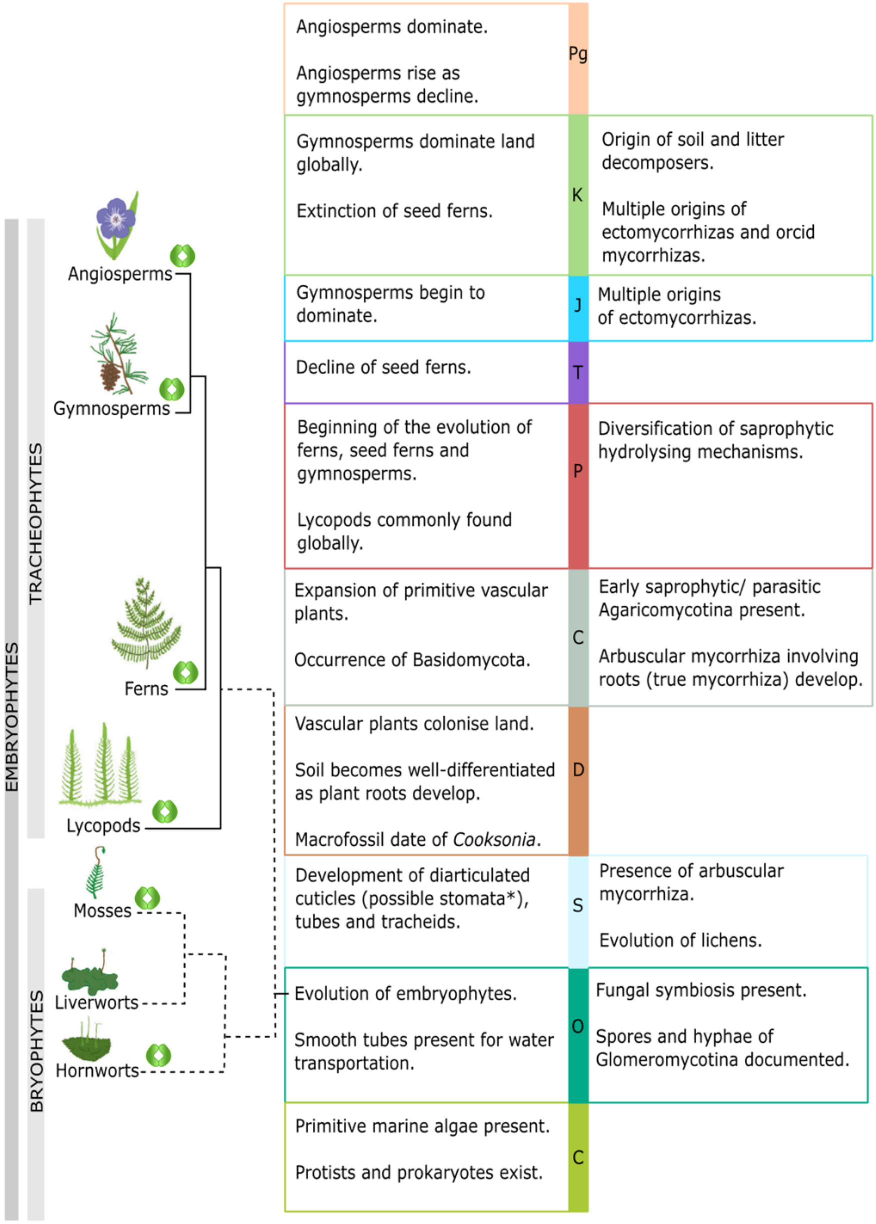

Angiosperms dominate. Angiosperms rise as gymnosperms decline.	Pg	
Gymnosperms dominate land globally. Extinction of seed ferns.	K	Origin of soil and litter decomposers. Multiple origins of ectomycorrhizas and orcid mycorrhizas.
Gymnosperms begin to dominate.	J	Multiple origins of ectomycorrhizas.
Decline of seed ferns.	T	
Beginning of the evolution of ferns, seed ferns and gymnosperms. Lycopods commonly found globally.	P	Diversification of saprophytic hydrolysing mechanisms.
Expansion of primitive vascular plants. Occurrence of Basidomycota.	C	Early saprophytic/ parasitic Agaricomycotina present. Arbuscular mycorrhiza involving roots (true mycorrhiza) develop.
Vascular plants colonise land. Soil becomes well-differentiated as plant roots develop. Macrofossil date of *Cooksonia*.	D	
Development of diarticulated cuticles (possible stomata*), tubes and tracheids.	S	Presence of arbuscular mycorrhiza. Evolution of lichens.
Evolution of embryophytes. Smooth tubes present for water transportation.	O	Fungal symbiosis present. Spores and hyphae of Glomeromycotina documented.
Primitive marine algae present. Protists and prokaryotes exist.	C	

Figure 1.1.3. Timeline of major plant and fungi innovations. *Fossil and molecular evidence suggest approximate timings of major innovations throughout the Phanerozoic (data taken from Kenrick and Crane, 1997; Field et al., 2015; Strullu-Derrien et al., 2018). Main land plant groups, conforming to a bryophyte monophyly hypothesis, are shown in relation to time and innovations (Modified from Hoysted et al., 2018). Dashed line indicates uncertainty within the phylogeny. *Earliest hypothesised appearance of the stomata; large uncertainty is attached to the time of their appearance due to multiple independent evolution or reduction. Plant groups that contain stomata are indicated (Harris et al., 2020).*

1.1.1 Embryophytes: 515 Ma

Land colonisation by plants is estimated to have occurred during the Ordovician to early Devonian periods (at least 450 Ma; Kenrick and Crane, 1997; Waters, 2003). The earliest land plants (embryophytes) are first identified in the Ordovician period and were morphologically simple compared to modern vascular plants, being rootless and non-vascular, and bearing some similarities to modern day bryophytes (Figure 1.1.3; Porada et al., 2016). The first fossil evidence for land-plant evolution is first observed during the Middle Ordovician period (472 Ma) in the form of cryptospores (fossilised primitive plant spores) (Magallón et al., 2013) while the oldest macrofossil *Cooksonia* points at a later Silurian and early Devonian appearance (Figure 1.1.3; Kraft et al., 2019). Megafossils for early land plants are rare, and the existing records are heavily biased towards plants containing recalcitrant tissues which contain molecules that are highly resistant to decay. Fossils also postdate its origin hence molecular clock analysis often estimate a much earlier origin time with embryophytes coming in during the Cambrian at 515 Ma (Figure 1.1.2; Morris et al., 2018). Early 'bryophyte-like' plants contained very little or completely lacked recalcitrant tissues therefore leaving a macrofossil gap for the evolution of land plants (Wellman et al., 2013). On the other hand, the fossil record of spores is abundant and less biased, therefore presenting a much more accurate picture of early plant assemblage. The mid-Ordovician cryptospore records indicate early ecosystems to be ecological generalists throughout the globe with very little variation (Steemans et al., 2009). Spore assemblages from high latitudes to the equator suggest the generalist founder population to consist of 'liverwort-like' plants (Wellman et al., 2013). It is entirely possible for a parent plant with widespread dispersal abilities and tolerance of a wide range of ecological and climatic conditions to be present and to colonise empty niches. The extant bryophytes show indirect evidence for this theory as they are able to tolerate high radiation environments and survive and reproduce under dry conditions (Wellman et al., 2013).

1.1.2 Bryophytes: 506 Ma

Bryophytes (liverworts, hornworts and mosses), the earliest diverging lineage of modern land plants, is postulated to appear as early as the Cambrian at 506 Ma soon after the emergence of embryophytes (Budke et al., 2018). Microfossil evidence of bryophytes (small fragments of decay-resistant tissues and spores) establish them on land during the Silurian, however macrofossil remains of bryophytes are not present until the Devonian and Carboniferous therefore leading to the debate of bryophyte origin (see chapter 5.7.2; Kodner and Graham, 2001). During this period, megafossil evidence indicating cell specialisation for survival on land (including features seen in bryophytes and vascular plants) are also present such as spores (reproduction methods), tracheids (vertical growth support), stomata (desiccation protection and gas exchange regulation) and banded tubes (water and nutrient transport) (Kenrick and Crane, 1997).

Although debated in their relationship and lineage in relation to tracheophytes (vascular plants) (Morris et al., 2018), many bryophytes display poikilohydry: suspension of metabolism during limited water availability due to the lack of mechanisms that control cell water content. Poikilohydry prevents desiccation of cells in low humidity environments and preservation of bryophytes during dry seasons (Proctor and Tuba, 2002). Several studies on modern bryophytes, such as the extant genus *Tortula*, show mechanisms of cellular structure protection during drying and rehydration-induced repair processes as they equilibrate to the surrounding water content (Oliver et al., 2005; Duckett and Pressel, 2018). However, most of the knowledge on this mechanism is derived from modern gametophytes (the sexual phase in the life cycle of plants and algae) (Duckett and Pressel, 2018) whose life history may not truly reflect that of ancient plants. Land plants consist of an alternating life cycle: sexual haploid gametophyte and asexual diploid sporophyte. Most megafossils from the Silurian are sporophytes with the earliest gametophyte discovery occurring in the Rhynie Chert confirming their existent from Early Devonian onwards (Kenrick and Crane, 1997). The evolutionary history of life cycles, especially the evolution from haploid to diploid phase, is mostly unknown (Taylor et al., 2005) therefore, it may not be entirely accurate to extend modern bryophyte abilities to ancient bryophyte-like plants. Numerous modern bryophyte species require moisture for their growth and sexual reproductive stages (Miller, 1982) whereas this may not have been the main limiting factor for ancient plants.

A plethora of innovative evolution must have occurred between bryophytes and tracheophytes to avoid drying and exploit habitats further away from a water source. At a relative humidity of 50% (at 28°C), bryophytes face lethal water deficit levels (Oliver et al., 2005) whereas some current desert angiosperms are adapted to survive below 33% relative humidity (Gaff, 1971). Firstly, dead cell wall skeletons made the base of a water conduction system; examples of the simplest system being in the innermost cell layer of stems (i.e. hydroids) of some mosses (Sperry, 2003). Thin, smooth walls allowed for easier movement of water along the plant body. Secondly, cell walls were rigidified and water-proofed by lignin (Sperry, 2003). Lignin increased the threshold for pressure within cells allowing tracheary elements to be held open without collapsing on itself, and its hydrophobic nature forced water to stay within the tubes. Finally, plasmodesmatal pores were used to control water movement between vascular and non-vascular tissues (Sperry, 2003). Channels between plant cells were now able to distribute water throughout the whole plant without the need for all cells to be part of the water transportation system. These physiological innovations are present in the fossil records by 410 Ma and a range in morphology can be observed by 390 Ma (Figure 1.1.3; Kenrick and Crane, 1997).

Fossil records show stomata and primitive xylem-like tissues to co-occur during the Silurian in most extant plants allowing the transition from poikilohydry to homiohydry (the ability to obtain water from the environment through a system of roots or similar organs rather than through the surface of leaves) (Sperry, 2003). Along with water, plants co-regulate intracellular CO_2 levels to prevent dynamic water stress via evaporation. Low transpiration rate limits CO_2 uptake, as the stomata are closed, however if the CO_2 uptake is unregulated, it reduces source water availability, as the stomata are open constantly and evapotranspiration transports water from its source to the atmosphere (Sperry, 2003). Modern plants achieve water control throughout the plant using stomata which also act as the main limiting factor for carbon uptake (Chaves and Pereira, 1992). Soil water is connected to atmospheric water via transpiration that occurs through the stomata, linking plants to the carbon, water and nutrient cycles (Kelliher et al., 1995). The origin of stomata for gas exchange is seen in sporophytes of mosses and hornworts (Doyle, 2013) with multiple points of origin depending on factors such as guard cell physiology and intracellular space ontogeny (Duckett and Pressel, 2018). Representatively present in all embryophytes, except liverworts, Devonian stomata from the Rhynie chert (found in Scotland) aligns with the paradigm that stomata have one common ancestor, and their role and regulation are conserved throughout land plant lineages (Duckett and Pressel, 2018). As liverworts do not possess stomata, an opposite hypothesis suggests the ancestral function of stomata to be water and nutrient transport limited (Sperry, 2003; Duckett and Pressel, 2018). Moss stomata are not responsive to CO_2 (Rensing, 2018), supporting the hypothesis that the ancestral function of stomata was primarily desiccation prevention.

1.1.3 Tracheophytes: 450 Ma

The early Silurian is hypothesised to be the period of origin and diversification of tracheophytes (clubmosses, ferns, horsetails, seed plants; Figure 1.1.3) due to major changes in spore assemblages and the appearance of vascular plant megafossils (Steemans et al., 2009). Desiccation tolerance mechanisms are observed in tracheophytes as they evolved water transport systems such as tracheids and vessel elements (cells that form the xylem) to avoid drying (Oliver et al., 2005). Further evolution of hair-like rhizoid cells on the gametophyte, the only free-living stage of the life cycle that is in direct contact with the substrate (Jones and Dolan, 2012), appear in paleosols as rhizoid imprints around the Silurian (Field, Pressel, et al., 2015). Prostrate stems with filamentous cells, that resemble living bryophyte structures which act as anchors and aid water and nutrient uptake, were modified to produce roots (Kenrick and Crane, 1997; Jones and Dolan, 2012). Roots evolved among the lycophytes by the Early Devonian as seen in the simple root-like structures of *Asteroxylon mackei* found in the Rhynie chert (Jones and Dolan, 2012).

Tracheophytes radiated in the Devonian as they became more prominent in plant records globally, including the Rhynie chert (Boyce and Lee, 2017). With the evolution of roots, independent evolution of trees led to several major plant clades supporting tree habitats by the Devonian (Kenrick and Crane, 1997; Kenrick et al., 2012). Major expansion of seed-plant floras with deeper root systems occurred during the Early Carboniferous (Chen et al., 2021). The late Carboniferous, also known as the ‘Coal Age’, saw terrestrial land covered in forested wetland with the dominant plant groups, arborescent lycophytes or club mosses. The combination of gymnosperms which contain difficult to biodegrade lignin, and wet, hot conditions created expansive deep peat deposits which were previously not as a prominent feature of plant ecology (DiMichele, 2014; Cleal, 2018).

A later major step in plant evolution was the divergence of the flowering plants (angiosperms), estimated to have occurred between 120-100 Ma, based on the occurrence of flowers in the fossil record (Sauquet et al., 2017). Terrestrial ecosystems rapidly changed from gymnosperm to angiosperm dominated flora over approximately 30 million years (Hochuli et al., 2006). The success of angiosperms can be attributed to their efficient photosynthesis and floral-based mechanisms of reproduction, pollination and dispersal (Brodribb and Feild, 2010; Boyce and Leslie, 2012). Higher photosynthesis rates per unit leaf area, growth rates and faster generation times and therefore higher productivity rates in general gave angiosperms the advantage to take over ecosystems (Boyce and Leslie, 2012). Angiosperms continued to diversify, eventually dominating present day terrestrial plant assemblages from the Cretaceous onwards (Figure 1.1.4).

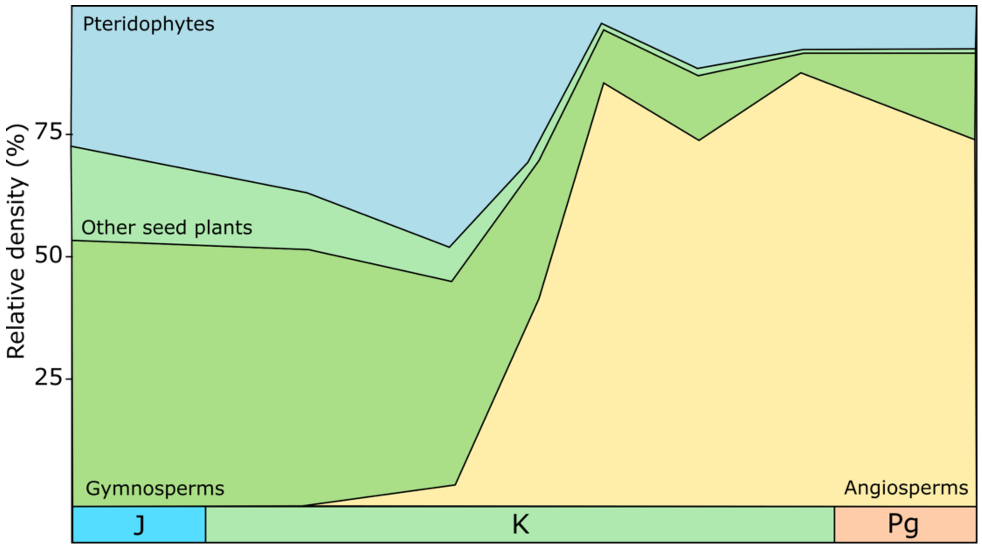

Figure 1.1.4. Dominant plant type turnover. *Angiosperms show a clear and rapid domination, making up >50% of total relative density of plants, from the mid-Cretaceous onwards. Gymnosperms and other land plant groups diminished in its land coverage as a result. Modified from Lidgard and Crane, 1988.*

1.2 Plants and biogeochemical cycles

The rise of land plants through the Paleozoic Era is thought to have marked a turning point in Earth history, with profound impacts on the planet's surface chemistry and climate (Beerling and Berner, 2005). Plants likely had dramatic impacts on the composition of the atmosphere by drawing down and photosynthetically fixing atmospheric CO_2 into organic biomolecules, and by altering the continental weathering processes which are a key part of most major biogeochemical cycles (Algeo et al., 1995; Berner, 1997). Through their influence on atmospheric composition and biogeochemical cycles, it has been hypothesised that plants had a key role in driving both the Hirnantian (~445 Ma) and Late Paleozoic (~300 Ma) ice ages (Berner, 1997; Lenton et al., 2012) as well as mid-Paleozoic oxygenation of the atmosphere (Lenton et al., 2016) and the more recent Cenozoic cooling (Retallack, 2001; Epihov et al., 2017). The rapid growth of plants, therefore the increase in nutrient requirement requires either a larger source of nutrients or improved ability for nutrient recycling processes. The morphological and physiological innovation of plants involved in nutrient cycling is assumed to substantially impact global biogeochemical cycles (Read and Perez-Moreno, 2003; Von Bloh et al., 2018).

Bryophytes are globally abundant in diverse biomes, existing in all ranges of temperature and water availability. They contribute to above-ground biomass, enrich the soil with nitrogen by hosting nitrogen-fixing bacteria, control soil chemistry and nutrition, form biological crusts on dry substrates preventing soil erosion and accelerate silicate weathering (Cornelissen et al., 2007). Lenton et al. (2012) demonstrated that non-vascular plant colonisation is capable of amplifying silicate weathering by a factor of 1.75 resulting in a CO_2 drop from 14-16 present-day atmospheric levels (PAL) to 8.4 PAL (~5500 ppm to ~3200 ppm). They also proposed an increase influx of phosphorus to the oceans due to increased weathering of phosphorus on land. As the ocean becomes phosphorus-rich, oceanic productivity increases which leads to organic carbon burial. Bryophytes and their impact on oceanic productivity may have driven the short-lived Hirnantian glaciation and changed global biogeochemical cycles during the Late Ordovician. The expansion of deep rooting system during the Carboniferous would have also increased silicate weathering and released large amounts of nutrients into the soil and oceans. As plants became more productive, it is thought to have accelerated the drawdown of atmospheric CO_2 via the combination of enhanced silicate weathering, elevated marine primary productivity and sequestration of organic carbon in terrestrial plant biomass (Kenrick and Crane, 1997; Chen et al., 2021).

Vegetation changes during the Silurian and Devonian could have further impacted biogeochemical cycles as dominant plant groups, globally and regionally, evolved. For example, *Sphagnum* peat-mosses are particularly resistant to decomposition along with various bryophyte litter compared to tracheophytes (Cornelissen et al., 2007). The decay resistant, lignin-rich plants contribute lower biomass recycling compared to easily degradable plants such as angiosperms. The quick nutrient cycling, and vast presence of angiosperms allows for higher plant productivity which contributes to more biomass production in both aquatic and terrestrial settings (Dai et al., 2020). A turnover in ecology (i.e. a predominantly bryophytic area being replaced by tracheophytes or vice-versa) therefore could lead to different soil carbon and nutrient turnover rates hence ushering in new dynamics to existing processes in biogeochemical cycles.

How and when plants have evolved are key considerations when modelling their effect on long-term global climate. Discrepancies on the timing of evolutionary steps exist due to the incomplete fossil record (Wellman et al., 2013). Molecular phylogenetic studies provide one way of figuring out the timelines however the potential loss of key evolutionary components (such as the loss of stomata in some bryophytes) create alternative timelines and make it a challenge to re-create an accurate picture of the past (Morris et al., 2018; Harris et al., 2020).

1.3 Mycorrhiza

Plant nutrient assimilation usually occurs at the root hair surface via diffusion if nutrient ions are present in sufficient concentrations in the soil water (Jones and Dolan, 2012). The extremely immobile phosphorus (P) in soil and genetic variability in plants for P efficiency, present a greater limiting factor to plant growth than soil nitrogen (N) availability (Gilroy and Jones, 2000). Many plants are able to obtain key limiting nutrients, including N and P, by forming mycorrhizas; symbiotic associations between plant roots and certain groups of soil fungi (Hoysted et al., 2018). When mycorrhizas are formed, the extraradical fungal hyphae increases the absorptive surface area from which limiting nutrients beyond the plant root nutrient depletion zone can be absorbed. The uptake of nutrients from the soil occurs at the hyphal tip and via an electrochemical gradient of protons (H^+). The circulation of H^+ between the hypha and soil lowers the external pH of soil. High respiration rates of mycorrhizal fungi also contribute towards lowered soil pH, which in turn speeds up weathering and mobilisation of soil nutrients (Taylor et al., 2009). In addition to the nutritional benefits of this symbiotic relationship, mycorrhizal plants also gain improved water relations and some resistance to pathogens (Cairney, 2000; Behie and Bidochka, 2014). It is important to note however, that mycorrhizal associations do not necessarily present the plant with a greater competitive advantage against non-mycorrhizal plants when growing in optimal environmental conditions (i.e. abundant nutrient availability).

In exchange for supplying the host plant with soil nutrients, plants provide the fungi with organic carbon. Today, approximately 85% of all modern terrestrial plants are known to form mutualistic symbioses with soil fungi (Cairney, 2000; Goltapeh et al., 2008; Strullu-Derrien et al., 2018). Among the seven recognised types of mycorrhizal fungi (Table 1.3.1), arbuscular mycorrhizas (AM) have the most geographically widespread associations with plants followed by ectomycorrhizas (ECM, Figure 1.3.1) (Brundrett, 2002; Rimington et al., 2018). AM fungi are associated with 77% of angiosperms, 45% of 84 species of gymnosperms and 52% of over 400 species of ferns and lycopods (Taylor et al., 2009).

The mycorrhizal symbiotic function lies on a scale of parasitism to mutualism where benefit to either partner varies depending on a variety of factors, including nutrient and light availability which may dictate the degree of "exploitative cheating" (Kiers and van der Heijden, 2006; van der Heijden et al., 2015). Co-operation is a rare trait in nature as species are assumed to have selfish interests. Mutualism therefore is seen as an attempt by both partners to gain additional resources, while maximising benefits and minimising costs (Kiers and van der Heijden, 2006). Hence when environmental conditions favour one partner over the other, cheating may occur. For instance, 10% of studies indicate mycorrhizal fungi reduce plant growth as plants are not able to exclude fungal symbionts (van der Heijden., 2015). Similarly, plants form multiple and simultaneous symbiosis with a range of mycorrhizal fungi and have been shown to take sugars from neighbouring plants (Simard et al., 2012). The symbiotic relationship is more complex than plants favouring AM fungi that produce the most nutrients and vice versa. The dynamic balance of resource exchange under varying environmental conditions adds a layer of difficulty to modelling symbiotic behaviour.

Mycorrhiza	**Plant taxa**	**Fungal taxa**
Endomycorrhizas		
Arbuscular	Bryophyta Pteridophyta Gymnosperms Angiosperms	Mucoromycota*
Monotropoid	Monotropoideae	Basidiomycota
Ericoid	Ericales Gymnosperms	Ascomycota
Arbutoid	Ericales	Basidiomycota Ascomycota
Orchid	Orchidaceae	Basidiomycota
Ectomycorrhizas		
Ecto-	Gymnosperms Angiosperms	Basidiomycota Ascomycota Mucoromycotina*
Ectendo-	Gymnosperms Angiosperms	Basidiomycota Ascomycota Mucoromycotina*

Table 1.3.1. Seven types of mycorrhiza, associated fungal taxa and plant host taxa. *Traditional mycorrhiza classification consisted of two types: ecto- and endo-mycorrhizas however this was too general, hence each classification is subdivided into further classifications. *Recent reclassification of Glomeromycotina and Mucoromycotina into the phylum Mucoromycota. Table modified from Barman et al., 2016.*

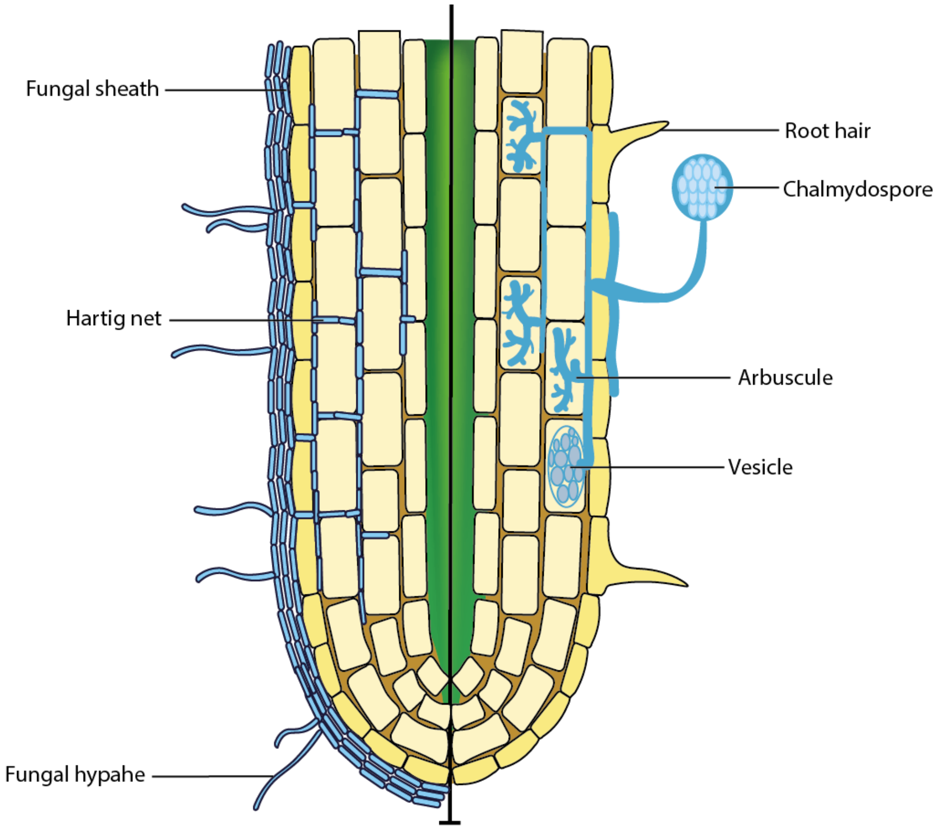

Figure 1.3.1. Different root associations present in ecto- and endo-mycorrhiza. *Simplified diagram showing ecto-(left) and endo-mycorrhizal (right) associations in blue with root tip in yellow. Green central region represents the xylem. Ecto-mycorrhizas are part saprophytic and form symbiosis with lateral roots by creating a network of mycelia around the epidermal and outer cortical cells (also known as the 'Hartig net') (Kenrick et al., 2012; Strullu-Derrien et al., 2018). Endo-mycorrhizas, such as arbuscular mycorrhizas, are obligate biotrophs (Rimington et al., 2018) and the symbiosis involves penetration of epidermal cells and formation of specialised branched structures known as arbuscules used for nutrient transfer, mainly phosphorous (Strullu-Derrien et al., 2018). Image modified from Kamal et al., 2010.*

Pirozynski and Malloch (1975) proposed the colonisation of land and the Phanerozoic “explosion” of life to have been made possible through symbiotic associations between semi-aquatic ancestral algae and aquatic fungi during the Silurian. Similarly, paleontological and molecular clock evidence suggest that the success of first land plants were most likely due to their involvement with AM associations (Taylor et al., 2009). Further fossil evidence from the Rhynie chert fossils indicate early plant-fungal interactions to be present around 407 Ma and the type of fungal structure to be similar to present-day AM fungi (Harper et al., 2017). The chert contains fossils of ancient land plants that include preserved individual cells of *Aglaophyton majus*, a primitive vascular plant, with intracellular fungal structures resembling the arbuscules of AM fungi, exclusive to Glomeromycotina (Field et al., 2015; Strullu-Derrien et al., 2018). More recent documentation of mycorrhizal associations in Rhynie plants however suggest Mucoromycotina associations to also be present. The two are now established under the phylum Mucoromycota (Strullu-Derrien et al., 2019).

Mucoromycota-like associations are thought to be present as early as 460 Ma while molecular clock data puts AM symbiosis at 462 Ma (Taylor et al., 2009; Strullu-Derrien et al., 2019). Mucoromycotina are coil forming endomycorrhizal species that are saprophytic and biotrophic unlike Glomeromycotina which are exclusively obligate biotrophs (Hoysted et al., 2018). Glomeromycotina, for a large part of their life, cannot live independently from plant roots and are unable to decay soil organic matter (Taylor et al., 2009). In contrast, some Mucoromycotina can form both ecto- and endomycorrhizal associations (Figure 1.3.1), with early diverging liverworts and therefore are thought to have diverged earlier than Glomeromycotina (Hoysted et al., 2018). Both form associations with a wide range of modern day vascular and non-vascular plants (Hoysted et al., 2019) however the difference in plant dependency suggests Mucoromycotina as the ancient fungal lineage. Regardless, it is clear that mycorrhizal symbiosis, possibly from the phylum Mucoromycota, play a large role in the terrestrialisation of plants, whether by creating nutrient-rich soils or by directly providing nutrients to early land plants that lacked complex root systems.

Considering the coexistence of plants and fungi (Figure 1.1.3), the interdependency between the two for nutrients and their widespread relationship, it is very plausible to hypothesise that the symbiosis played a key role in the successful colonisation of land by plants. Nutritional aid from fungi potentially could have allowed the initial growth and expansion of land plants, resulting in a progressive increment of global primary productivity. With help from mycorrhizal symbiosis, plants are able to use previously inaccessible nutrients for plant growth. Therefore, plants could have sequestered more carbon as organic matter than they were capable of on their own (Sulman et al., 2019). Overall, long-term climate change could have occurred due to the reduction in atmospheric CO_2 from enhanced processes such as silicate weathering (see Chapter 1.4.2) and increased rate of carbon burial. Plants with mycorrhizal symbiosis incur the cost of nutrient availability in carbon. As plants grow and their nutrient need increase, plants transfer more carbon to their fungal partners. This creates a large carbon sink as plant and fungal biomass due to increased plant productivity (Mills et al., 2018; Puttick et al., 2018). Through their involvement in plant nutrient acquisition, the role of mycorrhizal fungi in shaping the climate may be equally as significant as that of land plants.

1.3.1 Mycorrhizal associations and biogeochemical cycles

Mycorrhizal fungal mycelia hyphae (Figure 1.3.1) can link neighbouring plant roots together in a mycorrhizal network (Simard et al., 2012). These networks have been shown to facilitate the establishment, growth and survival of individual plants in a wide range of ecosystems and so mycorrhizal networks have the ability to influence ecosystem composition by favouring certain plant groups over others (Simard et al., 2012). The global presence of these networks, with absence only in areas of high soil disturbance, and vast associations with terrestrial plants suggests mycorrhizal symbiosis and mycorrhizal communities play a significant role in the global C, N and P cycles (Table 1.3.2; van der Heijden et al., 2015).

Mycorrhizal fungi redistribute organic C throughout the soil, feeding into the soil organic matter pool which mainly recycles carbon over short timescales (Jansa and Treseder, 2017). Experiments and field studies have shown plants to allocate between 10 – 20% of their photosynthates to AM fungal partners while EM fungi and ericoid mycorrhizal fungi receive from 20 – 50% (van der Heijden et al., 2015). Aboveground biomass in vegetation associated with mycorrhiza is estimated to be 347 GtC, with majority of it being found in tropical forests (Soudzilovskaia et al., 2018). With almost all terrestrial plants from a range of ecosystems forming symbiosis with mycorrhizal fungi, it is clear that there is a role (both direct and indirect) to be played by mycorrhizas within the global C cycle. Taylor et al., (2009) suggest the evolution and spread of EM fungi across ecosystems to be the main mechanism that enhanced silicate weathering during the Mesozoic, as opposed to the spread of angiosperms and their related enhancement of weathering. Currently, studies involving the changes in atmospheric CO_2 mention mycorrhiza but do not explicitly model hyphal networks responsible for some portion of global biogeochemical cycles (Jansa and Treseder, 2017).

Ecosystem process	Mycorrhizal type	Estimated mycorrhizal contribution to nutrient cycling processes (%)
Carbon cycle		
Plant productivity	AM	0-80
	ECM	0-80
Decomposition	AM	0-10
	ECM	0-30
Nitrogen cycle		
Plant nitrogen acquisition	AM	0-20
	ECM	0-80
Reduction of nitrogen	AM, ECM	0-50
Denitrification, N_2O losses	AM, ECM	Unknown*
Phosphorous cycle		
Plant phosphorous uptake	AM	0-90
	ECM	0-70

Table 1.3.2. Influence of mycorrhizal fungi on biogeochemical cycles processes. *Estimated influence of mycorrhizal associations on various nutrient cycle processes (carbon, nitrogen and phosphorous) by ECM and AM associations. Estimates are widely ranged as mycorrhizal contribution depends on soil disruption and nutrient availability. AM, arbuscular mycorrhiza; ECM, ectomycorrhiza. *Unknown due to lack of data on nutrient loss. Modified table from van der Heijden et al., (2015).*

Ecosystems can be dominated by different communities of mycorrhizas; tropical by AM, temperate and boreal by ECM (Soudzilovskaia et al., 2018). The distribution of the dominant type of mycorrhizal fungi depends on the limiting nutrient in soil for plant growth. AM fungi contribute towards phosphate cycling by mobilising P under low soil phosphorous levels (Smith et al., 2011). Hence many tree species in P-depleted tropical soils form AM associations (Taylor et al., 2009). EM fungi form associations with boreal and temperate dominant trees such as pines and oaks, typically in soil limited by N but not P (Taylor et al., 2009). Exudates secreted by EM fungi facilitate weathering of mineral surfaces to release N and P. Enzymes, such as phosphomonoesterase, hydrolyse organic P compounds in soil into their inorganic forms that are available for plant uptake (van der Heijden et al., 2015). AM fungi contribute up to 90% of plant P whereas EM fungi can acquire up to 80% of plant N and P (van der Heijden et al., 2015). Along with the active uptake of nutrients, mycorrhizal fungi also prevent nutrient leaching from soils which proves important in nutrient-poor ecosystems where plant productivity is nutrient limited (van der Heijden et al., 2015). In both cycles, mycorrhizal fungi act as a nutrient enhancer which increases the productivity of the host plant.

In terms of evolution, Glomeromycotina and Mucoromycotina fungi are hypothesised to form mutualistic mycorrhizal-like associations with early branching plant lineages (Strullu-Derrien et al., 2019). The two associations differ in their symbiotic functional efficiency, i.e. the amount of nutrient (both N and P) gained by the host plant for each unit of carbon transferred to the fungal partner, depending on atmospheric CO_2 concentrations. Field et al., (2015) demonstrated Mucoromycotina fungi, under ambient atmospheric CO_2 concentration (440 ppm), to have higher symbiotic functional efficiency compared with earlier Phanerozoic CO_2 concentration

(1500 ppm). Mucoromycotina partners received seven times more carbon at 1500 ppm compared to 440 ppm. In liverwort-Glomeromycotina associations, the opposite trend was observed as phosphorous-for-carbon exchange decreases at 440 ppm (Field et al., 2015). Dual associations incurred a higher carbon cost for plants however that may be countered by benefits gained such as decreased exudates in the soil that may aid other saprophytic soil microorganisms and pathogens (Field et al., 2016). Although it is unclear which fungal symbioses is ancestral or if the two co-existed, the presence of dual associations in plants suggests the existence of large underground biomass and more efficient nutrient cycling than can be achieved by non-mycorrhizal plants.

Plants that form AM symbioses tend to have low specificity (i.e. are susceptible to colonisation by AM of different taxa) however some can have preferential AM fungi, resulting in different densities of colonisation (Smith et al., 2011). Growth responses, and therefore carbon-nutrient exchange, also varies between plant species and AM species (van der Heijden et al., 2015), making it difficult to accurately simulate heterogenous ecosystems. Plant species sharing compatible mycorrhizal fungi have also been reported from a range of different ecosystems including temperate and tropical forests (Simard et al., 2012) suggesting a high probability of mycorrhizal network formations. Mycorrhizas can therefore have a varying impact depending on the dominant ecosystem and mycorrhizal community which needs to be considered when looking at global nutrient cycles over time.

Mycorrhizal species can co-colonise the same plant (Kiers et al., 2011), vary widely in their host specificity (van der Heijden et al., 2015), and create underground networks (Simard et al., 2012) making it difficult to decipher specific roles and their individual impact on processes. The dynamic turnovers of plants and fungal species that hold various amount of biomass, combined with underground networks and their influence on plant communities, prove a challenge to be modelled on long timescales.

1.3.2 Mycorrhizal symbiosis conclusion

Mycorrhizal-like fungi have been present on land and formed symbiotic relationships with plants since at least the Ordovician (Harper et al., 2017). The relationship between mycorrhizal fungi and plants is not straightforward as multiple species of mycorrhizal fungi can form symbioses with a singular plant. Vice versa, plants are able to form multiple symbioses with different species of fungi, although it has been shown that plants show selectivity in some cases (Kiers et al., 2011). Mycorrhizal fungi increase establishment and growth of plants across a range of ecosystems including forest, woodland and grassland (Simard et al., 2012). Their underground hyphal networks have been hypothesised to drive plant population biology and community ecology by affecting dispersal and establishment and regulating plant coexistence (Tedersoo et al., 2020). Although the importance of mycorrhizal existence has been long acknowledged, models of mycorrhizal nutrient cycling have only recently been developed (Schnepf and Roose, 2006; Sulman et al., 2019). Sulman et al., (2019) are among the pioneers in incorporating mycorrhizal associations into dynamic global vegetation models. Their results suggest carbon sequestration to be higher in plant communities that hosted ecto-mycorrhizal fungi as they enhance soil N compared to AM fungi. It is undeniable that a role is to be played by the evolution of mycorrhiza and their involvement in global primary productivity, nutrient availability, silicate weathering, and ultimately climate.

1.4 The long-term carbon cycle

The long-term carbon cycle regulates the concentration and cycling of atmospheric CO_2, the greenhouse gas responsible for altering surface temperatures and global climate on multimillion-year timescales (Beerling and Berner, 2005; Royer, 2006; Taylor et al., 2009). Succinctly, the long-term carbon cycle can be generalised into two key reactions:

$$CO_2 + CaSiO_3 \leftrightarrow CaCO_3 + SiO_2 \qquad (1.4.1)$$

$$CO_2 + H_2O \ \leftrightarrow CH_2O + O_2 \qquad (1.4.2)$$

Equation 1.4.1 represents silicate weathering on land responsible for removing atmospheric CO_2. Going from left to right, silicates such as $CaSiO_3$ react with dissolved carbon dioxide to trap carbon in the form of $CaCO_3$ (see Chapter 1.4.2). Equation 1.4.2 represents global photosynthesis (minus respiration) and burial of organic matter (represented by CH_2O) in sediments. Going from right to left, oxidative weathering of organic matter that is exposed by erosion slowly releases sequestered carbon (Berner, 2003). Environmental factors such as temperature and runoff can affect both of these equations, i.e. higher runoff leads to increased plant productivity, burial of organic matter, and also higher rates of silicate weathering.

The atmospheric concentration of CO_2 and O_2 over geological time is controlled by a combination of Calcium-Magnesium (Ca-Mg) silicate weathering, carbonate weathering, volcanic and metamorphic degassing, carbon burial in sediments, oxidative weathering of organic matter and thermal decomposition (Figure 1.4.1; Berner, 2006). Biotic factors regulating CO_2 concentration includes photosynthesis, respiration and enhancement of Ca-Mg silicate weathering via root systems and its associated mycorrhizal fungi (Berner, 2003; Berner, 2006; Taylor et al., 2009). The following section details how these processes occur and their individual contribution towards atmospheric CO_2 fluctuations.

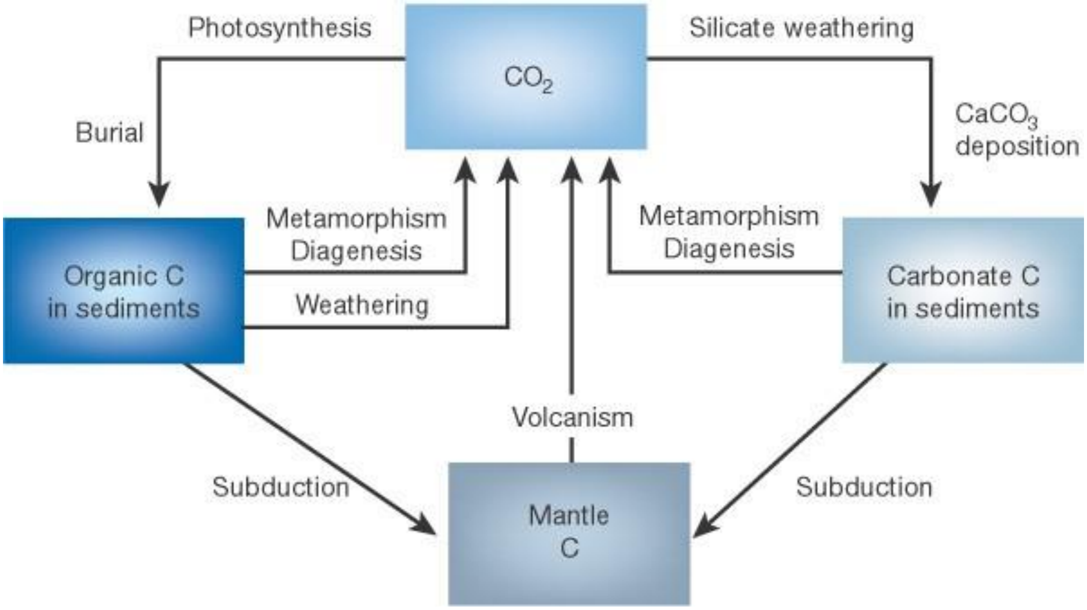

Figure 1.4.1. Flow diagram of the long-term carbon cycle. *CO_2 from the atmosphere is removed via photosynthesis and silicate weathering. The reverse is achieved via metamorphism and diagenesis: alteration of rocks due to temperature and pressure that releases CO_2 in the process, and volcanism. Image from Berner, 2003.*

1.4.1 Organic carbon burial

The largest surface pool of carbon lies in the oceanic reservoir and it plays a major part in determining the concentration of atmospheric CO_2. CO_2 is rapidly exchanged between the sea-air interface, therefore resulting in an approximate equilibrium between surface ocean water and atmospheric CO_2; the slight difference occurring due to processes such as mixing between shallow and deep layers of the ocean, that take CO_2 to deeper water (Post et al., 1990). Although the complex carbon cycle involves oceanic-land and oceanic-atmospheric exchanges, my focus will be on the role of plants in the terrestrial carbon cycle.

Photosynthesis and ecosystem respiration are the largest terrestrial carbon fluxes. The density or quantity of biomass determines the rate and magnitude of autotrophic respiration and therefore the amount of carbon being emitted into the atmosphere through burning (CO, CO_2) and decay (CH_4) (Houghton et al., 2009). The diversification and expansion of tree species, especially lignin-rich gymnosperms, during the Carboniferous and Permian (350-280 Ma) led to the storage of carbon in the form of lignin, a relatively non-biodegradable matter (see chapter 5.7.1, Dai et al., 2020). The burial of lignin, alongside other plant products, in a water-logged, warm environment promoted the formation of what are now coal basins, and thereby increased global organic carbon burial (Berner, 2003). The burial of carbon changes atmospheric composition as it removes CO_2 and adds oxygen (Equation 1.4.2). The reduction in the greenhouse gas CO_2 then promotes global cooling (Berner, 2003).

Biomass is related to vegetation structure which varies spatially, temporally and with ecosystem types due to various environmental limitations. Boreal, temperate and tropical forests have high above-ground biomass due to high productivity rates and storage of carbon as woody matter (Lefsky et al., 2002). For example, <5 megagram carbon per hectare (MgC ha^{-1}) is present in treeless grasslands, croplands and deserts whereas >300 MgC ha^{-1} is present in some forests (Houghton et al., 2009). The difference in plant communities as a result of differing optimum environments show spatial variability in carbon sequestration. Over time, changes in climate continue to shift ecosystems between boreal, temperate and tropical biomes leading to the replacement of dominant plant species (Gonzalez et al., 2010). As vegetation structure evolves spatially and temporally, physiological and metabolic changes of plant structure affect the rate of photosynthesis, respiration, growth, decay and therefore the rates of carbon accumulation and loss (Houghton et al., 2009). Biomass is heavily dependent on the spread and type of vegetation, making it a fluctuating source and sink of carbon. Therefore, the need for a spatial heterogeneity of biomass in biogeochemical models is necessary to more accurately represent the impact of changing vegetation on the global climate.

1.4.2 Silicate weathering

Weathering can be both a physical and chemical process; physical weathering involves the breakdown of larger material via mechanistic methods (e.g. moving water, falling off cliffs) whereas chemical weathering involves a change in the chemical composition under the influence of agencies (e.g. plant released enzymes) (Jackson and Sherman, 1953). Areas of high physical erosion are seen to correlate with high chemical erosion as physical weathering provides a newer mineral surface area and discourages the formation of thick soils, allowing for chemical weathering amplification. In terms of the global C cycle, areas where rocks and soils are mechanically fragile, a combination of temperature-runoff and physical denudation (erosion) are key factors in determining silicate weathering rates (Gaillardet et al., 1999). Among the two processes, chemical weathering provides an important feedback mechanism towards the control of atmospheric CO_2

Ca-Mg silicate weathering is thought to control global climate over long timescales via its consumption of atmospheric CO_2 (Walker et al., 1981; West et al., 2005). The process involves atmospheric carbon being converted into bicarbonate (HCO_3^-) and carbonate (CO_3^{2-}) ions in soil and groundwater, its transportation to the sea where it is ultimately stored as carbonates (calcium and magnesium) in the oceans (simplified representation of silicates in Equation 1.4.1 and 1.4.3; Taylor et al., 2009; Kenrick et al., 2012). Going from right to left, equations 1.4.1 and 1.4.3 represent deep burial and thermal decomposition of carbonates and release of CO_2 into the atmosphere and oceans.

$$CO_2 + MgSiO_3 \leftrightarrow MgCO_3 + SiO_2 \tag{1.4.3}$$

Global CO_2 levels stabilise as increased CO_2 concentrations leads to more efficient silicate weathering and higher soil acidity. An acidic environment drives the dissolution reaction and therefore increases the rate of silicate weathering (West et al., 2005). Higher temperatures also accelerate mineral dissolution (Li et al., 2008). This negative feedback on CO_2 prevents greenhouse conditions spiralling into extreme temperatures and creates a habitable environment for life (McKenzie et al., 2016). An alternative theory to this steady-state hypothesis is the ‘continental uplift hypothesis’ whereby the tectonic uplift increases weathering rates and influences climate without any metamorphic degassing to negate the removal of CO_2 (see chapter 1.4.3; Taylor et al., 2009).

The evolution of roots, and their associations with fungi, are also considered to be biological enhancers of weathering, promoting breakdown of rocks via physical soil disruption and acidification through root exudation of organic acids and other metabolites (Berner et al., 1991; Kenrick et al., 2012). Roots contribute towards soil erosion as rocks are weathered, ground surfaces are reshaped, and soil is redistributed across landscapes which in turn also controls sediment delivery to the ocean and oceanic productivity (Berhe et al., 2018). Rocks are physically broken apart by roots and symbiotic fungi to expose greater surface area to organic acid compounds released by plants and associated fungi (Porder, 2019). However, erosion disrupts soil aggregates and structural stability which reduces the nutrient holding capacity of soil, making less nutrients available for plants. Mycorrhizal networks counter this erosion via increasing soil aggregate frequency and stability (Simard et al., 2012). Some processes by which mycorrhizal networks increase soil aggregation are: root entanglement of host plants (branching and thickness of roots used to increase soil compression), influencing localised soil water content (mycorrhizal fungi dry soils near roots which promotes binding between root exudates and clay particles), and increasing root decomposition (fungi contribute to the increase in organic matter to create soil aggregates) (Rillig and Mummey, 2006). Roots and mycorrhizal fungi work together to increase nutrient availability in soil via weathering without compromising soil structure (i.e. preventing extreme drying out of soils and conversion of soil into sand). The increase in the capacity of land to support plant growth increases biomass production (and therefore leads to higher organic carbon burial) but also increases nutrient influx to the oceans which can contribute towards fluctuating atmospheric CO_2.

Biomass-related silicate weathering can act as a carbon sink with a potential consumption rate of 7.9 Tg CO_2 year^{-1} within forests (Song et al., 2018). In order to obtain biomass, plants must first produce net primary productivity (NPP), which refers to the net carbon stored as new plant material (Zhang et al., 2009). An increase in biomass (the accumulation of carbon) leads to an increase in nutrient demand hence higher rates of NPP is required. Present day weathering often show high productivity rates to correlate with high silicate weathering rates depending on lithology and plant functional type (Taylor et al., 2012). Weathering rates can also be dampened by biomass volume as it protects weathering material from the effects of precipitation (Oeser and Von Blanckenburg, 2020). Both NPP and biomass play a role in amplifying/dampening silicate weathering rates however coupled models such as the Hadley Centre general circulation model - Sheffield dynamic global vegetation model use NPP (Taylor et al., 2012).

The direct enhancement of weathering occurs via plants and soil microbe respiration as CO_2 is released into the soil, increasing soil acidity, making weathering of rocks easier. Production of organic acids, root respiration and organic degradation are ways in which vegetation increase soil acidity to 10 – 100 times that of the atmosphere (Brady and Carroll, 1994). Plants are also thought to have indirectly enhanced weathering by altering global hydrology through the evolution of stomata, vasculature and deep roots that access previously inaccessible groundwater. Such evolutions led to higher evaporation rates and the introduction of transpiration to global hydrology (see Chapter 5.6; Ibarra et al., 2019).

The Devonian is considered to be a critical interval during which the initial diversification of plants and the evolution of roots occurred (Kenrick and Crane, 1997). A noticeable drop in atmospheric CO_2 proxy concentrations during the late Devonian could be the result of the appearance and geographical expansion of large deep-rooted trees which increased river nutrient concentrations and enhanced marine productivity, therefore triggering the late Devonian anoxic events (Taylor et al., 2009). Ibarra et al., (2019) found global transpiration rates and an increase in soil CO_2 levels to have more than doubled weathering fluxes by deep-rooted vascular plants during the Devonian. An ecosystem dominated by angiosperms during the late Cretaceous and Cenozoic are also hypothesised to be capable of further increasing weathering concentrations by 7-55% as a result of expanding silicate weathering area. Higher transpiration rates lead to increased global precipitation and transport of water vapor into continental interiors that were previously shielded from weathering. In addition, the co-evolution of plants and mycorrhizal fungi can increase soil phosphorus concentrations, enhancing plant growth and further increasing weathering rates.

1.4.3 Tectonic movements

Metamorphic degassing from carbonates and organic matter along volcanic arcs and tectonic movement (subduction of oceanic crust and seafloor spreading) contribute to atmospheric CO_2 (Mills et al., 2014; Marcilly et al., 2021). As tectonic plates shift, the production and destruction of mountain ranges influences weathering but more importantly, powers arc-volcanism whose emissions are the main source of CO_2 (Marcilly et al., 2021). Volcanic eruptions, commonly formed above subduction zones, are explosive events that exude CO_2, volatiles and magma to the surface (Plank and Manning, 2019). Current continental volcanic arcs are estimated to emit as much as ~150 teragrams C per year (TgC year^{-1}) compared to ocean ridges (12 – 60 TgC year^{-1}) and oceanic volcanoes (1 – 30 TgC year^{-1}) (McKenzie et al., 2016). The spatial and temporal variability of volcanoes depends on tectonics which ultimately influences the carbon cycle at non-uniform intervals (McKenzie et al., 2016). The amount and timing of the volcanism can influence global climate on both long and short timescales (Liu et al., 2019).

As large volumes of carbon is emitted by volcanoes, equally large volumes are consumed by the mantle at subduction zones although not at the same time (Plank and Manning, 2019). Carbon that enters the subduction zones is spatially variable as it is often made up of various amounts of different carbonate rocks and reduced organic carbon (Liu et al., 2019). The process is however inefficient as metamorphic decarbonation releases some of the carbon back into the subduction zone to be carried out in volcanic plumes (Liu et al., 2019; Plank and Manning, 2019).

Silicate weathering is also influenced by plate tectonics and continental paleogeography. Earth's surface can be raised to form broad plateaus or mountains via uplift of tectonic plates. The process creates exposed land area of unweathered rocks at higher elevations where steep slopes and lack of vegetation (i.e., no roots to form aggregates or vegetation cover to protect rocks from rainfall) promote higher rates of weathering (Ruddiman and Prell, 1997). As larger land masses collated around the equator, the formation of Pangea during the Permian consisted of various uplifts to create vast mountain ranges (Scotese and Langford, 1995). The larger total land area exposed to equatorial climate (warm and wet conditions) hypothetically should increase potential silicate weathering and therefore the drawdown of CO_2. However, the reduction in rainfall and runoff in the interior of Pangea formed large arid areas where silicate weathering was limited as the reaction requires an aqueous environment (see Chapter 1.5; Marcilly et al., 2021).

Uplift combined with strong monsoonal rainfall increases the intensity of silicate weathering. Summer monsoons are created by the rising of hot air and the inflow of cool, moist air from the ocean which causes heavy rainfall and enhances soil weathering rates (Ruddiman and Prell, 1997; Li et al., 2008). A more recent example of this interaction is seen in the Tibetan Plateau uplift and the Asian monsoon circulation. Large volumes of water and moisture delivered by the East Asian summer monsoon promoted silicate weathering occurring at the exposed upper crustal rocks of the Tibetan Plateau (Yang et al., 2021). As explained above, silicate weathering acts as a carbon sink which lowers global temperatures. Tectonic-atmosphere interactions therefore can create new CO_2 sinks capable of shifting the carbon balance enough to cause global cooling.

1.5 Phanerozoic Earth History

Earth's climate is tightly linked to the global carbon cycle through the greenhouse effect of atmospheric CO_2. Major changes in Earth's biosphere have occurred during the Phanerozoic Eon (541 Ma to present). Global temperatures over the Phanerozoic show a pattern of icehouse and hothouse climates (Figure 1.5.1 and 1.5.2 C, Scotese et al., 2021) due to processes that change atmospheric CO_2 concentrations. Changes in the Phanerozoic continental configuration (Figure 1.5.1 and 1.5.2 E), especially the formation of the Pangea supercontinent, its breakup and eventual spread to present day configuration, involves processes that contribute towards CO_2 fluctuations which has helped shape present day climate. These fluctuations in temperature, hydrology and geography in turn presents the existing flora with new challenges to adapt and survive. For example, in the event of mass extinctions, a dramatic turnover in flora and fauna is observed.

The main driver of climate change during the Phanerozoic is atmospheric CO_2 concentration (Royer, 2006). Earth has undergone ‘icehouse’ and ‘greenhouse’ intervals that closely relate to changes in the partial pressure of atmospheric CO_2 (Figure 1.5.1 and 1.5.2; McKenzie et al., 2016; Mills et al., 2019). Changes in atmospheric CO_2 are related to long-term processes of carbon exchange due to tectonic degassing (volcanic and metamorphic outgassing), organic carbon burial and silicate weathering (Berner et al., 1991) (see Chapter 1.4). Atmospheric CO_2 also provides additional radiative forcing during a less luminous ancient sun (Kasting, 1989; Mills et al., 2019), strongly influencing glaciation history, and climate and ecosystem dynamics.

Paleogeography also plays a key role in climate change via contributions towards the carbon cycle. Paleogeography refers to past continental configurations which are often reconstructed to investigate paleoclimatology, biogeography, sedimentation and sea level variation through time (Barron et al., 1981). Changes in paleogeography occur via tectonic plate movement which can push land surfaces together (plate boundary collision and uplift or subduction) or pull them apart (seafloor spreading) (Figure 1.5.3; Scotese, 2021). The process is slow yet has profound effect on the global carbon cycle as it controls degassing and carbon burial rates (Goddéris et al., 2014; Marcilly et al., 2021). Paleogeography also controls global land area and hence the area affected by above-sea processes such as weathering via rainfall (Otto-Bliesner, 1995). The distribution of the land mass modifies regional and global climate through changes in oceanic circulation, albedo feedbacks and direct impacts on the precipitation/evaporation balance (Goddéris et al., 2014).

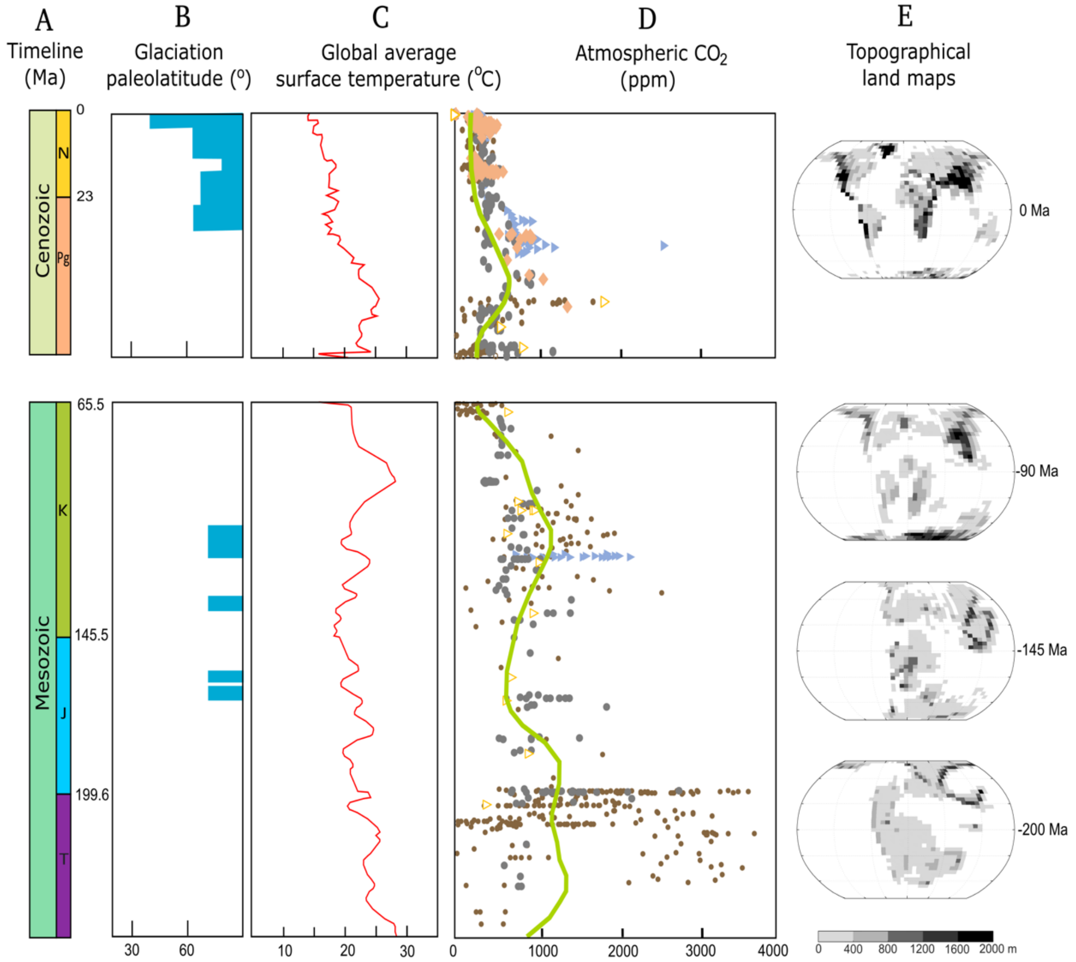

Figure 1.5.1. Cenozoic and Mesozoic ice line, temperatures, CO_2 level and topographical maps. *Graphs continue into figure 1.5.2.* ***(A)*** *Timeline of the Mesozoic and Cenozoic eras and periods. Ma: million years ago.* ***(B)*** *Period of existence of ice caps according to geological records.* ***(C)*** *Global average surface temperature derived from paleo-Köppen belts and oxygen isotopes.* ***(D)*** *CO_2 concentration as predicted from proxies (paleosols, alkenons, stomata, boron and liverworts). Data taken from Foster et al., 2017. CO_2 trendline (green) taken from Mills et al., 2019.* ***(E)*** *Topographical maps illustrating land configuration and elevation changes as Pangea separates.*

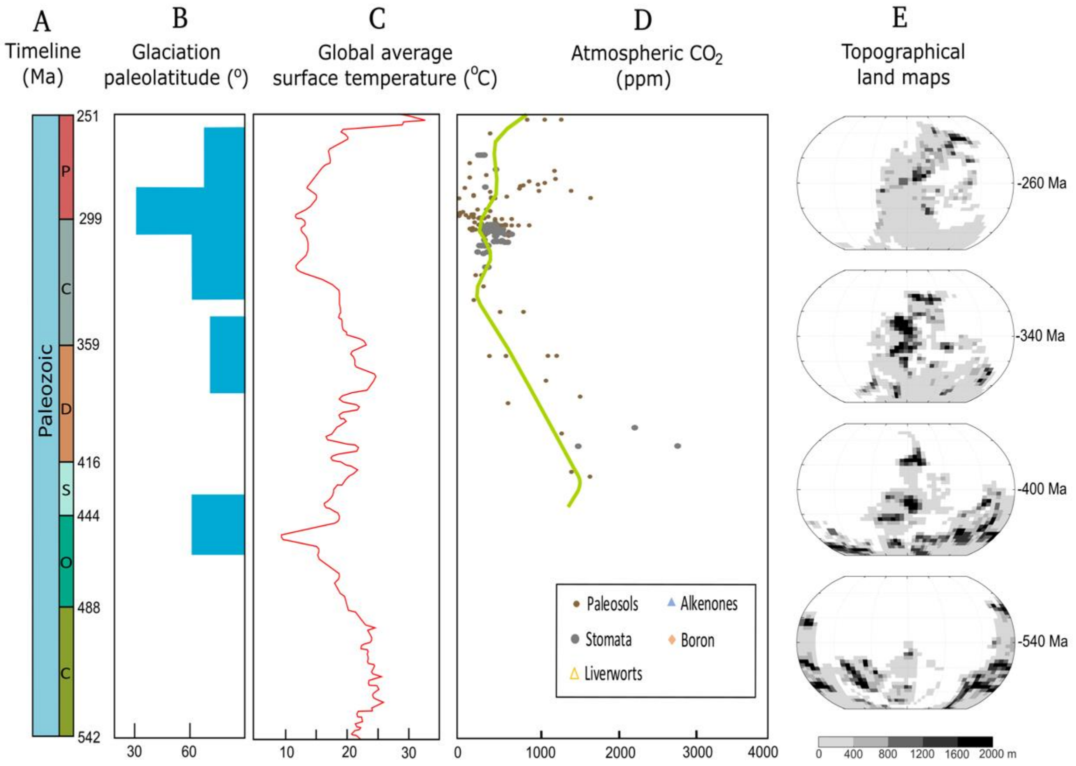

Figure 1.5.2. Paleozoic ice line, temperatures, CO₂ level and topographical maps. *Continued figure from figure 1.5.1* ***(A)*** *Timeline of the Paleozoic era and its periods.* ***(B)*** *Existence and extent of ice caps according to geological records.* ***(C)*** *Global average surface temperature derived from paleo-Köppen belts and oxygen isotopes. A large peak is observed at the end of the Permian.* ***(D)*** *CO_2 concentration as predicted from proxies (paleosols, alkenons, stomata, boron and liverworts). Data taken from Foster et al., 2017. CO_2 trendline (green) taken from Mills et al., 2019.* ***(E)*** *Topographical maps illustrating the change in land configuration and elevation along with the formation of Pangea.*

During the late Precambrian, the supercontinent Pannotia is hypothesised to have begun breaking and forming new ocean basins, with Gondwana (a large assembly of continents including Africa, Antarctica, Australia, India and South America) dominating the Southern Hemisphere (Blakey, 2008; Scotese, 2021). During this period, seafloor spreading increased, releasing CO_2 into the atmosphere and the rise of sea level warmed Earth to create the Cambro-Ordovician hothouse. As Earth moved into the Ordovician glaciation period, it is thought that extensive mountain building via plate tectonic movement, could be responsible for the cooling trend. However, paleogeographic changes are unlikely to be the sole cause of the glaciation due to its short-lived nature (<1 million years). Rather a combination of continental movement through the intertropical convergence zone, an area of high rainfall, and the evolution of first land plants could have enhanced weathering, lowered atmospheric CO_2 and promoted the onset of the late Ordovician glaciation (Lenton et al., 2012; Scotese, 2021). The following subsections look at Phanerozoic temperature, CO_2 levels and paleogeography for each era.

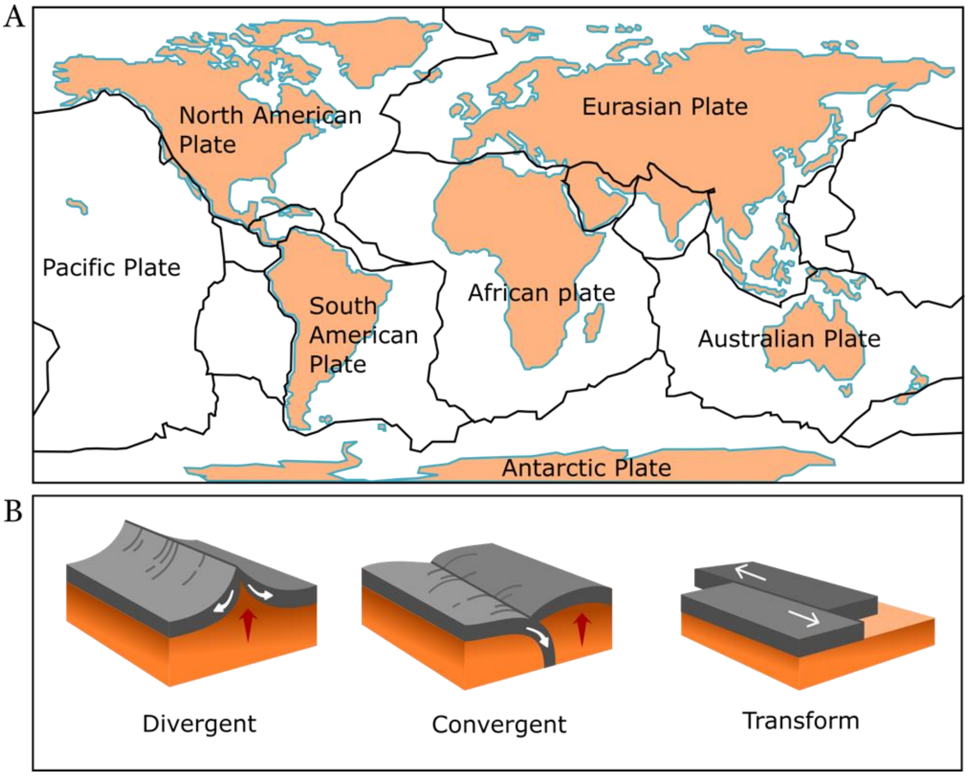

Figure 1.5.3. Present day major plate tectonic boundaries and types. (A) *Map of present-day continental configuration and the seven major plate boundaries.* ***(B)*** *Schematic representation of the three main types of plant boundaries. Divergent: two plates move away from each other creating troughs. Convergent: two plates move towards each other leading to either formation of mountains or subduction of denser plates. Transform: two plates move alongside each other. Grey = plate, orange = lithosphere. Image modified from Duarte and Schellart (2016).*

1.5.1 Paleozoic Era

The Cambrian, according to model predictions (Berner and Kothavala, 2001; Lenton et al., 2018), had the highest atmospheric CO_2 concentration during the Phanerozoic and is characterised by a warm, ‘greenhouse’ climate. Cooling then occurred towards the late Ordovician leading to the Hirnantian glaciation (McKenzie et al., 2016; Scotese et al., 2021). This short glaciation event at the end of the Ordovician may have occurred due to a combination of reduced CO_2 degassing, enhanced silicate weathering and increased organic burial, which reduced atmospheric CO_2 levels, cooling the planet and leading to extinction events (Algeo et al., 2016). Early non-vascular plants were also present on terrestrial land as evident by fossilised cryptospores from the Early Ordovician (Kenrick et al., 2012) and could have further enhanced the cooling effect via increased silicate weathering. Lenton et al. (2012) explored the possibility of silicate weathering enhancement by the presence of non-vascular plants between 475 and 460 Ma using the COPSE model. With land colonisation at 15%, the global average silicate weathering was amplified by a factor of 1.75, leading to a sufficient drop in CO_2 to ~8 PAL (from ~5500 ppm to ~3200 ppm) for the start of a glaciation.

Following the Late Ordovician mass extinction event, where an estimated ~85% of marine species died (Sheehan, 2001), temperatures rose to ~20°C over the Silurian (Figure 1.5.2). Major changes in the global carbon cycle and paleo-seawater temperatures during this period are linked to bio-events such as faunal turnover and carbon burial (Trotter et al., 2016). The Silurian contains a series of oceanic faunal and ecosystem evolution and extinction, perhaps due to a generally unstable marine environment (Calner, 2008). This created changes in the ocean-atmosphere carbon cycle by influencing the primary productivity of oceans which ultimately affected the climate. Changes to the global carbon cycle were also occurring on land due to the appearance of land plants and their expansion, which led to increased carbon sequestration (Berner, 2003; Algeo et al., 2016). Movement of unsettled continents during the Silurian was higher than other time periods, leading to fluctuating weathering and erosion processes, and transportation of continental sediments to the ocean (Calner, 2008). Gondwana persisted to be the largest land mass while the collision of Laurentia and South America created an extensive mountain range in the tropics and subtropics (Scotese, 2021; Calner, 2008).

By the mid-Carboniferous, the Pangean supercontinent was beginning to assemble with the collision of Laurussia and Gondwana (Grossman et al., 2002). The collision of continents led to mountain and volcanic ranges being built along the equator along with changes in sea levels and patterns of erosion and deposition along coastlines (Scotese, 2021). The northward movement of continents during the Carboniferous and into the early Permian, led to the Central Pangean Mountains lying across the equator (Figure 1.5.4) which accelerated weathering processes of newly exposed silicate rocks (Scotese, 2021). Exposure of Gondwana ice masses to latitude-controlled warmer climates would be also be a direct cause of melting ice sheets without the need for an increase in greenhouse gases (Beerling, 2002). The shift towards the equator created large tropical regions with vast equatorial rainforests on either side of the Central Pangean Mountains which reduced surface albedo, the fraction of sunlight reflected by Earth’s surface, leading to a warmer climate (Beerling, 2002; Scotese, 2021). Warmer, wetter conditions led to the expansion of land plants and burial of large amounts of carbon as coal (Scotese 2021). Changes in land structure and orientation led to changes in global temperature and precipitation (Ziegler et al., 1979). The effects of paleogeographic changes are most prominent during this period where it seems to be the main driver of regional and global climate.

A general decline is observed in atmospheric CO_2 concentration in paleosol and sparse stomatal index proxy data over the Devonian and Carboniferous, with a sustained period of low CO_2 during the Permo-Carboniferous (approximately 300 Ma; Figure 1.5.2). Isotopic studies of brachiopods from equatorial regions show an increase in $\delta^{13}C$ of seawater, suggesting enhanced burial of organic carbon in sediments and a shift from greenhouse to icehouse climate (Grossman et al., 2002; Scheffler et al., 2003). The reduction in atmospheric CO_2 contributed to a much cooler climate with large ice sheets forming over Gondwana (Beerling, 2002), and the beginning of the longest cold climate interval: the 'Late Paleozoic Ice Age' (Scotese et al., 2021). Paleogeography played a key role in cooling the planet during the Late Paleozoic Ice Age as the existence of a large part of Gondwana in the low-latitudes led to a series of ice sheet formation on Gondwanan continents, spanning almost 100 million years (Blakey, 2008; Montañez and Poulsen, 2013). The expansion of land plants is thought to have played a key role in triggering this ice age as increased primary productivity led to substantial organic carbon burial, silicate weathering enhancement and nutrient release to oceans which increased marine primary productivity (Berner, 1997; Chen et al., 2021). Coal swamps present during the Carboniferous are estimated to have sequestered $13 - 47 \times 10^9$ tonnes of carbon per year, reducing atmospheric CO_2 levels and coinciding with climatic cooling and glaciation (Cleal, 2018). This glaciation lasted approximately 90 million years until the late Permian.

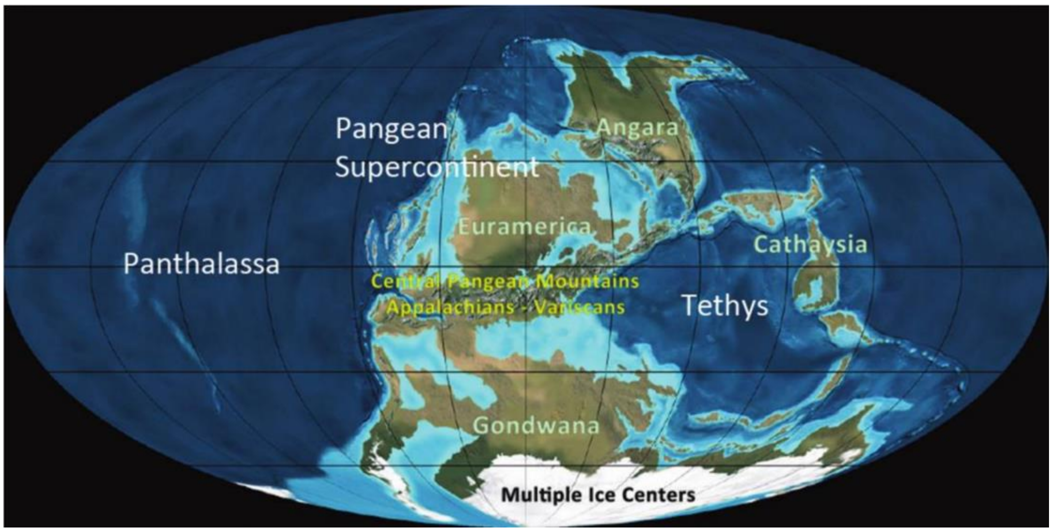

Figure 1.5.4. Carboniferous world map and major geographic features. *The Pangean supercontinent involves the joining of Euramerica and Gondwana and the formation of the Central Pangean Mountains. No single ice sheet covered Gondwana in the Southern Hemisphere. Rather they were more a collection of smaller ice centres spanning the Permo-Carboniferous. Image taken from DiMichele (2014).*

Paleogeographic conditions facilitated the Permo-Triassic extinction event as the arrangement of continents restricted oceanic mixing which promoted anoxia and reduced marine habitats (Figure 1.5.5; Scotese, 2021). The presence of large land surfaces near the equator also led to the Hadley Cell circulation patterns being replaced by megamonsoonal circulation which created drier and unfavourable conditions for life along the equator and subtropical arid belts (Scotese, 2021). The Hadley cell cycle involves the air rising near the equator and flowing towards the poles above Earth’s surface, creating seasonal variation of temperature and rainfall (Tabor et al., 2019). The megamonsoonal cycle involves extremely high rainfall concentrated in the summer months around coastal areas with persistently arid conditions in central Pangea (Zeng et al., 2019). Paleogeographic conditions can have a profound effect on environmental factors which can dictate the possibility of life on land.

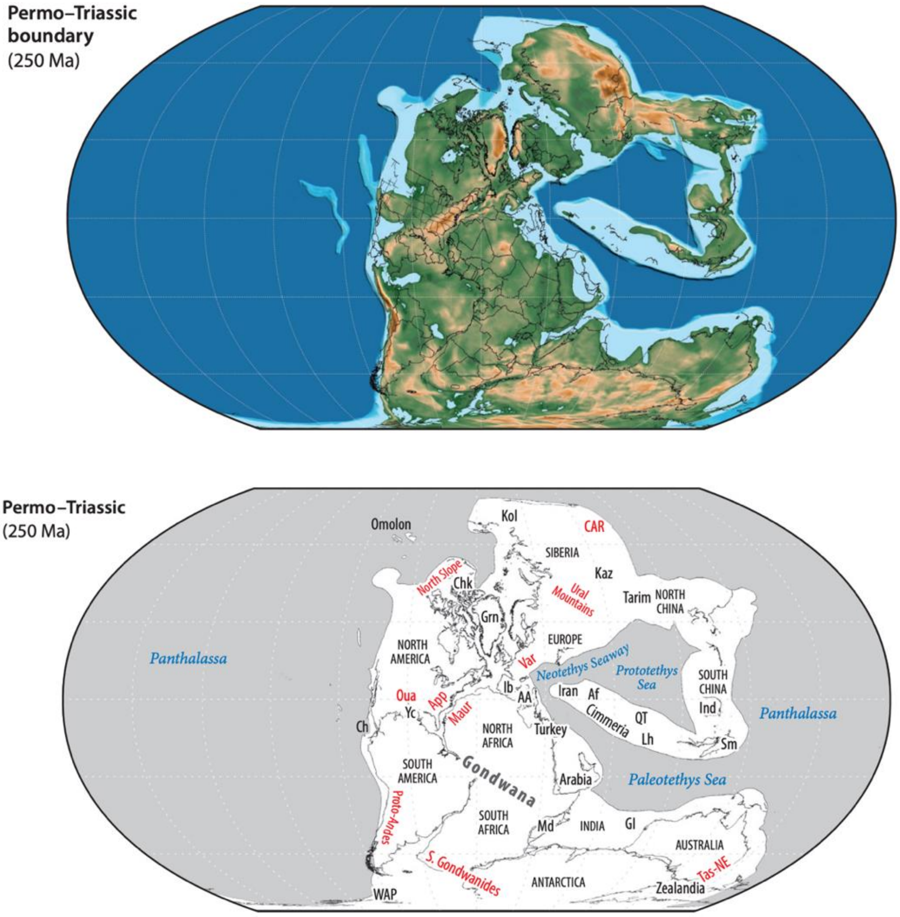

Figure 1.5.5. Permo-Triassic paleogeographic (above) and continental (below) map. *The orientation of the Pangean supercontinent and the location of the Panthalassa, Paleotethys and Neotethys oceans. Largely landlocked by Cimmeria, Southern China and Australia, the Paleotethys and Neotethys oceans had restricted ocean mixing. Images taken from Scotese, 2021.*

1.5.2 Mesozoic and Cenozoic Era

Following the events of the Siberian Traps, global conditions changed drastically including the aridification of the Pangean interior due to the extremely high temperatures (>40°C). The formation of Pangea was such that water could not penetrate central regions, creating abiotic deserts, which slowed down chemical weathering and allowed atmospheric CO_2 to build up (Scotese, 2021). The climate following the Permo-Triassic Boundary extinction contains bouts of humid episodes – alternating cooling and warming cycles of unusually warm, wet conditions within longer periods of cool, dry conditions (Trotter et al., 2015). The third largest Phanerozoic extinction event occurs in the early Jurassic (201.3 Ma) with the degassing of the Central Atlantic Magmatic Province (CAMP) which is estimated to have released 80,000 gigatons of CO_2 into the atmosphere (Scotese, 2021). A sharp increase in stomatal density is seen as a result of an increase in atmospheric CO_2 (Figure 1.5.1). Similar to the previous extinction cascade, the volcanic events brought about rapid global warming, increased terrestrial weathering and erosion due to higher temperatures and soil acidity and oceanic acidification leading to biotic extinctions (Davies et al., 2017; Scotese, 2021). Fossil pollen, spore leaf records show 90% of plant species to be extinct across North America, Greenland and Europe with warm, humid conditions favouring ferns (McElwain and Punyasena, 2007). During the late Triassic, eastern Pangea facing the Tethys (Figure 1.5.4) experienced monsoonal climate due to the difference in the high temperature of the large continental plate and the cooler sea. As eastern Pangea experienced harsh rainfall, the interior was becoming drier (Bonis and Kürschner, 2012).

The Jurassic through to the Cretaceous contains a series of cold and warm climates as indicated by glendonite (pseudomorphs formed from minerals in near-freezing waters) and anoxic events, respectively (Korte et al., 2015). A series of tectonics uplifts have been suggested as the main contributing mechanism towards global cooling as it increases silicate weathering rates but also interferes with marine heat transportation (Korte et al., 2015). Aridity of the Pangean interior continued throughout the Jurassic as it deflected the Intertropical Convergence Zone (ITCZ; an equatorial zone that faces heavy rainfall as northern and southern trade winds meet), creating ‘megamonsoonal’ circulation (Scotese, 2021). Throughout the Jurassic and Cretaceous, continental rifting and seafloor spreading saw the breakup of Pangea and Gondwana which eventually ended by the late Eocene (Blakey, 2008). The splitting of the supercontinent may have led to tropical cooling and increased vegetation on land which increases surface albedo and lowers global temperatures (Tabor et al., 2019). Earth’s current formation is the result of Pangea splitting into six large continents separated by expanding oceans (Scotese, 2021). The presence of Antarctica and its ice caps, and the collisions that led to the Himalayan Mountains and rise of the Tibetan Plateau are thought to have helped cool Earth into its pre-industrial conditions (Raymo and Ruddiman, 1992; Scotese, 2021).

Mantle degassing at mid-ocean ridges is thought to have caused the mid-Cretaceous hothouse (~100 Ma) with global temperatures at 28°C (Caldeira and Rampino, 1991; Scotese, 2021). Later in the Cretaceous, the Chicxulub impact is the largest known bolide impact of the Phanerozoic that changed the climate rapidly at the Cretaceous-Paleogene boundary (K/T boundary). The event vaporised 3000 megatons of crustal material and suspended fine particles into the atmosphere. This created pseudo-nights as sunlight was blocked for several months leading to a drop in land plant productivity (Claeys et al., 2002; Scotese, 2021). The cooling however was short-lived, and volcanic eruptions triggered global warming and led to one of the warmest climates in the Early Paleogene with ice-free polar regions and shallow latitudinal temperature gradients (Linnert et al., 2014).

The most recent geological period, the Cenozoic shows CO_2 levels, overall, being lower than in previous periods (McKenzie et al., 2016; Mills et al., 2019). The Earth is termed to be in an ‘ice house’ interval as polar ice caps form however, due to increased anthropogenic activity (e.g., fossil fuel burning, deforestation), CO_2 levels are now higher than expected (Ruddiman et al., 2016).

1.6 Conclusion

Plants have evolved and differentiated substantially from their ancestral algae species over the Phanerozoic. Their high rates of adaptation to the environment led to a range of features including the stomata, water transportation system that now contribute towards shaping climate. Similarly, mycorrhizal fungi have evolved alongside plants to facilitate symbiotic growth. A combination of plants and mycorrhizal fungi evolution appear to play a role within biogeochemical cycles however studies quantifying their collective roles are lacking. The plant-fungi symbiosis can change soil chemistry and shape their surroundings to increase growth and productivity.

The long-term carbon (C) cycle involves a balance between silicate weathering and photosynthesis (minus respiration). The knock on effect on the C cycle due to plant-fungi modification lies in organic carbon burial and silicate weathering rates. Organic carbon burial (plant biomass) removes CO_2 from the atmosphere along with enhanced silicate weathering rates via roots. Other abiotic controls on the global C cycle include tectonic movements which can enhance silicate weathering by exposing new rock surfaces or via degassing which releases CO_2. The culmination of these processes (plant-fungi evolution, tectonic movements) have led to a series of changes in climate over the Phanerozoic. Changes in land orientation (e.g. the formation and breakup of Pangea) created various niches for plants to evolve in leading to the present-day angiosperm domination on land. Throughout the Phanerozoic, a positive feedback between plants and climate has occurred whereby plants adapt to their environment which leads to a modification of the environment that has a global impact and thus changing climate. Similarly, as climate changes (due to a combination of biotic and abiotic factors), plants are forced to adapt to a new set of challenges.

This thesis aims to explore the relationship between plants and climate using a coupled vegetation and climate model. The primary goal of this thesis is to create a vegetation model that is simple enough to capture photosynthesis and plant growth to run alongside a larger climate-chemical model in order to help answer questions such as: How have plants helped shape the current climate or paleoclimate? How has the climate in turn facilitated/diminished plant evolution and growth?

Chapter 2. FLORA: Fast Land Occupancy and Reaction Algorithm

In this chapter, I introduce a deep-time vegetation model called FLORA (Fast Land Occupancy and Reaction Algorithm). The model is based on the Lund-Potsdam Jena Dynamic Global Vegetation Model (LPJ-DGVM, Sitch et al., 2003) with added modifications to enable longer timescale runs. Section 2.1 describes, in brief, the incorporation of the vegetation cycle into global biogeochemical models, which is the ultimate purpose of FLORA. I also outline the main features of the LPJ model that have ultimately been transferred to FLORA. Section 2.2 details the schematics of FLORA, equations involved to calculate plant biomass and validation when applied to present-day climate.

2.1 Global biogeochemical models

A model involves numerical representation of physical processes occurring within the system in question. Global biogeochemical models include interactions between reservoirs (i.e. pools of resources that can either be added to or removed from) within a planet’s surface, such as the amount of carbon available within the atmosphere and ocean, and how it can fluctuate and adapt to various forcings such as degassing rates. Biogeochemical cycles are often modelled using a box model (or “non-dimensional” model) which contains processes (e.g., weathering, burial, degassing) that act as either a sink or a source. For example, carbon burial acts as a carbon sink as it temporarily removes and stores carbon from the cycle. The processes affect reservoirs (e.g., carbon pool) that are represented by a single variable with no spatial heterogeneity (Mills et al., 2021). Within the climate system, biogeochemical cycles fall under the slow-response variable as it determines atmospheric composition on century or longer timescales, as opposed to fast-response variables like photosynthesis which is calculated on a daily or smaller timescale (Bartlein and Hostetler, 2003).

Various biogeochemical box models have been designed to predict the magnitude of fluxes in the carbon cycle (Mills et al., 2019). Models such as GEOCARB (Geological Carbon Cycle) (Berner and Kothavala, 2001) and COPSE (Carbon, Oxygen, Phosphorus, Sulphur, Evolution) (Bergman et al., 2004) incorporate geological, geochemical, biological and climatological data with equations to estimate atmospheric CO_2 concentrations over Phanerozoic time. These models are used both to predict the concentration of CO_2 for times when proxy data are unavailable, and to assess the relative ability of the biosphere and tectonics to control climate. However, as the reservoirs are comprised down to a global mean or sum, it creates a significant limitation when considering the distribution of continents, variation in environmental conditions and its effect on vegetation. Paleogeography is dynamic and constantly changing over long periods of time (see Chapter 1.5). As continents readjust, hydrological cycles change which influence regional variation of rainfall and processes such as silicate weathering. The assumption of one global mean can therefore underestimate the role of paleogeography on key processes that affect long-term atmospheric CO_2 (Goddéris et al., 2014).

In addition, these models focusing on geochemical changes and atmospheric CO_2 are largely based on weathering processes inferred from a generalised ecosystems that lacks plant evolutionary context (Morris et al., 2015). Plants, as hypothesised previously, have made a significant impact on the carbon cycle by acting as both a sink and source (Taylor et al., 2012). Plants photosynthesis and enhance weathering which leads to the drawdown of atmospheric CO_2 or they respire and burn to release CO_2. However, the degree of impact depends on the stage of their evolution. For example, silicate weathering is largely enhanced by the presence of roots compared to non-rooted plants (Raven and Edwards, 2001). Plants have evolved over the Phanerozoic from simple structures to complex modern day plants. Long-term biogeochemical models not only lack spatial heterogeneity of plant distribution but also leave out the increasing complexity of plant structure which may enhance or diminish impact on processes that control atmospheric CO_2.

Vegetation structure and processes couple the atmospheric boundary layer and land surface as they influences the exchange of carbon, energy and water (Bartlein and Hostetler, 2003; Fisher et al., 2018). Some broad examples include plant photosynthesis coupling atmospheric carbon to terrestrial carbon and evapotranspiration of water via plants coupling groundwater to atmospheric water cycles. The vegetation-climate interaction is ever-changing with terrestrial conditions influencing plant physiology (e.g., stomatal conductance) and the change in vegetation communities influencing climate by controlling the rate of exchanges (Bonan et al., 2003). Such biologically mediated feedbacks need to be incorporated into Earth System Models in order to accurately represent vegetation and its influence on biogeochemical cycles over time (Fisher et al., 2018). Increased realism of plant physiology and their responses to environmental variables however increases model complexity and computational expense (Fisher et al., 2018).

Global vegetation dynamics are highly spatially heterogeneous with broad-scale patterns (e.g., biomes) that rely heavily on local climate and tectonic factors such as precipitation, temperature and erosion rates (Smith et al., 1992). Different biomes contribute differently towards the global carbon fluxes (e.g., Table 2.1.1). One of the main roles of forests within the global carbon cycle is to sequester atmospheric CO_2 and mitigate global warming to some extent (Luyssaert et al., 2007). The cumulative effect of different biomes changes depending on the dominant biome present at a given time as dictated by environmental conditions. Along with different plant species capable of varying carbon sequestration within a biome, mycorrhizal fungi also dominate different biomes (see Chapter 1.3.1). The current generation of biogeochemical box models lack this spatial heterogeneity of vegetation and therefore are unable to properly quantify the contribution of plants and fungi towards climate regulation and long-term climate change.

2.1.1 Vegetation models

Emerging during the mid-1990s, dynamic global vegetation models (DGVMs) are used to project past, current and future vegetation patterns along with changes in biogeochemical cycles at regional and global scales (Scheiter et al., 2013; Wang et al., 2013). Unlike box models where each process is given a global mean number, DGVMs split Earth into grid boxes and calculate processes independently for each box (Figure 2.1.1). DGVMs are a component of land surface models that predict the global distribution of plant functional types (PFTs) from physiological principles (Fisher et al., 2018). Vegetation is characterised as patches of PFTs that occupy a portion of a gridcell depending on parameters such as temperature and rainfall that may be favourable to one PFT over another (Bonan et al., 2003). Examples of DGVMs include: Top-down Representation of Interactive Foliage and Flora Including Dynamics (TRIFFID; Cox, 2001) and Lund-Potsdam-Jena DGVM (LPJ-DGVM; Sitch et al., 2003). Coupling a DGVM with climate model proves useful in providing valuable reference estimates of feedback strengths (Wang et al., 2013). However, the incorporation of a DGVM and Earth System Models seldom contribute towards global biogeochemistry.

Biome	**Growth strategy**	**NPP (gC m^{-2} year^{-1})**	**Total biomass (gC m^{-2})**
Boreal humid	Evergreen	271 ± 17	7149
Boreal semiarid	Evergreen	334 ± 55	6370
	Deciduous	539 ± 73	
			8961
Temperate humid	Evergreen	783 ± 45	28496
	Deciduous	738 ± 55	13447
Temperate semiarid	Evergreen	354 ± 33	8521
Mediterranean warm	Evergreen	801 ± NA	9194
Tropical humid	Evergreen	864 ± 96	14314

Table 2.1.1. Mean NPP flux and total biomass of different forest biomes. *Some biomes contain different growth strategies (deciduous vs. evergreen). The NPP values are NPP ± the standard deviation. Total biomass contains both above and below-ground biomass. NPP: net primary productivity. Table modified from Luyssaert et al., 2007.*

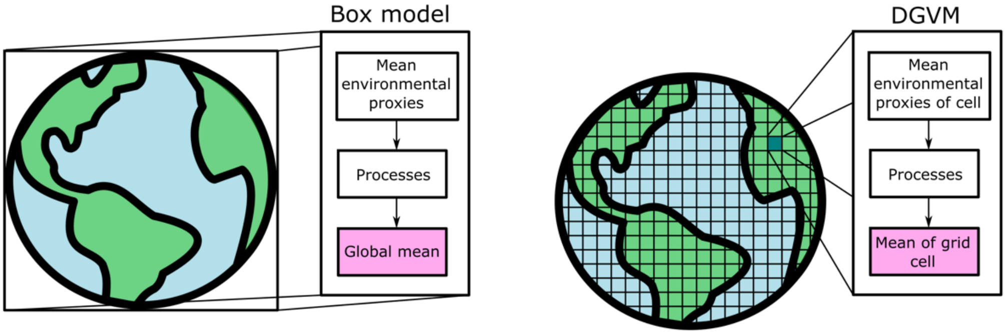

Figure 2.1.1. Schematics of a box model and DGVM. *Box models calculate the global mean of processes of Earth's climate. Dynamic global vegetation models (DGVMs) calculate process means using environmental conditions of each gridcell, creating spatially variable processes.*

Although land plants have been incorporated into biogeochemical models, they are often mainly depicted as influencing silicate weathering and organic matter burial without any spatial heterogeneity (Lenton et al., 2018). The use of singular values to represent a range of global exchange rates relating to plant interaction with climate is one of the biggest limitations currently present in models. For instance, the COPSE model calculates vegetation as a single parameter covering the globe and assumes an equal rate of enhancement to processes worldwide as a result (Lenton et al., 2018). As continental weathering is assumed to be partly responsible for regulating atmospheric CO_2 over long time periods (Berner and Kothavala, 2001), the assumption of a constant enhancement in silicate weathering rate therefore reduces the accuracy of such predictions.

Apart from modelling plant physiology to determine global distribution, the Köppen climate classification can also be used to limit plant distribution (Figure 2.1.2). The Köppen climate system uses monthly temperature and precipitation to define climate boundaries and link vegetation to climate as each zone is characterised by distinct flora (Chen and Chen, 2013; Scotese et al., 2021). Construction of paleo-Köppen climate belts require the use of lithological indicators of climate like coals, evaporites, soil minerals and glacial deposits (Scotese et al., 2021). The Köppen climate system can be used to study the past and future climates, as it shows changes in pole-to-equator temperature gradient which can indicate whether Earth is in a hothouse or icehouse period (Scotese et al., 2021). In terms of delineating vegetation based on the climate belts, limitations exist. Firstly, the width of the belts are an approximation (Scotese et al., 2021) so using the classification could lead to under- or over-estimation of global biomass. Secondly, a vegetation lag might be present (Cui et al., 2021). The turnover between two PFTs is not instantaneous as favourable climate declines. Finally, and more importantly, the Köppen classification does not account for changes in atmospheric CO_2 (Cui et al., 2021). Plant productivity is a function of atmospheric CO_2 therefore fluctuations of biomass within the same climate belt cannot be captured.

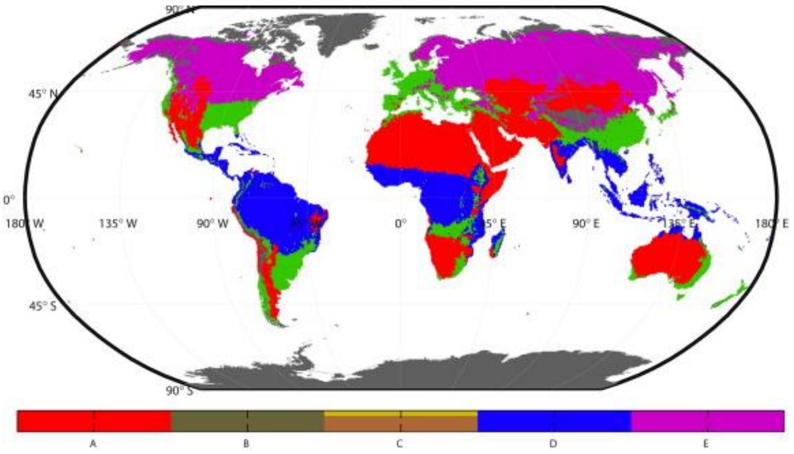

Figure 2.1.2. Five major Köppen climate types and distribution. *Global distribution of A: dry, B: polar, C: mild temperate (green), D: tropical, E: snow (subarctic) biomes according to the Köppen climate classification. Image taken from Chen and Chen, 2013.*

2.1.2 LPJ model

LPJ-DGVM combines terrestrial vegetation dynamics and land-atmosphere carbon and water exchanges for large spatial scales (Sitch et al., 2003). Vegetation structure responds rapidly to climate changes over timespans of years to decades (Bartlein and Hostetler, 2003) whereas biogeochemical cycles operate over thousands to millions of years. LPJ-DGVM couples fast hydrological and physiological processes, such as daily photosynthesis and respiration, to slower ecosystem processes, such as tissue turnover and mortality (Figure 2.1.3; Bonan et al., 2003).

10 PFTs represent vegetation within each gridcell (Table 2.1.2), each defined by temperature tolerance and mortality, longevity and fire resistance. Within a gridcell, each PFT is treated as a whole plant rather than collection of individual plants. Monthly inputs of climatology, soil type and atmospheric CO_2 concentration are used to derive daily processes like evapotranspiration per gridcell (Figure 2.1.2). Each PFT has a combined biomass, crown area, height, and stem diameter which covers a portion of the gridcell at any given location. Proceeding processes, such as carbon allocation, depend on the portion of PFT coverage (Figure 2.1.3). Biomass is further subdivided into three components: sapwood, leaf and fine root, which are calculated using yearly biomass allocation and turnover.

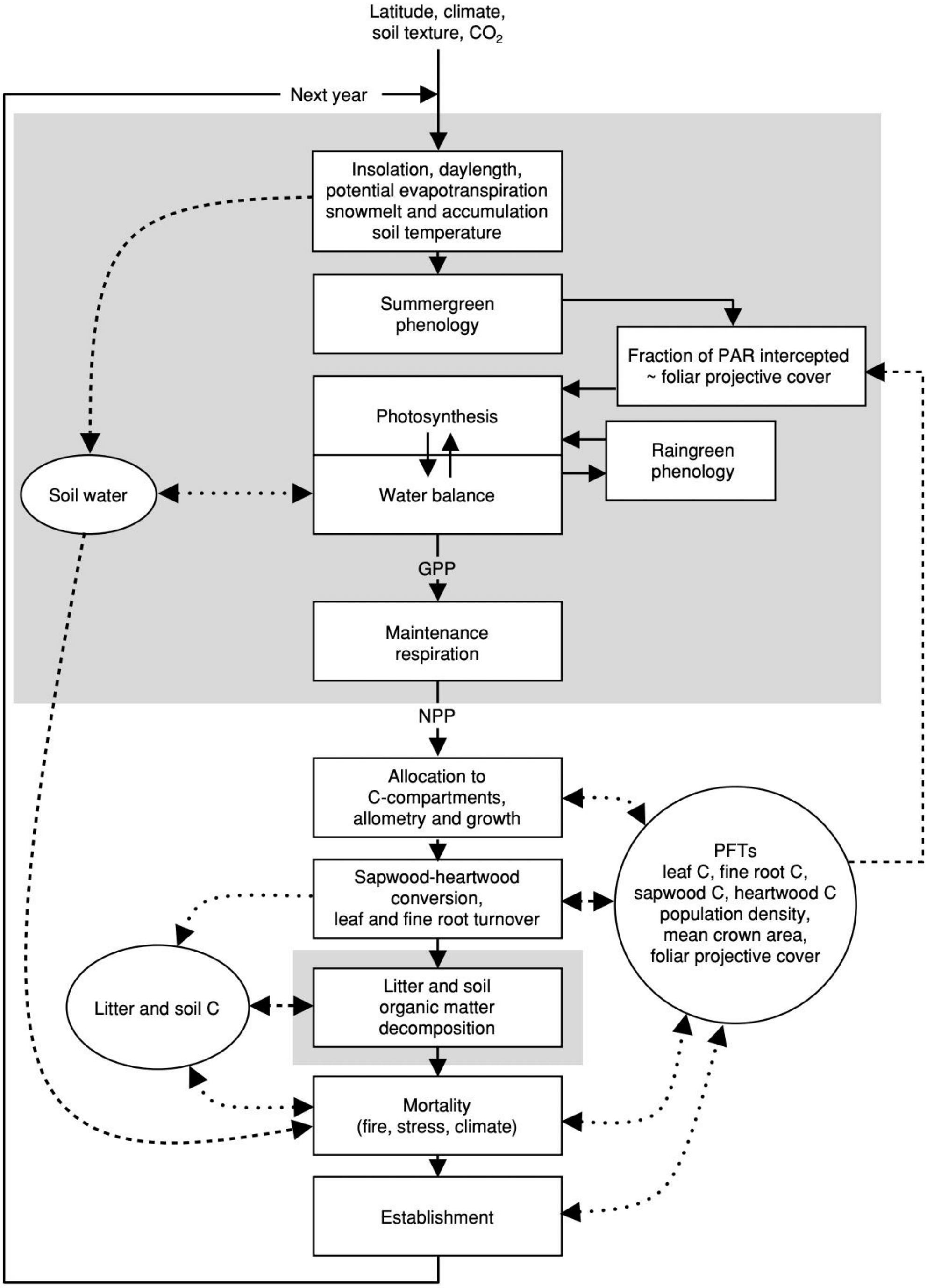

Figure 2.1.3. LPJ model flowchart. *Individual processes (boxes), known as modules are performed (solid lines) in the direction of the arrow in all gridcells. Information exchange (dashed lines) occur between vegetation and soil state variables. Grey boxes are calculated at a daily or monthly timestep whereas the rest are annually calculated. Image taken from Sitch et al., 2003.*

Climate	Leaf phenology	Growth type
Tropical	Broad-leaved	Evergreen, Raingreen
	Herbaceous	
Temperate	Needle-leaved	Evergreen
	Broad-leaved	Evergreen, Summergreen
	Herbaceous	
Boreal	Needle-leaved	Evergreen, Summergreen
	Broad-leaved	Summergreen

Table 2.1.2. Plant functional types present in the LPJ model. *8 woody and 2 herbaceous plant functional types that encapsulate vegetation in the LPJ model. Table taken from Sitch et al., 2003.*

Competition exists between PFT populations for light, water and space; all determined by the fractional coverage of gridcells. As biomass of a given PFT increases beyond what each gridcell can support, herbaceous biomass is reduced first as woody PFTs are assumed to dominate. Woody PFTs are constrained at 95% of gridcell coverage. Going beyond this limit incurs self-thinning processes whereby woody PFT biomass is reduced. Within woody PFTs, competition for resources and their ability to succeed, based on induced physiological thresholds and environmental conditions, dictate their biomass per gridcell.

Broad results from the LPJ model show that it is capable of capturing seasonal cycles of CO_2. Pre-industrial vegetation is predicted to hold 923 petagrams of C. However, assumptions and simplifications made along the processes of biomass calculation result in some over or under estimations of the CO_2 cycling. The model also predicts a similar distribution of dominant PFTs to the Köppen climate belts in most regions, such as boreal evergreen forests in Canada and northern Eurasia (Figure 2.1.4; Sitch et al., 2003).

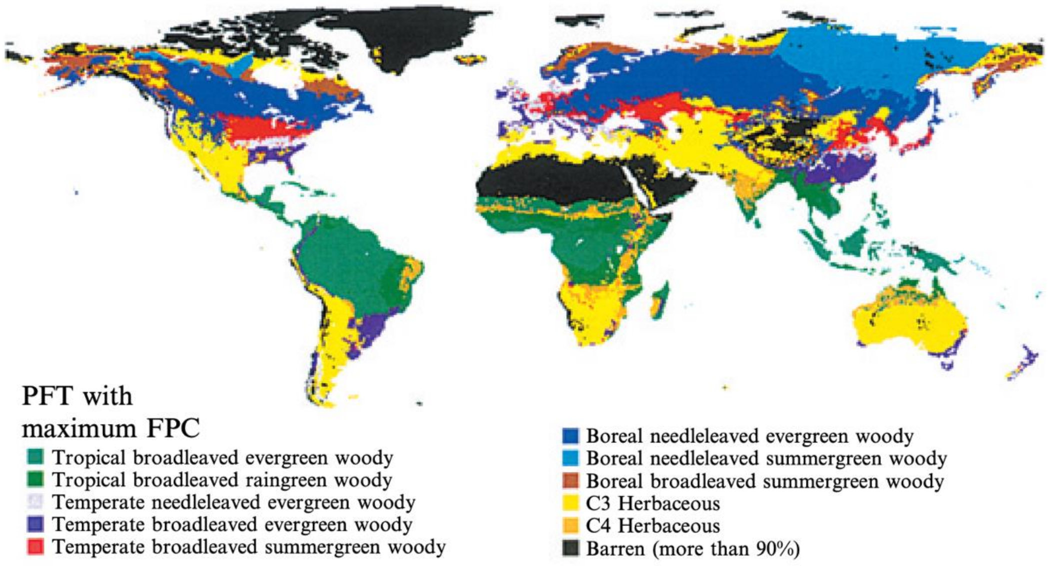

Figure 2.1.4. LPJ simulated vegetation map. *Map illustrating the 10 PFTs simulated by the LPJ model and their spread. Image taken from Sitch et al., 2003.*

2.2 FLORA model

FLORA captures the flow of carbon from its atmospheric form (CO_2) to storage as biomass in plants (Figure 2.2.1). Key considerations during the development of FLORA were: the computational speed, the ability to determine if each land gridcell in a climate model is suitable for plant growth, and providing an estimate of the total productivity and biomass for each cell through modelling the photosynthesis and respiration reactions. Net Primary Productivity (NPP) is defined as the net carbon stored after autotrophic respiration (Zhang et al., 2009). All plant carbon within the system from NPP is assumed to be stored in the form of leaf biomass for simplicity. The dominant factors for vegetation growth and expansion are solar radiation in the rainforest, precipitation in arid and semi-arid areas, and temperature at higher latitudes (Wu et al., 2015). Hence, FLORA incorporates the three environmental forcings to determine global plant potential biomass (Figure 2.2.1). Although root and sapwood biomass are present within the LPJ-DGVM (Sitch et al., 2003), they are closely linked to the other biomass pools and are not required to reproduce a reasonable fit to modern biomass (see Chapter 2.2.2). These features were absent from early non-vascular plants (Cornelissen et al., 2007), thus I opt for the simplest approach.

As with the LPJ-DGVM, FLORA divides Earth into gridcells (Figure 2.1.1). Each gridcell within a map is defined as either land or ocean; with the size of the gridcell depending on the chosen spatial resolution. Carbon flows and biomass are calculated over gridcells representing the continental surface (i.e. land), and for three basic PFTs: tropical, boreal and temperate. The only distinction between each PFT is their performance at different temperatures (Luyssaert et al., 2007); each PFT has a different optimum temperature for photosynthesis (Figure 2.2.2), turnover and respiration rate (Table 2.2.1). A simple version of “competition” is also present per gridcell where only the contribution of the functional type, for which the highest potential biomass is calculated, dictates the ‘biome’ of the gridcell. Establishment is another factor that can determine dominance. For example, encroachment of woody plants in grasslands increase in moist soils that facilitate seedling survival (Kennedy and Sousa, 2006). Currently FLORA does not take into account establishment/re-establishment factors and only considers forest biomes therefore the highest biomass is considered to ‘win’.

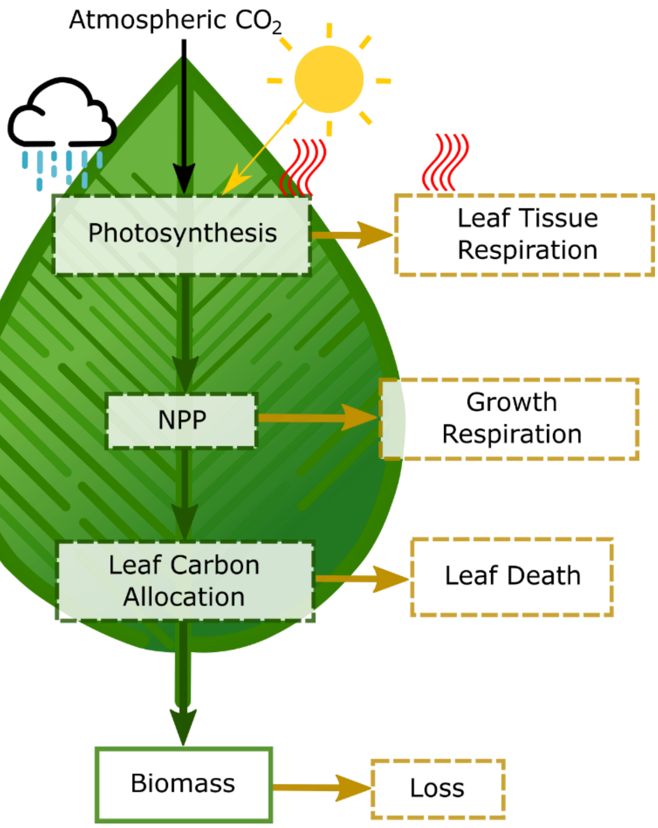

Figure 2.2.1. FLORA model flowchart. *Each arrow depicts the flow of carbon, green indicates carbon is preserved within the system while brown indicates its departure. Note: the model uses a single biomass pool and losses associated with respiration and leaf death affect the growth of the biomass pool. Processes are given in dashed boxes whereas reservoirs are presented in bold boxes. Processes that are affected by temperature (red lines), insolation (arrow from sun) and water availability (blue rain) are indicated. NPP: net primary productivity.*

Plant functional type	**Temperature optimum (°C ± s.d)**	**Turnover ratio**	**Respiration rate (gC gN^{-1} d^{-1})**
Tropical	27 ± 7	1	0.011
Temperate	15 ± 20	0.75	0.055
Boreal	0 ± 20	0.75	0.066

Table 2.2.1. FLORA plant functional types and associated differences. *Optimum temperature and temperature range (s.d: standard deviation), turnover ratio (* f_{leaf}*) and respiration rate (*r*) for each plant functional type.*

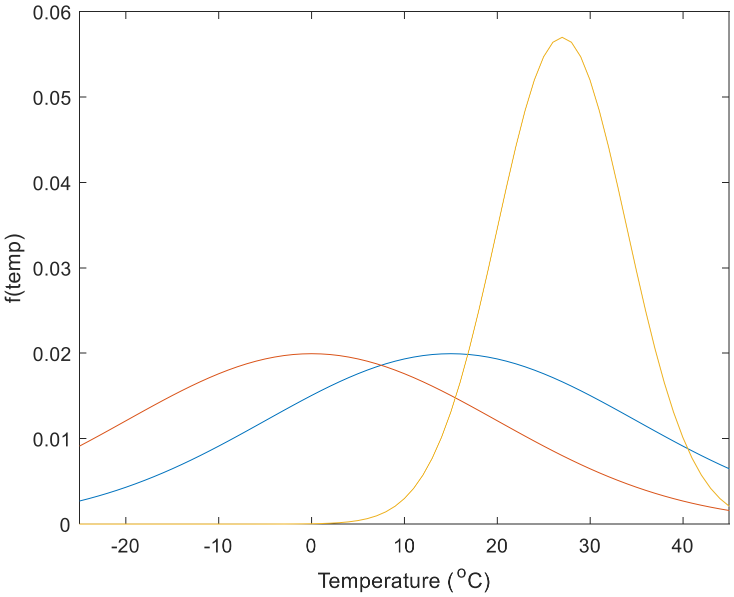

Figure 2.2.2. Plant functional type temperature function. *Temperate (blue line) and boreal (red line) plants have similar temperature function and are present in a wider range of temperatures compared to the tropical plants (yellow line).*

2.2.1 Model description

The equations within FLORA dictate the rate of photosynthesis and respiration, carbon allocation and turnover as a response to local solar insolation, temperature and water availability, as well as to the atmospheric CO_2 and O_2 levels. All constants used in equations throughout Chapter 2.2.1 can be found in Table 2.2.2. Photosynthesis is a process used by plants, algae and cyanobacteria to make organic molecules (such as glucose) for growth. Light energy is used, directly or indirectly, to generate organic molecules from carbon dioxide and water and oxygen is released into the atmosphere (Equation 2.2.1, Schaphoff et al., 2018; Stirbet et al., 2020).

$$6CO_2 + 12H_2O + light\ energy \rightarrow\ C_6H_{12}O_6 + 6O_2 + 6H_2O \qquad (2.2.1)$$

The process of photosynthesis occurs within the thylakoid membrane where two light reactions simultaneously take place within photosystem (PS) I and II reaction centres. A series of redox reactions leads to the production of ATP and NADPH, which are used for CO_2 assimilation within the stroma. Rubisco enzyme then catalyses the fixation of CO_2 on a five-carbon compound RuBP within the Calvin-Benson cycle. Energy preservation is high with only 2-10% of total energy being lost as heat or chlorophyll fluorescence (Stirbet et al., 2020).

Symbol	Value	Units	Q_{10}	Description
θ	0.7*			Co-limitation (shape) parameter
λ	0.7^{ϕ}			Optimal intracellular/ambient CO_2 ratio
α	0.08*			C_3 quantum efficiency of CO_2 uptake
K_C	30^{ϕ}	Pa	2.1	Michaelis constant of CO_2
K_O	30^{ϕ}	kPa	1.2	Inhibition constant of O_2
τ	2600^{ϕ}		0.57	CO_2/O_2 specificity ratio
h	24	hours		Daylight hours
a	0.015*			C_3 leaf respiration as a fraction of Rubisco capacity constant
pO_2	20.9	kPa		Ambient partial pressure of O_2 for present day
p_a	280	ppm		Ambient partial pressure of CO_2 for pre-industrial times
l_{max}	0.75			Maximum leaf carbon allocation ratio
cn_{leaf}	29*			Leaf C:N ratio
R_{growth}	0.25*			Growth respiration ratio

Table 2.2.2. FLORA parameters and constants. *Parameters in model equations of Chapter 2.2.1.* *Sitch et al., 2003; $^{\phi}$Haxeltine and Prentice 1996a

The mechanistic approach of modelling photosynthesis involves the optimality hypothesis as used by the LPJ method (Equations 2 – 18 in Sitch et al., 2003). The optimality hypothesis involves balancing of resource investment and plant carbon gain under specific environmental conditions (Stirbet et al., 2020; Jiang et al., 2020). The Farquhar model, often used in terrestrial biosphere models, relates enzyme kinetics and whole chain electron transport to gas exchange of whole leaves of C_3 plants (Farquhar et al., 1980). The combination of the Farquhar model and the optimal hypothesis results in CO_2 assimilation at large timescales (e.g., weeks, months and so on) becoming close to the point where Rubisco limited CO_2 assimilation rate is equal to the electron transport-limited CO_2 assimilation rate (Stirbet et al., 2020). As such, the photosynthesis rate (P) (gC m^{-2} year^{-1}) is given by:

$$P = 3650 \cdot ins\left(\frac{c_1}{c_2}\right)[\, c_2 - (2\theta - 1)s - 2(c_2 - \theta s)\sigma_c]\; \omega \qquad (2.2.2)$$

where the photosynthesis rate is controlled by a combination of parameters relating to enzyme activity and environmental parameters, $\sigma_c, c_1,$ and c_2 (explained below in equations 2.2.3 – 2.2.9). θ is the shape parameter that specifies the degree of co-limitation by light and Rubisco activity (Table 2.2.2); s is the relative leaf respiration per day. The photosynthetic light response curve of leaves is often described by a non-rectangular hyperbola and is helpful for identifying plant photosynthetic capability (Xu et al., 2019). Within Sitch et al., (2003), the photosynthesis rate and its relationship with the two limiting rates of photosynthesis (response of photosynthesis to absorbed PAR,c_1, and Rubisco limited rate of photosynthesis, σ_c) (Haxeltine and Prentice, 1996b) are written as:

$$\sigma_c = \left[1 - \frac{(c_2 - s)}{(c_2 - \theta s)} \right]^{0.5} \tag{2.2.3}$$

$$c_1 = \alpha f_{temp} \frac{(p_i - \Gamma_*)}{(p_i - 2\Gamma_*)} \tag{2.2.4}$$

$$c_2 = \frac{(p_i - \Gamma_*)}{(p_i - K_C \left(1 + \frac{pO_2}{K_O}\right))} \tag{2.2.5}$$

$$s = \left(\frac{24}{h}\right) a \tag{2.2.6}$$

where α is the effective ecosystem-level quantum efficiency (Table 2.2.2); f_{temp} is a function that limits photosynthesis at high and low temperatures depending on the PFT (Table 2.2.1). h is the daylight hours which for model simplicity is considered to be 24; a = 0.015 is the constant for C_3 leaf respiration as a fraction of Rubisco capacity. Both Haxeltine and Prentice (1996a, b) and Sitch et al., (2003) calculate leaf respiration, within the context of Rubisco activity, to be a proportion of photosynthetic capacity. As $h = 24$, a constant influx of light is assumed which results in maximum photosynthetic capacity with minimum cost due to leaf respiration within the chloroplast. h can vary widely depending on seasonality and latitude hence we first opt for a perpetual daylight simulation. Photosynthesis would be fractionally lower when h is < 24.

Γ_* is the CO_2 compensation point, where CO_2 uptake from carboxylation is equal to CO_2 loss from photorespiration (Brooks and Farquhar, 1985), given by:

$$\Gamma_* = \frac{pO_2}{2\tau} \tag{2.2.7}$$

where pO_2 is the ambient partial pressure of O_2 (Pa), and τ is the CO_2/O_2 specificity ratio (Table 2.2.2). τ determines the relative rate of the enzyme to catalyse either carboxylation or oxygenation at any given CO_2 and O_2 concentrations (Galmes et al., 2005). p_i is the intracellular partial pressure of CO_2 (Pa) calculated using p_a, the ambient partial pressure of CO_2:

$$p_i = \lambda p_a \tag{2.2.8}$$

Both pO_2 and p_a reflect the average partial pressure of O_2 and CO_2 respectively (Table 2.2.2). λ is a positive parameter that represents the stomata opening and closing to balance intracellular and extracellular CO_2 concentration (Table 2.2.2). Under non-water-stressed conditions, the stomata maintains a constant ratio of intracellular to ambient CO_2 which ranges between 0.6-0.8 for C_3 plants (Haxeltine and Prentice, 1996a; Haxeltine and Prentice, 1996b). Therefore, a constant of 0.8 for C_3 plants is used (Sitch et al., 2003). Water-stress present in FLORA acts on the whole plant and is related to soil water availability whereas stomatal water-stress is more related towards photosynthetic rates. As the model is not concerned with limiting daily rates of photosynthesis, the maximum value for λ is used.

The enzyme ribulose-1,5-bisphosphate (RuBP) can act as a carboxylase or an oxygenase (Rubisco) as it catalyses two different reactions in the chloroplast stroma depending on the CO_2 and O_2 concentrations (Brooks and Farquhar, 1985). Rubisco partakes in the CO_2 uptake of photosynthesis and photorespiration with O_2, therefore the net uptake of leaf CO_2 depends on the simultaneous reaction rates. The Michaelis constants for CO_2 (K_C,) and O_2 (K_O) (Table 2.2.2) describes the point at which Rubisco switches between acting as a carboxylase or an oxygenase. The kinetic parameters are also temperature dependent as an increase in temperature leads to an increase in the CO_2 compensation point (the point at which the uptake of CO_2 via photosynthesis is equal to the respiratory release of CO_2, therefore leading to a net assimilation of zero) and inhibition of net photosynthesis by O_2 (Brooks and Farquhar, 1985). The temperature dependence of K_C, K_O and τ are modelled using:

$$k = k_{25}{Q_{10}}^{0.1(T-25)} \qquad (2.2.9)$$

taken from Haxeltine and Prentice (1996b). k_{25} is the parameter value at 25ºC and Q_{10} is the relative change in parameter for every 10ºC change in temperature (Table 2.2.2). Equation 2.2.9 is used within equation 2.2.5 to determine the limiting rate of photosynthesis by Rubisco at any given CO_2 concentration.

The rate is further scaled by water availablity (ω) and insolation (ins); as ω increases or ins decreases, P decreases due to reduced resources and energy levels. Insolation is assumed to be in a Gaussian relationship with latitude (f_{lat}). Insolation increases as latitudes get closer to the equator and decrease as they go towards the poles (Figure 2.2.3).

$$ins_0 = 150 + 250\, f_{lat} \qquad (2.2.10)$$

$$ins = ins_0 - \; ins_0 \; \times 0.046 \left(\frac{t}{570}\right) \qquad (2.2.11)$$

Equation 2.2.10 is a rough replication of the mean annual insolation curve (Figure 4 in Hay et al., 1997). Present day insolation, ins_0, decrease linearly over time, t, in strength by 4.6% until 570 Ma (Equation 2.2.11; Berner, 1993). The model assumes PAR (Photosynthetically Active Radiation) scales with insolation. PAR is the wavelength (0.4 - 0.7 micrometer) related to plant photosynthetic activity (Meek et al., 1984) whereas insolation is the total amount of solar radiation in a given area. The LPJ model uses daily integral of absorbed PAR per unit leaf area to calculate daily net photosynthesis. However, as FLORA deals with longer timeframes, it limits photosynthesis by using the mean annual radiation received at each latitudinal point. It assumes that if there is a higher amount of radiation being received, more radiation and ultimately PAR, is being received by plants therefore increasing plant productivity relative to areas receiving less radiation.

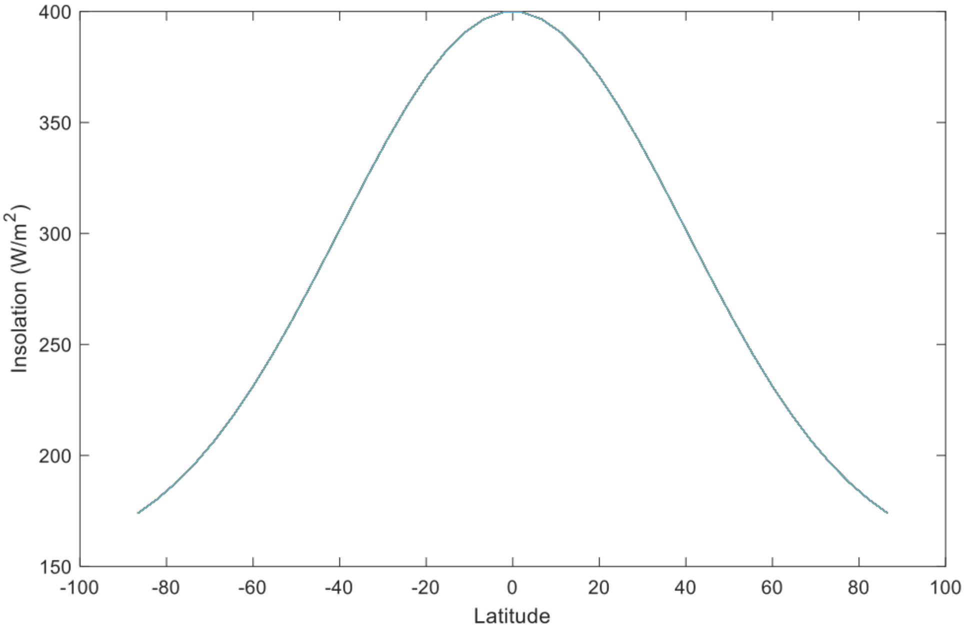

***Figure 2.2.3*. *Annual average latitudinal insolation curve*.** *The amount of insolation received at either poles are the lowest (175 W/m^2) and it increases as it gets closer to the equator where it peaks at 400 W/m^2.*

$$\omega = \frac{1}{1 + e^{-0.005(runoff-450)}} \qquad (2.2.12)$$

Water is an integral component of photosynthesis as the oxidation of water is used to generate ATP which subsequently is used to produce organic molecules for plant growth (Stirbet et al., 2020). Therefore, the availability of water can act as a limiter to plant growth. Within the LPJ model, water stress is a balance between soil moisture availability and evaporation. It is used to determine leaf and root carbon allocation as plants in water-stressed environments allocate more carbon towards fine root biomass (Sitch et al., 2003). Since FLORA allocates its entire carbon reservoir into the leaves, water stress is brought in at the end of the process. ω is calculated as a fraction of runoff, $runoff$, that ranges from 0-1 using a sigmoidal curve (Figure 2.2.4, Equation 2.2.12); 0 being no water available and 1 being maximum water availability for plants. Runoff represents the balance between precipitation and evaporation. The assumption made here is that the greater the runoff, the more water is available within the soil for plant use.

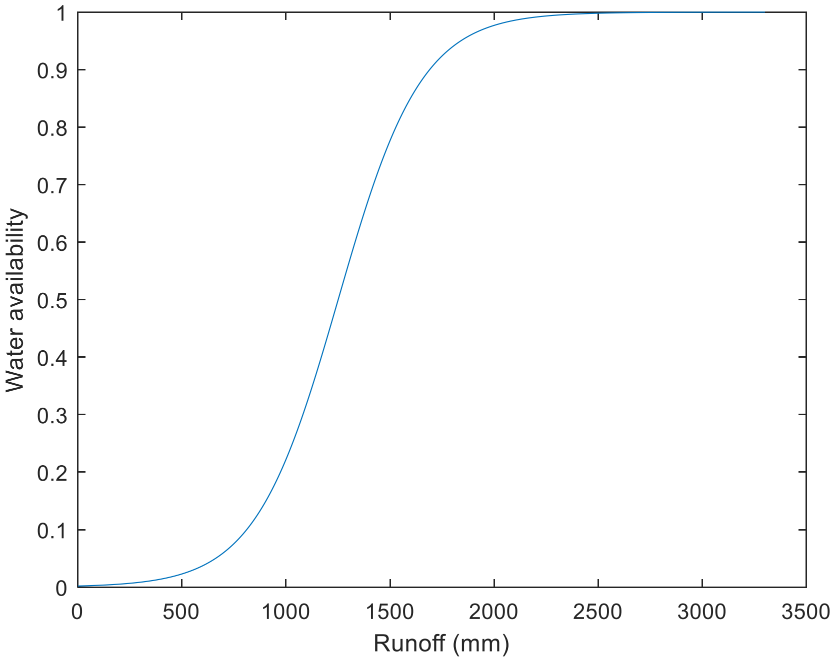

***Figure 2.2.4*. *Water availability curve*.** *As runoff increases, more water is assumed to be available for plants, therefore allowing photosynthesis to reach its maximum rate. Photosynthesis rate is limited by water availability with lower runoff values.*

The original equation was further scaled by 365 to calculate yearly rates, rather than daily, and by a factor of 10 to produce sufficient carbon assimilation to reflect present-day plant biomass, which includes above and belowground plant storage systems. The further increment required for potential biomass to match present-day biomass could be due to the 2D structure of each cell. P is limited by the area of each grid cell whereas in reality, plants occupy a volume of space. Leaf area index (LAI) is most generally defined as half the total green leaf area per unit of horizontal ground surface area (Fang et al., 2019). The LAI parameter relates to canopy size, density and leaf orientation to each other and to light. As FLORA does not factor in LAI or canopy cover, this may create an underestimation of the photosynthesis rate therefore requiring a factor of 10 to compensate for the lack of overlapping biomass and volume.

Initial carbon allocation to leaves (C_{leaf}) (gC m^{-2} year^{-1}) of the carbon acquired via photosynthesis is calculated using:

$$C_{leaf} = l_{max}P \qquad (2.2.13)$$

with a maximum leaf carbon allocation ratio (l_{max}) (Table 2.2.2; Sitch et al., 2003). Under constant conditions, an allocation ratio of 0.88 is given towards shoot growth (Chen and Reynolds, 1997). Carbon accumulation overtime in leaves is then calculated by:

$$C_{leaf(n+1)} = C_{leaf(n)}\left(1 - f_{leaf}\right) + l_{max}NPP \qquad (2.2.14)$$

where f_{leaf} represents leaf turnover for each PFT (Table 2.2.2). Initial leaf carbon allocation is calculated using photosynthesis (Equation 2.2.13) however subsequent calculations use net primary productivity (NPP). The initial photosynthesis rate does not account for increases in leaf population or quantity overtime. As leaf turnover is not 100%, C_{leaf} accumulates overtime therefore NPP is used to account for increases in leaf population. NPP (gC m^{-2} year^{-1}) calculates plant carbon storage pools after the cost of respiration.

$$NPP = \left(1 - R_{growth}\right)\left(P - R_{leaf}\right) \qquad (2.2.15)$$

Carbon is acquired by photosynthesis and lost through growth respiration (R_{growth}) and maintenance respiration (R_{leaf}). 25% of total NPP goes towards R_{growth} (Sitch et al., 2003). Within angiosperms and gymnosperms, allocation towards leaves has a maximum of approximately 0.75 (Poorter et al., 2012) which decreases with plant growth as more biomass is allocated towards the stems. Without the distinction of various carbon pools, all resources are directed towards new leaf tissue. The maximum value of the ratio is used therefore assuming 75% of photosynthetic carbon from NPP is allocated towards the leaves while 25% goes towards new growth (Sitch et al. 2003). R_{leaf} is calculated using:

$$R_{leaf} = r\left(\frac{C_{leaf}}{cn_{leaf}}\right)g(T) \tag{2.2.16}$$

$$g(T) = exp\left[308.56\left(\frac{1}{56.02} - \frac{1}{T + 46.02}\right)\right] \tag{2.2.17}$$

R_{leaf} depends on temperature given by a modified Arrhenius equation ($g(T)$), tissue respiration (r) and leaf specific C:N ratio (cn_{leaf}). r is the PFT specific respiration rate (gC gN^{-1} year^{1}) at 10°C (Table 2.2.1). Values for the tropical and boreal plant types are taken from Sitch et al., (2003) and modified for the temperate plant-type (Table 2.2.1). It follows the observation that plants of warmer environments have a lower respiration rate at any given temperature compared to plants from colder environments (Sitch et al., 2003).

Biomass (B) (gC m^{-2} year^{-1}) is the reservoir of carbon with inflow from leaf carbon accumulation and a constant 10% outflow, representing combined biomass degradation processes (e.g. herbivory, enzymatic breakdown by fungi and bacteria, fire) and chosen to reproduce overall modern biomass.

$$B_{(n+1)} = B_{(n)} + \left(C_{leaf(n)} - 0.1B_{(n)}\right) \tag{2.2.18}$$

Initial biomass for all gridcells is set at 25 kgC m^{-2} which serves as the baseline for biomass growth/loss. As re-establishment is not considered in FLORA, gridcells are seeded with this amount at the start of each time-slice. Without seeding, gridcells that reach zero biomass would stay barren during whole-Phanerozoic runs, which is not realistic as areas with no plant growth can be repopulated once conditions are permissive.

2.2.2 Model validation

FLORA was run subject to boundary conditions of the preindustrial CO_2 (280 ppm) and O_2 levels (20.9 kPa), 0.5 degree gridded global runoff (mm year^{-1}; Fekete et al., 2000) and temperature (°C; Mitchell & Jones, 2005) measurements, and a standardised insolation curve peaking at 400 W m^{-2} at the equator (Figure 2.2.5; Meek et al., 1984). Despite the simplicity of the model, the predicted global pattern of biomass shows good agreement with the measured global biomass ($R^2 = 0.5$, Figures 2.2.6 and 2.2.7) (Ruesch and Holly, 2008). The largest errors occur in the tropics but vary from over-prediction in South Asia and Indonesia, to under-prediction in tropical Africa. The maximum error in a single gridcell is about 2×10^4 gC m^{-2}, but errors tend to be balanced when considering larger areas (Figure 2.2.6 and 2.2.7). Our model also tends to slightly over-represent biomass in the northern high mid-latitudes and under-represent biomass in the southern high mid-latitudes. The over and under-representation could largely be due to the lack of monthly runoff fluctuation. For instance, the Amazon rainforest experiences dry seasons as well as months of heavy rainfall which imposes a large influence on vegetation distribution and fluxes of energy, water and carbon (Baker et al., 2008). As FLORA uses a mean yearly average, the short cycles of disruption and amplification in biomass accumulation is ignored which may cause the discrepancies observed. With the turnover rate acting as a tuning parameter, FLORA predicts biomass to be 550 gigatonne carbon (GtC) while the observed biomass from Ruesch and Holly (2008) lies at 489 GtC. Global plant biomass estimations have been reported to be ~450 GtC (Bar-On et al., 2018). LPJ vegetation biomass lies on the higher end at 923 GtC (Sitch et al., 2003). Overall, FLORA achieves the task it is designed for; a simple and fast model for the estimation of present-day potential biomass which can be easily run ‘offline’ using climate model data, or ‘online’ in a biogeochemical framework. It suitably reconstructs the major patterns of plant biomass on the present-day Earth.

Figure 2.2.7 shows the longitudinal and latitudinal biomass comparisons and the relationship between the modelled and the global database (Ruesch and Holly, 2008). These highlight that the model has reasonable capabilities in capturing the key trends, and again show the over-prediction of biomass in South-East Asia and under-prediction in tropical Africa. These differences may be attributable to the yearly-averaged datasets that are used as forcings. As discussed before, seasonal changes in runoff and productivity are not captured due to monsoonal climates not being well-represented.

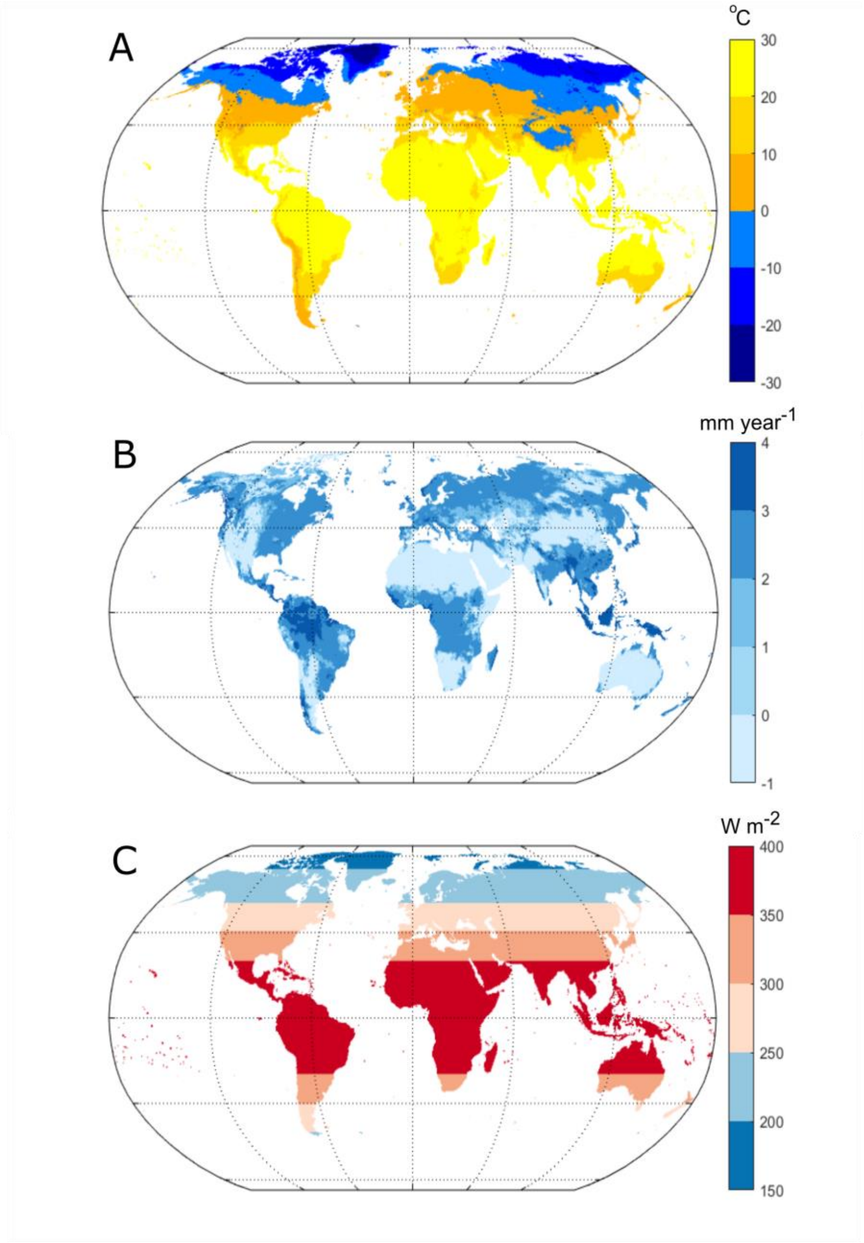

Figure 2.2.5. Temperature, runoff and insolation data. *Initial environmental proxies used to calculate present-day potential biomass.* ***(A)*** *Temperature data taken from Mitchell and Jones (2005).* ***(B)*** *Runoff data taken from Fekete et al., (2000).* ***(C)*** *Insolation rate calculated using equation 2.2.10 and 2.2.11.*

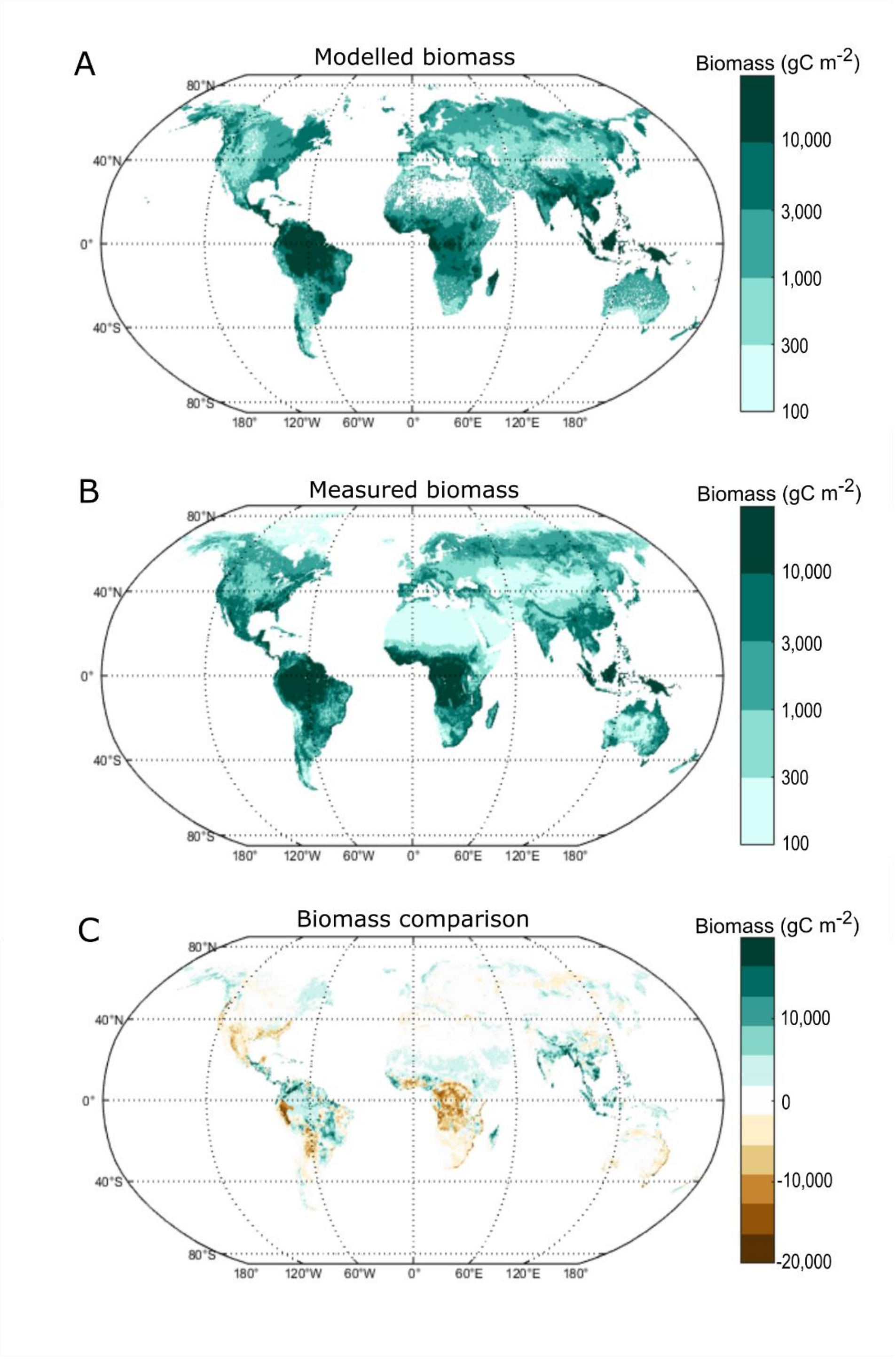

Figure 2.2.6. Modelled and measured biomass comparison. *The model predicts a reasonable approximation of current biomass.* ***(A)*** *Model predicted biomass given average temperatures (between 1900-1990) and 'best estimation' of yearly runoff from the year 2000.* ***(B)*** *Actual above- and below-ground global biomass for the year 2000 obtained from CDIAC (Ruesch and Holly, 2008).* ***(C)*** *Areas of over-prediction (green) and under-prediction (brown) of biomass.*

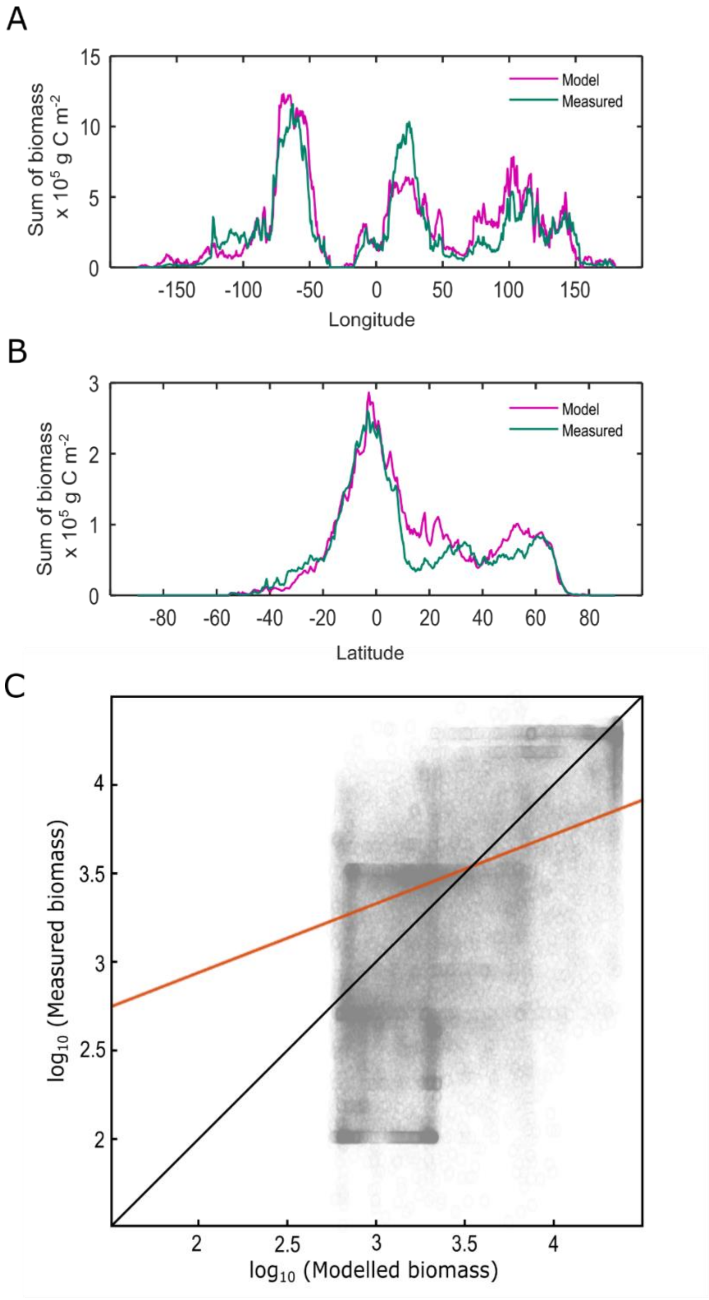

Figure 2.2.7. Further modelled and measured biomass comparison. (A, B) *Sum of biomass between modelled (pink line) and measured (green line) data (Ruesch and Holly, 2008) show overall longitude (-180^{o}W to 180^{o}E) and latitude (-90^{o}S to 90^{o}N) biomass patterns are preserved. Highest global plant biomass is present closer to the equator (0^{o} Latitude). Note: the comparison does not take into account area of either set of values.* ***(C)*** *Model predicted and measured biomass show a linear relationship with an R-squared value of 0.332 in log space (orange line), or 0.496 in linear space. A 1:1 line is shown for comparison in black.*

A comparison between NPP for present-day FLORA simulation and the Sheffield dynamic global vegetation model (SDGVM, Taylor et al., 2012) show similar patterns of NPP distribution; higher overall productivity around the equator that decreases in higher latitudes (Figure 2.2.8). Similar to global biomass, FLORA NPP predictions are higher than the SDGVM estimates around the tropics and some underestimation around 40^{o}N latitude. A large area around (40^{o}N, 60^{o}E) in the SDGVM produce no NPP (grey area, Figure 2.2.8A) which contradicts measured biomass (Figure 2.2.6B) that shows some biomass to be present. This may be the result of the watershed exclusion (areas with <30% natural vegetation) applied in their study suggesting FLORA and the SDGVM runs to be different due to parameter datasets being used.

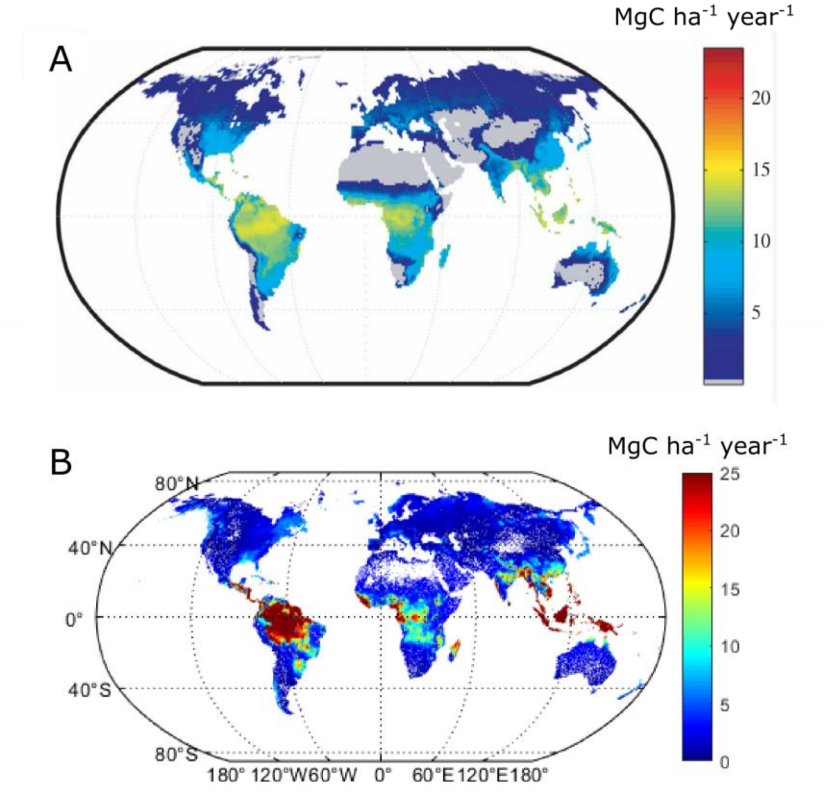

Figure 2.2.8. Net primary productivity (NPP) comparison for present day. (A) *Modelled NPP using the Sheffield dynamic global vegetation model (SDGVM) by Taylor et al. (2012).* ***(B)*** *Modelled NPP using FLORA.*

As competition is present between the three plant functional types, they each dominate different sections of the map hence creating biomes (Figure 2.2.9A). The term ‘biome’ refers to the largest-scale unit of community and reflects the relationship between climate (in particular, temperature and moisture gradients) and vegetation (Mucina, 2019). When compared to a simplified present-day biome distribution (Figure 2.2.9B), the overall patterns of tropical, boreal and temperate biomes are conserved within FLORA. The over-simplification of plant functional types could be another contributing factor towards the mismatch in biomass. In relation to photosynthesis and carbon uptake, leaf functional types vary in their productivity rates based on light requirements/shade tolerance and resistance to water loss (Box, 1996). As such, leaf phenology (i.e. broadleaf and needleleaf) and growth type (i.e. evergreen and deciduous) are other sets of broad biome categories that can be later incorporated into FLORA to better represent present-day biomass distribution.

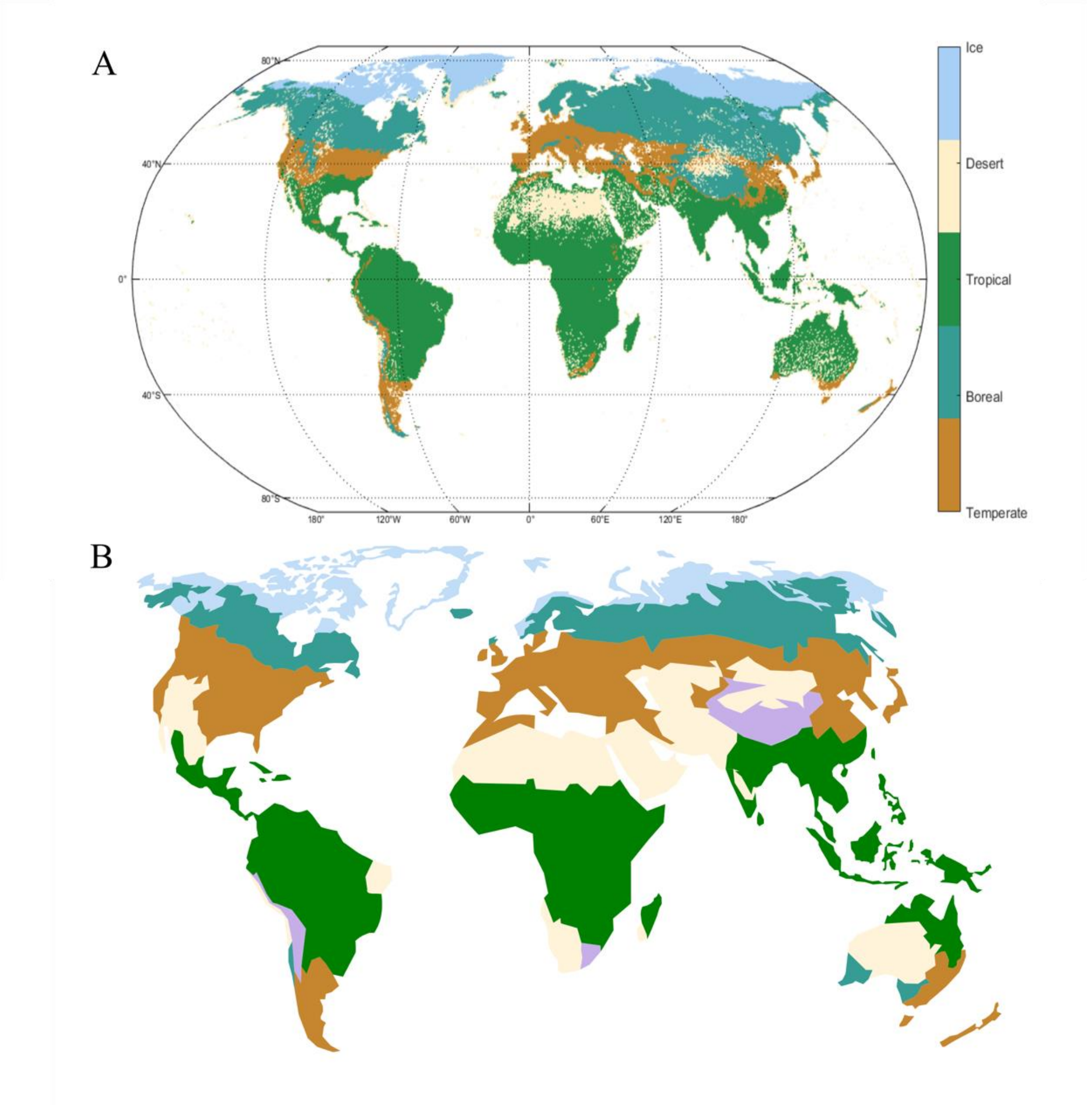

***Figure 2.2.9. Biome distribution comparison. (A)** FLORA predicted biomes when 'competition' is applied between the three main plant functional types; the biome with the highest biomass dominates the gridcell. When temperatures are <-10℃, the biome is considered to be an ice biome. When runoff is absent, the land is considered to be a desert biome. **(B)** World map coverage of terrestrial biomes modified from Trimble and Van Aarde (2012). A similar pattern is broadly observed between the two maps. The original 14 biomes were condensed down to the five main biomes used within FLORA, with the exception of the montane biome (purple).*

Chapter 3. Application of FLORA to paleoclimate

How suitable was the environment for plants during the Phanerozoic? This chapter discusses the results of FLORA when applied to 22 time-slices spanning the Phanerozoic and sheds some light on the ability of Earth to host plant biomass. FLORA predicts potential biomass based on climate model data from the Phanerozoic such as temperature and runoff. Model results show a coincidence between plant potential biomass peaks and plant evolutionary radiations during the Ordovician and Jurassic-Cretaceous. Environmental conditions on Earth may have been suitable for plant life from the beginning of the Phanerozoic; it may have been plant evolution holding terrestrialisation back.

FLORA was run ‘offline’ using the paleogeography, surface air temperature and runoff calculated by Goddéris et al., (2014) using the FOAM (Fast Ocean Atmosphere Model) (Jacob, 1997) ocean-atmosphere climate model for 22 time points over the Phanerozoic. FOAM is a 3-dimensional, low-resolution, climate system model with coupled ocean, land surface and sea ice dynamics used to study long-term climate changes (Jacob et al., 2001). FOAM is able to reproduce spatial distributions of temperature and continental runoff which is a more accurate representation of the heterogenic nature of forcings compared to a non-dimensional model (e.g., GEOCARB) with a singular global average. It is used widely in paleoclimate studies due to its ability to simulate millennium long timescales in a short amount of time (Pohl et al., 2014). CO_2 concentration for each run was set based on proxy information, and box modelling where proxies were unavailable (Table 3.1.1). For these runs, evolutionary changes in the land biosphere were not considered thus the calculation is for ‘potential biomass’ under a generalised photosynthesis-respiration model with modern plant functional types. Plants are present before the hypothesised land evolution of around 470 Ma, as the intention here is to understand the biomass potential of past climates based on fundamental photosynthetic processes and parameters and how they interact with paleogeography and paleoclimate.

The following figures (Figure 3.1.1 – 3.1.22) illustrate the model parameters (temperature and runoff) used at each time-slice along with the FLORA biome divisions and potential biomass output. Biomes are a result of competition whereby the plant functional type with the highest biomass within the gridcell dominates. Ice and desert biomes are added where temperatures are <-10°C and runoff is ≤ 0 mm year^{-1}, respectively. Each figure is accompanied by their average global temperature and runoff values, and a brief description. Tropical biomes are consistently found around the equator which coincides with high biomass. Warmer global temperatures also prevent the formation of ice biomes during the Triassic and Jurassic (Figure 3.1.14 and 3.1.15). Aridity is mainly observed around the equator when runoff is relatively low. For example, aridity on the interior of Pangea on either side of the equator (Figure 3.1.10 and 3.1.11) where runoff was inhibited as a result of the formation of Pangea (Fluteau et al., 2001).

The maps also illustrate the continental configuration changes occurring over the Phanerozoic consistent with FOAM. Land configurations in FOAM are derived from the default land model of CCM2 (Community Climate Model 2, Hack et al., 1993) which were compiled using a large number of prior papers. Fragmentation of land is observed from the Cretaceous onwards (Figure 3.1.16) as Pangea breaks up and spreads to present-day configuration (Figure 3.1.22).

Time (Ma)	CO_2 (ppm)	O_2 (kPa)	Biomass (GtC)
540	5600	1.9	458
500	3360	5.14	558
470	3360	3.74	679
450	2800	5.05	530
430	2240	14.94	555
400	1680	16.76	436
370	1400	16.22	438
340	700	24.76	393
300	560	25.52	347
280	700	27.25	340
260	700	31.05	365
245	1120	30.77	352
220	1680	32.38	398
200	1680	28.6	604
180	1680	25.13	606
145	840	25.86	594
90	1120	26.65	547
70	560	27.69	685
52	700	25.12	681
30	560	21.41	731
15	360	21.57	592
0	280	20.72	453

Table 3.1.1. Phanerozoic time-slices, associated CO_2 and O_2 levels and FLORA biomass outputs. *O_2 (kPa) (Krause et al., 2018) and CO_2 level (ppm) used (Mills et al., 2019) for each time-slice spanning the Phanerozoic, and the sum of potential global biomass (GtC: gigatonne carbon) as predicted by FLORA. Estimated CO_2 using GEOCARB and COPSE models are highlighted in blue. Ma: million years ago.*

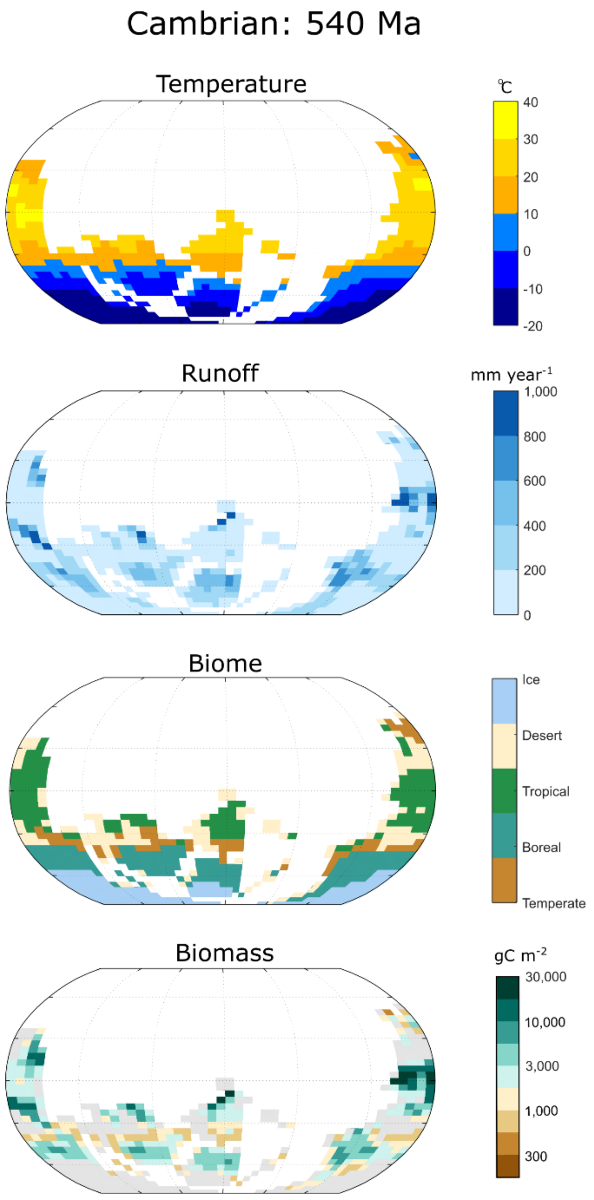

Figure 3.1.1. Cambrian (540 Ma) environmental parameters and model output maps. *Average global temperature and runoff are 18.1°C and 181 mm year*$^{-1}$ *respectively. Although plants are not present on land during this time period, the potential for plant productivity is.*

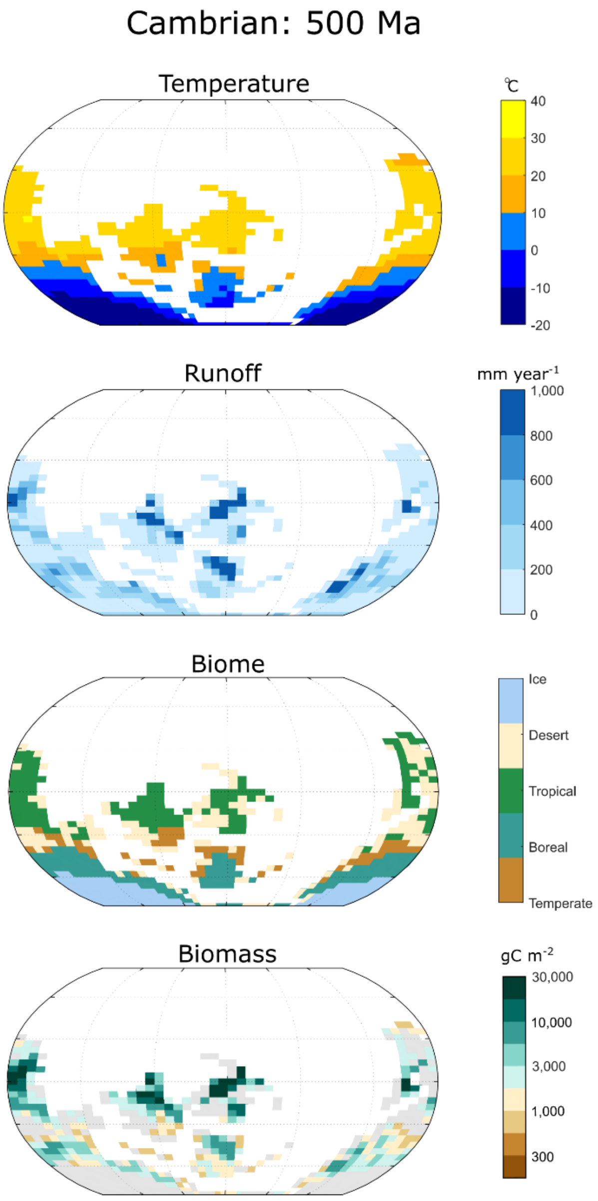

Figure 3.1.2. Cambrian (500 Ma) environmental parameters and model output maps. *Average global temperature and runoff are 18.7°C and 191 mm year*$^{-1}$ *respectively. Similar to the previous figure, Cambrian plant productivity is possible.*

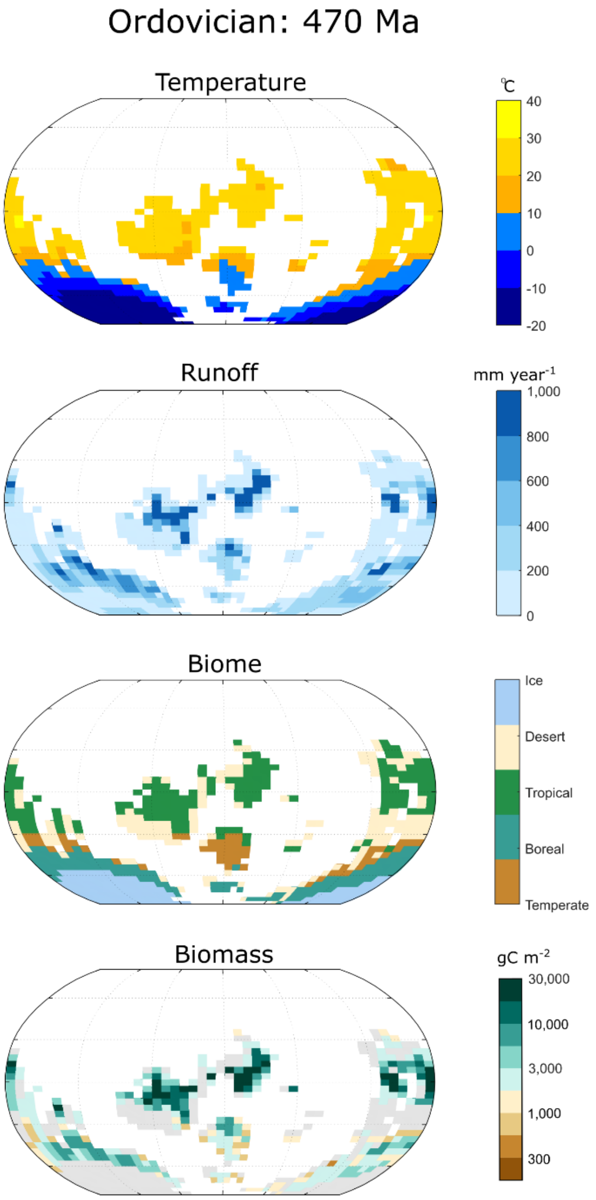

Figure 3.1.3. Ordovician (470 Ma) environmental parameters and model output maps. *Average global temperature and runoff are 18.9°C and 215 mm year^{-1} respectively. Large portion of land lies in the southern hemisphere.*

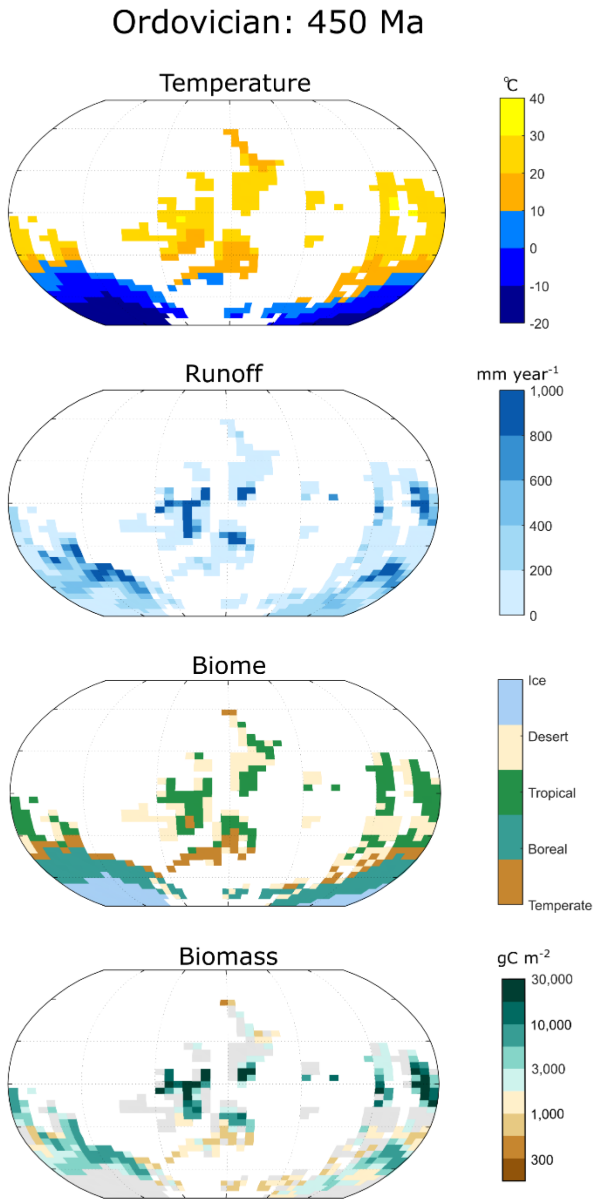

Figure 3.1.4. Ordovician (450 Ma) environmental parameters and model output maps. *Average global temperature and runoff are 19.6°C and 223 mm year^{-1} respectively. A decrease in polar biome is observed at the southern latitudes as global warming occurs.*

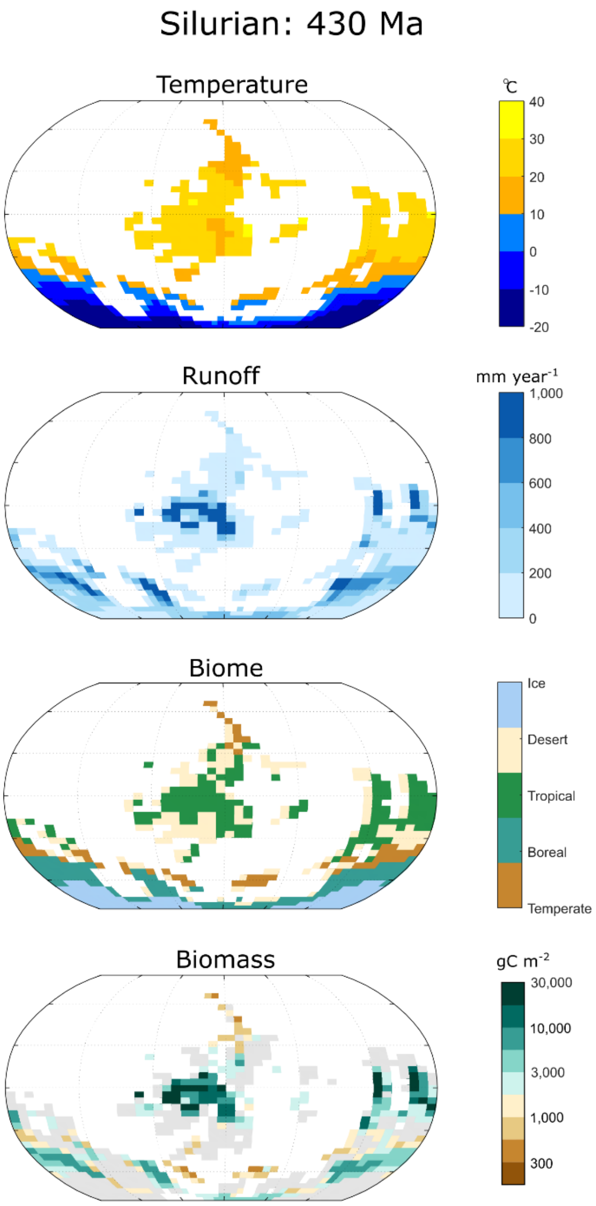

Figure 3.1.5. Silurian (430 Ma) environmental parameters and model output maps.

Average global temperature and runoff are 19.8°C and 222 mm year^{-1} *respectively.*

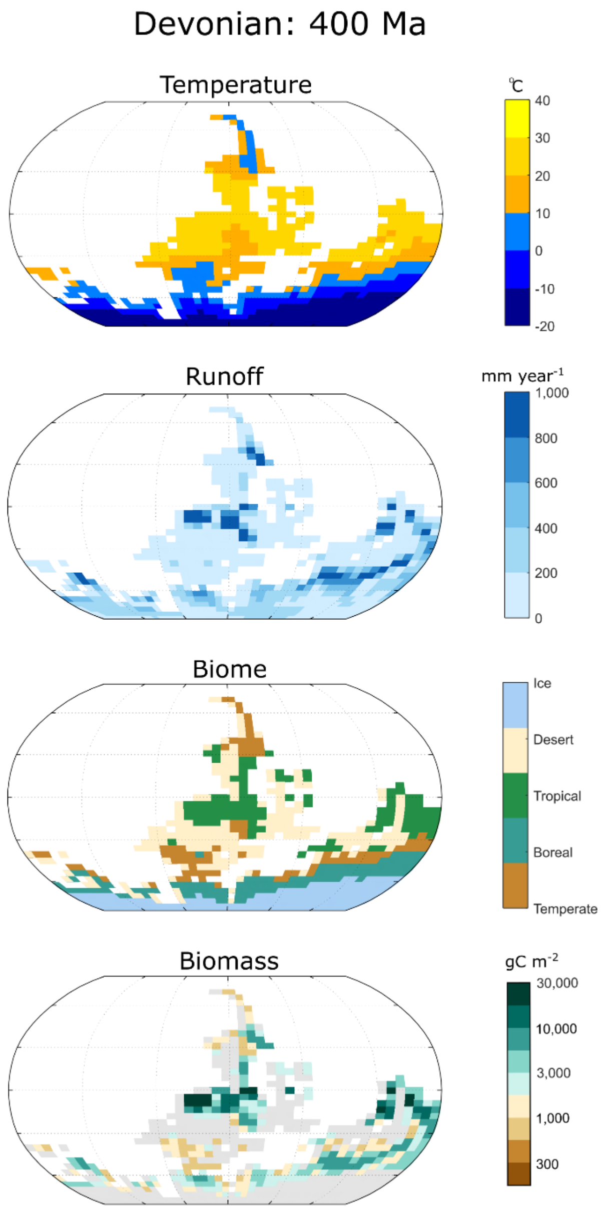

Figure 3.1.6. Devonian (400 Ma) environmental parameters and model output maps. *Average global temperature and runoff are 18°C and 186 mm year*$^{-1}$ *respectively. Aridity increases as runoff decreases mainly in the southern hemisphere.*

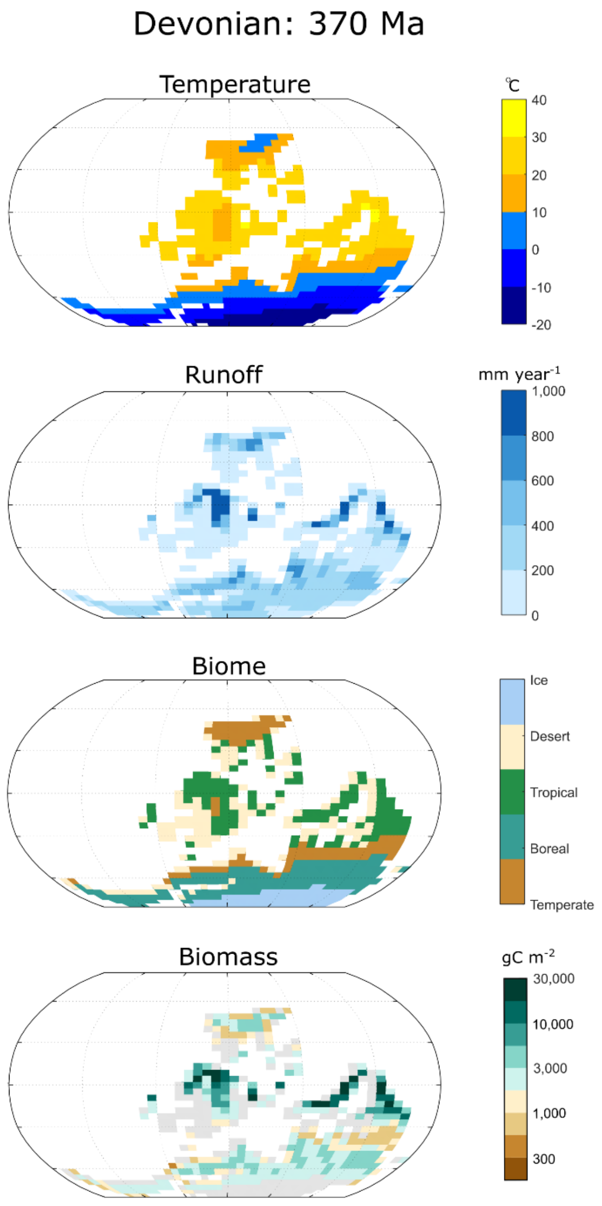

Figure 3.1.7. Devonian (370 Ma) environmental parameters and model output maps. *Average global temperature and runoff are 19.1°C and 211 mm year^{-1} respectively. Large increase in runoff creates more boreal biomes and decreases the spread of desert biomes. Ice biomes are also confined to a small area in the southern pole.*

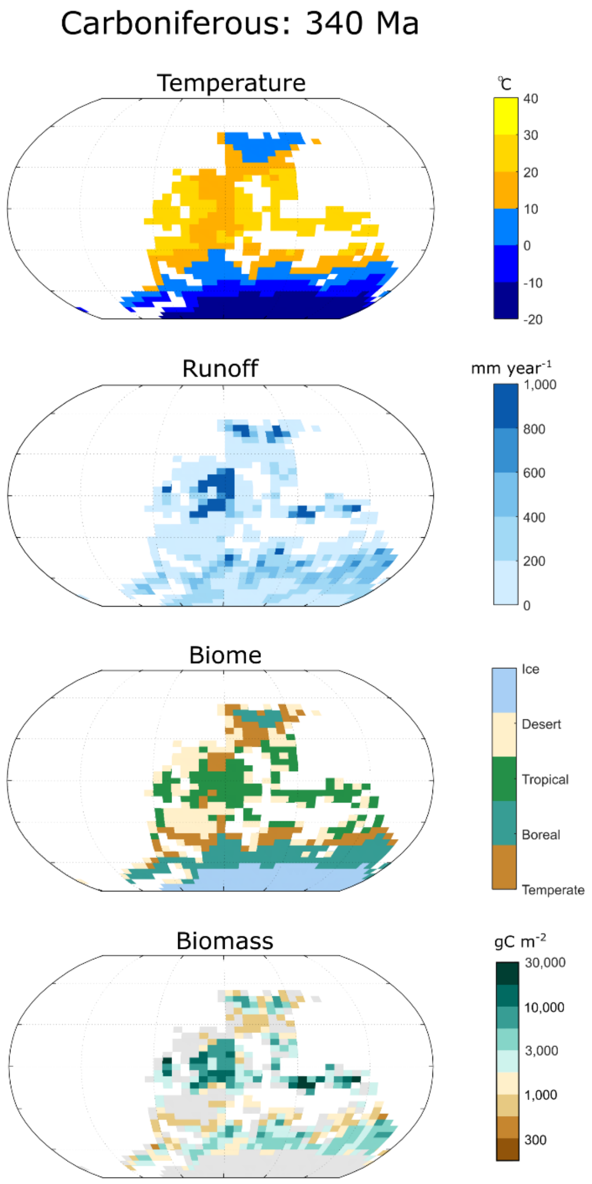

Figure 3.1.8. Carboniferous (340 Ma) environmental parameters and model output maps. *Average global temperature and runoff are 16.8°C and 202 mm year^{-1} respectively. Large decrease in global temperature promotes the spread of ice biomes over boreal. Temperate biomes present in fragmented areas.*

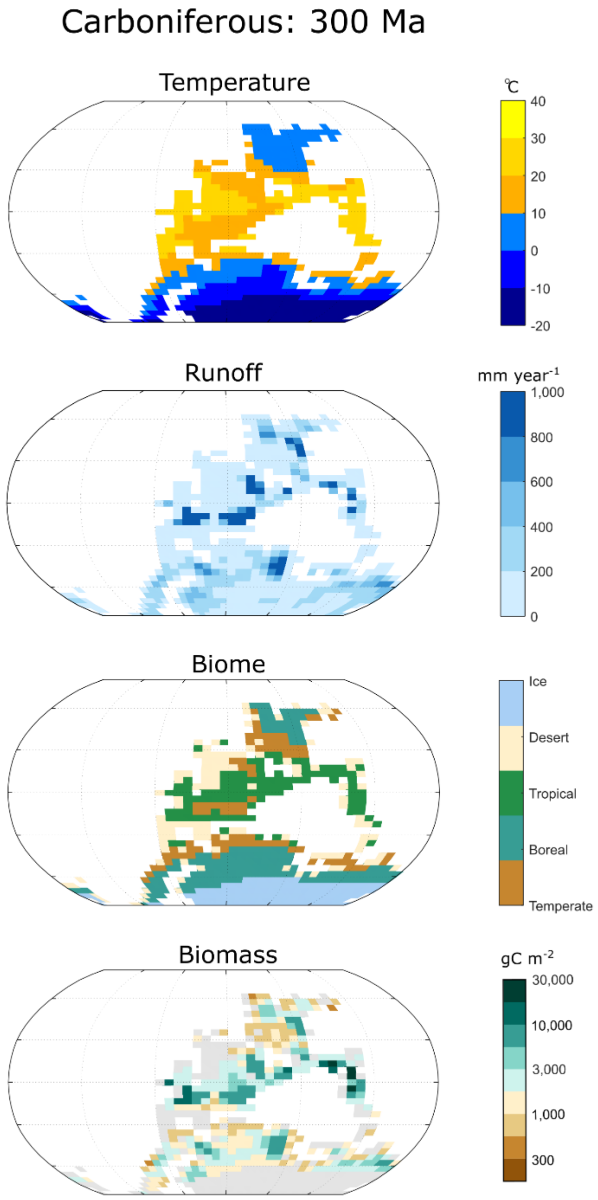

Figure 3.1.9. Carboniferous (300 Ma) environmental parameters and model output maps. *Average global temperature and runoff are 15.9°C and 221 mm year^{-1} respectively. Tropical biomes located mainly around the equator.*

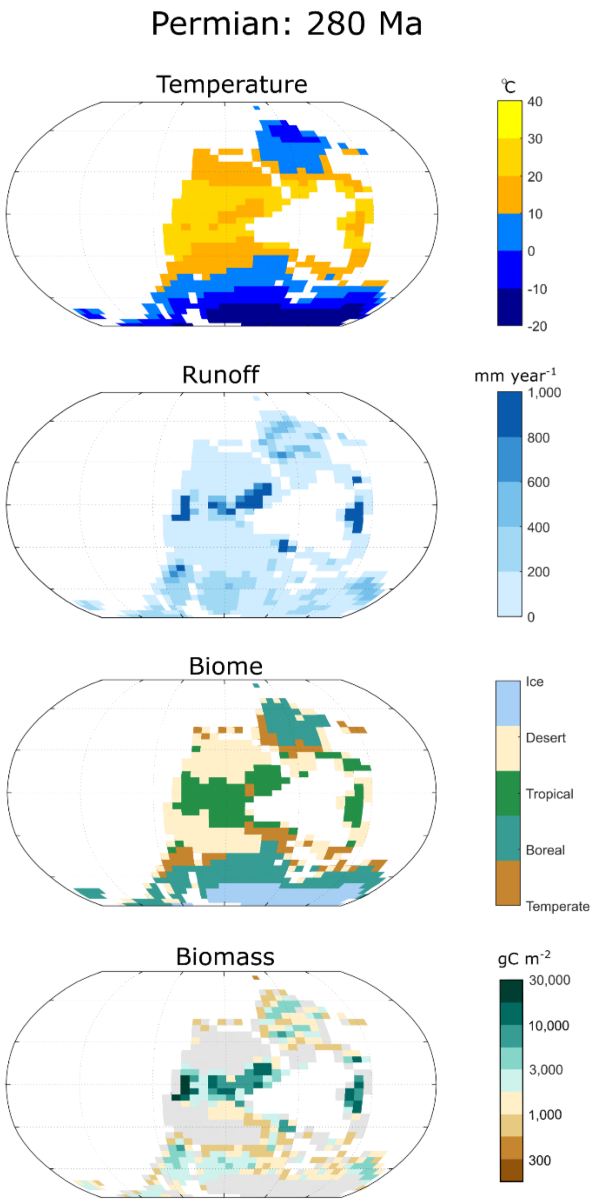

Figure 3.1.10. Permian (280 Ma) environmental parameters and model output maps. *Average global temperature and runoff are 15.7°C and 205 mm year*$^{-1}$ *respectively. Aridity increases at either sides of the equator as runoff decreases in the area as a result of the formation of Pangea. Biomass largely restricted to the equator.*

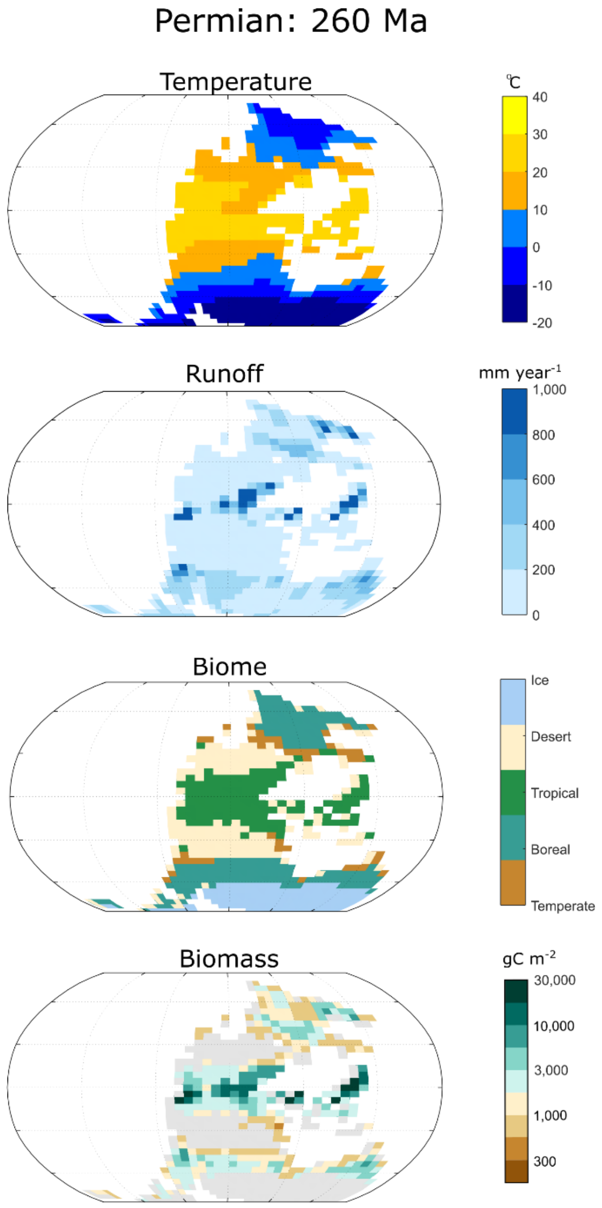

Figure 3.1.11. Permian (260 Ma) environmental parameters and model output maps. *Average global temperature and runoff are 15.1°C and 172 mm year^{-1} respectively. Temperate biomes are rarely present.*

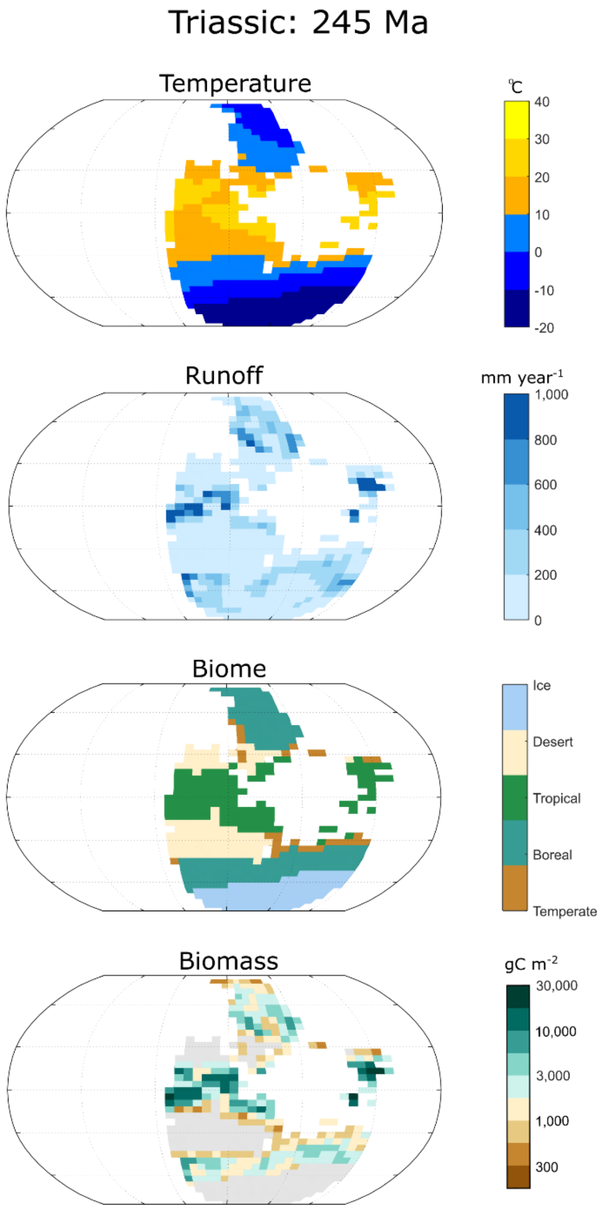

Figure 3.1.12. Triassic (245 Ma) environmental parameters and model output maps. *Average global temperature and runoff are 13.7°C and 220 mm year*$^{-1}$ *respectively. Global temperature is at its Phanerozoic lowest. Biomass distribution largely around the equator and northern hemisphere as ice and desert biomes dominate the southern hemisphere.*

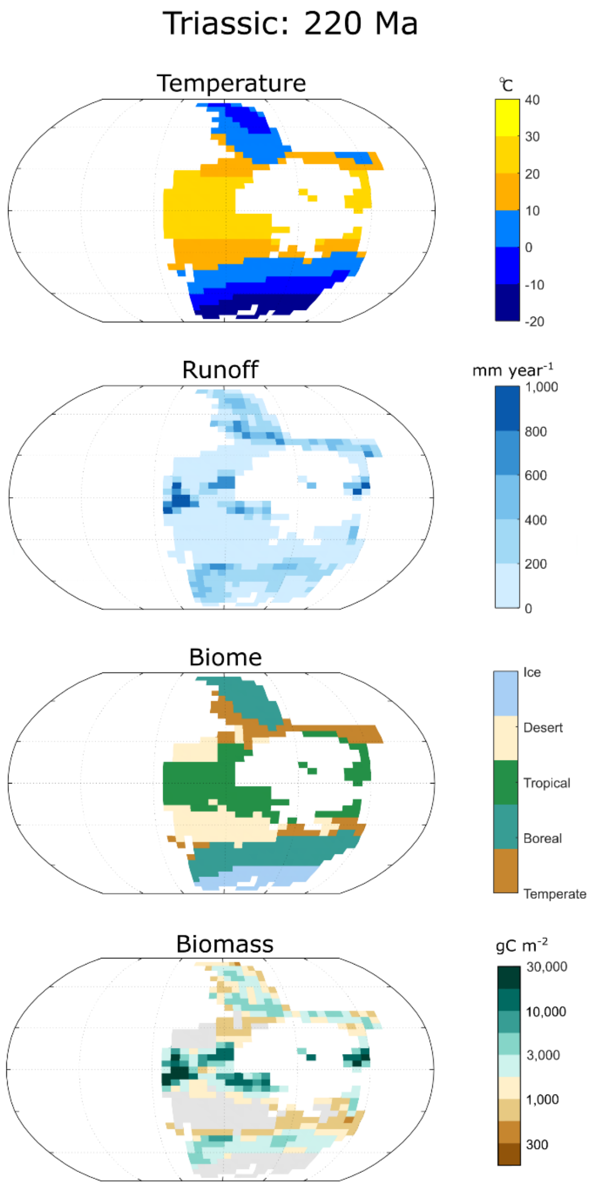

Figure 3.1.13. Triassic (220 Ma) environmental parameters and model output maps. *Average global temperature and runoff are 15.7°C and 191 mm year^{-1} respectively. Land masses migrate northwards which decreases ice biomes in the southern pole.*

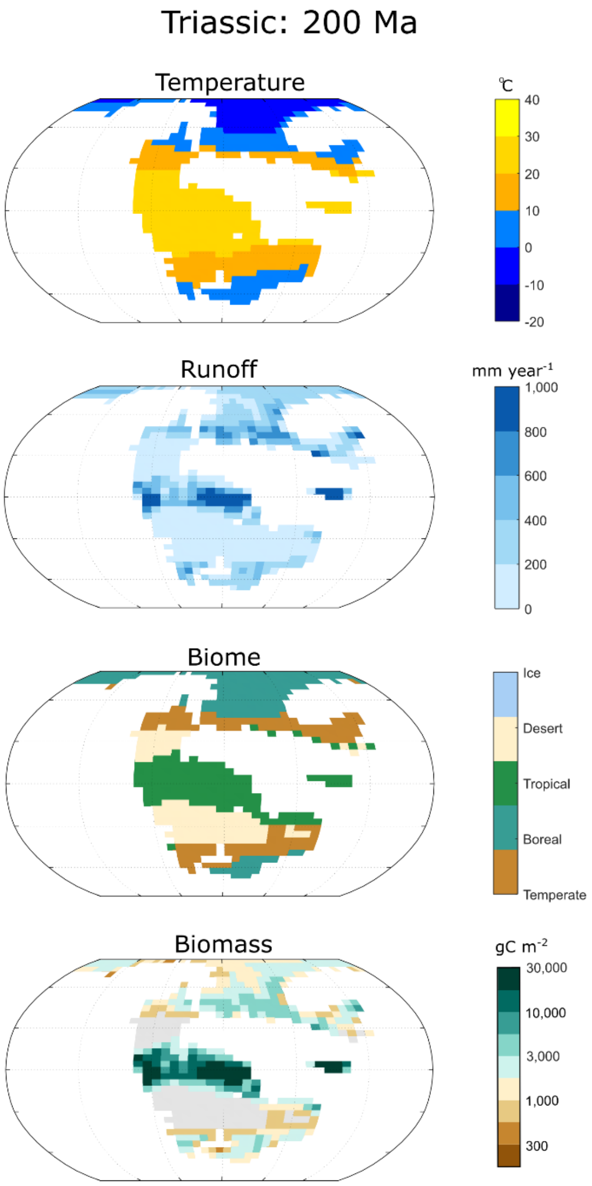

Figure 3.1.14. Triassic (200 Ma) environmental parameters and model output maps. *Average global temperature and runoff are 19.5°C and 254 mm year*$^{-1}$ *respectively. High temperatures and northward movement of continents lead to no ice biomes present and large boreal biomes in the northern poles. High biomass present around the equator.*

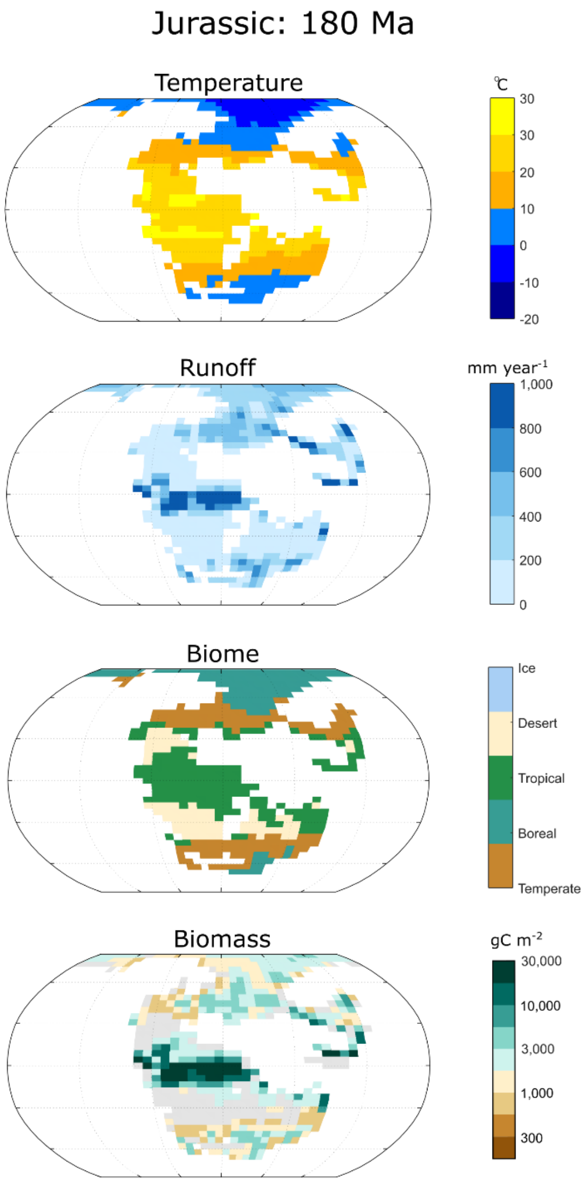

Figure 3.1.15. Jurassic (180 Ma) environmental parameters and model output maps. *Average global temperature and runoff are 21°C and 301 mm year*$^{-1}$ *respectively. Slow fragmentation of Pangea increases runoff on land leading to a decrease in desert biomes. Temperatures continue to rise with no ice biomes on either poles.*

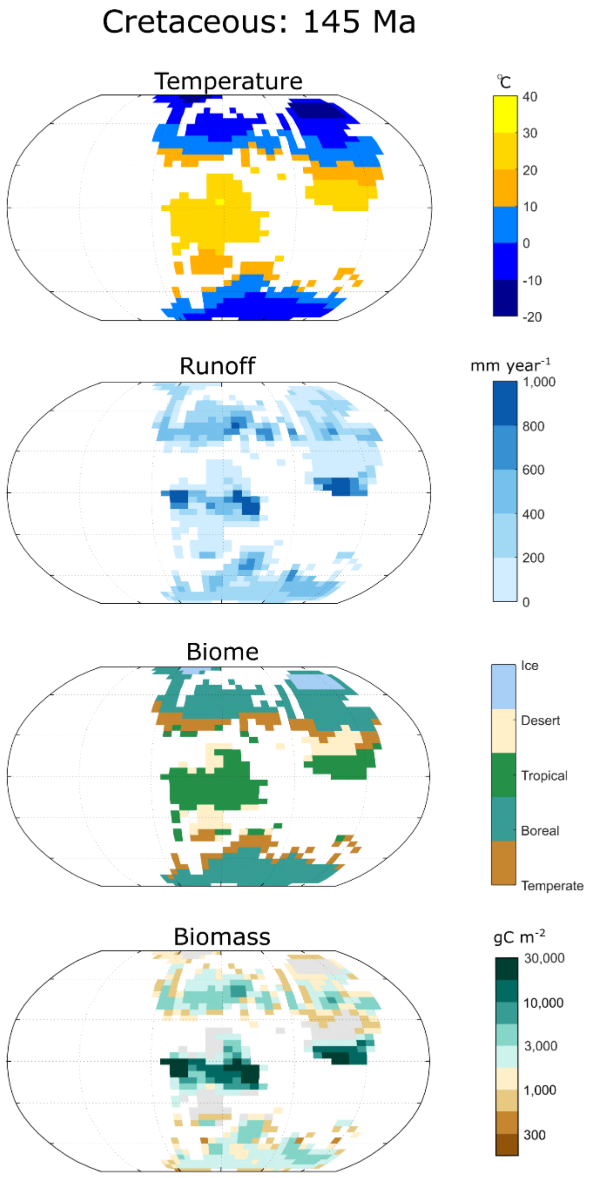

Figure 3.1.16. Cretaceous (145 Ma) environmental parameters and model output maps. *Average global temperature and runoff are 17.8°C and 275 mm year^{-1} respectively. Pangea no longer present. Large decrease in temperature sees the rise of ice biomes in the northern pole. Biomass is largely evenly distributed on land with the tropical biomes still producing the most biomass.*

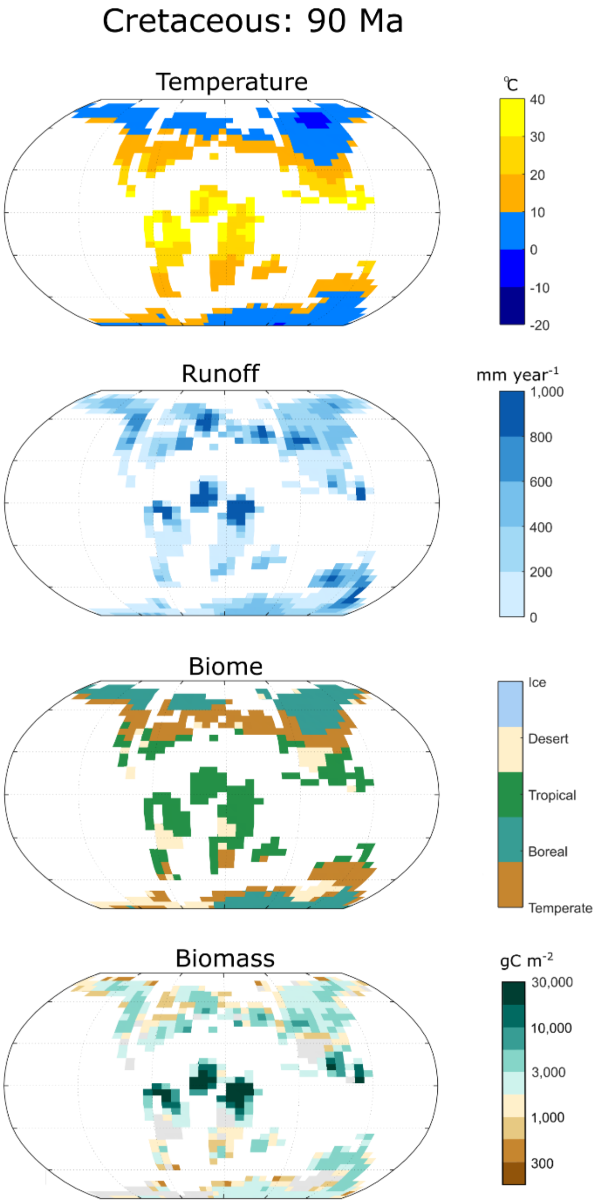

Figure 3.1.17. Cretaceous (90 Ma) environmental parameters and model output maps. *Average global temperature and runoff are 22.7°C and 359 mm year*$^{-1}$ *respectively. Highest temperatures of the Phanerozoic. Land masses fragment more into present-day continents. Some biomass present in almost all land gridcells.*

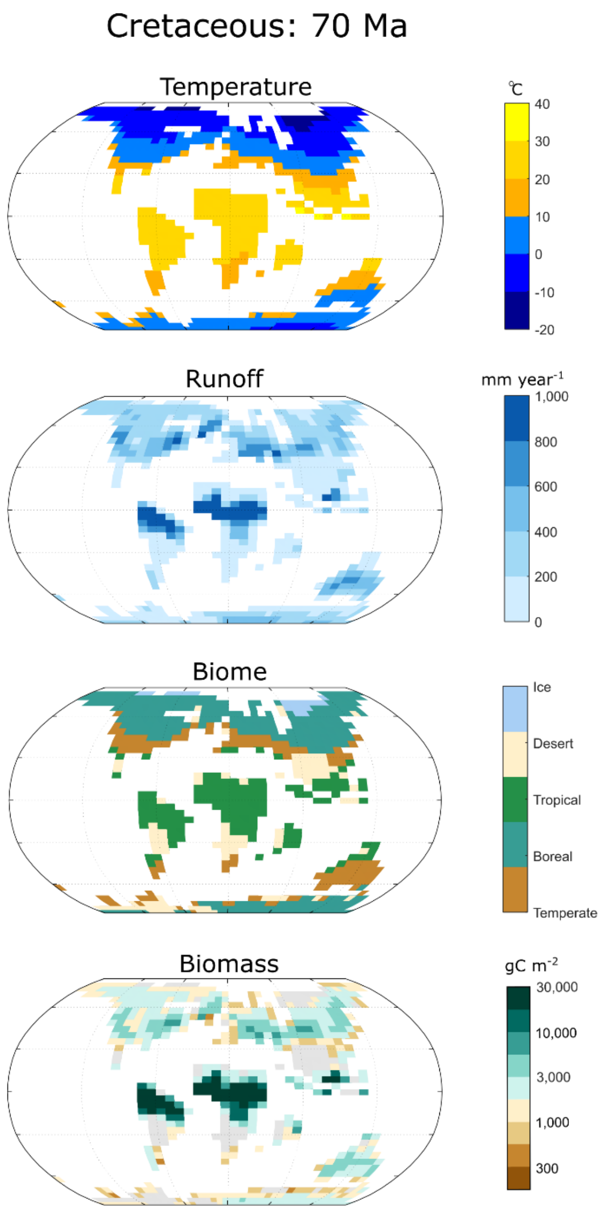

Figure 3.1.18. Cretaceous (70 Ma) environmental parameters and model output maps. *Average global temperature and runoff are 18.9°C and 318 mm year*$^{-1}$ *respectively.*

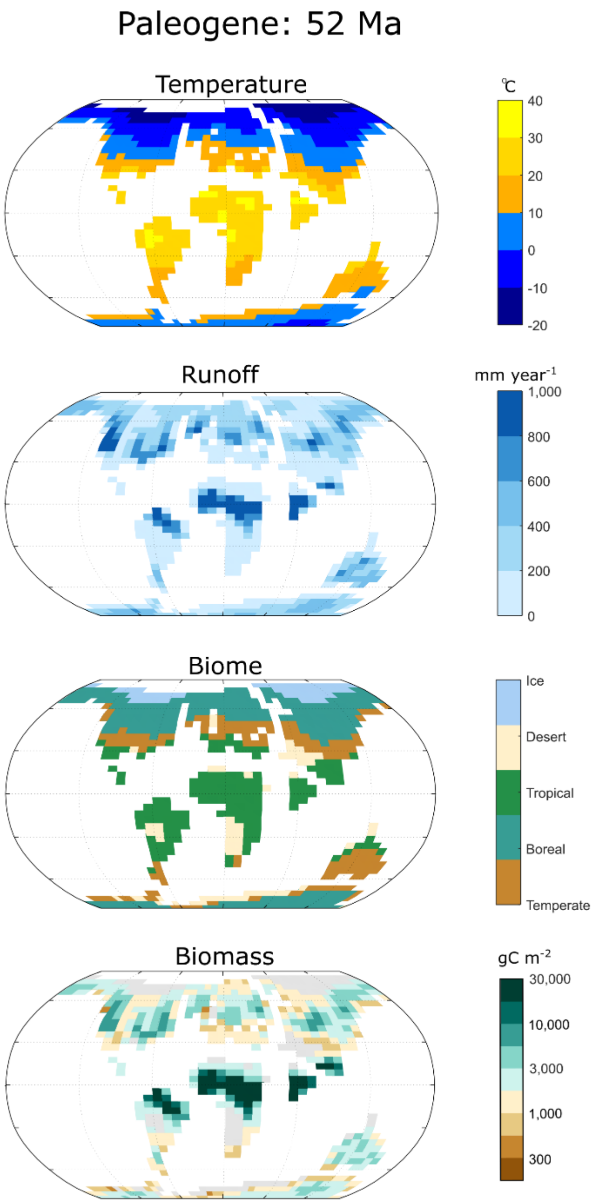

Figure 3.1.19. Paleogene (52 Ma) environmental parameters and model output maps. *Average global temperature and runoff are 19.8°C and 352 mm year^{-1} respectively. Large tropical and boreal biomes present throughout. Most of the land mass is gathered around the northern pole.*

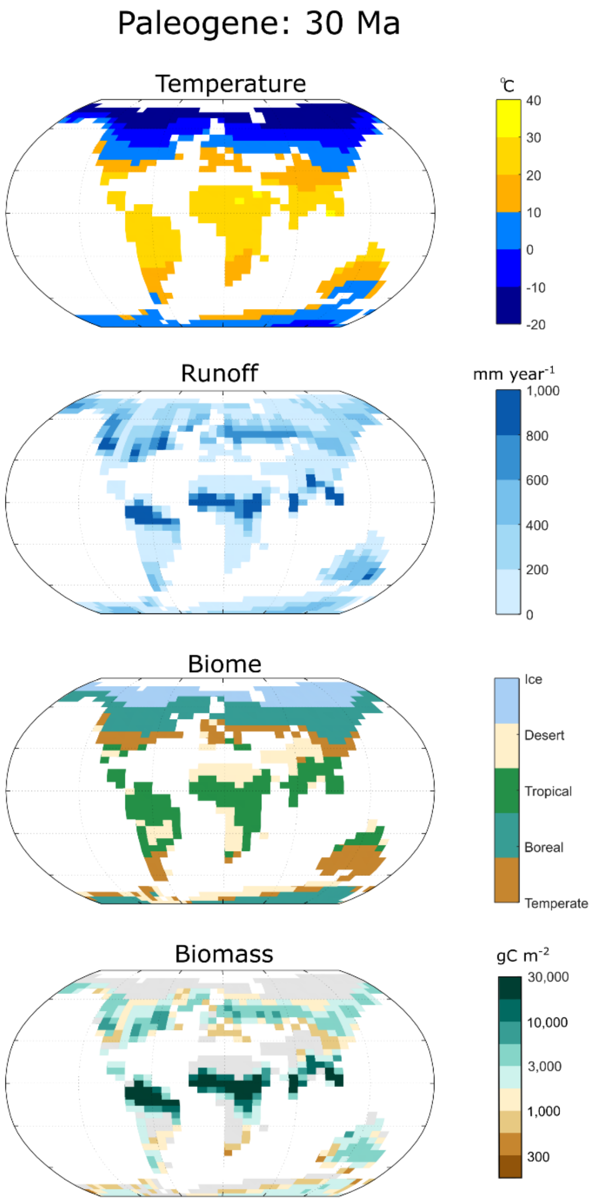

Figure 3.1.20. Paleogene (30 Ma) environmental parameters and model output maps. *Average global temperature and runoff are 18.3°C and 293 mm year*$^{-1}$ *respectively. Large ice biomes created in the northern hemisphere due to a decrease in global temperature and its location.*

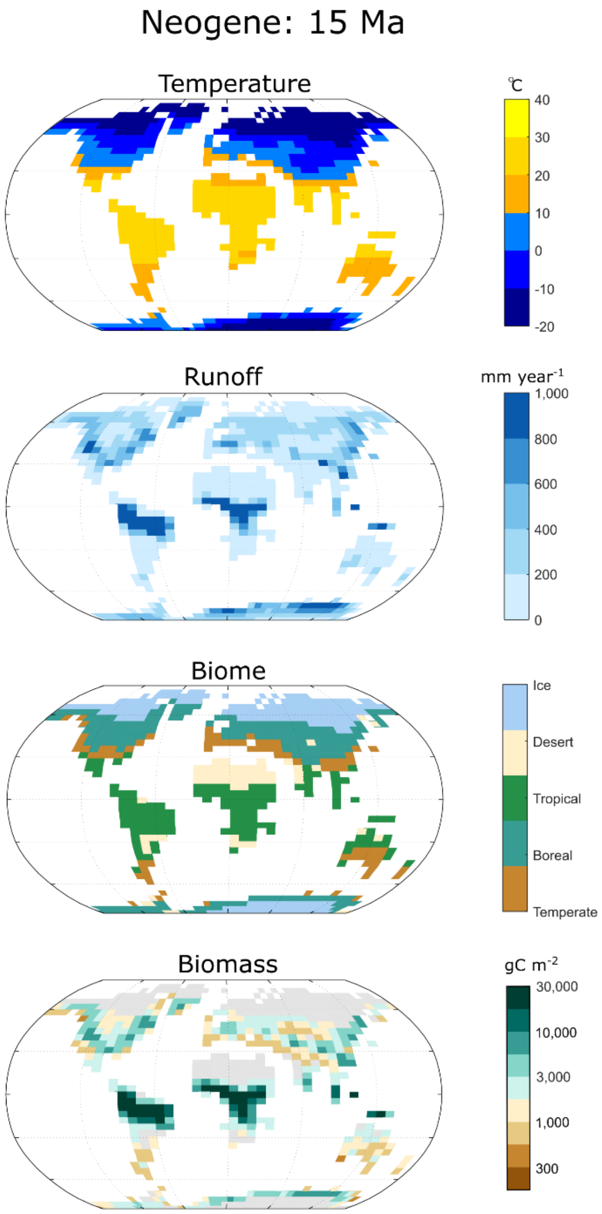

Figure 3.1.21. Neogene (15 Ma) environmental parameters and model output maps.

Average global temperature and runoff are 16.4°C and 288 mm year^{-1} respectively.

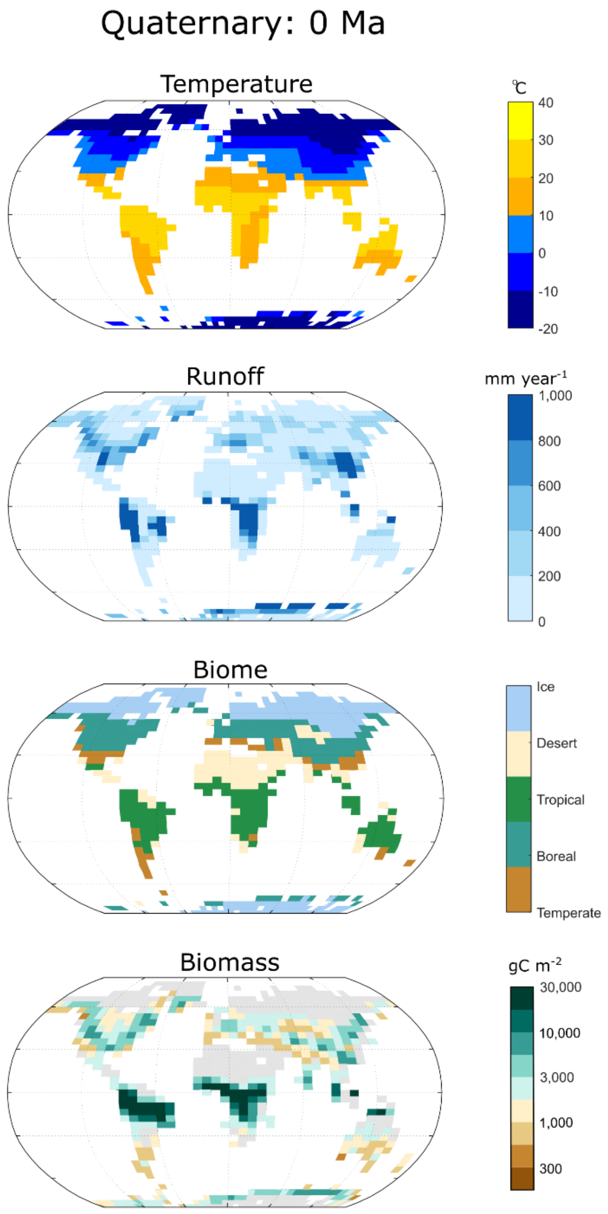

Figure 3.1.22. Quaternary (0 Ma) environmental parameters and model output maps. *Average global temperature and runoff are 14.3°C and 297 mm year*$^{-1}$ *respectively. Present-day land formation, temperature and runoff sees most of the polar regions covered in ice and large desert biomes above the equator.*

3.1 Potential plant biomass over the Phanerozoic

Biomass fluctuates over the Phanerozoic due to a combination of model parameters (land area, runoff, CO_2 and O_2 levels, solar radiation and average temperature) (Figure 3.1.23). Potential biomass refers to the maximum photosynthesis rate (minus the cost of growth and maintenance) given the parameters and its accumulation until the point of steady state. These results indicate two clear peaks in potential biomass; the first being during the Ordovician, and the second being a broader peak from the Jurassic to the Paleogene (Figure 3.1.23 and 3.1.24). Large changes in the tropical biome appear to control the peaks in potential biomass (Figure 3.1.24) suggesting that the expansion and contraction of tropical habitats is a key factor in global biomass calculations. In comparison, temperate and boreal plants show little fluctuation over the Phanerozoic (Figure 3.1.24B).

Our findings compare well to those of Taylor et al., (2012), who coupled the Sheffield-Dynamic Global Vegetation Model (SDGVM) to the Hadley Centre general circulation model (HadCM3L) for a more limited set of paleoclimates. They also found high reconstructed global biomass across the Cretaceous and Paleogene. The large disparity seen in the Cenomanian (Cretaceous period) appears to be due to differences in the exposed land area in the tropics creating higher runoff rates between the climate model runs (Figure 3.1.23). The large increase in runoff between the Jurassic and Cretaceous subsequently increases relative biomass in Taylor et al., (2012) as productivity increases. Nevertheless, both the previous work, and our new analysis agree that the breakup of Pangaea was accompanied by a substantial increase in the habitable space available for plants.

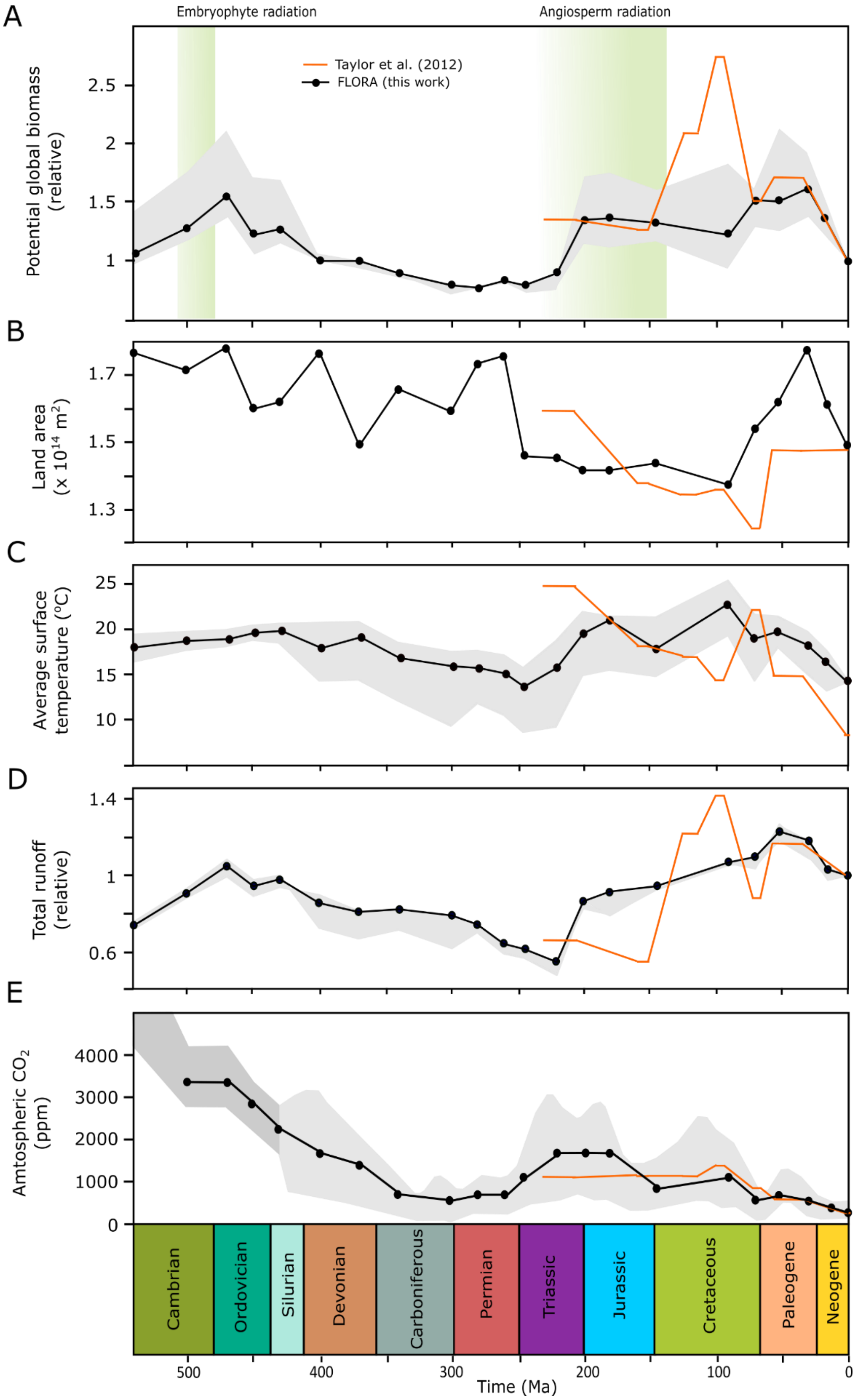

Figure 3.1.23. Global potential relative biomass, runoff, average temperature and CO_2 level during the Phanerozoic (540-0 Ma). *Caption on following page.*

Figure 3.1.23. Global potential relative biomass, runoff, average temperature and CO_2 level during the Phanerozoic (540-0 Ma). *Proxies (temperature and runoff) depend on the predicted CO_2 level. Grey area represents the min/max values obtained at the min/max CO_2 level. Time periods are highlighted at the bottom of the figure. Parameters and biomass used in Taylor et al., 2012 are shown in orange; the length of the solid line represents time periods used.* ***(A)*** *Relative biomass over time (kgC relative to present). Green highlights show predicted origin times: Em = embryophyte, Ang = Angiosperm (Sauquet et al., 2017; Morris et al., 2018).* ***(B)*** *Total terrestrial land area (m^2) present at each time point.* ***(C, D)*** *Average surface temperature (^0C) and relative runoff, respectively. Data taken from Goddéris et al., 2014.* ***(E)*** *Average CO_2 level (ppm). Light grey area: an approximate CO_2 value was chosen for time periods between 430 – 0 Ma using Royer et al., 2006. Dark grey area: predicted CO_2 level chosen from a combination of COPSE and GEOCARBSULF model. Data taken from Mills et al., 2019.*

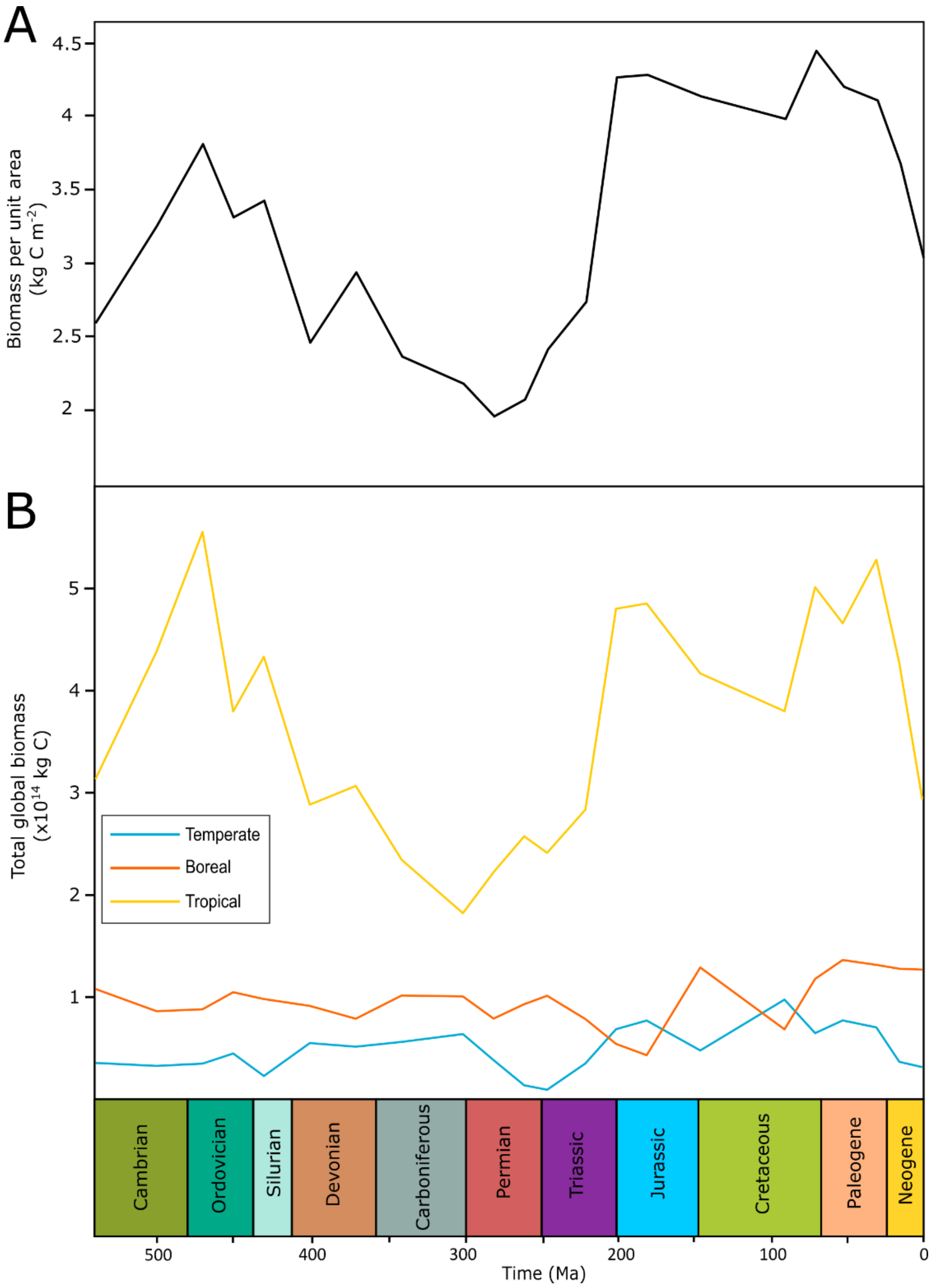

Figure 3.1.24. Global potential biomass per unit and contribution of each plant functional type. *Potential biomass shows peaks during the Ordovician (470 Ma) and Triassic-Jurassic boundary (200 Ma; million years ago). Tropical plants contribute the most potential biomass over the Phanerozoic followed by boreal and temperate plants.*

Biome comparison between FLORA and a FOAM-LPJ output (Figure 3.1.25; Chaboureau et al., 2014) shows similar patterns of biome distribution. Land around the equator is dominated by tropical trees with small areas of desert while boreal plants are present in both the north and south pole (Figure 3.1.25). The largest difference is seen in the northern latitude where boreal plants may be slightly overestimated. As FLORA is a simplification of the LPJ model, the biome comparison highlights that FLORA is able to largely capture the biome distribution (despite only 3 PFTs being present).

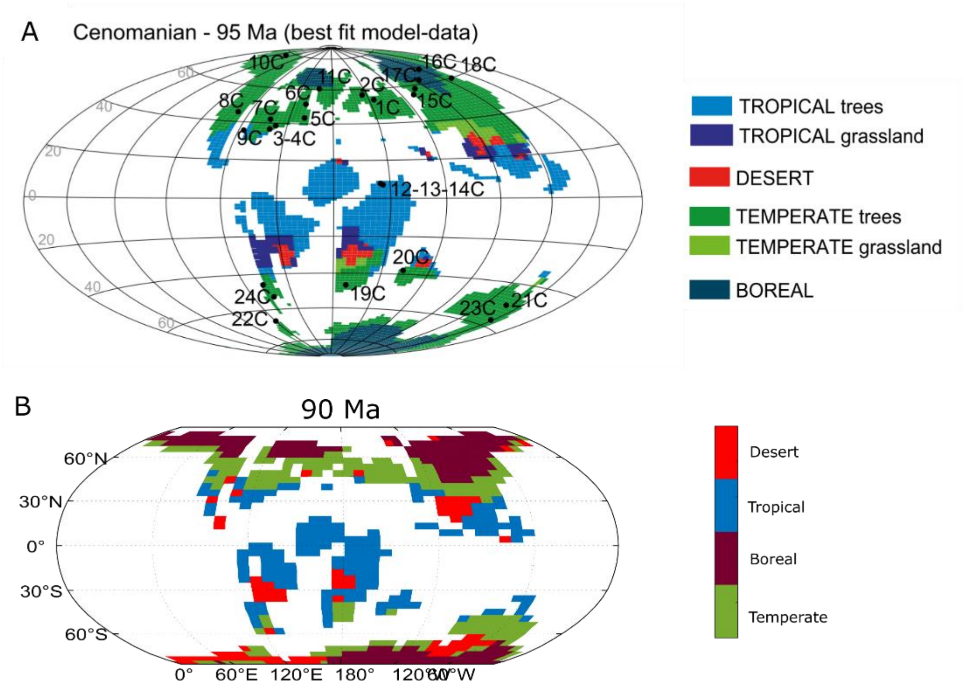

Figure 3.1.25. Biome distribution comparison during the Cenomanian. (A) *Cenomanian (95 Ma; million years ago) biome as predicted by a coupled FOAM-LPJ model. Figure taken from Chaboureau et al. (2014).* ***(B)*** *90 Ma biome distribution as predicted by FLORA that uses FOAM environmental parameters (i.e. temperature, runoff and land orientation).*

Water availability is a major factor in influencing vegetation productivity and distribution (Gholz et al., 1990). The peaks in potential biomass predicted by our model are consistent with times of generally elevated global runoff (Figure 3.1.23A and D), which is understandable given the absolute requirement for water for plant growth. Runoff also has the highest average r-squared value across all time points ($r^2 = 0.72$) suggesting potential biomass is most influenced by water availability. A Spearman's rank correlation also shows runoff to positively correlate with biomass ($r_s = .55$, $p < .05$, Figure 3.1.26). The relationship between continental runoff and potential biomass also appears to be sigmoidal where after a certain point ($\sim 1 \times 10^{16}$ gC), although runoff increases, biomass does not. A strong sigmoidal relationship is seen in tropical PFTs especially at 200 and 70 Ma (Figure 3.1.26) suggesting that at high levels of water availability, tropical plants are limited by the water availability function. This is also observed most prominently in tropical plants as boreal and temperate settings do not receive high levels of runoff. The pattern is however not absolute. Despite high average runoff values at 0 Ma (297 mm), tropical plants do not plateau in biomass suggesting a separate limiting factor, possibly temperature or land orientation (i.e., leaving the equatorial region where tropical biomes are likely to be present) to be affecting potential biomass more so than runoff. Churkina et al., (1999) tested the dependency of NPP on water availability and a similar pattern was observed; in dry areas, increasing water availability leads to an increase in the maximum potential vegetation productivity however in areas with excess water availability, a saturation point is reached. The plateau or saturation point could be due to biomass being limited by another variable such as temperature or CO_2.

Although runoff is a key influencer in driving biomass, the variability in the results suggests a combination of factors influence primary production. For example, 245 Ma and 145 Ma show very different runoff-biomass relationship (Figure 3.1.26). 245 Ma shows a more linear pattern whereas 145 Ma has a steep increase in biomass over a short range of runoff values. During 245 Ma, a large portion of land lies near the southern pole and due to the cooler global temperatures, most of the land is considered to be ice as temperatures are below -10°C (Figure 3.1.12). A difference of 4.1°C in global average temperature suggests low temperature is the limiting factor at 245 Ma. Similarly, 15 Ma and 0 Ma (Figure 3.1.27) show a difference in dispersal of biomass due to the difference in pole-to-equator temperature gradient. A larger part of land experiences temperatures between 20-30°C at 15 Ma (Figure 3.1.21). Although runoff only differs by 9 mm year^{-1}, high runoff rates cannot compensate for lower temperatures therefore capping biomass at a lower threshold at 0 Ma.

A tentative linear correlation is also observed between potential biomass and temperature ($r^2 = 0.2615$) whereas the Spearman's rank correlation shows a positive relationship ($r_s = .52$, $p < .05$, Figure 3.1.27). Biomass is seen to exponentially increase when temperatures are between 20-30°C (Figure 3.1.27). Present-day tropical forests are high in productivity, stable and account for 50% of the carbon stored in global vegetation (Pärtel et al., 2007; Brinck et al., 2017). The rate of photosynthesis is highly temperature dependent with tropical plants having an optimum temperature range between 23.7 to 28.1°C (Tan et al., 2017). Therefore, it is unsurprising to see high tropical biomass correlating with higher temperatures around the equator where temperatures stay >20°C (Figure 3.1.27). The expansion of ice caps during the late Paleozoic and the late Cenozoic limited the habitable space, but very warm climates like the late Cretaceous also limited productivity. With the highest global average temperature (22°C) at 90 Ma (Figure 3.1.17), despite the relatively high runoff (359 mm year^{-1}), high continental flooding leads to less area present for plant expansion.

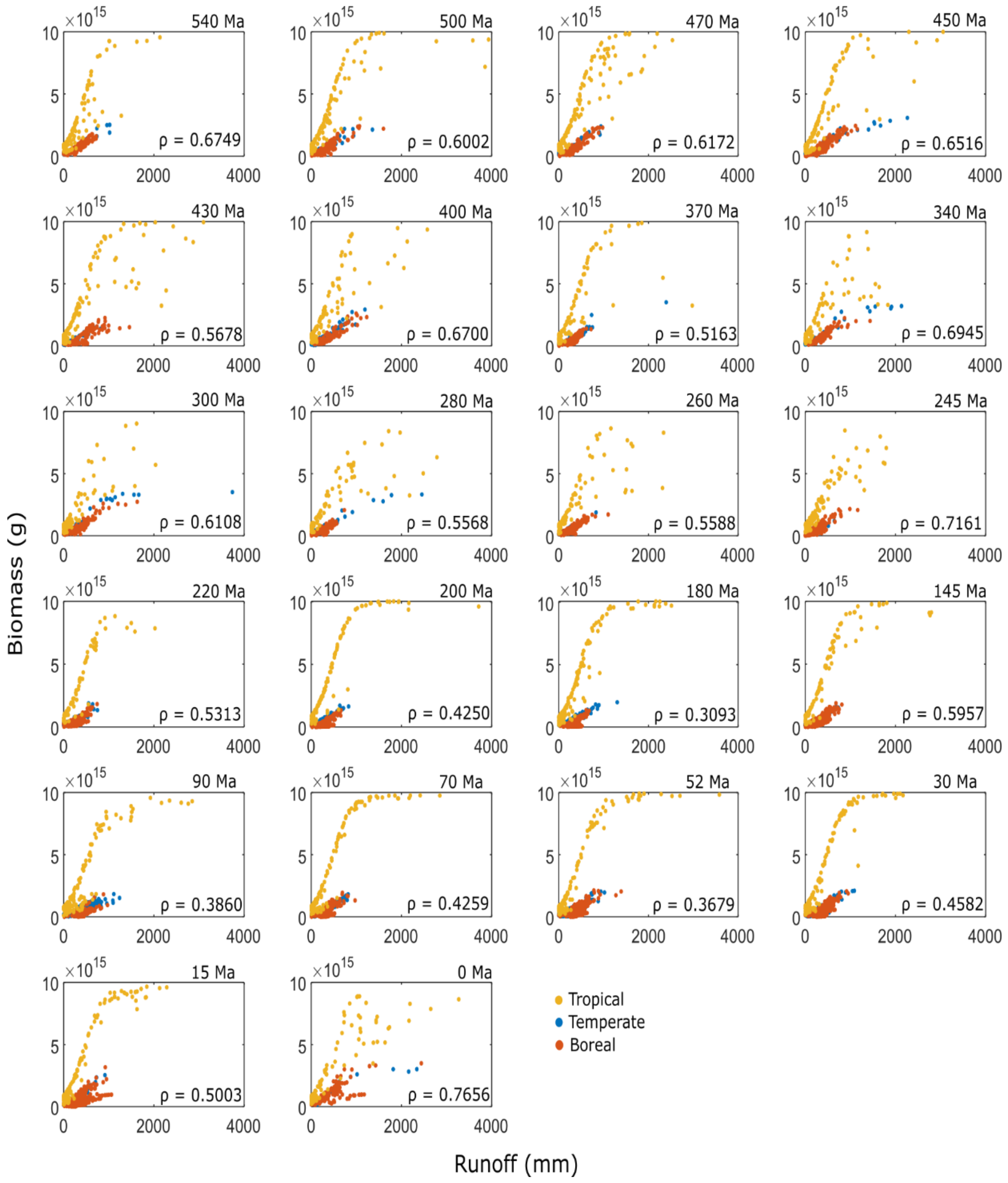

Figure 3.1.26. Spearman's rank correlation between potential biomass and continental runoff for each time-slice. *The average Spearman's rank correlation shows a positive correlation between runoff and biomass with the average being 0.5546. All values have* $p < 0.05$*. The strongest correlation is observed at 0 Ma (million years ago) where* $\rho = 0.7656$*. The three plant functional types are also highlighted; yellow = tropical, blue = temperate, orange = boreal.*

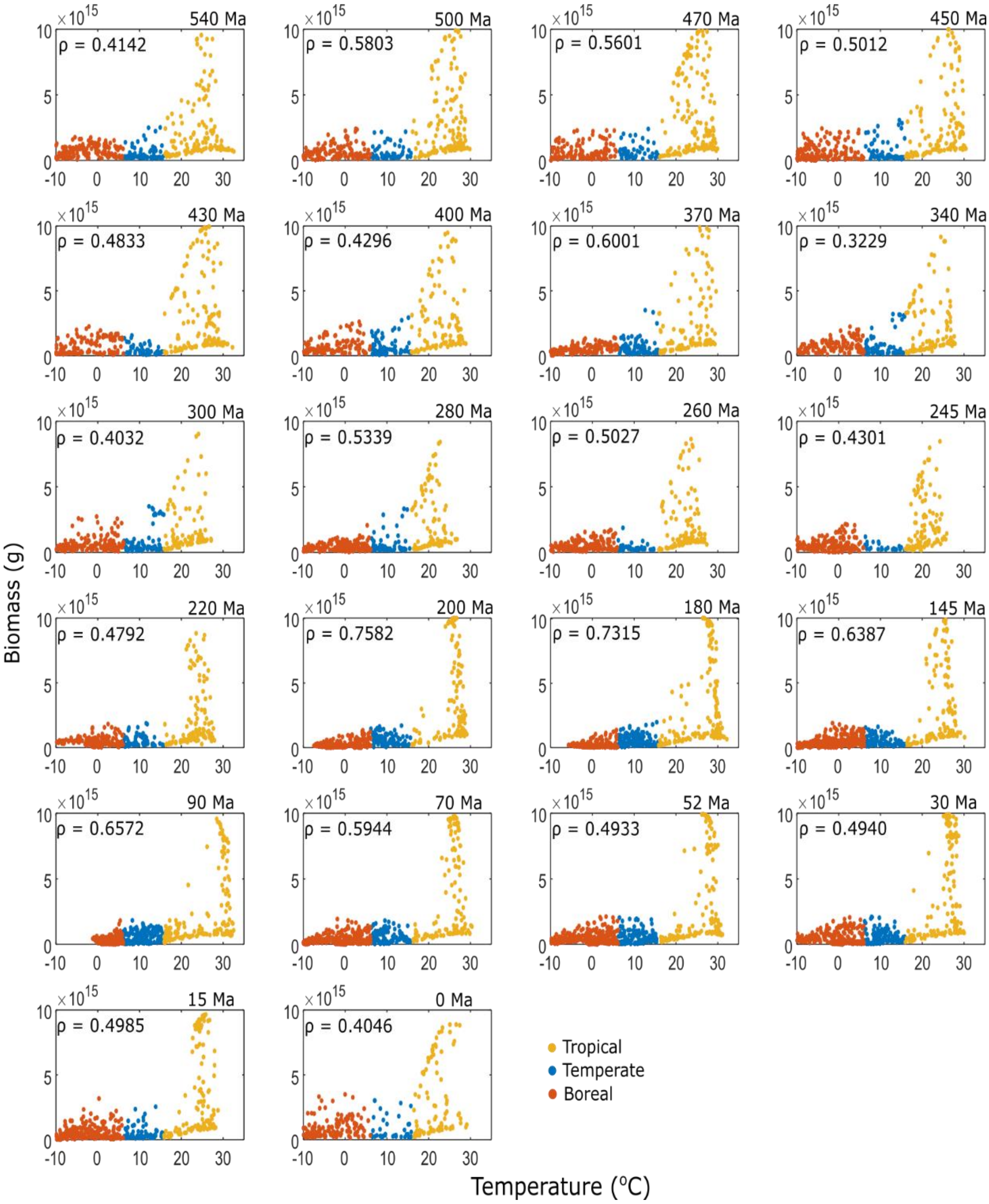

Figure 3.1.27. Spearman's rank correlation between potential biomass and temperature for each time-slice. *The average Spearman's rank correlation shows a positive correlation between temperature and biomass with the average being 0.5232. All values have* $p < 0.05$*. The strongest correlation is observed at 200 Ma (million years ago) where ρ = 0.7582. The three plant functional types are also highlighted; yellow = tropical, blue = temperate, orange = boreal.*

3.2 Linking climate and plant evolution

FLORA results show an early peak in potential biomass at around 470 Ma (Figure 3.1.23A) suggesting temperature and water availability were optimal for high plant productivity. During this time period there was substantial low-latitude land mass which was sufficiently dispersed to maintain a strong hydrological cycle, continental temperatures were also warm and there were no permanent ice caps (e.g., Scotese et al., 2021). FLORA predicts ice biomes to be present during 470 Ma in the southern latitudes (Figure 3.1.3) due to the inherent inability of FOAM to predict higher temperatures at as atmospheric CO_2 increases (Mills et al., 2021). Due to its low climate sensitivity, an unrealistic amount of CO_2 is required to raise temperature. Embryophytes and other morphologically simple plants present during the Ordovician lacked specialised vascular tissues such as roots or stems (Porada et al., 2016) that are typically associated with water conduction. These early plants likely existed mostly in equilibrium with surrounding air (Oliver et al., 2005) and so, in order to avoid desiccation, their distributions were restricted to environments of high water availability. Colonisation of more arid, inland environments would require the evolution of morphological and physiological strategies to prevent plant water loss. According to the FOAM climate model runs, global runoff was increasing between 540-470 Ma (Figure 3.1.23D). This increase in water availability on land would allow for the expansion of plant-habitable areas during the Ordovician, allowing plants similar to poikilohydric bryophytes (Oliver et al., 2005) to persist on land with lower risk of dehydration. As the area of land with adequate plant growth conditions increased, global plant productivity is likely have increased in tandem.

In FLORA, the favourability of the land surface to plant growth decreases throughout the post-Ordovician Paleozoic. Precipitation and runoff decrease markedly as the amalgamation of Pangaea is completed, and the effects of the cooling in the late Paleozoic reduced the habitable space for plants. Silurian mesofossils indicate the presence of lignified cell walls and tubular structures essential for water supply towards the peripheral regions of plants which were further developed towards the Devonian (Edwards, 2003). Tracheophytes evolved between around 450–430 Ma (Morris et al., 2018) and the evolution of roots also falls between the Silurian-Devonian period, beginning with rhizoid structures and ending with extensive rooting systems (Raven and Edwards, 2001; Matsunaga and Tomescu, 2016). Thus, this period of increasing aridity is associated with evolution of morphological and physiological innovations in plants, focused towards water acquisition, transport and retention.

Separation of Gondwana and Laurasia by the Permian Tethys Sea and warmer and drier climates favoured drought-adapted or niche-specific groups (Miller, 1982). According to Kraft et al. (2019), the Prague Basin and its islands in the periphery of the Gondwanan shelf acted as refugee areas where spores were transported by ocean currents. The Prague Basin plant colonisation during the Silurian was most likely to be on volcanic islands that provided variety of environments, substrates and isolation for terrestrial plants to diversify (Kraft et al., 2019).

The oldest angiosperm fossil is dated to 136 Ma (Magallón et al., 2013), but molecular clocks suggest the early history of angiosperms is cryptic (Barba-Montoya et al., 2018), with diversification potentially as early as 195-246 Ma (Morris et al., 2018). The potential biomass predictions from FLORA show a significant increase around 200 Ma which is sustained until the Neogene (Figure 3.1.23A). This increase in plant habitability is strongly linked to a large rise in global precipitation and runoff following the breakup of Pangea. During this time, equatorial Pangea transitioned from arid conditions to a 'megamonsoonal' circulation which has previously been proposed to set the stage for the ecological expansion of flowering plants (Chaboureau et al., 2014). The separation of landmasses creates a water cycle in areas that previously were arid (Donnadieu et al., 2006) and the spread of land around the equator increases the land area experiencing high-moderate temperatures for plant growth. Thus, this work supports the inference of a large expansion of habitable space for plants being linked to the mid-late Mesozoic angiosperm radiation.

Global plant biomass is controlled by a combination of surface air temperature, hydrology and photosynthetically-active radiation, and the simple model, FLORA, based on these factors can reproduce a fair representation of present day biomass distribution. In Earth's past, these factors have changed markedly largely due to the positioning of the continents. When FLORA is run under the FOAM climate model outputs, two clear peaks are found in the 'potential biomass'– a measure of the Earth surface's ability to host plant life. This analysis shows a strong environmental incentive for plant expansion during the Ordovician and a later window during the Jurassic-to-Paleogene, which correspond with the initial land colonisation and the major radiation of angiosperms respectively. Moreover, the Silurian-Devonian saw increasing aridity, correlating with a succession of plant adaptions in favour of water transport and retention. These windows of opportunity may have played a key part in initiating evolutionary expansions of terrestrial plants.

Chapter 4. Integrating FLORA into the SCION climate-chemical model

This chapter briefly summarises the 2-D climate-chemical model SCION (Spatial Continuous Integration) and the dynamic coupling of FLORA with SCION, which replaces the previous non-dimensional vegetation in that model. The coupling of FLORA creates a dynamic feedback between the continental climate conditions (surface temperature and runoff) and vegetation productivity and biomass, which feeds back into the carbon cycle through organic carbon burial and spatial weathering rate amplification. Coupling the FLORA model improves the SCION predictions for CO_2 and temperature during the Mesozoic and Cenozoic, particularly it slightly improves upon the SCION predicted low surface temperatures during the Triassic and Jurassic by better incorporating the effect of the aridity of Pangaea on terrestrial productivity.

4.1 SCION model introduction

SCION is a climate-biogeochemical model that combines a 4-D climate data-structure (2D spatial distribution of continents and climate simulations that change with CO_2 level and time; Goddéris et al., 2014) with a long-term biogeochemical box model based on the Carbon, Oxygen, Phosphorus, Sulphur, Evolution model (COPSE; Bergman et al., 2004; Lenton et al., 2018a). COPSE has been used frequently for Phanerozoic and Precambrian long-term climate and surface chemistry predictions. It predicts $\delta^{13}C$ and $\delta^{34}S$ records, for comparison to proxy records, by simulating global fluxes in the carbon and sulfur cycles (Lenton et al., 2018). This allows for mechanistic hypothesis testing as proxy records can be compared against model outputs as opposed to being used as forcings within the model. However, COPSE is limited in its spatial accuracy as global variables such as temperature are allocated single values.

The SCION climate data-structure was used before in GEOCLIM, which is a coupled Earth system model that simulates spatially variable continental runoff and temperature to estimate weathering rates (Donnadieu et al., 2004). The model has been used to explore feedbacks between continental weathering and paleoclimate (Goddéris et al., 2014), and continental vegetation and climate (Donnadieu et al., 2009), however it is limited in its temporal capabilities. GEOCLIM cannot be run continuously (i.e. >10 million year timescales) as it is limited to individual snapshots of continental configurations and therefore is suited to interpretations of more rapid changes in the global carbon cycle rather than Phanerozoic-scale climate reconstructions (Arndt et al., 2011).

The physical climate model used to produce the GEOCLIM/SCION climate fields is FOAM (Fast Ocean Atmosphere Model). It uses a 7.5° longitude × 4.5° latitude grid to represent the spatial distribution of Earth (Tobis et al., 1997). Over the Phanerozoic, specific 'keyframe' timepoints are chosen for the continental configuration snapshots (Mills et al., 2021). Climate model outputs from FOAM (the same version used to calculate FLORA outputs) using a wide range of CO_2 concentrations for the chosen 'keyframes' include surface temperature, topographic height and runoff. SCION combines the COPSE model approach and FOAM climate outputs to make a 2-D climate-chemical model that can be run continuously to assess

Earth surface processes over a changing continental configuration (Mills et al., 2021). To do this, a weighted average is taken between two ‘keyframe’ timepoints to compute surface processes and a linear relationship is assumed between the bulk fluxes from the two timepoints, creating a continuous prediction of Phanerozoic processes at the global scale. Due to the coarse resolution between timepoints in FOAM, this approach loses smaller perturbations and spikes over the Phanerozoic however this can be rectified by using climate models with shorter time increments (Mills et al., 2021).

4.2 SCION-FLORA

Vegetation within SCION exists as a singular global value that enhances weathering and land-derived organic carbon burial by a factor depending on the mass of the terrestrial biosphere. SCION does not use the outputs from the vegetation within FOAM as this uses fixed O_2 concentration, wildfires and nutrient uptake assumptions which are not compatible with the current SCION approach (Mills et al., 2021). The following equations document the terrestrial vegetation in SCION, which is taken from the COPSE model:

$$V_T = 1 - (\frac{T_{surf} - 25}{25})^2 \tag{4.2.1}$$

$$V_{CO_2} = \frac{CO_2ppm - \ p_{minimum}}{p_{half} + CO_2ppm - p_{minimum}} \tag{4.2.2}$$

$$V_{O_2} = 1.5 - 0.5\left(\frac{O}{O_0}\right) \tag{4.2.3}$$

Vegetation is limited by temperature (V_T), CO2 (V_{CO_2}) and O2 (V_{O_2}). Equation 4.2.1 limits vegetation using global average surface temperatures (T_{surf}); temperatures above or below 25°C decrease the probability of vegetation presence. Equation 4.2.2 and 4.2.3 also calculates the probability of vegetation presence using respective atmospheric concentrations and the minimum values required for the existence of plants (Table 4.2.1). The mass of the terrestrial biosphere, $VEG,$ is calculated as a fraction of NPP, $V_{NPP},$ regulated by wildfires, $firef$:

$$VEG = V_{NPP} \times firef \tag{4.2.4}$$

where the contribution of NPP is related to the limiting factors above:

$$V_{NPP} = 2 \times EVO \times V_T \times V_{CO_2} \times V_{O_2} \tag{4.2.5}$$

and the fire function takes the form:

$$firef = \frac{k_{fire}}{k_{fire} - 1 + ignit} \tag{4.2.6}$$

$$ignit = \min(\max(48 \times O_{2mr} - 9.08, 0), 5) \tag{4.2.7}$$

$$O_{2mr} = \frac{\frac{O}{O_0}}{\frac{O}{O_0} + k_{mr}} \tag{4.2.8}$$

where O_{2mr} is the mixing ratio of oxygen, $ignit$ is the ignition probability scaling and EVO is the non-dimensional plant evolution scaling. Following the latest COPSE model, plant evolution is represented as a scaling value for vegetation mass. Between 540 – 465 Ma, no vegetation is assumed to be present therefore $EVO = 0$. As plants become part of the terrestrial biosphere in the form of simple plants, between 465-445 Ma, EVO increases to 0.15. Simple plant enhanced weathering is also assumed to be 15% that of modern-day plants. After the establishment and evolution of more complex land plants, EVO increases to 1 between 400 – 350 Ma. The effect of modern-day plants therefore is assumed to be fully present from 350 Ma. Parameter values for equations 4.2.1 - 4.2.8 are given in Table 4.2.1.

Description	**Name**	**Value**
Global average surface temperature	T_{surf}	
Atmospheric CO_2	CO_2ppm	
Vegetation CO_2 minimum	$p_{minimum}$	10 ppm
Vegetation CO_2 half saturation	p_{half}	183.6 ppm
Fire effect on vegetation biomass	k_{fire}	3
Atmospheric O_2 mixing ratio conversion	k_{mr}	3.762
Present day O_2 reservoir	O_0	3.7×10^{19} mol
Pre-plant weathering enhancement factor	$k_{plantenhance}$	0.25

Table 4.2.1. SCION parameters. *Model parameters relating to vegetation calculations within SCION. Taken from Mills et al., 2021.*

In SCION, silicate and carbonate weathering rates are calculated in 2-D maps and the resulting global flux is scaled by a single value used to represent biotic weathering enhancement. The presence of plants and their evolution in SCION leads to a weathering enhancement between zero and a 7-fold enhancement in the uncertainty analysis (Mills et al., 2021). Silicate weathering is the balance of the carbonic acid dissolution reaction with its rate being dependent on temperature, erosion rates and runoff (West et al., 2005; Maffre et al., 2018). Weathering occurs regardless of plant presence therefore the pre-plant weathering enhancement is set at a constant value.

Terrestrial biotic weathering enhancement, f_{biota}, is calculated as:

$$f_{biota} = \{1 - \min(VEG \cdot W, 1)\} \cdot k_{plantenhance} \cdot {RCO_2}^{0.5} + VEG \cdot W \qquad (4.2.9)$$

$$f_i = \omega_i f_{biota} \qquad (4.2.10)$$

where W is the effect of plant colonisation on chemical weathering rates. The first term with pre-plant weathering enhancement, $k_{plantenhance}$ (Table 4.2.1), represents abiotic weathering whereas the second term represents biotic weathering. The subsequent weathering, f_i, of basalt, granite and carbonate are then scaled accordingly.

To update SCION, FLORA is inserted in place of the above equations. FLORA is coupled with SCION (Figure 4.2.1) to calculate biomass at each timestep using SCION maps for temperature, continental configuration and runoff, alongside the global O_2 and CO_2 values. The biomass then feeds back into the silicate and carbonate weathering rates in each gridbox and the global rate of organic carbon burial. For every SCION timestep, FLORA runs until a near-steady state for potential biomass (<0.5% change between the subsequent biomass calculations) is reached.

This creates a 2-D continental map of NPP and potential biomass which is scaled with the existing evolution parameter and used to calculate weathering enhancement rates and organic carbon burial for the next SCION timestep (Figure 4.2.1). At the beginning of each FLORA run, the terrestrial biosphere is 'seeded' at a homogenous value of 2.5×10^{14} gC m^{-2} which represents the average present day biomass. The inclusion of FLORA within SCION creates a continuous, spatial model that can be used to explore the regional and global effect of vegetation on biogeochemical cycles. Henceforth, SCION with the addition of FLORA will be referred to as SCI-FI (SCION-FLORA Integration).

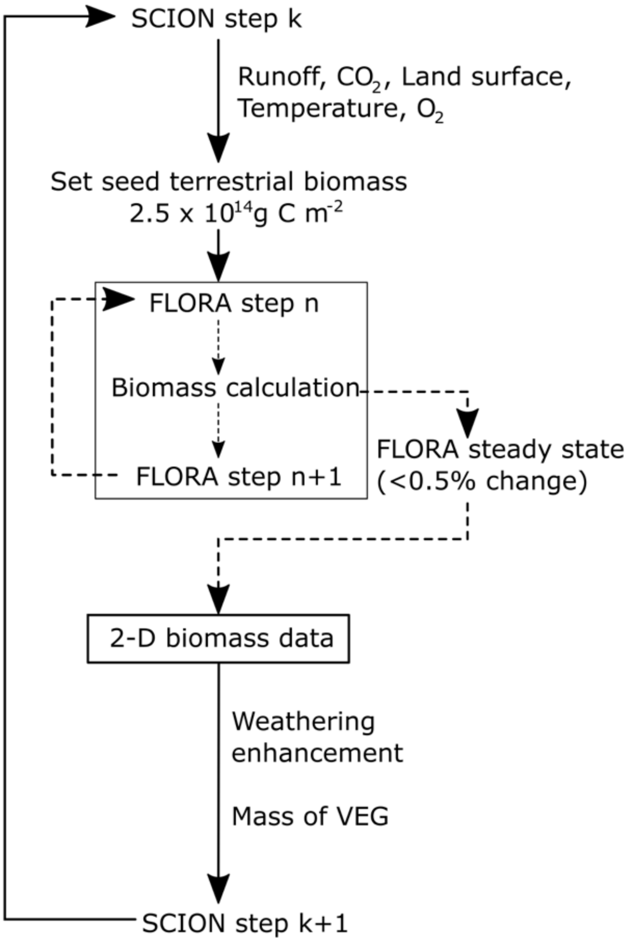

Figure 4.2.1. Schematics of SCI-FI (SCION-FLORA Integration). *Description in following page.*

Figure 4.2.1. Schematics of SCI-FI (SCION-FLORA Integration). *FLORA uses SCION parameters to calculate potential biomass for each timestep. The potential biomass (once there is <0.5% change between the current and next biomass) is then used to calculate weathering enhancement rates which effects the silicate weathering cycles in the next timestep of SCION. Dashed lines represent steps performed by FLORA within SCION.*

Using FLORA, the biotic weathering enhancement term f_{biota} is converted into a 2-D data structure where the spatial weathering rate enhancement per gridcell is related to biomass using a square root function and relative atmospheric CO_2, RCO_2:

$$f_{biota} = 0.005(B)^{0.5} + f_{minbiota} \cdot {RCO_2}^{0.25} \tag{4.2.11}$$

This embodies the assumption that higher biomass will lead to a greater degree of biotic enhancement, but that the effects may reach saturation towards very high biomass (Figure 4.2.2). The large range of potential vegetation enhanced weathering rates (Lenton, 2001) makes it a challenge to form a single relationship between biomass and weathering. Without the presence of vegetation, the weathering enhancement ratio is kept at a minimum constant, $f_{minbiota} = 0.5$, with an abiotic weathering function. Following GEOCARB models use ${RCO_2}^{0.5}$ to represent pre-vascular plant weathering to compensate for high CO_2 levels (Berner and Kothavala, 2001) however this function renders SCI-FI CO_2 levels too low. Hence the older GEOCARB I function of ${RCO_2}^{0.25}$ is used (Berner, 1992). The enhancement ratio ranges between 0.5 and 1.5 with a maximum of a 3-fold increase when considering present day maximum biomass (Figure 4.2.2). Within SCION, silicate weathering is based on an erosion rate calculated using runoff, temperature, topographic slope and exposed areas of basalt and granite whereas carbonate weathering is directly scaled with runoff (Mills et al., 2021). High runoff rates and temperature increase erosion rates which amplifies overall silicate weathering. f_{biota} is then used to further enhance silicate and carbonate weathering within SCION.

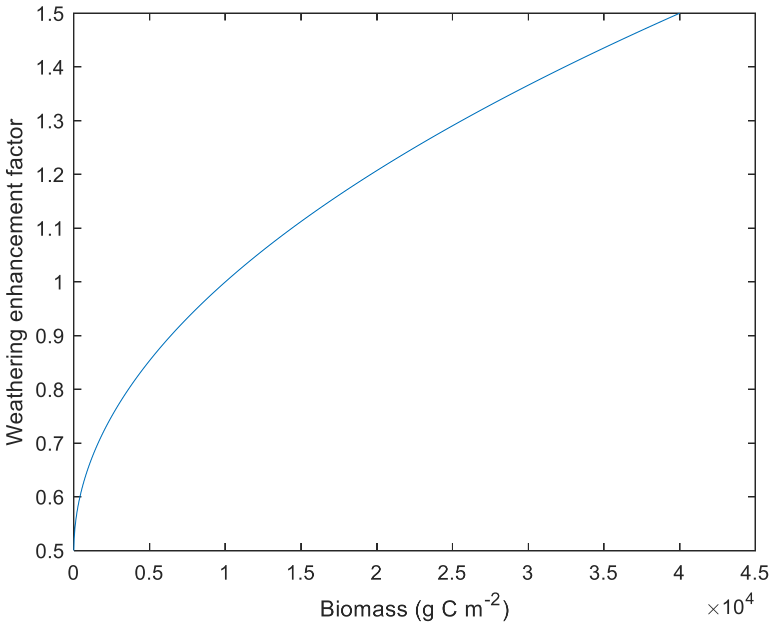

Figure 4.2.2. SCI-FI weathering enhancement relationship. *The weathering enhancement ratio increases along with potential biomass per gridcell, leading to a control on silicate weathering rates dependent on vegetation.*

Biomass death, $B_{turnover}$, and biomass are also updated to include the consequences of increased atmospheric oxygen, and the evolution parameter.

$$B_{(n+1)} = \{B_{(n)} + \left(C_{leaf(n)} - B_{turnover}B_{(n)}\right)\} \times EVO \qquad (4.2.12)$$

$$B_{turnover} = min(max(\ 0.0092 \cdot (100 \times O_{2mr}) - 10), 0.08), 0.2) \qquad (4.2.13)$$

As oxygen increases from 17%, the percentage of biomass turnover increases until it reaches a maximum of 20% (i.e. double the turnover at present day oxygen levels) (Figure 4.2.3). Wildfires at >25% atmospheric oxygen are widespread, especially in wetter climatic areas due to the increased frequency of lightning. At >30%, fire activity is present globally and >35% lies the upper limit of O_2 beyond which fires cannot be extinguished and plants are predicted to burn irrespective of moisture content (Scott and Glasspool, 2006). In SCI-FI, maximum biomass death is assumed to be 20% of total biomass to compensate for the lack of re-establishment in FLORA and separation of localised and global wildfire events. Without an upper limit, a complete biomass turnover would result in no plants within the current and following timesteps. Combustion occurs when O_2 levels reach >13% (Bowman et al., 2009) hence below 21% atmospheric O_2 (present-day), turnover subsides and stays at to 8% (Figure 4.2.3).

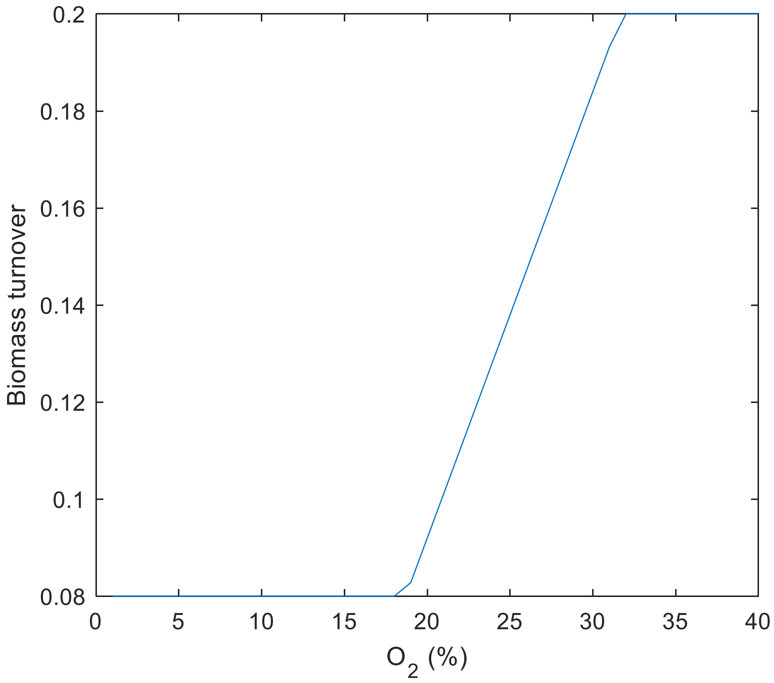

Figure 4.2.3. Biomass turnover and oxygen relationship. *Turnover increases by 12% between 18-32% atmospheric oxygen. Present-day oxygen (21%) has a turnover of 10%. The maximum turnover rate is a two-fold increase from present-day.*

$$s = \left(\frac{24}{h}\right) a \tag{4.2.14}$$

The daylight hours to calculate leaf respiration, s, (Equation 2.2.7) is also updated to $h = 12$ instead of the prior 24 hours. Half of each day is assumed to be in full sunlight.

4.3 Paleoclimate and biogeochemistry results

Here, I have achieved the main aim of FLORA: to be a simple vegetation model that can be easily inserted into a larger climate-chemical model. The ‘offline’ FLORA operates on predicted levels of CO_2 and runoff that are pre-determined whereas the ‘online’ SCI-FI changes CO_2 levels over each run to reflect the effect of plants on Phanerozoic climate and chemical changes.

Figures 4.3.1 to 4.3.22 illustrate the influence of FLORA on paleoclimate and surface conditions (temperature, runoff, biomass, weathering enhancement ratio and silicate weathering at each keyframe timepoint. As the changes in weathering enhancement depend on plant presence, a constant ratio is observed between 540 - 470 Ma due to the assumption of no presence of land plants (Figures 4.3.1 – 4.3.4). Although the biotic weathering enhancement factor is calculated for all land areas, silicate weathering is zero in regions with no runoff (grey areas). The absence of silicate weathering follows a similar pattern to that of biomass absence once plants have evolved. Carbonate and silicate weathering rates within SCION are assumed to scale with runoff as the chemical reactions require an aqueous environment (Mills et al., 2021). Similarly, biomass scales with runoff as water is an important component of photosynthesis and an essential resource for plant survivability and growth. Insufficient runoff therefore leads to low potential biomass and silicate weathering. Conversely, high potential biomass areas increase weathering enhancement ratios and therefore higher silicate weathering rates are observed.

Throughout the Phanerozoic, silicate weathering is seen to follow a pattern based on topography, runoff and biomass. The formation of Pangea over the Carboniferous (Figures 4.3.8 - 4.3.10) shows silicate weathering and intensification of biomass productivity to start localising around the equator. The increased silicate weathering rates would be largely due to the initial collision of continents rather than an enhancement due to plant productivity. As Pangea formed, the uplift needed to create the Central Pangean Mountains (see Chapter 1.5; Scotese, 2021) would have exposed unweathered rocks to the environment. Although a strong relationship is observed between biomass and silicate weathering, the model needs to incorporate the dynamics between plant presence and altitude to better distinguish between the role of geography and plants on silicate weathering.

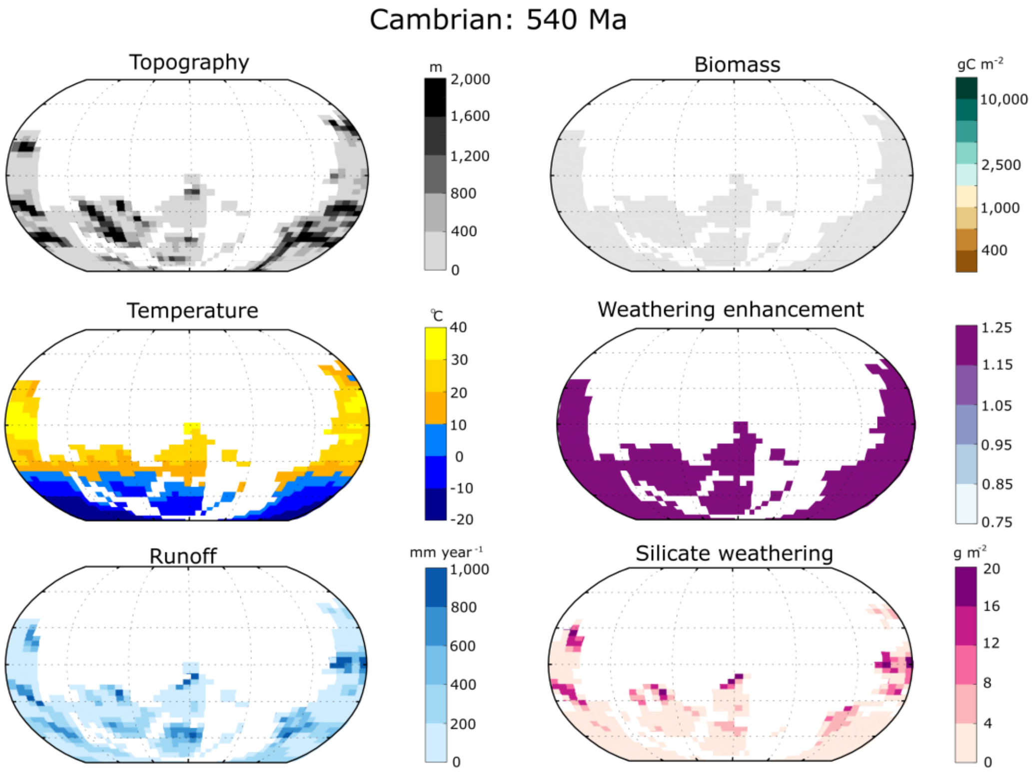

Figure 4.3.1. Cambrian (540 Ma) SCI-FI results and environmental condition maps. *Global average temperature and runoff are 19.97°C and 186 mm year*$^{-1}$ *respectively. A constant high silicate weathering rate is observed in all areas as* CO_2 *levels are high. No plants are assumed to be present therefore no biomass and weathering enhancement due to plants are present. Weathering enhancement is homogenous at 1.15.*

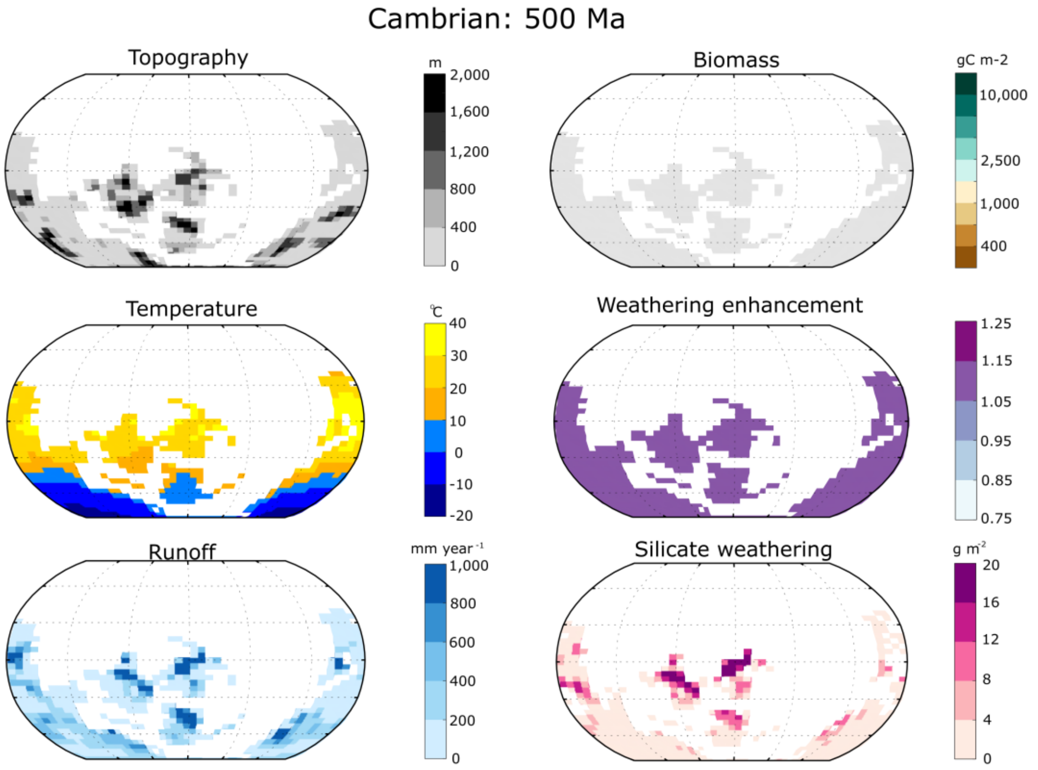

Figure 4.3.2. Cambrian (500 Ma) SCI-FI results and environmental condition maps. *Global average temperature and runoff are 21.27°C and 256 mm year*$^{-1}$ *respectively. Silicate weathering follows a similar pattern to topography. Weathering enhancement is homogenous at 1.07 as no plants are present.*

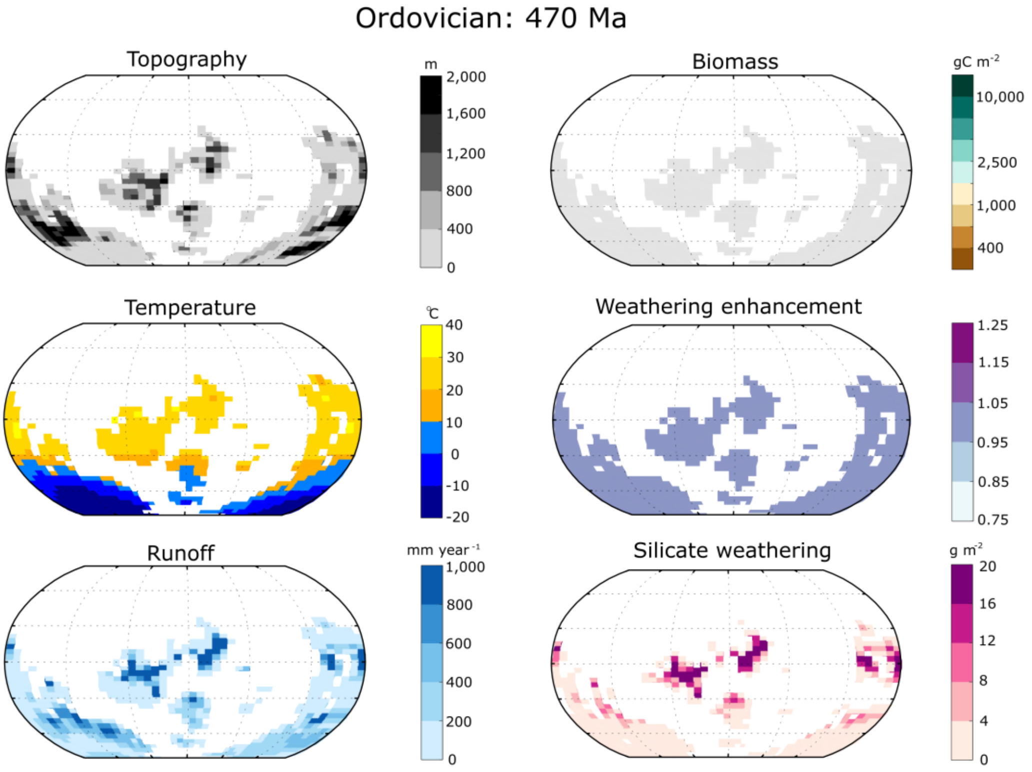

Figure 4.3.3. Ordovician (470 Ma) SCI-FI results and environmental condition maps. *Global average temperature and runoff are 19.52°C and 255 mm year*$^{-1}$ *respectively. Silicate weathering rates are lower than previous timepoints due to lower* CO_2 *levels. No plants are assumed to be present therefore no biomass and weathering enhancement due to plants are present. Weathering enhancement is homogenous at 0.96.*

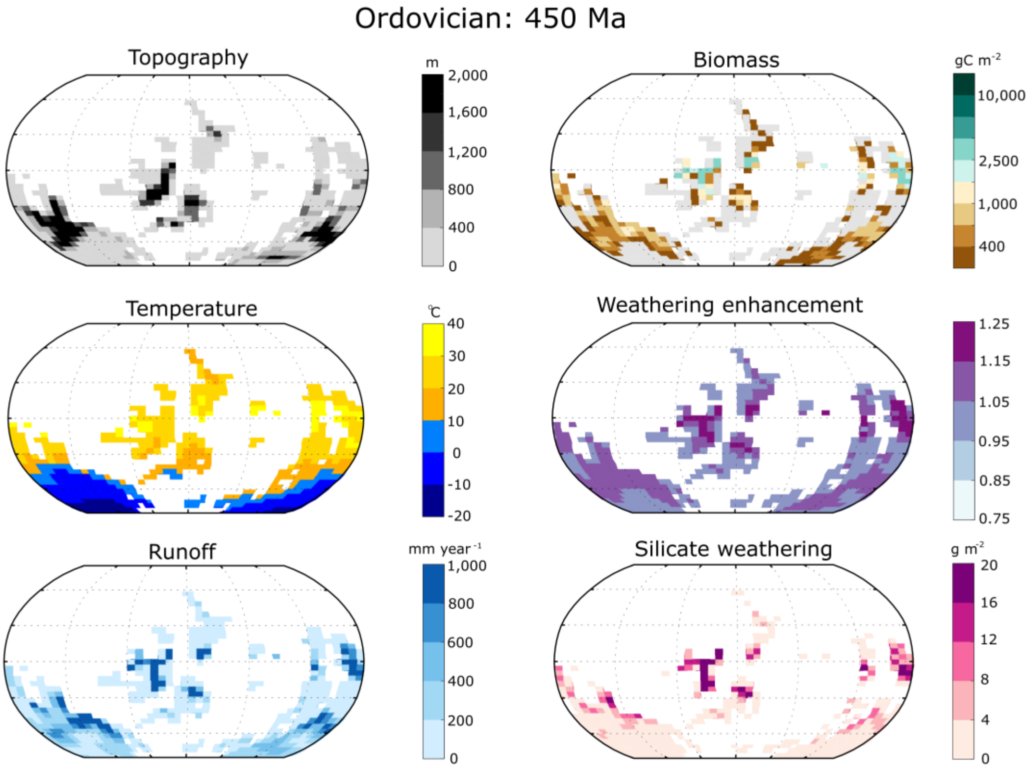

Figure 4.3.4. Ordovician (450 Ma) SCI-FI results and environmental condition maps. *Global average temperature and runoff are 21°C and 254 mm year*$^{-1}$ *respectively. First instance of plant presence increases weathering enhancement rates in areas of relatively high biomass. Total global biomass is 80 GtC. Biomass is however limited by the evolution parameter. Silicate weathering is now dictated by a combination of topography,* CO_2 *level, runoff and biomass.*

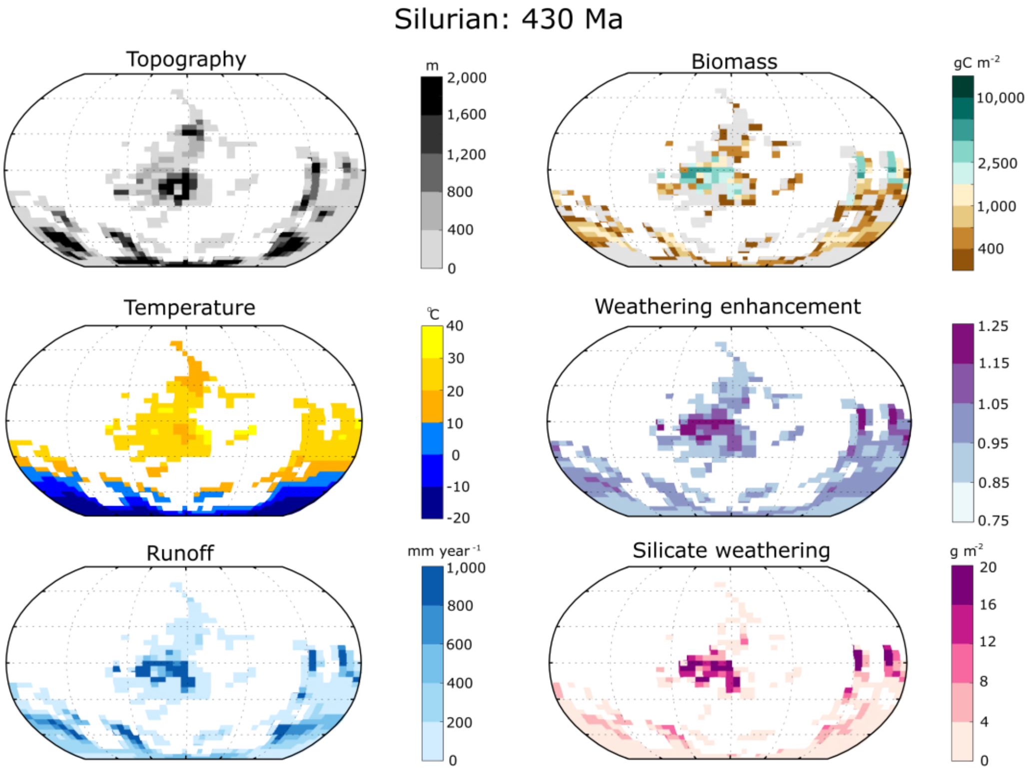

Figure 4.3.5. Silurian (430 Ma) SCI-FI results and environmental condition maps. *Global average temperature and runoff are 20.34 °C and 266 mm year*$^{-1}$ *respectively. Increased expansion of plants, especially in the southern hemisphere increases total global biomass to 108 GtC. High silicate weathering is concentrated at the equator where the highest biomass and runoff are present.*

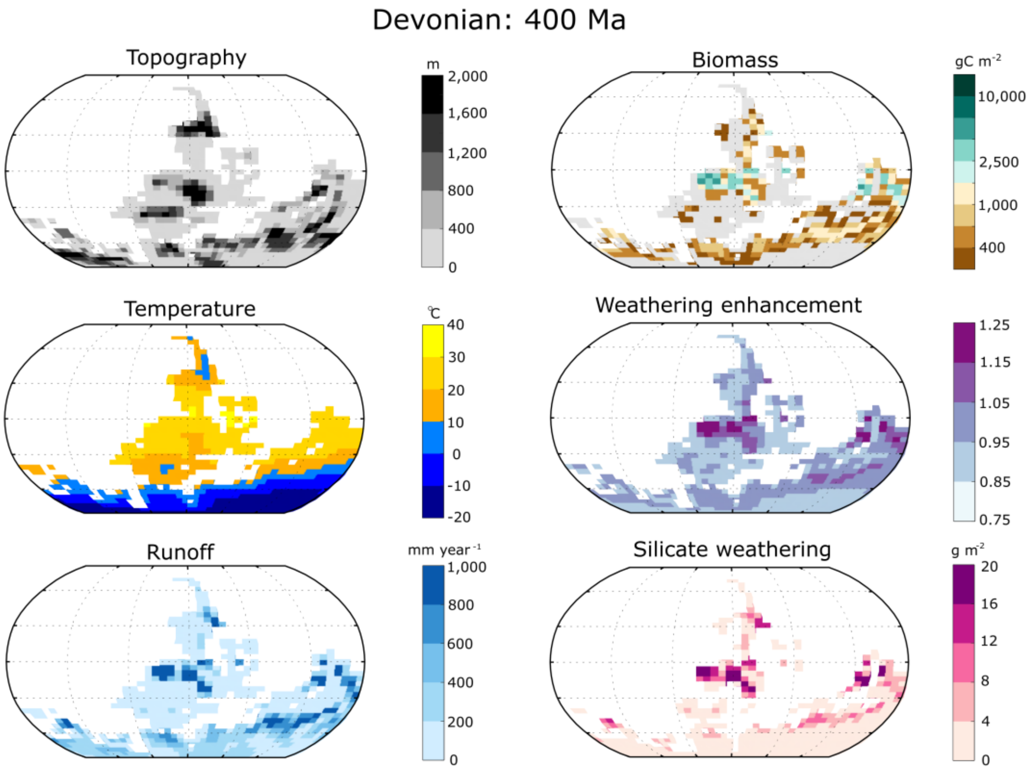

Figure 4.3.6. Devonian (400 Ma) SCI-FI results and environmental condition maps. *Global average temperature and runoff are 19.71°C and 238 mm year*$^{-1}$ *respectively. Lower silicate weathering is observed in areas with no runoff. Total biomass increases to 100 GtC.*

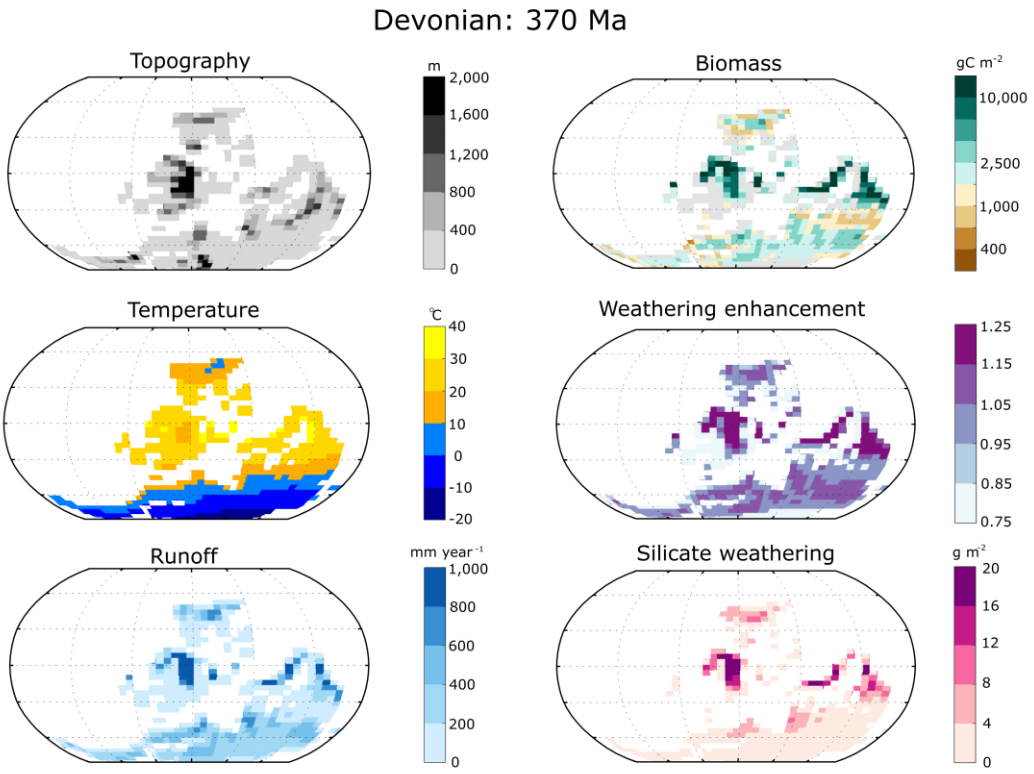

Figure 4.3.7. Devonian (370 Ma) SCI-FI results and environmental condition maps. *Global average temperature and runoff are 20.27°C and 228 mm year^{-1} respectively. Higher relative biomass in all areas is observed as both global temperature and runoff are at more optimal levels. Total biomass is nearly quadrupled to 394 GtC.*

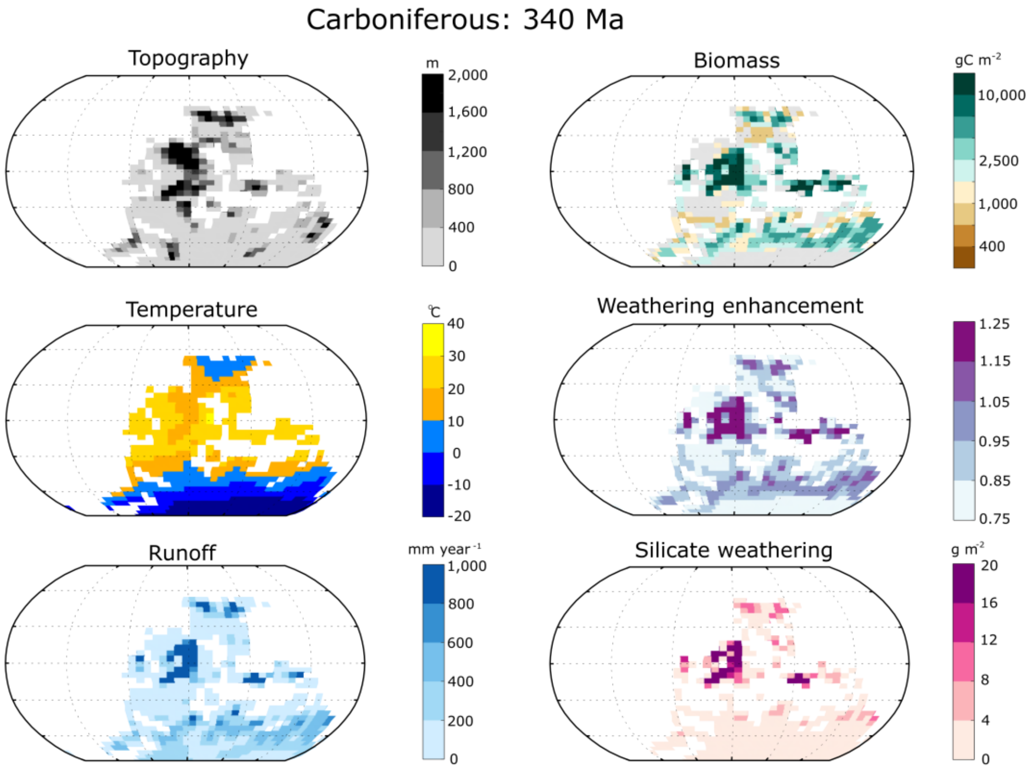

Figure 4.3.8. Carboniferous (340 Ma) SCI-FI results and environmental condition maps. *Global average temperature and runoff are 18.2°C and 183 mm year*$^{-1}$ *respectively. Biomass increases on either side of the hemisphere as temperatures decrease, increasing the total land area suitable for plant growth. Total global biomass continues to rise and reaches 466 GtC. By this timepoint, plants are assumed to have fully evolved therefore no limitation is put on biomass via the evolution parameter. Weathering is enhanced around the equator.*

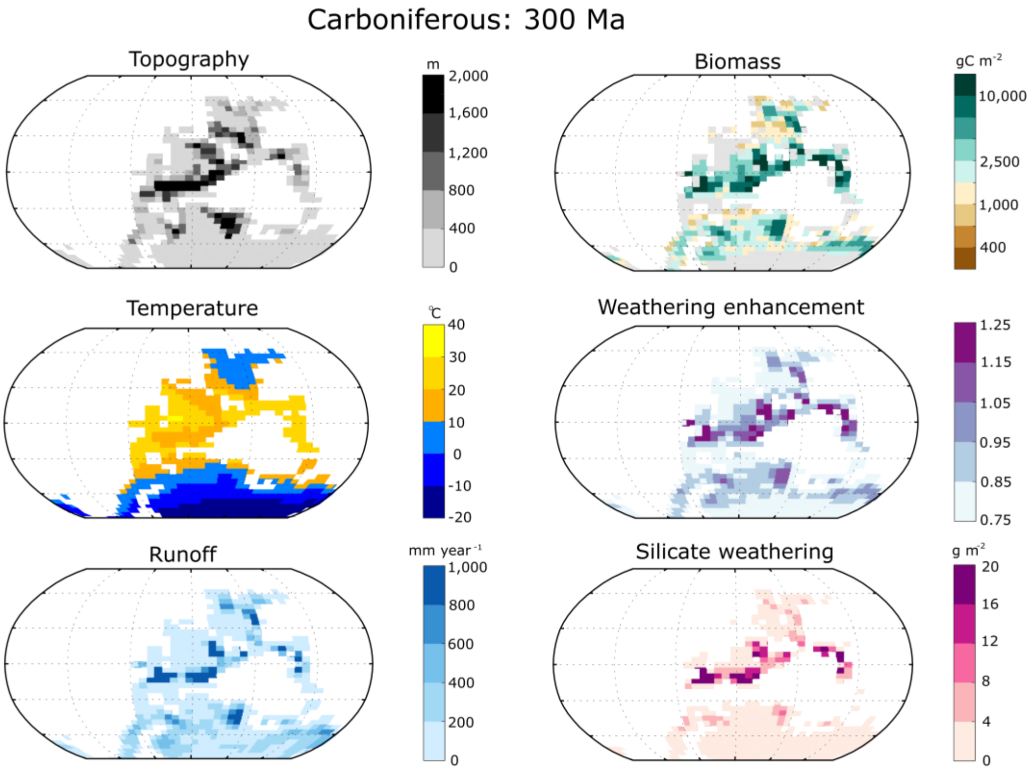

Figure 4.3.9. Carboniferous (300 Ma) SCI-FI results and environmental condition maps. *Global average temperature and runoff are 17.15°C and 197 mm year*$^{-1}$ *respectively. A drop in temperature decreases total global biomass to 447 GtC. Weathering enhancement is more homogenous at a lower rate than before due to the absence of plants (especially in the south pole) and low* CO_2 *levels. Silicate weathering is relatively high only around the equator as the formation of Pangea created mountainous ranges in that area.*

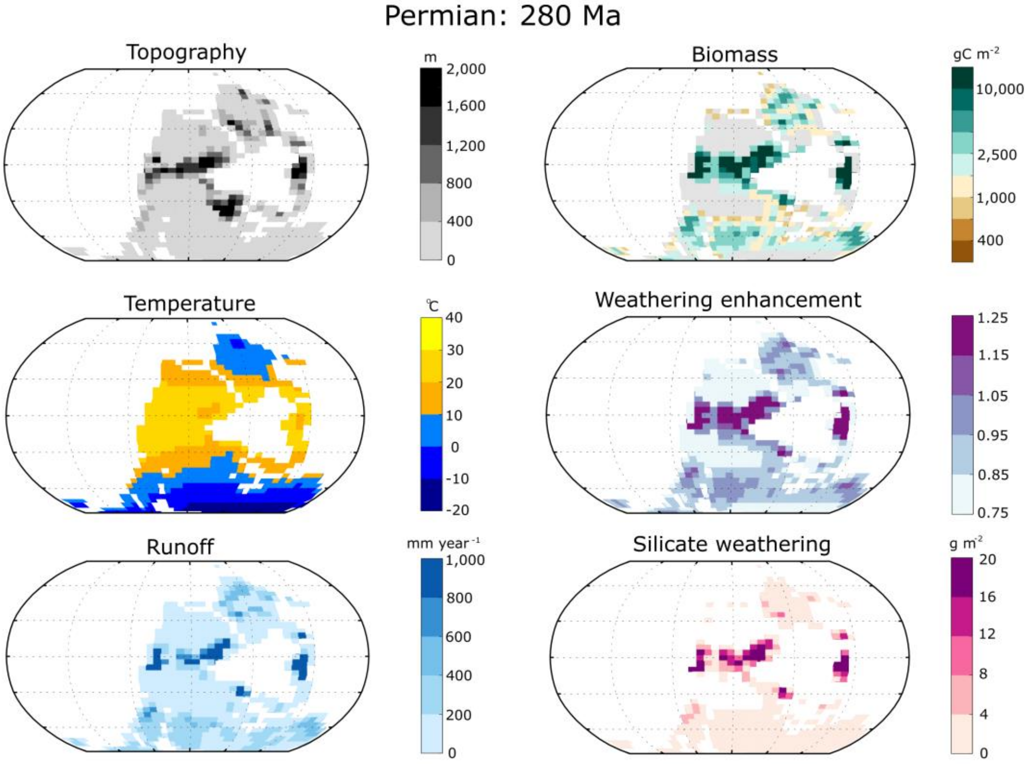

Figure 4.3.10. Permian (280 Ma) SCI-FI results and environmental condition maps. *Global average temperature and runoff are 17.35°C and 205 mm year*$^{-1}$ *respectively. Large arid areas present due to the formation of Pangea on either side of the equator however moderate temperatures and runoff increase productivity in areas that are suitable for plants. Total biomass increases to 479 GtC.*

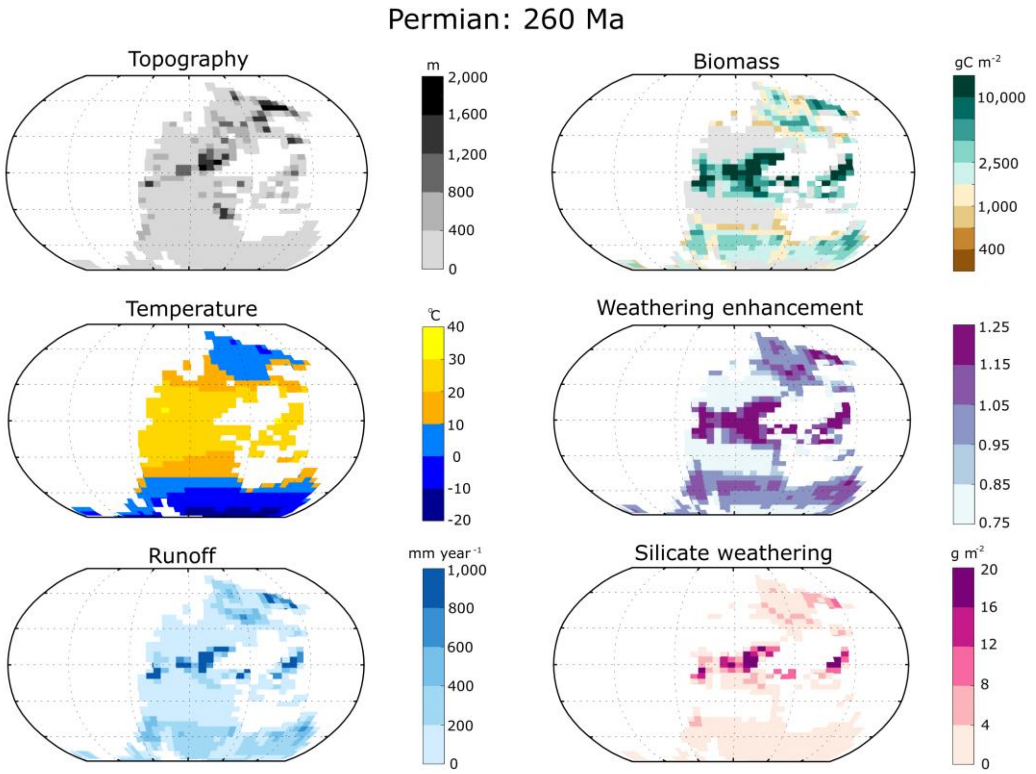

Figure 4.3.11. Permian (260 Ma) SCI-FI results and environmental condition maps. *Global average temperature and runoff are 18.89°C and 186 mm year*$^{-1}$ *respectively. Productivity increases in the northern and southern poles leading to total global biomass of 533 GtC despite the drop in runoff. Silicate weathering is absent areas with no runoff. Weathering enhancement from plants is highest around the equator as the area contains the highest productivity.*

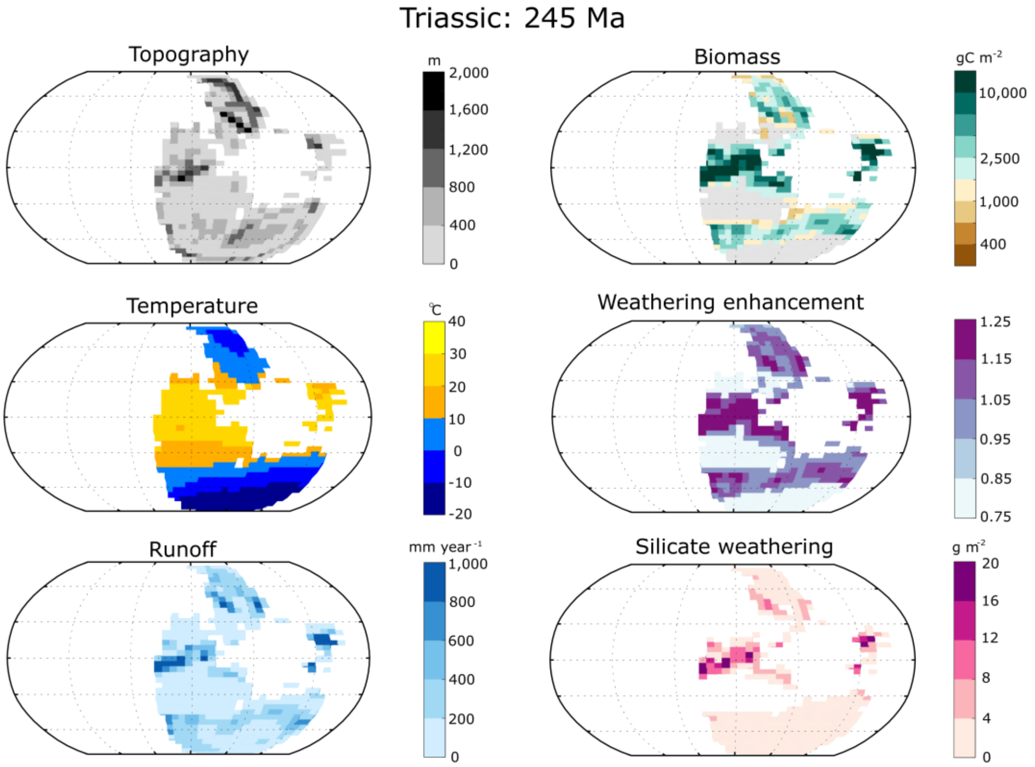

Figure 4.3.12. Triassic (245 Ma) SCI-FI results and environmental condition maps. *Global average temperature and runoff are 16.19°C and 228 mm year*$^{-1}$ *respectively. Total global biomass decreases to 502 GtC as temperatures decrease and reduce areas suitable for plant growth in the southern pole.*

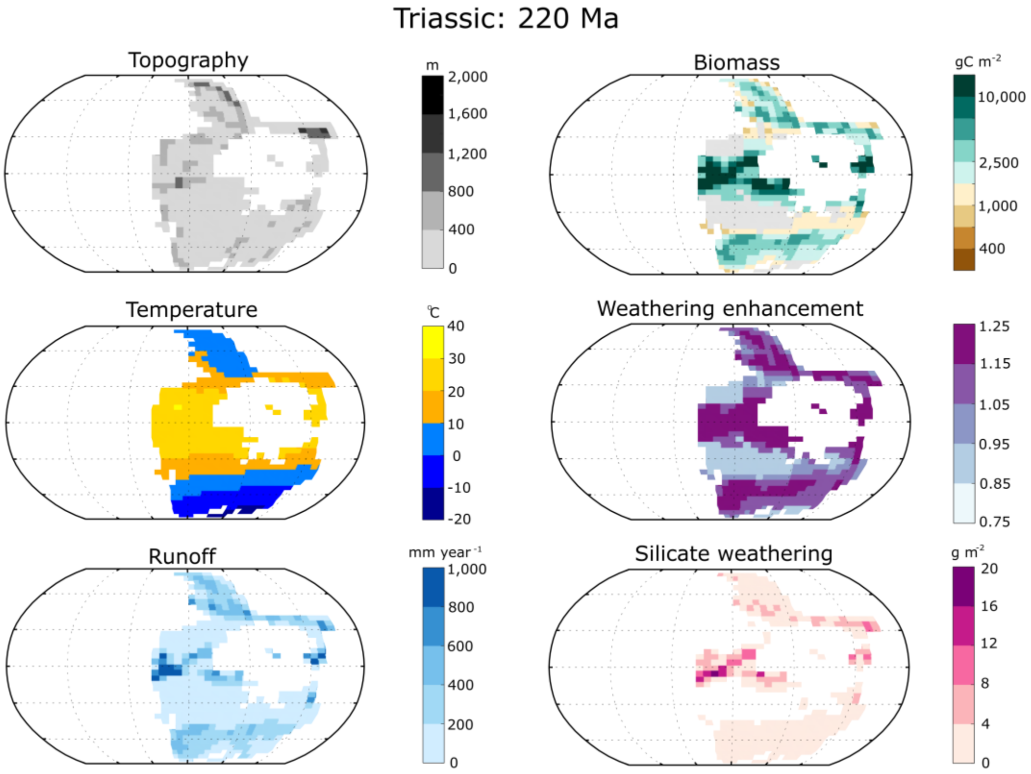

Figure 4.3.13. Triassic (220 Ma) SCI-FI results and environmental condition maps. *Global average temperature and runoff are 18.32°C and 209 mm year^{-1} respectively. Total global biomass increases and reaches 563 GtC as runoff decreases. Topography indicates a very flat Pangea therefore silicate weathering is mainly high around areas of high biomass and runoff.*

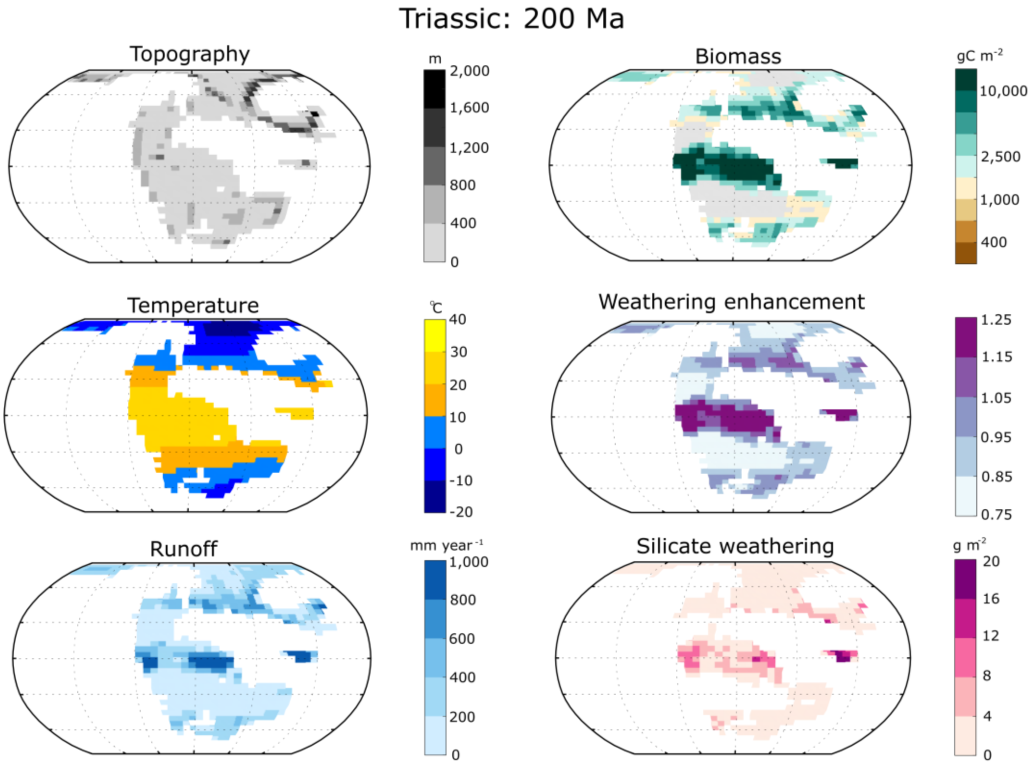

Figure 4.3.14. Triassic (200 Ma) SCI-FI results and environmental condition maps. *Global average temperature and runoff are 16.65 °C and 270 mm year*$^{-1}$ *respectively. Decrease in temperature and increase in runoff leads to very high total global biomass at 702 GtC. A large land mass being present at the equator increases the area for optimum plant productivity. Despite high biomass and weathering enhancement around the equator, silicate weathering is relatively low in the area possibly due to the flatness of the topography.*

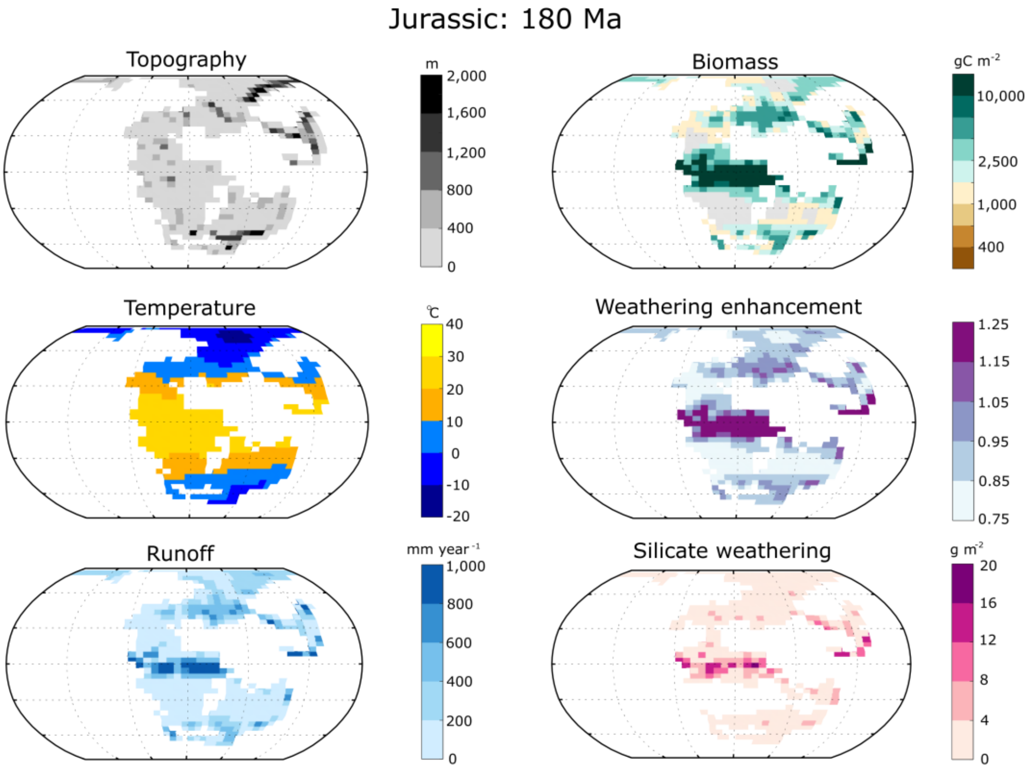

Figure 4.3.15. Jurassic (180 Ma) SCI-FI results and environmental condition maps. *Global average temperature and runoff are 17.22°C and 264 mm year*$^{-1}$ *respectively. Total global biomass rises to its highest in the Phanerozoic to 714 GtC as Pangea slowly breaks up and decreases arid areas.*

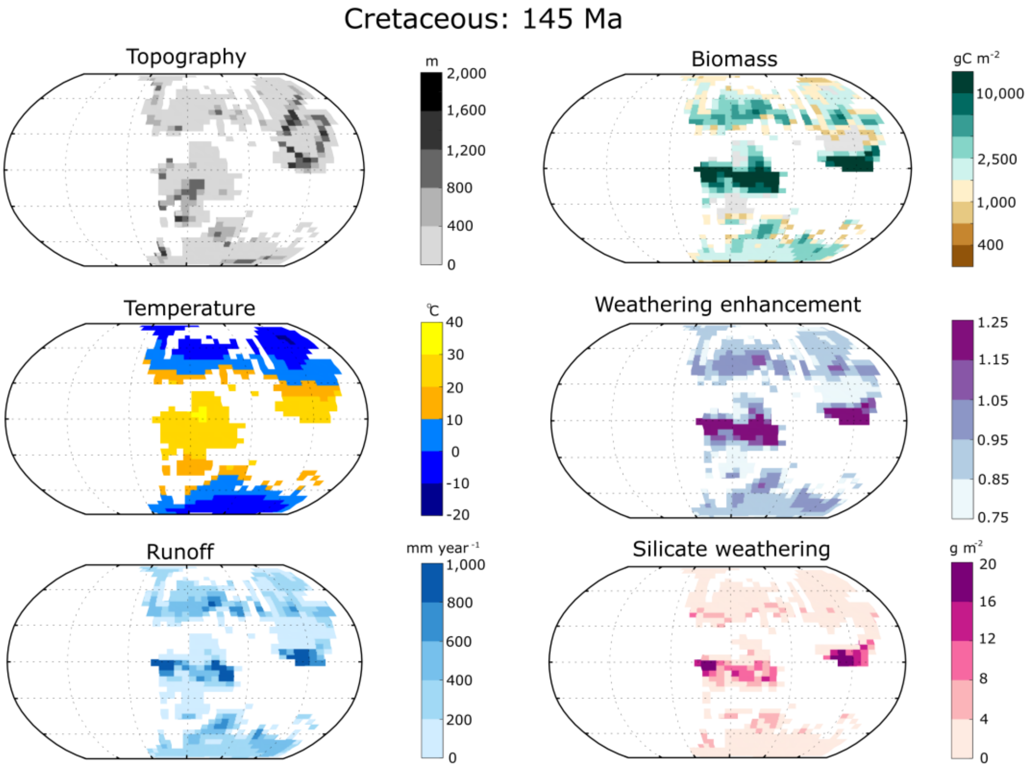

Figure 4.3.16. Cretaceous (145 Ma) SCI-FI results and environmental condition maps. *Global average temperature and runoff are 18.39°C and 271 mm year*$^{-1}$ *respectively. Total global biomass is at 639 GtC. Almost all of land is productive to some degree increasing the global weathering enhancement.*

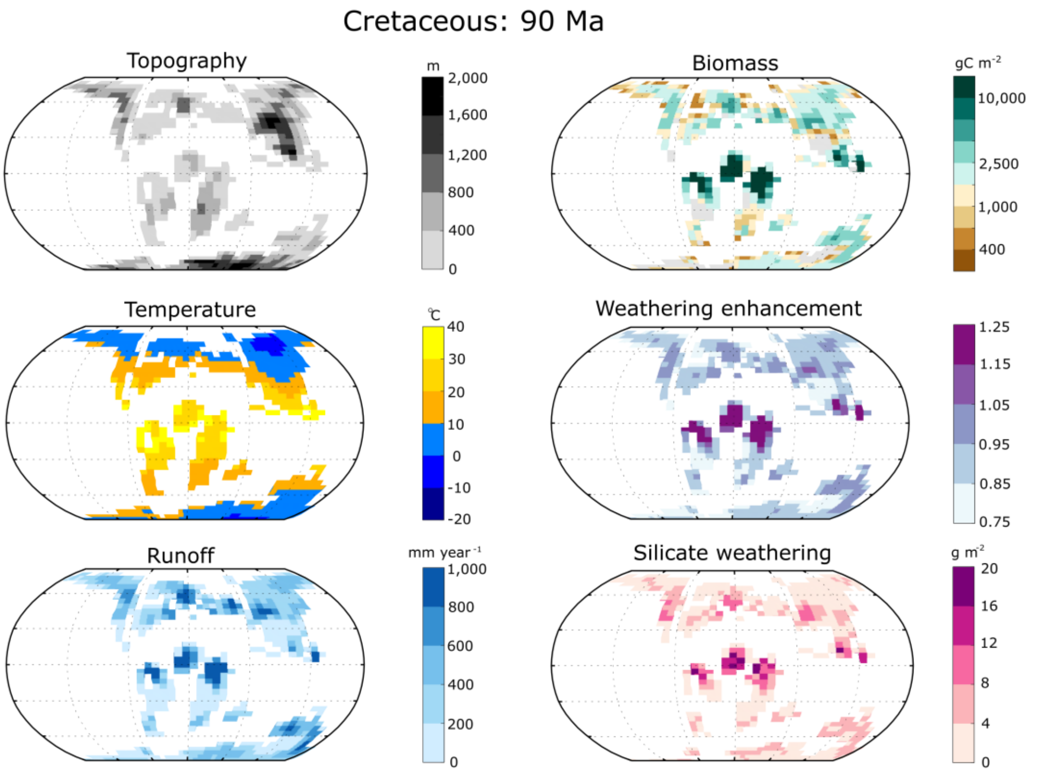

Figure 4.3.17. Cretaceous (90 Ma) SCI-FI results and environmental condition maps. *Global average temperature and runoff are 22.29 °C and 314 mm year^{-1} respectively. Fragmentation of land induces a large increase in runoff. A large decrease of total global biomass to 446 GtC is observed despite a large increase in runoff, as temperatures continue to rise, limiting productivity in the northern hemisphere.*

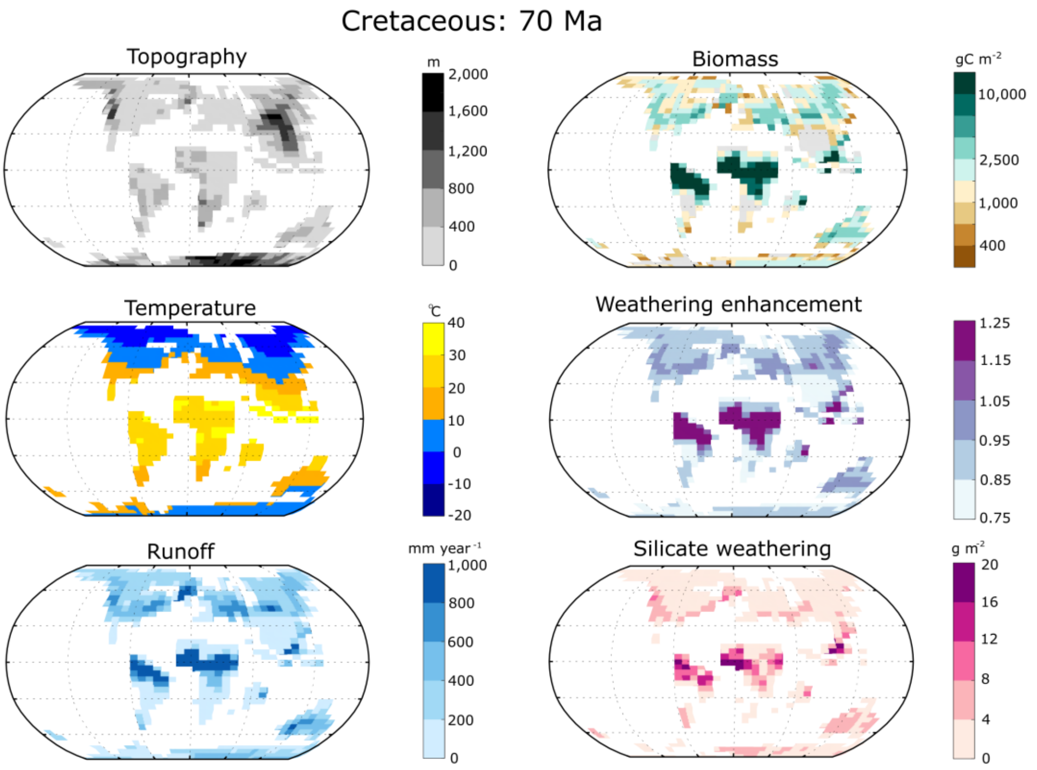

Figure 4.3.18. Cretaceous (70 Ma) SCI-FI results and environmental condition maps. *Global average temperature and runoff are 21.29°C and 300 mm year*$^{-1}$ *respectively. As both temperature and runoff become more suitable for plants, total global biomass increases to 548 GtC. Silicate weathering is observed globally and follows the same pattern as biomass.*

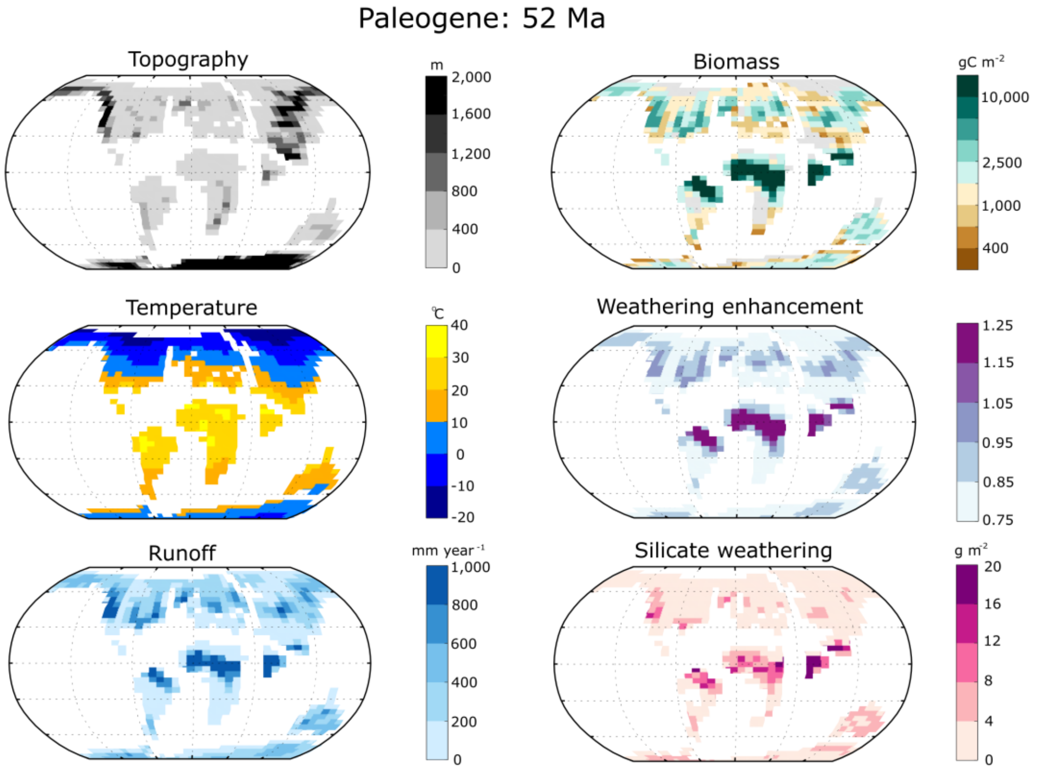

Figure 4.3.19. Paleogene (52 Ma) SCI-FI results and environmental condition maps. *Global average temperature and runoff are 19.84°C and 320 mm year*$^{-1}$ *respectively. As temperatures continue to decrease, polar regions become less productive and decrease total global biomass to 539 GtC.*

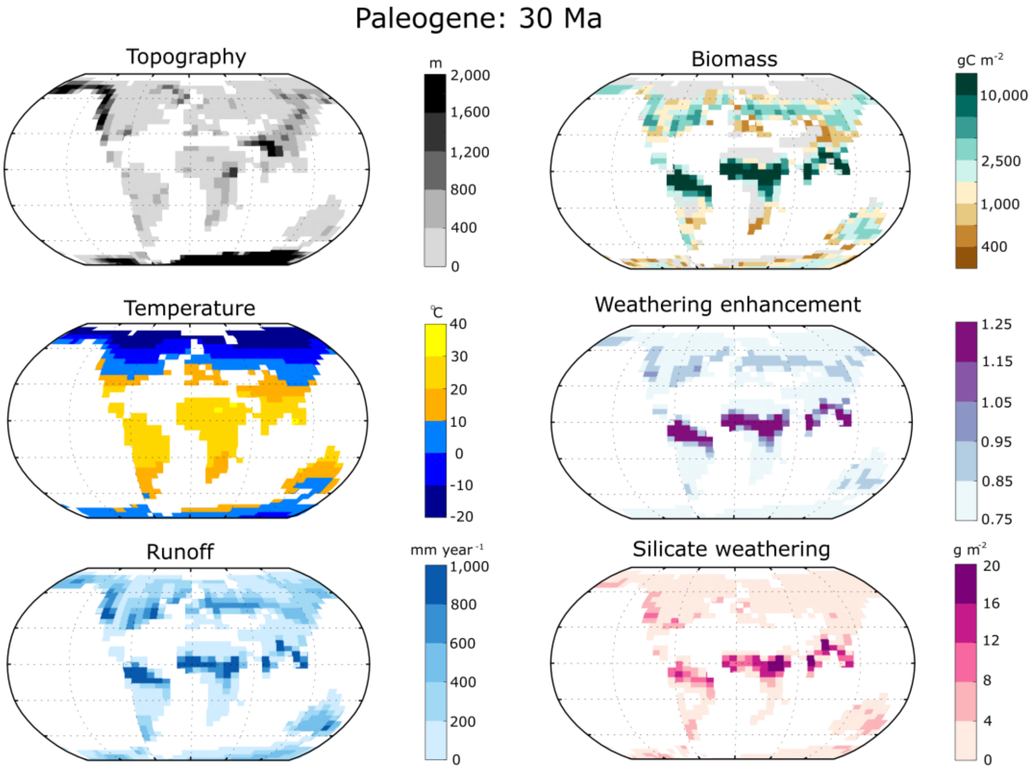

Figure 4.3.20. Paleogene (30 Ma) SCI-FI results and environmental condition maps. *Global average temperature and runoff are 18.41°C and 287 mm year^{-1} respectively. Total global biomass is 550 GtC. Rearrangement of land mass around the equator compensates for lost plant productivity in much colder northern and southern poles.*

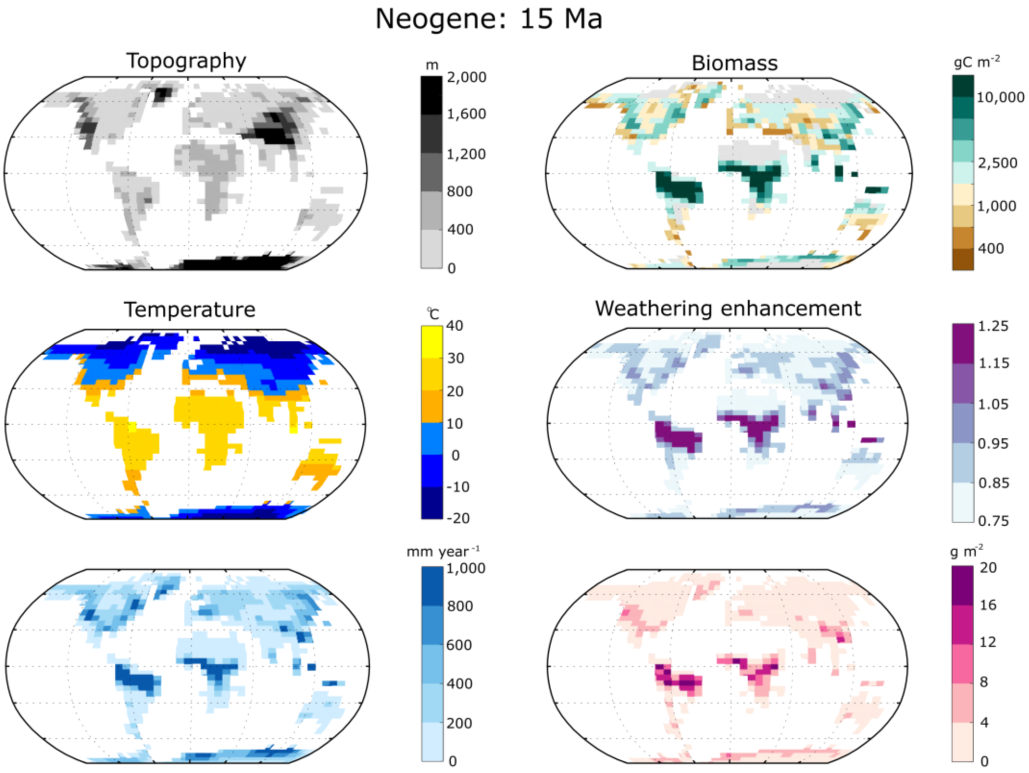

Figure 4.3.21. Neogene (15 Ma) SCI-FI results and environmental condition maps.

Global average temperature and runoff are 18.65°C and 285 mm year^{-1} respectively.

Total global biomass decreases to 519 GtC as areas without runoff increases.

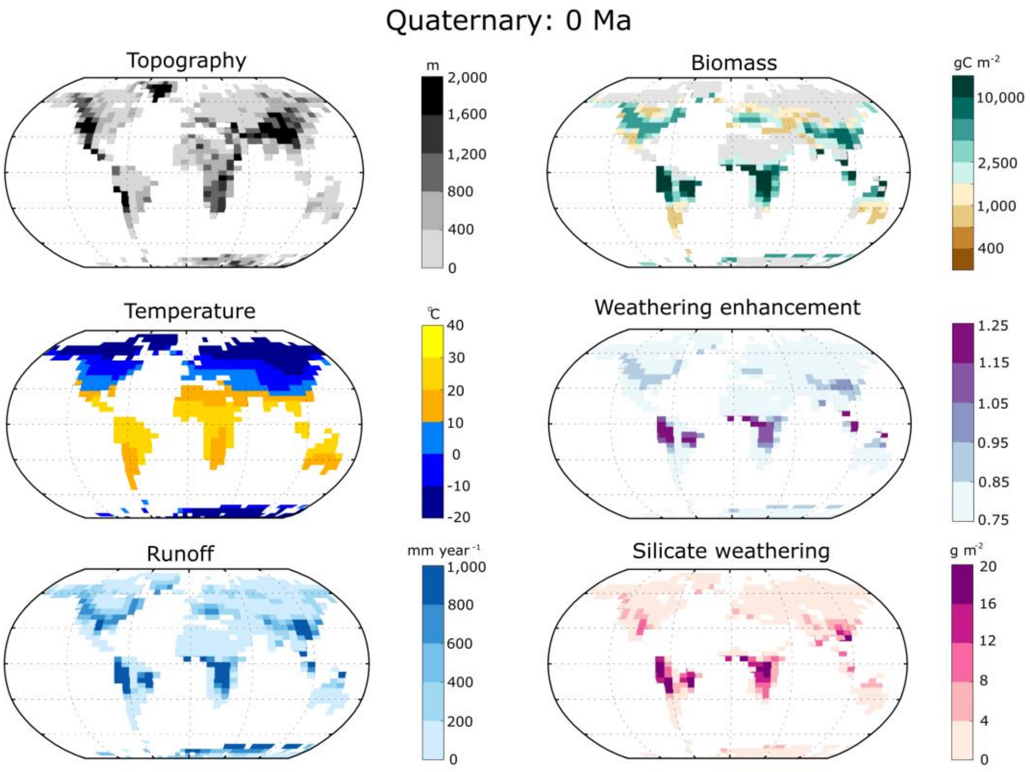

Figure 4.3.22 Quaternary (0 Ma) SCI-FI results and environmental condition maps. *Global average temperature and runoff are 15°C and 291 mm year*$^{-1}$ *respectively. Total global biomass continues to decrease to 434 GtC. Low temperatures and lack of runoff reduce habitable areas in the northern hemisphere.*

4.4 Comparison of SCION results with and without FLORA

Overall, the addition of FLORA leads to some improvements within SCION predictions of atmospheric CO_2 levels, global temperature and marine SO_4. Smaller features (<10 million years) of the global geochemical datasets are not represented in either model due to the coarse resolution of climate reconstructions used. The sensitivity analysis of SCI-FI consisted of 500 model runs. Each run varied in their degassing rates (upper and lower boundary from Mills et al., (2021)), distribution of lithology between ‘basaltic’ and ‘granitic’(± 20%), and isotope fraction factors of carbon (for photosynthesis, ± 5‰) and sulfur (for microbial sulfate reduction, ± 10‰) to create an uncertainty range. The fractionation factor is the factor by which two isotopes change in abundance during chemical and physical processes. For example, biotic and environmental factors like soil water content change the magnitude of carbon fractionation during decomposition (Wang et al., 2015). The various points within a process that can affect isotopic fractionation and variation in magnitude therefore demands that a range of values are considered.

The failed runs were a result of varying the mentioned parameters too much, resulting in one of the model reservoirs (like CO_2 levels) not being stabilised. Figures 4.4.1 – 4.4.9 in the following sections compare the average of the sensitivity runs of SCI-FI predictions (green) with baseline SCION predictions (pink) and proxy data (yellow) in order to evaluate the fit of the model. A 95% confidence interval is used (green shading) for each prediction.

4.4.1 SCI-FI biomass

When FLORA is run in parallel with SCION, the simulated biomass differs from the offline FLORA runs under the idealised climates (Figure 4.4.1). Biomass is not present until the Ordovician due to the assumption of land plant evolution occurring between the Ordovician and early Devonian, and in other periods the climate of the linked model differs from the assumptions used in the offline FLORA runs. The feedbacks between SCION and FLORA increases total biomass over the Paleozoic and Mesozoic, and a decrease it over the Cenozoic compared to FLORA only estimates. The stepwise increase of biomass between Jurassic and Paleogene is modified by a transient decrease in potential biomass in the Jurassic-Cretaceous boundary. Nevertheless, SCI-FI results reinforce the conclusions made in Chapter 3:

1. Environmental conditions were more permissive than present for land plant productivity over the late Paleozoic and Mesozoic era, including times coinciding with major plant evolution such as the angiosperm radiation during the Cretaceous.
2. Pangea and the increase in aridity limited plant expansion and productivity over the mid to late-Paleozoic.
3. Biomass is a product of its environmental setting: temperature, runoff and land area. With spatial patterns of biomass closely correlating to patterns of runoff.

The main difference that is observed between the offline and online FLORA models is, rather than a step-wise increase in biomass with a peak during the Paleogene, the Jurassic period is seen as the most productive in SCI-FI (Figure 4.4.1).

With high temperatures and runoff, the large drop within the Cretaceous (from 145 Ma to 90 Ma) is possibly due to migration of land away from the equatorial zone towards the northern hemisphere and continental flooding (Figure 4.3.16 and 4.3.17). Although global temperatures and runoff increase, land mass around the poles experience colder temperatures compared to the equator leading to lower biomass production. Less land being available also limits global biomass (see Figure 3.1.23B).

Baseline SCION predictions of biomass (pink line) are relatively higher throughout the Paleozoic and Mesozoic (Figure 4.4.1). Vegetation in SCION is directly related to atmospheric CO_2 and temperature, hence high biomass during the Triassic-Jurassic period is the model's response to high CO_2 levels. This high biomass leads to greater sequestration of carbon and therefore lowers CO_2 levels over the Jurassic (Figure 4.4.3). SCI-FI also produces lower biomass during the presence of Pangea (Carboniferous-Jurassic, Figure 4.4.1) when compared to SCION. The formation of Pangea and its arid interior reduced runoff and therefore lowered biomass whereas in SCION, the non-dimensional calculation of vegetation may have increased overall biomass. As SCION uses an average runoff, arid areas are misrepresented therefore allowing for vegetation to exist in areas that might not be able to support them.

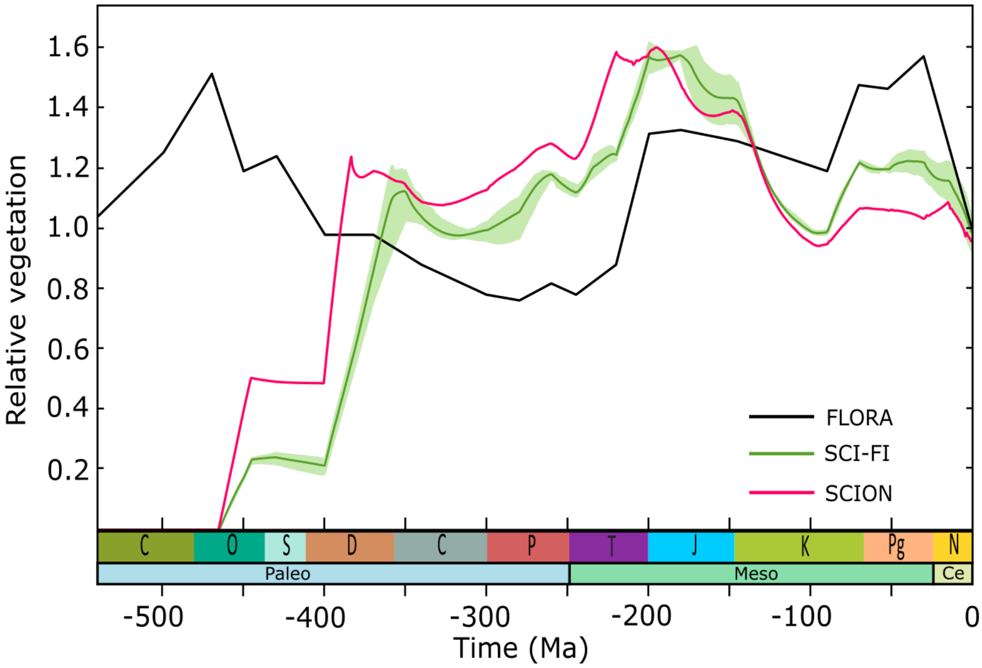

Figure 4.4.1. Relative global vegetation of FLORA, SCION and SCI-FI over the Phanerozoic. *All biomass values are given as relative to approximate present-day biomass of 434 GtC. The 'offline' FLORA (black line) uses ideal* CO_2 *and runoff values whereas the 'online' SCI-FI model (green line) includes the effect of plants on environmental conditions at each timestep. SCION biomass with COPSE vegetation (pink line) taken from Mills et al., 2021. Green shade: 95% confidence interval of SCI-FI sensitivity analysis.*

Previously not present in FLORA, a large decrease in potential biomass (~190 Gt C) is also observed from the end Cretaceous until mid-Cretaceous (145 and 90 Ma, Figure 4.4.1). Despite an increase in runoff and temperature, biomass decreases possibly due to the movement of continents to higher latitudes that cannot sustain high biomass biome - tropical (Figures 4.3.16 and 4.3.17). Lower CO_2 may also contributes towards overall lower global biomass. A slight increase in biomass can also be seen mid-Cretaceous in all model predictions (Figure 4.4.1), coinciding with the estimated angiosperm domination (Figure 1.1.3; Sauquet et al., 201). Despite a more efficient photosynthesis and reproduction rates (related to angiosperm success; Brodribb and Field, 2010) not being modelled explicitly in FLORA, the increase in biomass indicates overall environmental conditions to have improved between the mid-Cretaceous and Paleogene. The possible improvement in conditions may have given angiosperms a window of opportunity to overtake other plant groups and dominate on a global scale.

Comparison between the SCI-FI predictions and other studies are difficult due to the scarcity of studies that look at Phanerozoic biomass along with variation in parameter datasets such as land orientation. Porada et al. (2016) explore the weathering effects of lichens and bryophytes during the late Ordovician (450 Ma Figure 4.4.2A). A visual comparison shows the latitudinal pattern of NPP to be similar with higher NPP in tropical zones around the equator compared to colder areas in the higher latitudes, although at a lower intensity (Figure 4.4.2). Their simulated global NPP is 14.4 Gt C year^{-1} and 7.6 Gt C year^{-1} with ice sheets (CO_2 = 2,240 p.p.m, O_2 = 14%), while SCI-FI NPP lies at 8.59 Gt C (CO_2 = 8,049 p.p.m, O_2 = 12%). SCI-FI does not feature any significant ice sheet coverage during the Ordovician as CO_2 levels are too high leading to high temperatures (Figure 4.3.4). A low CO_2 level is used to simulate the late Ordovician glaciations (Porada et al., 2016) whereas SCI-FI predicts CO_2 levels based on mass balance equations using the outputs from the previous run. Hence, the short-lived Hirnantian glaciation is not present within SCI-FI. Potential NPP jumps to 65.6 Gt C when FLORA is used with Porada et al. (2016) conditions and without the evolution parameter. Apart from the differences in conditions used to simulate biomass, the comparison highlights the caveat present within the evolution parameter (Equation 4.2.12). As physiological differences between early plants such as bryophytes are not taken into account, a simple scaling down of forest biomass may not be sufficient to reproduce the productivity of early land plants. As such, SCI-FI may not be encapsulating the full extent of weathering enhancement due to land plants.

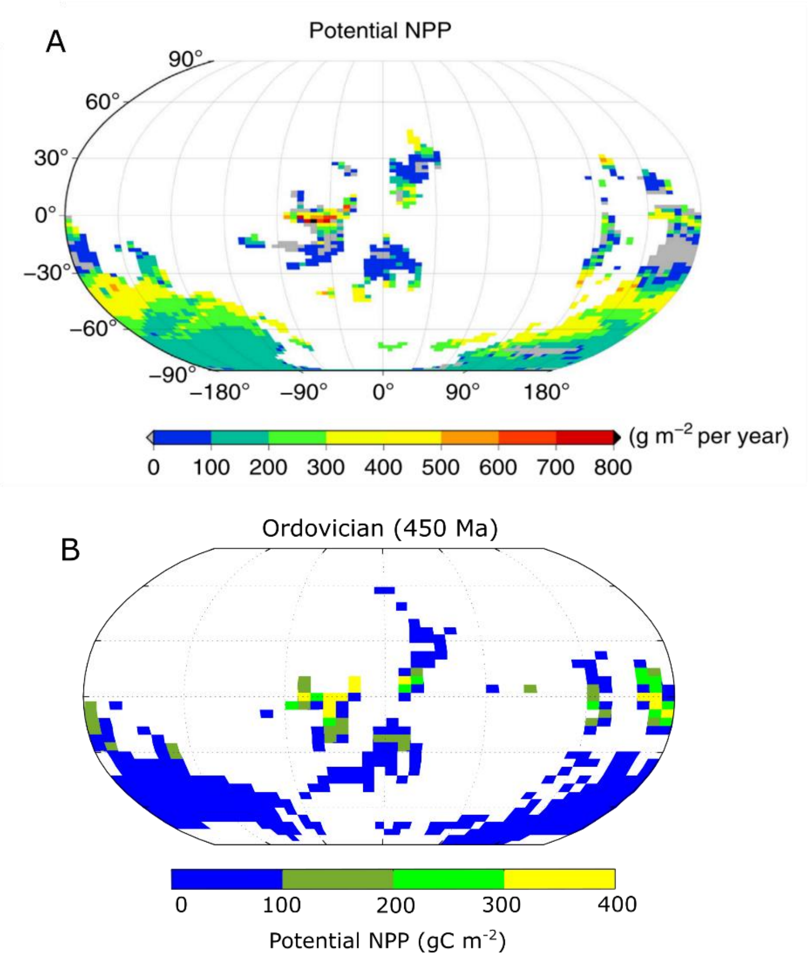

Figure 4.4.2. Potential Net Primary Productivity (NPP) comparison for the Ordovician. (A) *Potential NPP taken from Porada et al. (2016) showing lichen and bryophyte productivity for the Late Ordovician (450 Ma; million years ago).* ***(B)*** *Potential NPP from the SCI-FI model.*

4.4.2 Temperature and atmospheric CO_2

The addition of plants to the SCION climate-chemical model has improved the overall CO_2 and temperature estimations (Figures 4.4.3 and 4.4.4). Comparison in differences between the proxy record and model outputs give an average error of 3.02°C in SCI-FI and 3.45°C in SCION showing a slight improvement in temperature predictions with the addition of FLORA. CO_2 levels show the opposite pattern of change as biomass during the Jurassic and Cretaceous periods between the SCI-FI and SCION estimates. SCI-FI is overall a closer predictor of CO_2 levels as it correlates with the proxies of CO_2 (mainly stomata and paleosol data; Foster et al., 2017) more so than the baseline SCION model. The SCION atmospheric CO_2 level is driven by a combination of degassing rate and silicate weathering amplification, along with a simplified non-dimensional vegetation (Mills et al., 2021) therefore any changes observed in the SCI-FI CO_2 estimates result from the effect of spatial representation of plants on the above process. Temperature closely corresponds to atmospheric CO_2 changes as the two are tightly linked (Figure 4.4.3 and 4.4.4) (Tobis et al., 1997; Donnadieu et al., 2006). The improvements discussed below suggest the addition of FLORA to carbon cycling is a more accurate approach towards climate-chemical modelling compared to the COPSE simple vegetation assumption.

Before the Silurian, SCI-FI predictions of atmospheric CO_2 are slightly higher than baseline SCION due to the absence of plants (Figure 4.4.3). Within SCION, silicate weathering depends on CO_2 concentration directly (Equation 4.2.9). The high CO_2 levels during the Cambrian led to increased silicate weathering in SCION and drove lower atmospheric CO_2 concentrations compared to SCI-FI where a low pre-plant weathering enhancement and CO_2 dependence led to a smaller drawdown of

CO_2, although not significantly. Proxies for atmospheric CO_2 are rare before the Silurian (Figure 4.4.3) however reconstructions of paleo-temperatures speculate Cambrian-Ordovician to be around ~25°C (Figure 4.4.3, Scotese et al., 2021). Although high atmospheric CO_2 has the potential to lower soil pH and increase silicate weathering rates, the process is more closely dependent on temperature and runoff rates (Brady and Carroll, 1994). A direct CO_2 dependence along with the effect of spatial biomass on weathering enhancement has led to an overall lower CO_2 and temperature prediction when compared to SCION (Figure 4.4.3 and 4.4.4).

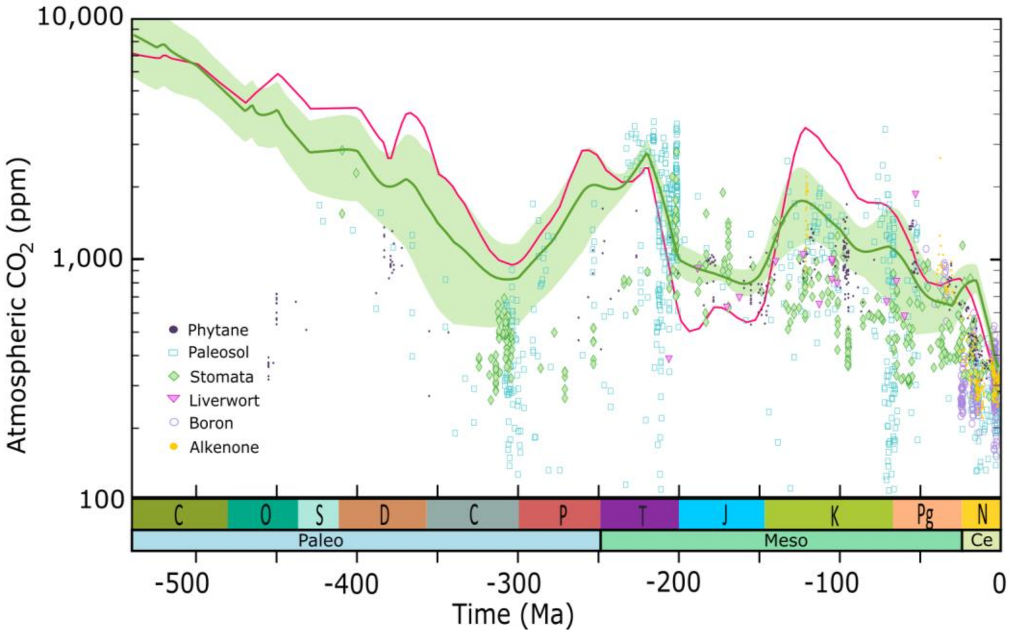

Figure 4.4.3. Comparison of modelled atmospheric CO_2 concentrations and proxy data. *SCI-FI CO_2 concentration (green line) show a similar trend line to the SCION estimates (pink line). SCI-FI estimations run higher during the Cambrian however shows a better similarity to proxy data (symbols) during the Jurassic and Paleozoic. Proxy data taken from Foster et al., 2017, Witkowski et al., 2018. SCION data taken from Mills et al., 2021. Green shade: 95% confidence interval of SCI-FI sensitivity analysis.*

Low temperatures during the Ordovician, in particular the Hirnantian glaciation (~444 Ma with average global temperatures around 9°C) are not predicted in either model possibly due to the relatively short timespan (~2-3 million years; Finnegan et al. 2011) and fast onset of the glaciation (Longman et al., 2021). Plants have a diminished capability of CO_2 drawdown during the Ordovician as biomass is limited to 15% of its full capacity through the 'evolution' parameter. Porada et al., (2013) show modern lichens and bryophytes to uptake around 7-9% of global carbon. However, non-vascular plants have demonstrated to dramatically enhance weathering rates, potentially leading to glacial temperatures (Lenton et al., 2012). Nevertheless, it may be more likely that a catastrophic transient event (such as volcanism) triggered the Ordovician glaciation rather than the increasing weathering enhancement via plants, due to the rapid and transient nature of the event (Longman et al., 2021). These uncertainties highlight the need for an evolutionary timeline within the FLORA model with stepwise evolution of plants and their related capacity of weathering and biomass accumulation.

A decrease in temperature is observed during the late Devonian following a substantial increase in plant productivity with the evolutionary ratio at >0.9. Similarly, the Permo-Carboniferous low temperatures are not captured in either models possibly due to the lack of peat (coal) swamp formation. Peat formation is largely dependent on temperature, humidity and plant productivity excess over decomposition (Moore, 1989). Microfossils (pollen and spores) and macrofossils (coal-balls) indicate ferns, lycopsids, cordaites, sphenopsids and pteridosperms to have dominated peat swamps and contributed to 95% of the peat biomass (DiMichele and Phillips, 1994). These swamps can be responsible for $13 - 47 \times 10^9$ tonnes of carbon sequestration per year and therefore represent a large carbon sink that remain inaccessible in the short term

(Cleal, 2018). Additionally, the lower Permo-Carboniferous temperatures could be due to the presence of vast forests present during the Carboniferous (Boyce and Lee, 2017), amplifying biotic silicate weathering. The spatial distribution of weathering enhancement is absent within SCION, therefore maybe creating an inaccurate picture of global silicate weathering rates, leading to higher CO_2 predictions and temperature than proxy data (Figure 4.4.4).

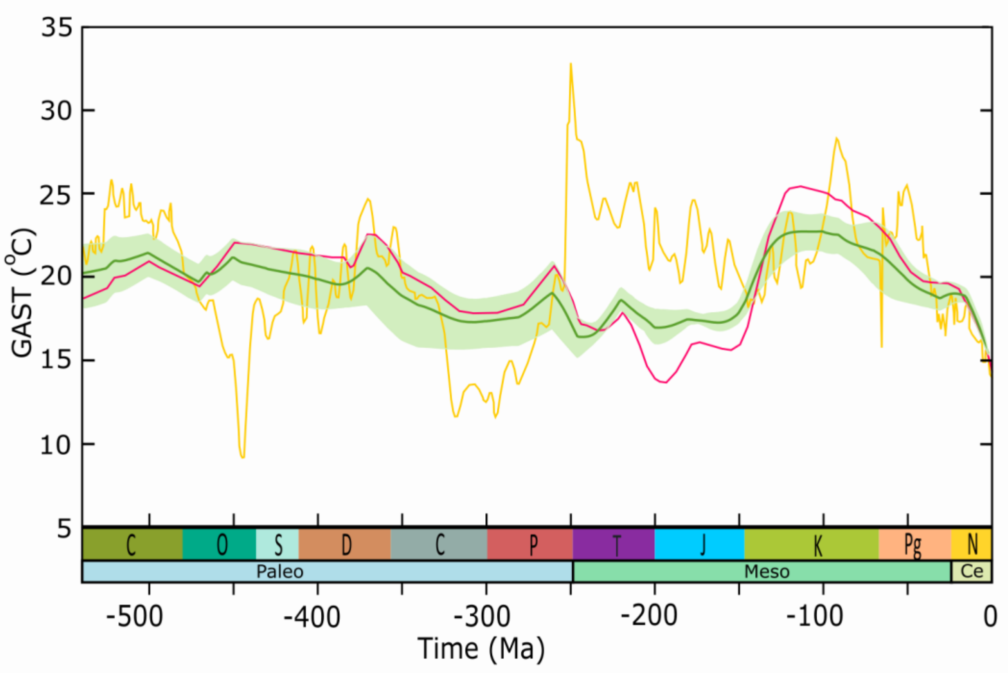

Figure 4.4.4. Comparison of modelled global average surface temperature (GAST). *SCI-FI temperature estimates (green line) show a better fit to the derived GAST from paleo-Köppen belts and oxygen isotopes (yellow line, Scotese et al., 2021) compared to SCION temperature estimates (pink line) over the Phanerozoic. Green shade: 95% confidence interval of SCI-FI sensitivity analysis.*

A combination of high temperatures during the Devonian, slow continental alignment of Pangea along the equator and the high O_2:CO_2 ratio led to the expansion of wetland tropical forests susceptible to peat formation (Montañez et al., 2016). It was previously debated that the lag between the evolution of lignin (biodegradable resistant organic matter) and lignin degrading fungi led to the accumulation of lycopsid-dominated forests during the Carboniferous (Montañez et al., 2016). However, recent genomic and phylogenetic studies show the Agaricomycetes fungi, capable of degrading lignin, along with lycopsids made of unlignified cells to be largely present during the Carboniferous (Robinson, 1990a; Nelsen et al., 2016). Peat swamps were therefore a result of Pangea formation which created humid, equatorial zones with high water tables and plant productivity rather than an evolutionary lag (Nelsen et al., 2016). Peats present a long-term carbon preservation method as a direct result of plant evolution shaped by environmental conditions. The expansion of peat swamps and their large role as a carbon sink needs to be considered within climate-chemical models to rectify the temperature inaccuracy seen during the Permo-Carboniferous (see Chapter 5.7.1).

Temperatures reached their Phanerozoic peak during the early Triassic (global average temperature of 33°C, Scotese et al., 2021) due to the ongoing effects of Siberian Traps volcanism. Over the Jurassic, degassing from CAMP would have also contributed to higher temperatures (see Chapter 1.5). Similar to the Hirnantian glaciation, past volcanic activities and events that lead to large fluctuations of atmospheric CO_2 are not explicitly modelled in SCION therefore it is impossible for the model to predict past high temperatures and CO_2 levels that were a direct result of these chance events. SCI-FI however does predict higher atmospheric CO_2 levels and global temperatures during the Triassic and Jurassic compared to SCION (maximum difference of 4°C, Figures 4.4.3 and 4.4.4). Pangea did not always prove to be suitable for plant growth. A progressive expansion of aridity as a result of Pangea interfering with the hydrological cycle, can be observed between 260 – 200 Ma (Figures 4.3.11 – 4.3.14) with peak global temperature estimates reaching 22.29°C at 90 Ma. Limited water circulation towards a large part of the interior of Pangea created large arid areas, and restricted biomass to the equator. As plant productivity becomes more isolated in the tropics, less CO_2 is sequestered, less organic C burial and silicate weathering enhancement occurs leading to increased temperatures. The opposite trend can be seen in the Cretaceous as predictions of CO_2 and temperature are lower due to increased plant productivity as Pangea disperses and runoff increases, creating more viable land for plants (Figures 4.4.3 and 4.4.4).

Addition of a spatial vegetation model seems to have improved the late Triassic – early Jurassic hothouse and cooler Cretaceous estimations (Scotese et al., 2021). The addition of plant influence on the global C cycle has generally improved model estimations to match proxy data. As temperatures increase, the chances of permanent ice caps being present decrease. Overall, the Paleozoic in SCI-FI is colder than SCION, leading to an overestimation of ice line (Figure 4.4.5). The biggest discrepancy being over the Triassic – Jurassic period where high temperatures prevent the formation of ice sheets however, in both SCION and SCI-FI, the lack of an external CO_2 driver (i.e., volcanism) has led to extensive ice sheet formation (Figure 4.4.5). Compared to SCION, the effect of plants on climate is better represented within SCI-FI which allows for a more accurate hypothesis testing model however some issues regarding the FOAM climate sensitivity and lack of external forcings to the C cycle persist.

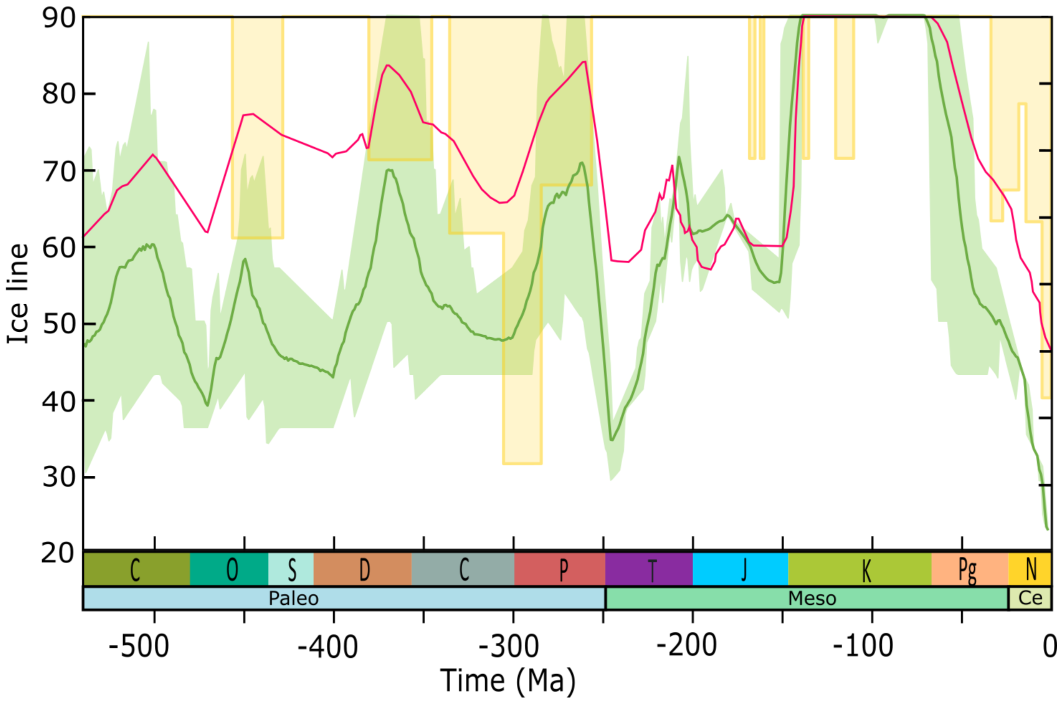

Figure 4.4.5. Ice line latitude comparison. *Extent of actual ice caps (yellow line) compared against estimated SCI-FI (green line) and SCION (pink line) ice line latitudes. Geological records compiled by Cather et al., 2009. Green shade: 95% confidence interval of SCI-FI sensitivity analysis.*

Chapter 5. Additional SCI-FI results and future works

This chapter briefly looks at the rest of the outputs by SCI-FI ($\delta^{13}C_{carb}$, atmospheric O_2, marine SO_4 and oceanic sulfate, and strontium) and compares it against prior SCION results. FLORA is far from complete in terms of accurately being able to depict the evolution of plants over the Phanerozoic. Plants are dynamic and adaptive, they have developed various efficient ways of growing, such as arborescence and roots. I also highlight some of the key areas that require further development in modelling plants for long-term climate change evaluation.

5.1 $\delta^{13}C_{carb}$

Changes in the carbon isotopes composition of marine carbonate rocks ($\delta^{13}C_{carb}$) are controlled by the exchange of carbon between organic and inorganic reservoirs (Figure 5.1.1; Saltzman and Thomas, 2012). Plants and microbes strongly prefer the lighter isotope of carbon (^{12}C) during photosynthesis as it is theorised to diffuse more rapidly and have a proportionally greater reactivity with Rubisco than its heavier counterpart ^{13}C (Busch et al., 2020). Due to this relationship, a positive excursion in $\delta^{13}C_{carb}$ can be interpreted as higher plant (and algal) productivity as lighter isotopes are being fixed in organic matter, leaving the heavier isotope to be buried during carbonate deposition. This relationship can be observed in the biomass as $\delta^{13}C_{carb}$ fluctuations mimic plant productivity (Figure 5.5.1). Land derived organic carbon burial strongly resembles biomass and its evolution parameter with a large peak during the Cretaceous. Marine organic carbon burial is lower between 250 – 150 Ma possibly due to high biomass on land which reduces the phosphorus influx into the ocean hence decreasing marine productivity (Figure 5.1.1)

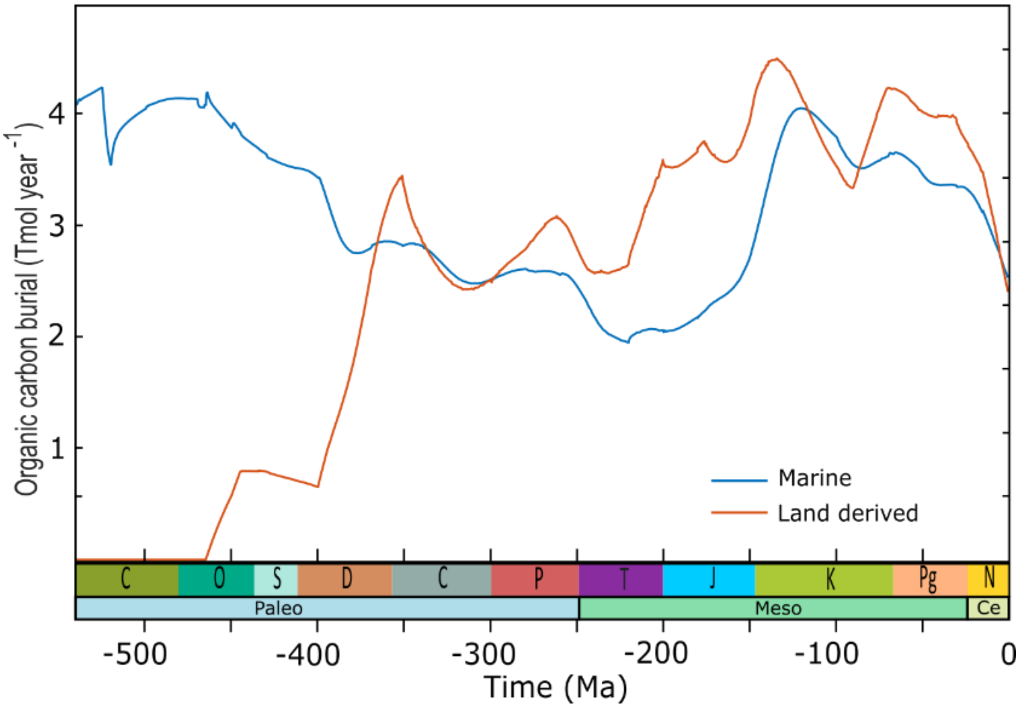

Figure 5.1.1. Organic carbon burial. *Land derived organic carbon burial (orange) and marine organic carbon burial (blue).*

SCION predicts an increase in $\delta^{13}C_{carb}$ during the Devonian, reflecting the use of a single value for vegetation and the assumption of a complete evolution of land plants at 380 Ma (Figure 5.1.2). However SCI-FI has a more gradual increase in $\delta^{13}C_{carb}$ over the Devonian until the Carboniferous as plant productivity is dampened by parameters other than CO_2, such as the configuration of land which can affect plant expansion (Figure 5.1.1). As the full potential of biomass is not reached until 350 Ma, this could be limiting plant productivity and therefore $\delta^{13}C_{carb}$. The timing of the initial rise in plant productivity and their associated effects on $\delta^{13}C_{carb}$ is heavily dependent on when land plants are introduced in the model therefore there is a need for a comprehensive plant evolution timeline within the model to more accurately predict large changes in plant productivity.

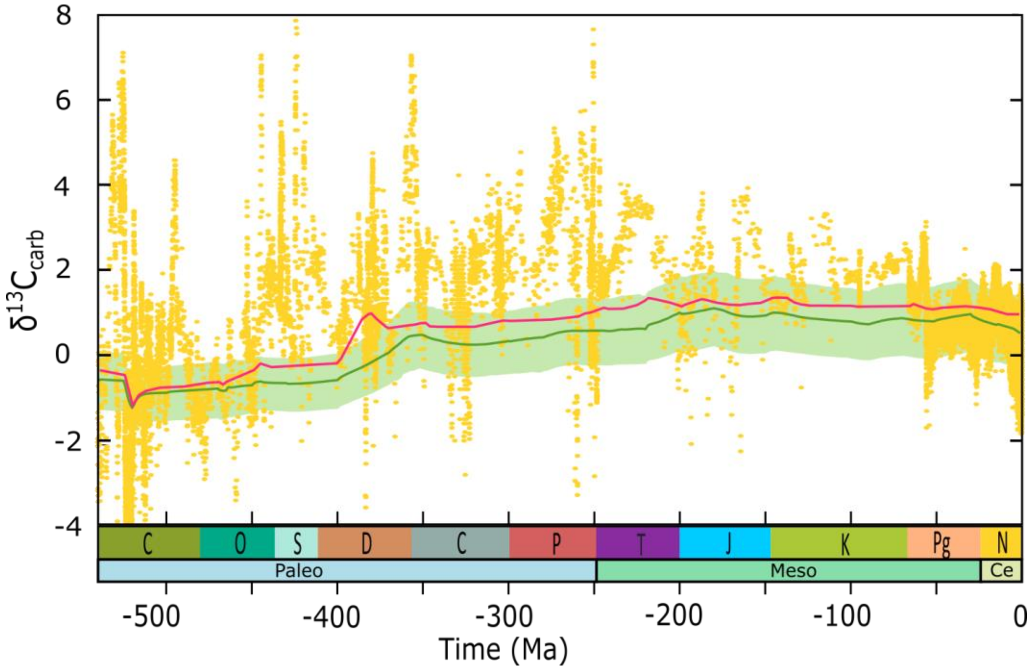

Figure 5.1.2. Comparison of carbon isotope estimations of marine carbonate rocks. *SCI-FI results (green line) show a similar pattern to SCION (pink line) and the geological records of carbon isotopes of marine carbonate rocks (*$\delta^{13}C_{carb}$*) (yellow dots; Saltzman and Thomas, 2012). Green shade: 95% confidence interval of SCI-FI sensitivity analysis.*

The $\delta^{13}C_{carb}$ record is spatially and temporally variable which can be due to variation in regional oceanic mixing at any given time, which creates spatial heterogeneity, and the use of various carbonate materials during data collection (Saltzman and Thomas, 2012; Mackensen and Schmiedl, 2019). The rapid changes observed in the proxy data are due to a multitude of marine factors and not solely the changes in photosynthetic productivity. Along with plant productivity, $\delta^{13}C_{carb}$ values also reflects oceanic productivity, carbon preservation and volcanic inputs; ocean anoxia can therefore also manifest as negative $\delta^{13}C_{carb}$ excursions (van Breugel et al., 2007). For example, the Permo-Triassic mass extinction involved large marine extinctions related to anoxia and ocean acidification. These events occur alongside negative excursions of $\delta^{13}C_{carb}$ likely due to volcanic inputs (Ripperdan, 2001).

5.2 Atmospheric O_2

SCION uses the COPSE oxygen feedback mechanism which involves the effect of marine oxygenation on nutrient burial rate and organic carbon preservation, and photorespiration and wildfires on limiting the terrestrial vegetation (Figure 5.2.1, Bergman et al., 2004; Lenton et al., 2018). Over long time periods, sedimentary pyrite (FeS_2) burial is an important source of atmospheric O_2 along with burial of organic matter (CH_2O) in sediments whereas the opposite reaction, weathering of rocks and oxidation of pyrite, creates a sink for atmospheric O_2 (Berner, 1989; Berner and Canfield, 1989; Glasspool and Scott, 2010). The following equations demonstrate the two reactions involved in global oxygen fluctuation:

$$CO_2 + H_2O \leftrightarrow CH_2O + O_2 \tag{5.2.1}$$

$$\begin{aligned} &2Fe_2O_3 + 16Ca^{2+}16HCO_3{}^{-} + 8SO_4{}^{2-} \\ &\quad \leftrightarrow 4FeS_2 + 16CaCO_3 + 8H_2O + 15O_2 \end{aligned} \tag{5.2.2}$$

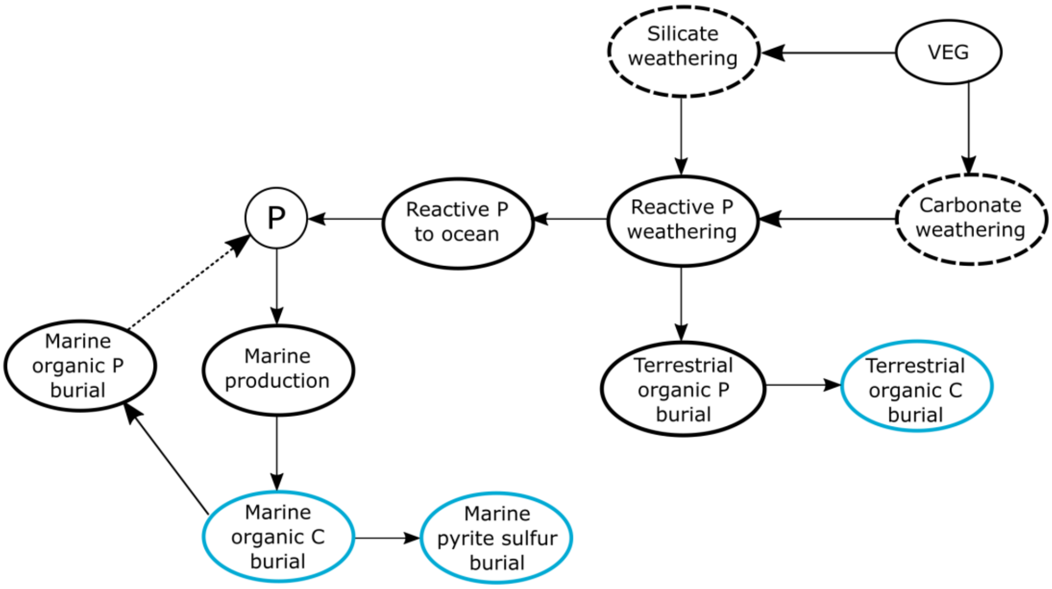

Figure 5.2.1. Partial COPSE framework with vegetation. *Arrows show positive (solid) and negative (dashed) relationship between model parameters. Weathering enhancement related to vegetation (VEG) effects processes in dashed ovals. Vegetation also affects phosphorus (P) weathering which reduces oceanic phosphorus influx. Blue ovals relate to long term sources of atmospheric oxygen. Modified from Lenton et al., 2018.*

The large increase in O_2 during the early Cretaceous (Figure 5.2.2) is due to the large increase in CO_2 at the same time (Figure 4.4.3). Higher temperatures as a result of CO_2 degassing leads to higher silicate weathering rates (especially at 145 Ma). As weathering increases, more phosphorous (P) is available in the soil which increases organic carbon burial and releases atmospheric O_2 (Equation 5.2.1). The opposite can be observed over the Paleozoic (Figure 5.2.2). Lower atmospheric O_2 in SCI-FI compared to SCION is due to decreased land biosphere mass (due mainly to aridity) and decreased silicate weathering. Nutrient cycling of P decreases and less is transported to the ocean. Lower marine productivity decreases pyrite sulfur and marine organic carbon burial. Both equations 5.2.1 and 5.2.2 occur at a lower rate leading to less O_2 being released into the atmosphere.

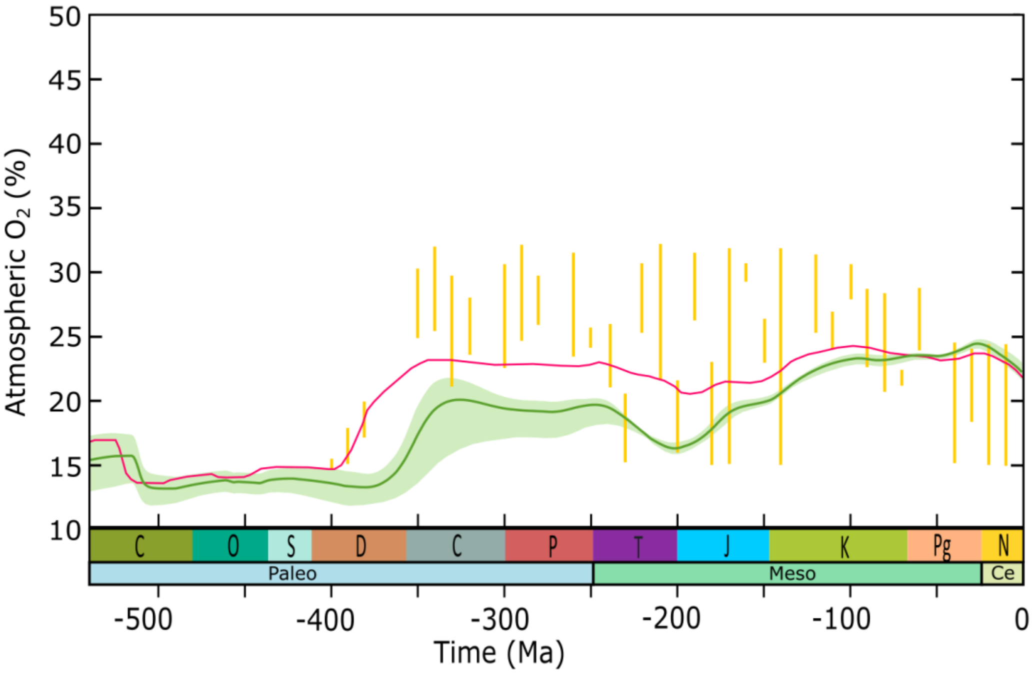

Figure 5.2.2. Comparison of atmospheric O_2. *SCI-FI (green line) shows a lower atmospheric O_2 concentration until the Cretaceous when compared to SCION (pink line) O_2 levels and the charcoal records (yellow lines; Glasspool and Scott, 2010). Green shade: 95% confidence interval of SCI-FI sensitivity analysis.*

SCI-FI has relatively lower biomass (and lower weathering enhancement) over the Paleozoic and early Mesozoic compared to SCION and therefore reproduces lower O_2 levels whereas higher biomass is predicted from the Mesozoic onwards which reflects in the rising levels of O_2 (Figure 5.2.2). On long timescales, global organic carbon burial is determined by the supply flux of P (the main limiting nutrient) from weathering and the ratio of C:P material that is buried. Plants have a much higher

C:P ratio than marine plants due to carbon-rich but P-poor structures like lignin (Lenton et al., 2016). Terrestrial vascular plants have an estimated C:P ratio of ~2,000 whereas marine plants have ~100 (Kump, 1988), showing a clear difference in organic C burial per unit of P burial. Although an increase in terrestrial productivity reduces P transportation to marine systems and lowers marine C organic burial, the efficiency of plants compensates for the decrease in marine C burial and oxygen release.

The inclusion of vegetation and their significant influence on organic C burial, and response to increased O_2 levels, has reduced atmospheric O_2 concentrations over the Phanerozoic. Fires cause several changes in terrestrial systems including the removal of P from land biota and soils (Kump, 1988). As a result, ecological disturbance and enhanced soil erosion increases transfer of P from land to sea. Although more P is available, the C:P efficiency of marine plants leads to lower organic C burial and therefore lower O_2.

5.3 Marine SO_4 and oceanic sulfate

Despite similar patterns, SCI-FI predicts a much lower marine sulfate concentrations [SO_4] compared to SCION predictions during the Paleozoic and Mesozoic, reaching SCION values over Paleogene and Neogene (Figure 5.3.1). Marine SO_4 in SCI-FI is however closer to proxy data due to lowered oxygen concentrations and therefore less global weathering of pyrite. Pyrite burial (left-to-right equation 5.2.2) is associated with marine SO_4 removal. If lower O_2 concentration is present due to decreased terrestrial activity, less pyrite weathering occurs and therefore less marine SO_4 is present. Slightly heavier isotopic composition of seawater sulfates ($\delta^{34}S$) in the ocean are observed in SCI-FI (Figure 5.3.2) as reduced pyrite burial is balanced by reduced pyrite weathering.

The discrepancy between marine SO_4 and proxy data may also be explained by the simplification of atmospheric and marine oxygenation in the underlying ocean model (Bergman et al., 2004). High levels of marine anoxia results to higher microbial sulfate reduction rates via anaerobic microbes which then leads to greater pyrite burial (Berner, 1985). Therefore, if the underlying model had more sensitivity between widespread marine anoxia and O_2 levels, the model predictions may replicate low sulphate levels under current atmospheric O_2.

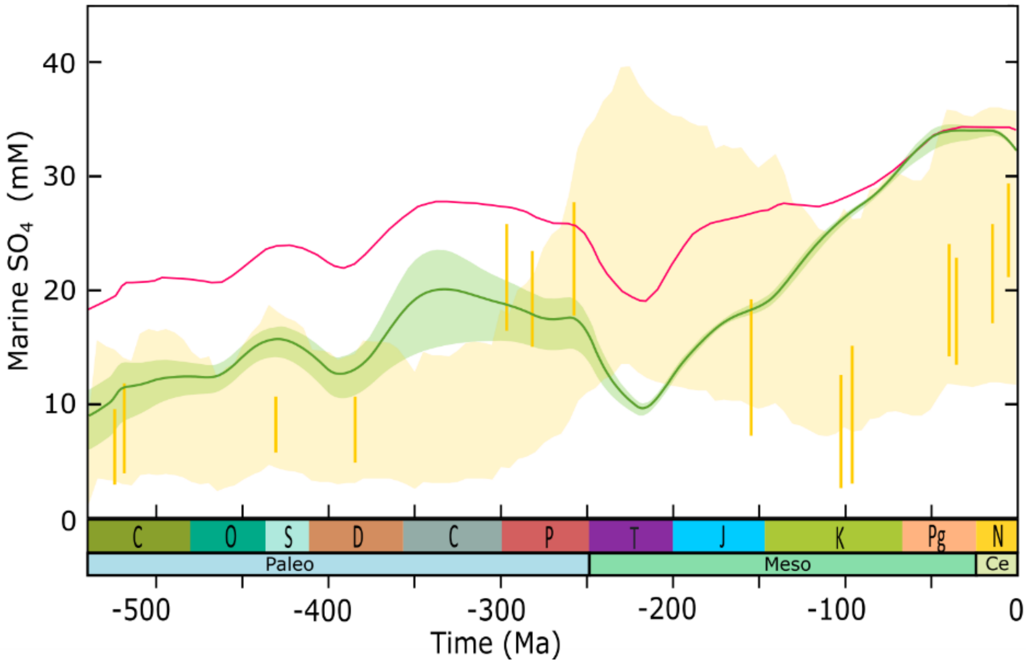

Figure 5.3.1. Comparison of marine sulfate concentration. *SCI-FI (green line) plotted against fluid inclusion data (vertical yellow bars; Horita et al., 2002; Brennan et al., 2004; Lowenstein et al., 2005) and sulfer isotope fractionation factors between*

buried sulfates and pyrite (yellow shading; Algeo et al., 2015). Green shade: 95% confidence interval of SCI-FI sensitivity analysis.

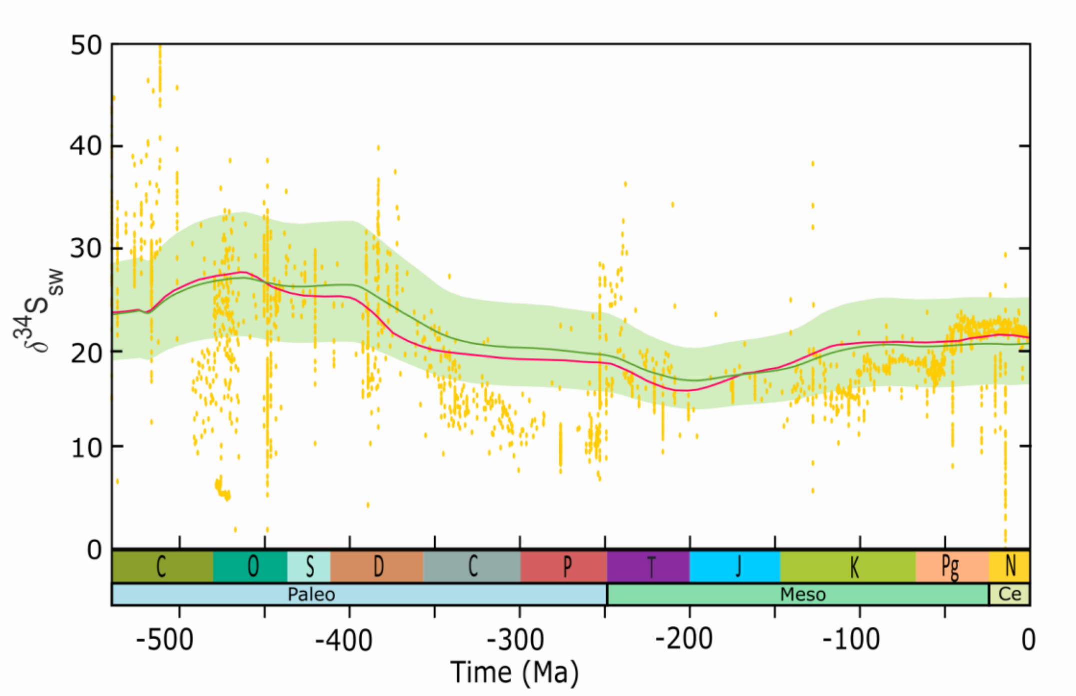

Figure 5.3.2. Comparison of oceanic isotopic sulfate composition. *SCI-FI (green line) estimates of seawater $\delta^{34}S$ plotted against geological records in evaporites, barites and calcium associated sulfates (yellow dots; Crockford et al., 2019), and SCION predictions (pink line). Green shade: 95% confidence interval of SCI-FI sensitivity analysis.*

5.4 Strontium

The marine strontium isotope ratio varies due to the weathering of different types of lithologies on land, and it reflects the balance between continental and hydrothermal weathering. A challenge present in modelling seawater strontium is the lack of a detailed surface lithology (Mills et al., 2021). The new biosphere is less productive overall, leading to lower continental weathering than the SCION model therefore SCI-FI predictions are slightly lower (Figure 5.4.1).

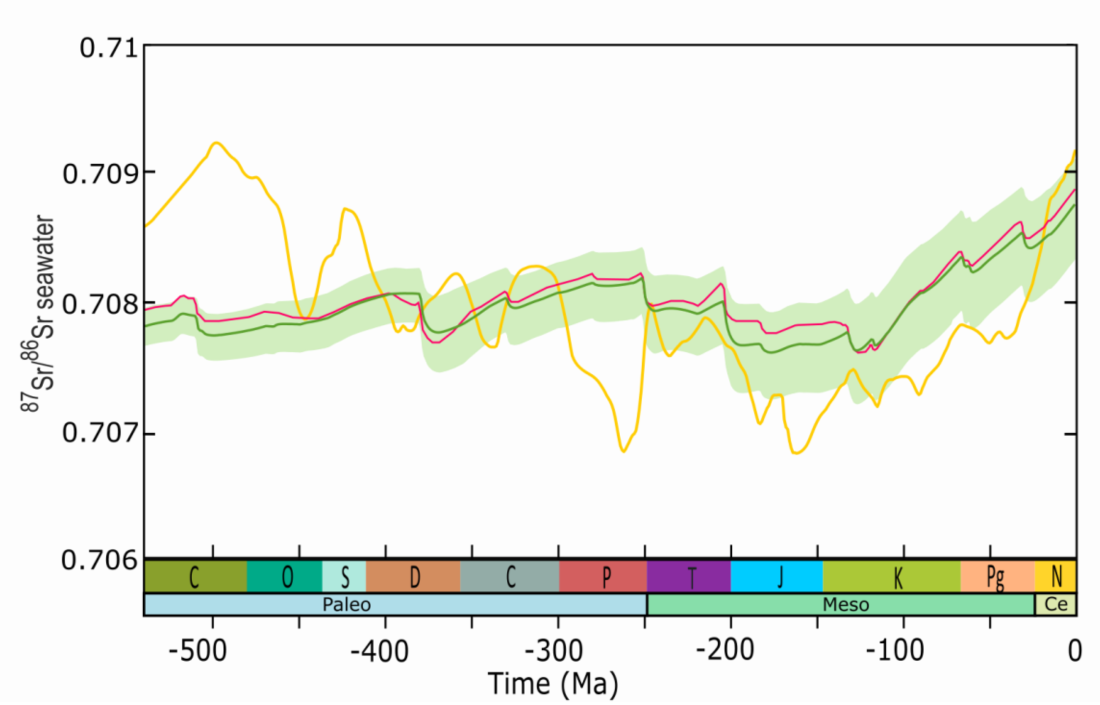

Figure 5.4.1. Comparison of seawater strontium ratio. *SCI-FI (green line) estimates of seawater strontium (^{87}Sr/^{86}Sr) plotted against geological record (yellow line; McArthur et al., 2012), and SCION predictions (pink line). Green shade: 95% confidence interval of SCI-FI sensitivity analysis.*

5.5 SCI-FI conclusion

SCI-FI represents biomass in a spatial setting, as opposed to SCION's non-dimensional vegetation setup. The combined model shows there was sufficient CO_2 and suitable conditions present for plants to continue flourishing in particular parts of the world, especially the tropics. Including a spatial aspect to vegetation and silicate weathering enhancement within SCION has improved CO_2 (Figure 4.4.3), temperature (Figure 4.4.4) and marine SO_4 (Figure 5.3.1) predictions. Aridity on to the interior of Pangea during the Permian-early Mesozoic led to lower biomass and increased CO_2 predictions that better match proxy data. Aridity based on geography is therefore an important forcing mechanism in driving climate change. To reiterate, the findings of Chapter 4 align with the results of Chapter 3, especially the role of Pangean geography and runoff on vegetation. FLORA focuses on the effect of plants specifically on the carbon cycle therefore the improvements in SCI-FI are observed mainly in processes involving the global carbon cycle. It highlights the need for, not only a spatial setting for vegetation, but also a more accurate representation of plant-climate interactions. SCI-FI creates a better overall model that can be used for further hypothesis testing regarding the effect of plants on climate.

5.6 Transpiration

Stomata, microscopic pores with guard cells that increase or decrease in turgor to dictate pore size, control CO_2 and water loss from the leaf (Chaves and Pereira, 1992; Nilson and Assmann, 2007). Fossil records show stomata and primitive xylem-like tissues to co-occur during the Silurian in most extant plants however their origin is highly debated (see Chapter 1.1.2 for stomatal evolution; Sperry, 2003). Transpiration is the redistribution of soil water to increase photosynthesis within vascular plants (Boyce and Lee, 2017). The process of transpiration acts as the main limiting factor for carbon uptake as stomata close to prevent water loss but also prevents carbon uptake at the same time.

Precipitation on land surface is lost to runoff, groundwater, or evapotranspiration (ET) (Schlesinger and Jasechko, 2014). Evaporation (from soil) and transpiration (from the stomata) occur simultaneously and cannot be distinguished (Mu et al., 2007; Katsoulas and Stanghellini, 2019) therefore are often grouped together as ET. Transpiration accounts for more than 80% of continental ET (Jasechko et al., 2013) while ET is responsible for 60% of precipitation being evaporated back into the atmosphere (Or and Lehmann, 2019) therefore making ET a key water recycling process. Climate change affects global transpiration which can then lead to physiological changes of vegetation. Changes in tree cover impact the atmospheric water cycle as more than half of land-derived atmospheric moisture comes from transpiration by plants (Sheil, 2018). As vegetation evolves or changes, the associated changes in transpiration rate will affect land temperatures and runoff rates by altering latent heat fluctuations from continents (Jasechko et al., 2013).

The evolution of transpiration and soil water absorption results in an increase of precipitation recycling via ET and therefore global precipitation (Boyce and Lee, 2017). However, not all plants contribute equally towards transpiration or the hydrologic cycle. Bryophytes do not possess the structure xylem (made of lignin) used for water transportation, although they do have xylem-like analogues (Raven, 2003). Bryophytes lack a waxy cuticle on the surface of their thalli and leaves, which allows for a more efficient diffusion of atmospheric water, and they display poikilohydry to survive conditions where transpiration exceeds water uptake (Raven, 2003). Non-vascular plants (bryophytes and lichens) can store between 300-3,000% of their dry weight in water. Their presence in the understory therefore affects rainfall interception and evaporation rather than transpiration (Porada et al., 2018). The evolution of vasculature is hypothesised as the first instance where plants take an active role in the hydrological cycle (Boyce and Lee, 2017). The leaf structure of angiosperms contains a high density of veins forming pipe networks that carry water across the leaf stem to photosynthetic tissue (Beerling and Franks, 2010). Angiosperm leaf structure is expected to have a fourfold increase in transpiration capacity of tropical rainforests (Boyce and Lee, 2017). However, this induces higher costs as it requires the production of lignin (carbon-rich structures) (Beerling and Franks, 2010). Over the Phanerozoic, an evolutionary change (i.e. the introduction of vasculature) or a change in ecology (i.e. transitioning from a bryophyte to vascular plant community) can create regional changes in the hydrological cycle and therefore could affect rates of precipitation and temperature. For example, if regions change from a bryophyte dominated community to forested areas, rainfall interception capacity reduces which could lead to regional warming as water is lost as runoff, and other climatic changes (Porada et al., 2018).

ET also varies for each biome (Table 5.6.1). Changes in geographical regions of boreal, temperate and tropical biomes over the Phanerozoic may have had an impact on global transpiration rates. Areas of high primary productivity correlate to areas of higher transpiration rates and ET (Jasechko et al., 2013). Therefore, as the tropics are the most productive biome (Boyce and Lee, 2017), the spread and shrinkage of tropical settings over the Phanerozoic could have changed global transpiration rates and affected the global hydrological cycle. Plant evolution, along with continental configuration changes that dictate temperature and runoff, determine which biome is dominant. As biomes evolve and change, transpiration rates change alongside.

Biome	Land area (%)	Precipitation (mm year^{-1})	ET (%)
Tropical rainforest	16	1830	51
Tropical grassland	12	950	76
Temperate deciduous forests	9	850	60
Boreal forest	14	500	63
Temperate grassland	8	470	86
Desert	18	180	103
Temperate coniferous forest	4	880	46
Steppe	4	440	78
Mediterranean shrubland	2	480	82

Table 5.6.1. Evapotranspiration rates of different biomes. *A large range of precipitation exists between biomes along with land area. Evapotranspiration (ET) is calculated as total ET from Food and Agriculture Organisation divided by total precipitation. Table modified from Schlesinger and Jasechko (2014).*

5.6.1 Preliminary work on the water cycle

Preliminary work on incorporating the water cycle into FLORA involved the calculation of an evaporation rate which factored into the water reservoir for plant uptake. Instead of calculating transpiration for plants at each gridcell, the cell would contain water available which would dictate the water stress that a plant might face. A simplified version of the Penman equation, which describes evaporation rate from well-watered vegetation with an albedo of 0.25 (Linacre, 1977), was used to calculate the water reservoir available for plant biomass (W).

$$W = precip - e \tag{5.6.1}$$

$$e = \min\left(W, e_{pot}\right) \tag{5.6.2}$$

$$e_{pot} = \max\left(60 \times 365 \times \frac{\frac{500T}{100 - A} + 15T_d}{(80 - T)}, 0\right) \tag{5.6.3}$$

$$T_d = \frac{0.23 + 0.37T + 0.53R + 0.35R_{ann} - 10.9}{12} \tag{5.6.4}$$

Evaporation ($e, mm\ year^{-1}$) was taken as the minimum of plant water or potential evaporation $\left(e_{pot},\ mm\ year^{-1}\right)$ to prevent a negative water reservoir; a plant cannot lose more water than the amount it holds. e_{pot} depends on altitude ($A, meters$), dew point (the atmospheric temperature at which water droplets begin to condense and form dews) ($T_d, °C$) and temperature ($T, °C$). An approximation of T_d is calculated using a mean range of temperature ($R = 15°C$) and the difference between the mean temperatures of the hottest and coldest months ($R_{ann} = 25°C$). W would then be calculated as precipitation ($precip, mm\ year^{-1}$) minus evaporation, and used to limit plant productivity within the biomass equation (Equation 2.2.2).

While this version of the Penman equation is useful and simple, it does not capture the interaction between plant cover and water loss, i.e. evaporation rates might not follow this relationship in areas where vegetation has a lower albedo, like the desert. ET generally increases with plant cover, which may accelerate the recycling of atmospheric moisture and eventually affect regional precipitation rates, soil moisture and runoff (Liu et al., 2018). The above equations are a start to coupling plant-hydrology interactions however it is a complex interaction that needs further research. Currently, FLORA uses runoff as a simple scaling factor, as opposed to precipitation, to limit plant productivity and link the water and carbon cycles.

5.7 Stepwise evolution of plants

The evolution of plants (Figure 1.1.3) shows an increase in both physiological and morphological complexity. Plants have been hypothesised to impact climate since their onset on land (Beerling and Berner, 2005), however the fluctuating degree of impact as plants evolve is difficult to explore. FLORA does not incorporate a stepwise increase in plant complexity, such as the change from the domination of high water stress tolerant bryophytes during the Devonian to tracheophytes with efficient water transport systems (Kodner and Graham, 2001), and the addition of high transpiration control of angiosperms from the Cretaceous onwards (Boyce and Leslie, 2012). In SCI-FI, a crude version of stepwise evolution is present whereby the limit on biomass decreases in a linear fashion overtime. Ideally, this would be replaced by adding plant traits at approximate timepoints of their evolution and building this into the competition model. The long list of plant evolutionary changes is beyond what I can discuss within this chapter. Hence, I have chosen lignin, which involves the evolution of vasculature (key for the cycling of water), and phylogeny order that could have impacted global biogeochemical cycles and climate.

5.7.1 Lignin

Present since the evolution of tracheophytes, lignin provides plants with structural support and rigidity to stand upright, and strengths cell walls to withstand pressure generated during transpiration (Weng and Chapple, 2010). The additional benefits of lignin allowed tracheophyte trees to dominate landscapes over bryophytes from the Devonian onwards (Boyce and Lee, 2017). Lignin content varies between tissue types (leaf, periderm, wood), age (sapwood, heartwood, young and old foliage) and taxonomic lines (angiosperms, gymnosperms, pteridophytes) (Robinson, 1990b). Paleozoic trees (ferns, pteriodophytes, lycopsids) contained periderm (bark), the outermost tissue of plant body, rather than wood as mechanical support (Robinson, 1990). Paleozoic trees likely had lignin contents of 40% or higher whereas over the Mesozoic, gymnosperms with wood over periderm support dominated, decreasing the overall lignin content in plants (Robinson, 1990).

Carboniferous peat forests are a consequence of lignin-rich plants and water-logged environments (Nelsen et al., 2016). The slow degradation of lignin and high plant productivity meant that large amounts of atmospheric carbon were being fixed by early tracheophytes. Lignin production outweighed fungi degradation of lignin, resulting in a significant drop in atmospheric CO_2 during the late Paleozoic (Weng and Chapple, 2010; Nelsen et al., 2016). In FLORA, if a separate biomass turnover rate equal to lignin degradation potential or a separate carbon pool for lignin was introduced during the Devonian, it may solve the issue of obtaining low atmospheric CO_2 during the Permo-Carboniferous as the carbon sink would increase in capacity.

5.7.2 Phylogeny debate

One of the most debated phylogenies in plant evolution is the placement of the bryophyte phyla (liverworts, hornworts and mosses) (Budke et al., 2018). Two of the supported evolutionary hypotheses involve: (1) liverwort and mosses in a monophyletic clade with hornworts as an independent lineage and (2) all phyla are members of a single clade, sister to vascular plants (Budke et al., 2018). Bryophyte phylogeny contains a large uncertainty due to their evolution having multiple convergent losses and gains of key morphological features (Rensing, 2018). Analyses with diverse molecular and morphological data results in every possible branching order of relationships (Gitzendanner et al., 2018). Liverworts were thought to be basal with hornworts following and mosses being the sister group to vascular plants however recent molecular studies suggest a monophyletic clade with hornworts being basal and liverworts to have secondarily lost complexity (Rensing, 2018; Puttick et al., 2018).

Although the model includes broad categories of plants, the timeline of the larger splits such as between tracheophytes and bryophytes is important. Such branches affect the interpretation of trait evolution and therefore need resolving. The sequences in which embryophyte, bryophyte and tracheophyte body plant characters were assembled cannot be accurately modelled until the phylogeny is established (Rensing, 2018). Vegetation is known to enhance weathering and the total carbon sequestration by plants depends on vegetation properties such as the size range of plants, and their rooting and vascular systems (Kenrick et al., 2012). Changing the order of evolutionary traits leads to a change in the development of biogeochemical cycles and their effect on various Earth systems.

Chapter 6. Conclusion

FLORA presents a simple, fast vegetation model that can be easily incorporated into larger climate-chemical models to better represent the plant-climate interaction that is currently missing. Using this model I have shown Earth's climate to be more than optimal for plant productivity at specific times during the Phanerozoic, and through their integration into SCION, I have improved its climate and biogeochemical predictions. The following points summarise the main findings in this thesis:

1. Spatial maps of potential biomass in FLORA (Chapter 3) show two major peaks in potential biomass which coincide with times associated with the terrestrialisation of land (Ordovician) and angiosperm radiation (Jurassic-Cretaceous). This suggests that local environmental conditions played a role in plant life flourishing and evolving during these times.

2. A combination of available land area, runoff and temperature drive plant productivity over the Phanerozoic, and runoff is the main impact on biomass. Water availability is seen to be the main limiting factor to plant productivity at the global scale, however, this may be because nutrient cycling has not been incorporated into FLORA yet.

3. Large areas of aridity formed as the interior of Pangea suffered from minimal runoff and high temperatures. Plants persisted on the continental edges of Pangea therefore global biomass is still present albeit in lower amounts. The breakup of Pangea removed arid areas as more land area encountered water. The spread of

the continents also created various niches in which plants were able to diversify in, possibly leading to the angiosperm radiation.

4. Incorporating FLORA into the larger climate-chemical model SCION (Chapter 4), leads predictions of atmospheric CO_2 levels, temperature and marine SO_4 to improve over the Mesozoic-to-present. This is due to the spatial integration of vegetation that creates a heterogeneous enhancement of silicate weathering and carbon sequestration patterns. Throughout the Phanerozoic, the tropics are seen as the most active area (both in biomass and weathering).

5. Temperature estimates during the Triassic-Jurassic and Cretaceous are better matched to proxy data by SCI-FI as opposed to SCION due to a more accurate reflection of vegetation and subsequently, weathering, during those periods. In order to predict large anomalies in temperature, unpredictable events that cause dramatic changes to the climate (e.g., volcanic eruptions) need to be factored into the model prior to its run.

6. Some areas of SCI-FI require further investigation such as the low oxygen predictions throughout the Phanerozoic and low temperatures during the Cambrian.

7. FLORA still requires further work on plant complexity, especially the introduction of carbon-rich structures such as lignin. The Permo-Carboniferous temperatures may be partly explained by large amounts of carbon being sequestered in peats. However, the lack of peat formation in FLORA leads it to overpredict carbon turnover therefore it predicts a warmer global temperature.

Bibliography

Algeo, T.J., Berner, R.A., Maynard, J.B. and Scheckler, S.E. 1995. Late Devonian oceanic anoxic events and biotic crisis: 'rooted'' in the evolution of vascular land plants?' *GSA Today*. **5**(3).

Algeo, T.J., Luo, G.M., Song, H.Y., Lyons, T.W. and Canfield, D.E. 2015. Reconstruction of secular variation in seawater sulfate concentrations. *Biogeosciences*. **12**(7), pp.2131–2151.

Algeo, T.J., Marenco, P.J. and Saltzman, M.R. 2016. Co-evolution of oceans, climate, and the biosphere during the 'Ordovician Revolution': A review. *Palaeogeography, Palaeoclimatology, Palaeoecology*. **458**, pp.1–11.

Arndt, S., Regnier, P., Goddéris, Y. and Donnadieu, Y. 2011. GEOCLIM reloaded (v 1.0): A new coupled earth system model for past climate change. *Geoscientific Model Development*. **4**(2), pp.451–481.

Baker, I.T., Prihodko, L., Denning, A.S., Goulden, M., Miller, S. and Rocha, H.R. da 2008. Seasonal drought stress in the Amazon: Reconciling models and observations. *Journal of Geophysical Research: Biogeosciences*. **113**(G1), pp.0–01.

Bar-On, Y.M., Phillips, R. and Milo, R. 2018. The biomass distribution on Earth. *Proceedings of the National Academy of Sciences*. **115**(25), pp.6506–6511.

Barba-Montoya, J., Reis, M. dos, Schneider, H., Donoghue, P.C.J. and Yang, Z. 2018. Constraining uncertainty in the timescale of angiosperm evolution and the veracity of a Cretaceous Terrestrial Revolution. *New Phytologist*. **218**(2), pp.819–834.

Barman, J., Samanta, A., Saha, B. and Datta, S. 2016. Mycorrhiza. *Resonance*. **21**(12), pp.1093–1104.

Barron, E., Harrison, C.G., Sloan II, J.L. and Hay, W.W. 1981. Paleogeography, 180 million years ago to the present. *Eclogae geol. Helv*. **74**(2), pp.443–470.

Bartlein, P.J. and Hostetler, S.W. 2003. Modeling paleoclimates *In*: *Developments in Quaternary Science* [Online]. Elsevier, pp.565–584. [Accessed 27 September 2021]. Available from: https://linkinghub.elsevier.com/retrieve/pii/S1571086603010273.

Bateman, R.M., Crane, P.R., DiMichele, W.A., Kenrick, P.R., Rowe, N.P., Speck, T. and Stein, W.E. 1998. Early evoluion of land plants: Phylogeny, Physiology, and Ecology of the Primary Terrestrial Radiation. *Annual Review of Ecology and Systematics*. **29**(1), pp.263–292.

Beerling, D.J. 2002. Low atmospheric CO 2 levels during the Permo-Carboniferous glaciation inferred from fossil lycopsids. *PNAS*. **99**(20), pp.12567–12571.

Beerling, D.J. and Berner, R.A. 2005. Feedbacks and the coevolution of plants and atmospheric CO2. *Proceedings of the National Academy of Sciences*. **102**(5), pp.1302–1305.

Beerling, D.J. and Franks, P.J. 2010. The hidden cost of transpiration. *Nature 2010 464:7288*. **464**(7288), pp.495–496.

Behie, S.W. and Bidochka, M.J. 2014. Nutrient transfer in plant–fungal symbioses. *Trends in Plant Science*. **19**(11), pp.734–740.

Bergman, N.M., Lenton, T.M. and Watson, A.J. 2004. COPSE: A new model of biogeochemical cycling over Phanerozoic time. *American Journal of Science*. **304**(5), pp.397–437.

Berhe, A.A., Barnes, R.T., Six, J. and Marín-Spiotta, E. 2018. Role of Soil Erosion in Biogeochemical Cycling of Essential Elements: Carbon, Nitrogen, and Phosphorus. *Annual Review of Earth and Planetary Sciences*. **46**(1), pp.521–

548.

Berner, R.A. 1989. Biogeochemical cycles of carbon and sulfur and their effect on atmospheric oxygen over phanerozoic time. *Global and Planetary Change*. **1**(1–2), pp.97–122.

Berner, R.A. 2006. GEOCARBSULF: A combined model for Phanerozoic atmospheric O2 and CO2. *Geochimica et Cosmochimica Acta*. **70**(23), pp.5653–5664.

Berner, R.A. 1993. Paleozoic Atmospheric CO2: Importance of Solar Radiation and Plant Evolution. *Science*. **261**(5117), pp.68–70.

Berner, R.A. 1985. Sulphate reduction, organic matter decomposition and pyrite formation. *Philosophical Transactions of the Royal Society of London. Series A, Mathematical and Physical Sciences*. (A315(1531)), pp.25–38.

Berner, R.A. 2003. The long-term carbon cycle, fossil fuels and atmospheric composition. *Nature*. **426**(6964), pp.323–326.

Berner, R.A. 1997. The Rise of Plants and Their Effect on Weathering and Atmospheric CO2. *Science*. **276**(5312), pp.544–546.

Berner, R.A. 1992. Weathering, plants, and the long-term carbon cycle. *Geochimica et Cosmochimica Acta*. **56**(8), pp.3225–3231.

Berner, R.A. and Canfield, D.E. 1989. A new model for atmospheric oxygen over Phanerozoic time. *American Journal of Science*. **289**(4), pp.333–361.

Berner, R.A. and Kothavala, Z. 2001. GEOCARB III: A revised model of atmospheric CO2 over Phanerozoic time. *American Journal of Science*. **301**(2), pp.182–204.

Berner, R.A., Univ., R.A. (Yale, Haven, N. and States)), C. (United 1991. A model for atmospheric CO 2 over Phanerozoic time. *American Journal of Science*. **291**(4), pp.339–376.

Blakey, R.C. 2008. Gondwana paleogeography from assembly to breakup- A 500 m.y. odyssey. *Resolving the Late Paleozoic Ice Age in Time and Space: Geological Society of America Special Paper*. **441**, pp.1–28.

Von Bloh, W., Schaphoff, S., Müller, C., Rolinski, S., Waha, K. and Zaehle, S. 2018. Implementing the nitrogen cycle into the dynamic global vegetation, hydrology, and crop growth model LPJmL (version 5.0). *Geoscientific Model Development*. **11**(7), pp.2789–2812.

Bonan, G.B., Levis, S., Sitch, S., Vertenstein, M. and Oleson, K.W. 2003. A dynamic global vegetation model for use with climate models: concepts and description of simulated vegetation dynamics. *Global Change Biology*. **9**(11), pp.1543–1566.

Bonis, N.R. and Kürschner, W.M. 2012. Vegetation history, diversity patterns, and climate change across the Triassic/Jurassic boundary. *Paleobiology*. **38**(2), pp.240–264.

Bowman, D.M.J.S., Balch, J.K., Artaxo, P., Bond, W.J., Carlson, J.M., Cochrane, M.A., D'Antonio, C.M., DeFries, R.S., Doyle, J.C., Harrison, S.P., Johnston, F.H., Keeley, J.E., Krawchuk, M.A., Kull, C.A., Marston, J.B., Moritz, M.A., Prentice, I.C., Roos, C.I., Scott, A.C., Swetnam, T.W., van der Werf, G.R. and Pyne, S.J. 2009. Fire in the Earth System. *Science*. **324**(5926), pp.481–484.

Box, E.O. 1996. Plant functional types and climate at the global scale. *Journal of Vegetation Science*. **7**(3), pp.309–320.

Boyce, C.K. and Lee, J.-E. 2017. Plant Evolution and Climate Over Geological Timescales. *Annu. Rev. Earth Planet. Sci*. **45**, pp.61–87.

Boyce, C.K. and Leslie, A.B. 2012. The Paleontological Context of Angiosperm Vegetative Evolution. *International Journal of Plant Sciences*. **173**(6), pp.561–568.

Brady, P. V. and Carroll, S.A. 1994. Direct effects of CO2 and temperature on silicate weathering: Possible implications for climate control. *Geochimica et Cosmochimica Acta*. **58**(7), pp.1853–1856.

Brennan, S.T., Lowenstein, T.K. and Horita, J. 2004. Seawater chemistry and the advent of biocalcification. *Geology*. **32**(6), pp.473–476.

van Breugel, Y., Schouten, S., Tsikos, H., Erba, E., Price, G.D. and Damsté, J.S.S. 2007. Synchronous negative carbon isotope shifts in marine and terrestrial biomarkers at the onset of the early Aptian oceanic anoxic event 1a: Evidence for the release of 13C-depleted carbon into the atmosphere. *Paleoceanography*. **22**(1).

Brinck, K., Fischer, R., Groeneveld, J., Lehmann, S., Dantas De Paula, M., Pütz, S., Sexton, J.O., Song, D. and Huth, A. 2017. High resolution analysis of tropical forest fragmentation and its impact on the global carbon cycle. *Nature Communications 2017 8:1*. **8**(1), pp.1–6.

Brodribb, T.J. and Feild, T.S. 2010. Leaf hydraulic evolution led a surge in leaf photosynthetic capacity during early angiosperm diversification. *Ecology Letters*. **13**(2), pp.175–183.

Brodribb, T.J., Feild, T.S. and Sack, L. 2010. Viewing leaf structure and evolution from a hydraulic perspective. *Functional Plant Biology*. **37**(6), p.488.

Brooks, A. and Farquhar, G.D. 1985. Effect of temperature on the CO2/O2 specificity of ribulose-1,5-bisphosphate carboxylase/oxygenase and the rate of respiration in the light - Estimates from gas-exchange measurements on spinach. *Planta*. **165**(3), pp.397–406.

Brundrett, M.C. 2002. Coevolution of roots and mycorrhizas of land plants. *New Phytologist*. **154**(2), pp.275–304.

Budke, J.M., Bernard, E.C., Gray, D.J., Huttunen, S., Piechulla, B. and Trigiano, R.N. 2018. Introduction to the Special Issue on Bryophytes. *Critical Reviews in Plant Sciences*. **37**(2–3), pp.102–112.

Busch, F.A., Holloway-Phillips, M., Stuart-Williams, H. and Farquhar, G.D. 2020. Revisiting carbon isotope discrimination in C3 plants shows respiration rules when photosynthesis is low. *Nature Plants 2020 6:3*. **6**(3), pp.245–258.

Cairney, J.W.G. 2000. Evolution of mycorrhiza systems. *Naturwissenschaften*. **87**(11), pp.467–475.

Caldeira, K. and Rampino, M.R. 1991. The Mid-Cretaceous Super Plume, carbon dioxide, and global warming. *Geophysical Research Letters*. **18**(6), pp.987–990.

Calner, M. 2008. Silurian global events – at the tipping point of climate change *In*: *Mass Extinction* [Online]. Berlin, Heidelberg: Springer Berlin Heidelberg, pp.21–57. [Accessed 22 January 2019]. Available from: http://link.springer.com/10.1007/978-3-540-75916-4_4.

Cather, S.M., Dunbar, N.W., McDowell, F.W., McIntosh, W.C. and Scholle, P.A. 2009. Climate forcing by iron fertilization from repeated ignimbrite eruptions: The icehouse–silicic large igneous province (SLIP) hypothesisClimate forcing by ignimbrite eruptions. *Geosphere*. **5**(3), pp.315–324.

Chaboureau, A.C., Sepulchre, P., Donnadieu, Y. and Franc, A. 2014. Tectonic-driven climate change and the diversification of angiosperms. *Proceedings of the National Academy of Sciences of the United States of America*. **111**(39), pp.14066–14070.

Chaves, M.M. and Pereira, J.S. 1992. Water Stress, CO 2 and Climate Change. *Journal of Experimental Botany*. **43**(8), pp.1131–1139.

Chen, B., Chen, J., Qie, W., Huang, P., He, T., Joachimski, M.M., Regelous, M., Pogge von Strandmann, P.A.E., Liu, J., Wang, X., Montañez, I.P. and Algeo, T.J. 2021. Was climatic cooling during the earliest Carboniferous driven by expansion of seed plants? *Earth and Planetary Science Letters*. **565**, p.116953.

Chen, D. and Chen, H.W. 2013. Using the Köppen classification to quantify climate variation and change: An example for 1901–2010. *Environmental Development*. **6**(1), pp.69–79.

Chen, J.L. and Reynolds, J.F. 1997. A Coordination Model of Whole-plant Carbon Allocation in Relation to Water Stress. *Annals of Botany*. **80**(1), pp.45–55.

Churkina, G., Running, S.W., Schloss, A.L. and Intercomparison, T.P.O.T.P. 1999. Comparing global models of terrestrial net primary productivity (NPP): the importance of water availability. *Global Change Biology*. **5**(S1), pp.46–55.

Claeys, P., Kiessling, W. and Alvarez, W. 2002. Distribution of Chicxulun ejecta at the Cretaceous-Tertiary boundary *In*: C. Koeberl and K. G. MacLeod, eds. *Catastrophic Events and Mass Extinctions: Impacts and Beyond, Colorado, Geological Society of America Special Pape* [Online]., pp.55–68. [Accessed 18 November 2021]. Available from: https://books.google.co.uk/books?hl=en&lr=&id=ZaIO8wl_OZIC&oi=fnd&pg=PA55&dq=kt+boundary+chicxulub&ots=lFM3YvzNlO&sig=borU4qQryTL7zDgi-jp1f80OeVM&redir_esc=y#v=onepage&q=kt boundary chicxulub&f=false.

Cleal, C.J. 2018. The Carboniferous coal swamp floras of England: a window on an ancient tropical ecosystem. *Proceedings of the Geologists' Association*. **129**(3), pp.329–351.

Cornelissen, J.H.C., Lang, S.I., Soudzilovskaia, N.A. and During, H.J. 2007. Comparative Cryptogam Ecology: A Review of Bryophyte and Lichen Traits that Drive BiogeochemistryCornelissen et al. — Comparative Cryptogam EcologyCornelissen et al. — Comparative Cryptogam Ecology. *Annals of Botany*. **99**(5), pp.987–1001.

Cox, P.M. 2001. *Description of the 'TRIFFID' Dynamic Global Vegetation Model*.

Crockford, P.W., Kunzmann, M., Bekker, A., Hayles, J., Bao, H., Halverson, G.P., Peng, Y., Bui, T.H., Cox, G.M., Gibson, T.M., Wörndle, S., Rainbird, R., Lepland, A., Swanson-Hysell, N.L., Master, S., Sreenivas, B., Kuznetsov, A., Krupenik, V. and Wing, B.A. 2019. Claypool continued: Extending the isotopic record of sedimentary sulfate. *Chemical Geology*. **513**, pp.200–225.

Cui, D., Liang, S. and Wang, D. 2021. Observed and projected changes in global climate zones based on Köppen climate classification. *WIREs Climate Change*. **12**(3).

Dai, S., Bechtel, A., Eble, C.F., Flores, R.M., French, D., Graham, I.T., Hood, M.M., Hower, J.C., Korasidis, V.A., Moore, T.A., Püttmann, W., Wei, Q., Zhao, L. and O'Keefe, J.M.K. 2020. Recognition of peat depositional environments in coal: A review. *International Journal of Coal Geology*. **219**.

Davies, J.H.F.L., Marzoli, A., Bertrand, H., Youbi, N., Ernesto, M. and Schaltegger, U. 2017. End-Triassic mass extinction started by intrusive CAMP activity. *Nature Communications 2017 8:1*. **8**(1), pp.1–8.

DiMichele, W.A. 2014. Wetland-Dryland Vegetational Dynamics in the Pennsylvanian Ice Age Tropics. *International Journal of Plant Sciences*. **175**(2), pp.123–164.

DiMichele, W.A. and Phillips, T.L. 1994. Paleobotanical and paleoecological constraints on models of peat formation in the Late Carboniferous of Euramerica. *Palaeogeography, Palaeoclimatology, Palaeoecology*. **106**(1–4), pp.39–90.

Donnadieu, Y., Goddéris, Y. and Bouttes, N. 2009. Exploring the climatic impact of the continental vegetation on the Mezosoic atmospheric CO2 and climate history. *Climate of the Past*. **5**(1), pp.85–96.

Donnadieu, Y., Goddéris, Y., Pierrehumbert, R., Dromart, G., Fluteau, F. and Jacob, R. 2006. A GEOCLIM simulation of climatic and biogeochemical consequences of Pangea breakup. *Geochemistry, Geophysics, Geosystems*. **7**(11).

Donnadieu, Y., Goddéris, Y., Ramstein, G., Nédélec, A. and Meert, J. 2004. A 'snowball Earth' climate triggered by continental break-up through changes in runoff. *Nature 2004 428:6980*. **428**(6980), pp.303–306.

Doyle, J.A. 2013. Phylogenetic Analyses and Morphological Innovations in Land Plants. *Annual Plant Reviews*. **45**, pp.1–50.

Duarte, J.C. and Schellart, W.P. 2016. Introduction to Plate Boundaries and Natural Hazards *In*: *Plate Boundaries and Natural Hazards* [Online]. American Geophysical Union (AGU), pp.1–10. [Accessed 27 October 2021]. Available from: https://onlinelibrary.wiley.com/doi/full/10.1002/9781119054146.ch1.

Duckett, J.G. and Pressel, S. 2018. The evolution of the stomatal apparatus: intercellular spaces and sporophyte water relations in bryophytes—two ignored dimensions. *Philosophical Transactions of the Royal Society B: Biological Sciences*. **373**(1739), p.20160498.

Edwards, D. 2003. Xylem in early tracheophytes. *Plant, Cell & Environment*. **26**(1), pp.57–72.

Epihov, D.Z., Batterman, S.A., Hedin, L.O., Leake, J.R., Smith, L.M. and Beerling, D.J. 2017. N2-fixing tropical legume evolution: a contributor to enhanced weathering through the Cenozoic? *Proceedings of the Royal Society B: Biological Sciences*. **284**(1860).

Fang, H., Baret, F., Plummer, S. and Schaepman-Strub, G. 2019. An Overview of Global Leaf Area Index (LAI): Methods, Products, Validation, and Applications. *Reviews of Geophysics*. **57**(3), pp.739–799.

Farquhar, G.D., von Caemmerer, S. and Berry, J.A. 1980. A biochemical model of photosynthetic CO2 assimilation in leaves of C3 species. *Planta 1980 149:1*. **149**(1), pp.78–90.

Fekete, B.M., Vorosmarty, C.J. and Grabs, W. 2000. *Global, Composite Runoff Fields Based on Observed River Discharge and Simulated Water Balances* [Online]. [Accessed 2 April 2021]. Available from: https://www.compositerunoff.sr.unh.edu//html/paper/ReportA4.pdf.

Field, K.J., Pressel, S., Duckett, J.G., Rimington, W.R. and Bidartondo, M.I. 2015. Symbiotic options for the conquest of land. *Trends in Ecology & Evolution*. **30**(8), pp.477–486.

Field, K.J., Rimington, W.R., Bidartondo, M.I., Allinson, K.E., Beerling, D.J., Cameron, D.D., Duckett, J.G., Leake, J.R. and Pressel, S. 2015. First evidence of mutualism between ancient plant lineages (Haplomitriopsida liverworts) and Mucoromycotina fungi and its response to simulated Palaeozoic changes in atmospheric CO2. *New Phytologist*. **205**(2), pp.743–756.

Field, K.J., Rimington, W.R., Bidartondo, M.I., Allinson, K.E., Beerling, D.J., Cameron, D.D., Duckett, J.G., Leake, J.R. and Pressel, S. 2016. Functional analysis of liverworts in dual symbiosis with Glomeromycota and Mucoromycotina fungi under a simulated Palaeozoic CO2 decline. *The ISME journal*. **10**(6), pp.1514–26.

Fisher, R.A., Koven, C.D., Anderegg, W.R.L., Christoffersen, B.O., Dietze, M.C., Farrior, C.E., Holm, J.A., Hurtt, G.C., Knox, R.G., Lawrence, P.J., Lichstein, J.W., Longo, M., Matheny, A.M., Medvigy, D., Muller-Landau, H.C., Powell, T.L., Serbin, S.P., Sato, H., Shuman, J.K., Smith, B., Trugman, A.T., Viskari, T., Verbeeck, H., Weng, E., Xu, C., Xu, X., Zhang, T. and Moorcroft, P.R.

2018. Vegetation demographics in Earth System Models: A review of progress and priorities. *Global Change Biology*. **24**(1), pp.35–54.

Fluteau, F., Besse, J., Broutin, J. and Ramstein, G. 2001. The Late Permian climate. What can be inferred from climate modelling concerning Pangea scenarios and Hercynian range altitude? *Palaeogeography, Palaeoclimatology, Palaeoecology*. **167**(1–2), pp.39–71.

Foster, G.L., Royer, D.L. and Lunt, D.J. 2017. Future climate forcing potentially without precedent in the last 420 million years. *Nature Communications*. **8**(1), pp.1–8.

Gaff, D.F. 1971. Desiccation-tolerant flowering plants in southern Africa. *Science (New York, N.Y.)*. **174**(4013), pp.1033–4.

Gaillardet, J., Dupré, B., Louvat, P. and Allègre, C.J. 1999. Global silicate weathering and CO2 consumption rates deduced from the chemistry of large rivers. *Chemical Geology*. **159**(1–4), pp.3–30.

Galmes, J., Flexas, J., Keys, A.J., Cifre, J., Mitchell, R.A.C., Madgwick, P.J., Haslam, R.P., Medrano, H. and Parry, M.A.J. 2005. Rubisco specificity factor tends to be larger in plant species from drier habitats and in species with persistent leaves. *Plant, Cell and Environment*. **28**(5), pp.571–579.

Gholz, H.L., Ewel, K.C. and Teskey, R.O. 1990. Water and forest productivity. *Forest Ecology and Management*. **30**(1–4), pp.1–18.

Gilroy, S. and Jones, D.L. 2000. Through form to function: root hair development and nutrient uptake. *Trends in Plant Science*. **5**(2), pp.56–60.

Gitzendanner, M.A., Soltis, P.S., Wong, G.K.-S., Ruhfel, B.R. and Soltis, D.E. 2018. Plastid phylogenomic analysis of green plants: A billion years of evolutionary history. *American Journal of Botany*. **105**(3), pp.291–301.

Glasspool, I.J. and Scott, A.C. 2010. Phanerozoic concentrations of atmospheric oxygen reconstructed from sedimentary charcoal. *Nature Geoscience 2010 3:9*. **3**(9), pp.627–630.

Goddéris, Y., Donnadieu, Y., Le Hir, G., Lefebvre, V. and Nardin, E. 2014. The role of palaeogeography in the Phanerozoic history of atmospheric CO2 and climate. *Earth-Science Reviews*. **128**, pp.122–138.

Goltapeh, E.M., Danesh, Y.R., Prasad, R. and Varma, A. 2008. Mycorrhizal Fungi: What We Know and What Should We Know? *In*: *Mycorrhiza* [Online]. Berlin, Heidelberg: Springer Berlin Heidelberg, pp.3–27. [Accessed 13 December 2018]. Available from: http://link.springer.com/10.1007/978-3-540-78826-3_1.

Gonzalez, P., Neilson, R.P., Lenihan, J.M. and Drapek, R.J. 2010. Global patterns in the vulnerability of ecosystems to vegetation shifts due to climate change. *Global Ecology and Biogeography*. **19**(6), pp.755–768.

Grossman, E.L., Bruckschen, P., Mii, H.-S., Chuvashov, B.I., Yancey, T.E. and Veizer, J. 2002. Carboniferous paleoclimate and global change: Isotopic evidence from the Russian Platform. *Carboniferous stratigraphy and Paleogeography in Eurasia*., pp.61–71.

Hack, J.J., Boville, B.A., Briegleb, B.P., Kiehl, J.T., Rasch, P.J. and Williamson, D.L. 1993. Description of the NCAR Community Climate Model (CCM2). *NCAR Technical Note NCAR/TN-420+STR*.

Harper, C.J., Krings, M., Dotzler, N., Taylor, E.L. and Taylor, T.N. 2017. Deciphering interfungal relationships in the 410-million-yr-old Rhynie chert: Morphology and development of vesicle-colonizing microfungi. *Geobios*. **50**(1), pp.9–22.

Harris, B.J., Harrison, C.J., Hetherington, A.M. and Williams, T.A. 2020. Phylogenomic Evidence for the Monophyly of Bryophytes and the Reductive Evolution of Stomata. *Current Biology*. **30**(11), pp.2001–2012.

Haxeltine, A. and Prentice, I.C. 1996a. *A General Model for the Light-Use Efficiency of Primary Production*.

Haxeltine, A. and Prentice, I.C. 1996b. BIOME3: An equilibrium terrestrial biosphere model based on ecophysiological constraints, resource availability, and competition among plant functional types. *Global Biogeochemical Cycles*. **10**(4), pp.693–709.

Hay, W.W., DeConto, R.M. and Wold, C.N. 1997. Climate: Is the past the key to the future? *Geologische Rundschau 1997 86:2*. **86**(2), pp.471–491.

van der Heijden, M.G.A., Martin, F.M., Selosse, M.-A. and Sanders, I.R. 2015. Mycorrhizal ecology and evolution: the past, the present, and the future. *New Phytologist*. **205**(4), pp.1406–1423.

Hochuli, P.A., Heimhofer, U. and Weissert, H. 2006. Timing of early angiosperm radiation: recalibrating the classical succession. *Journal of the Geological Society*. **163**, pp.587–594.

Horita, J., Zimmermann, H. and Holland, H.D. 2002. Chemical evolution of seawater during the Phanerozoic: Implications from the record of marine evaporites. *Geochimica et Cosmochimica Acta*. **66**(21), pp.3733–3756.

Houghton, R.A., Hall, F. and Goetz, S.J. 2009. Importance of biomass in the global carbon cycle. *Journal of Geophysical Research: Biogeosciences*. **114**(G2).

Hoysted, G.A., Jacob, A.S., Kowal, J., Giesemann, P., Bidartondo, M.I., Duckett, J.G., Gebauer, G., Rimington, W.R., Schornack, S., Pressel, S. and Field, K.J. 2019. Mucoromycotina Fine Root Endophyte Fungi Form Nutritional Mutualisms with Vascular Plants. *Plant Physiology*. **181**(2), pp.565–577.

Hoysted, G.A., Kowal, J., Jacob, A., Rimington, W.R., Duckett, J.G., Pressel, S., Orchard, S., Ryan, M.H., Field, K.J. and Bidartondo, M.I. 2018. A mycorrhizal revolution. *Current Opinion in Plant Biology*. **44**, pp.1–6.

Ibarra, D.E., Caves Rugenstein, J.K., Bachan, A., Baresch, A., Lau, K. V., Thomas, D.L., Lee, J.E., Kevin Boyce, C. and Page Chamberlain, C. 2019. Modeling the consequences of land plant evolution on silicate weathering. *American Journal of Science*. **319**(1), pp.1–43.

Jackson, M.L. and Sherman, G.D. 1953. Chemical Weathering of Minerals in Soils. *Advances in Agronomy*. **5**(C), pp.219–318.

Jacob, R., Schafer, C., Foster, I., Tobis, M. and Anderson, J. 2001. Computational Design and Performance of the Fast Ocean Atmosphere Model, Version One. *Lecture Notes in Computer Science (including subseries Lecture Notes in Artificial Intelligence and Lecture Notes in Bioinformatics)*. **2073**, pp.175–184.

Jacob, R.L. 1997. *Low frequency variability in a simulated atmosphere ocean system*. University of Wisconsin.

Jansa, J. and Treseder, K.K. 2017. Introduction: Mycorrhizas and the Carbon Cycle. *Mycorrhizal Mediation of Soil: Fertility, Structure, and Carbon Storage*., pp.343–355.

Jasechko, S., Sharp, Z.D., Gibson, J.J., Birks, S.J., Yi, Y. and Fawcett, P.J. 2013. Terrestrial water fluxes dominated by transpiration. *Nature 2013 496:7445*. **496**(7445), pp.347–350.

Jiang, C., Ryu, Y., Wang, H. and Keenan, T.F. 2020. An optimality-based model explains seasonal variation in C3 plant photosynthetic capacity. *Global Change Biology*. **26**(11), pp.6493–6510.

Jones, V.A.S. and Dolan, L. 2012. The evolution of root hairs and rhizoids. *Annals of Botany*. **110**(2), pp.205–212.

Kamal, S., Prasad, R. and Varma, A. 2010. Soil Microbial Diversity in Relation to Heavy Metals. , pp.31–63.

Kasting, J.F. 1989. Long-term stability of the earth’s climate. *Global and Planetary*

Change. **1**(1–2), pp.83–95.

Katsoulas, N. and Stanghellini, C. 2019. Modelling Crop Transpiration in Greenhouses: Different Models for Different Applications. *Agronomy 2019, Vol. 9, Page 392*. **9**(7), p.392.

Kelliher, F.M., Leuning, R., Raupach, M.R. and Schulze, E.-D. 1995. Maximum conductances for evaporation from global vegetation types. *Agricultural and Forest Meteorology*. **73**(1–2), pp.1–16.

Kennedy, P.G. and Sousa, W.P. 2006. Forest encroachment into a Californian grassland: Examining the simultaneous effects of facilitation and competition on tree seedling recruitment. *Oecologia*. **148**(3), pp.464–474.

Kenrick, P. and Crane, P.R. 1997. The origin and early evolution of plants on land. *Nature*. **389**(6646), pp.33–39.

Kenrick, P., Wellman, C.H., Schneider, H. and Edgecombe, G.D. 2012. A timeline for terrestrialization: consequences for the carbon cycle in the Palaeozoic. *Philosophical Transactions of the Royal Society B: Biological Sciences*. **367**, pp.519–536.

Kiers, E.T., Duhamel, M., Beesetty, Y., Mensah, J.A., Franken, O., Verbruggen, E., Fellbaum, C.R., Kowalchuk, G.A., Hart, M.M., Bago, A., Palmer, T.M., West, S.A., Vandenkoornhuyse, P., Jansa, J. and Bücking, H. 2011. Reciprocal Rewards Stabilize Cooperation in the Mycorrhizal Symbiosis. *Science*. **333**(6044), pp.880–882.

Kiers, E.T. and van der Heijden, M.G.A. 2006. Mutualistic stability in the arbuscular mycorrhizal symbiosis: exploring hypotheses of evolutionary cooperation. *Ecology*. **87**(7), pp.1627–1636.

Kodner, R.B. and Graham, L.E. 2001. High-temperature, acid-hydrolyzed remains of Polytrichum (Musci, Polytrichaceae) resemble enigmatic Silurian-Devonian tubular microfossils. *American Journal of Botany*. **88**(3), pp.462–466.

Korte, C., Hesselbo, S.P., Ullmann, C. V., Dietl, G., Ruhl, M., Schweigert, G. and Thibault, N. 2015. Jurassic climate mode governed by ocean gateway. *Nature Communications 2015 6:1*. **6**(1), pp.1–7.

Kraft, P., Pšenička, J., Sakala, J. and Frýda, J. 2019. Initial plant diversification and dispersal event in upper Silurian of the Prague Basin. *Palaeogeography, Palaeoclimatology, Palaeoecology*. **514**, pp.144–155.

Krause, A.J., Mills, B.J.W., Zhang, S., Planavsky, N.J., Lenton, T.M. and Poulton, S.W. 2018. Stepwise oxygenation of the Paleozoic atmosphere. *Nature Communications 2018 9:1*. **9**(1), pp.1–10.

Kump, L.R. 1988. Terrestrial feedback in atmospheric oxygen regulation by fire and phosphorus. *Nature*. **335**(6186), pp.152–154.

Lefsky, M.A., Cohen, W.B., Harding, D.J., Parker, G.G., Acker, S.A. and Gower, S.T. 2002. Lidar remote sensing of above-ground biomass in three biomes. *Global Ecology and Biogeography*. **11**(5), pp.393–399.

Lenton, T.M. 2001. The role of land plants, phosphorus weathering and fire in the rise and regulation of atmospheric oxygen. *Global Change Biology*. **7**(6), pp.613–629.

Lenton, T.M., Crouch, M., Johnson, M., Pires, N. and Dolan, L. 2012. First plants cooled the Ordovician. *Nature Geoscience*. **5**(2), pp.86–89.

Lenton, T.M., Dahl, T.W., Daines, S.J., Mills, B.J.W., Ozaki, K., Saltzman, M.R. and Porada, P. 2016. Earliest land plants created modern levels of atmospheric oxygen. *Proceedings of the National Academy of Sciences of the United States of America*. **113**(35), pp.9704–9709.

Lenton, T.M., Daines, S.J. and Mills, B.J.W. 2018. COPSE reloaded: An improved model of biogeochemical cycling over Phanerozoic time. *Earth-Science*

Reviews. **178**, pp.1–28.

Li, G., Ji, J., Zhao, L., Mao, C. and Chen, J. 2008. Response of silicate weathering to monsoon changes on the Chinese Loess Plateau. *CATENA*. **72**(3), pp.405–412.

Lidgard, S. and Crane, P.R. 1988. Quantitative analyses of the early angiosperm radiation. *Nature 1988 331:6154*. **331**(6154), pp.344–346.

Linacre, E.T. 1977. A simple formula for estimating evaporation rates in various climates, using temperature data alone. *Agricultural Meteorology*. **18**(6), pp.409–424.

Linnert, C., Robinson, S.A., Lees, J.A., Bown, P.R., Pérez-Rodríguez, I., Petrizzo, M.R., Falzoni, F., Littler, K., Arz, J.A. and Russell, E.E. 2014. Evidence for global cooling in the Late Cretaceous. *Nature Communications 2014 5:1*. **5**(1), pp.1–7.

Liu, M., Adam, J.C., Richey, A.S., Zhu, Z. and Myneni, R.B. 2018. Factors controlling changes in evapotranspiration, runoff, and soil moisture over the conterminous U.S.: Accounting for vegetation dynamics. *Journal of Hydrology*. **565**, pp.123–137.

Liu, Y., Chen, C., He, D. and Chen, W. 2019. Deep carbon cycle in subduction zones. *Science China Earth Sciences 2019 62:11*. **62**(11), pp.1764–1782.

Longman, J., Mills, B.J.W., Manners, H.R., Gernon, T.M. and Palmer, M.R. 2021. Late Ordovician climate change and extinctions driven by elevated volcanic nutrient supply. *Nature Geoscience 2021 14:12*. **14**(12), pp.924–929.

Lowenstein, T.K., Timofeeff, M.N., Kovalevych, V.M. and Horita, J. 2005. The major-ion composition of Permian seawater. *Geochimica et Cosmochimica Acta*. **69**(7), pp.1701–1719.

Luyssaert, S., Inglima, I., Jung, M., Richardson, A.D., Reichstein, M., Papale, D., Piao, S.L., Schulze, E.-D., Wingate, L., Matteucci, G., Aragao, L., Aubinet, M., Beer, C., Bernhofer, C., Black, K.G., Bonal, D., Bonnefond, J.-M., Chambers, J., Ciais, P., Cook, B., Davis, K.J., Dolman, A.J., Gielen, B., Goulden, M., Grace, J., Granier, A., Grelle, A., Griffis, T., Grunwald, T., Guidolotti, G., Hanson, P.J., Harding, R., Hollinger, D.Y., Hutyra, L.R., Kolari, P., Kruijt, B., Kutsch, W., Lagergren, F., Laurila, T., Law, B.E., Maire, G. LE, Lindroth, A., Loustau, D., Malhi, Y., Mateus, J., Migliavacca, M., Misson, L., Montagnani, L., Moncrieff, J., Moors, E., Munger, J.W., Nikinmaa, E., Ollinger, S. V., Pita, G., Rebmann, C., Roupsard, O., Saigusa, N., Sanz, M.J., Seufert, G., Sierra, C., Smith, M.-L., Tang, J., Valentini, R., Vesala, T. and Janssens, I.A. 2007. CO2 balance of boreal, temperate, and tropical forests derived from a global database. *Global Change Biology*. **13**(12), pp.2509–2537.

Mackensen, A. and Schmiedl, G. 2019. Stable carbon isotopes in paleoceanography: atmosphere, oceans, and sediments. *Earth-Science Reviews*. **197**.

Maffre, P., Ladant, J.B., Moquet, J.S., Carretier, S., Labat, D. and Goddéris, Y. 2018. Mountain ranges, climate and weathering. Do orogens strengthen or weaken the silicate weathering carbon sink? *Earth and Planetary Science Letters*. **493**, pp.174–185.

Magallón, S., Hilu, K.W. and Quandt, D. 2013. Land plant evolutionary timeline: Gene effects are secondary to fossil constraints in relaxed clock estimation of age and substitution rates. *American Journal of Botany*. **100**(3), pp.556–573.

Marcilly, C.M., Torsvik, T.H., Domeier, M. and Royer, D.L. 2021. New paleogeographic and degassing parameters for long-term carbon cycle models. *Gondwana Research*. **97**, pp.176–203.

Matsunaga, K.K.S. and Tomescu, A.M.F. 2016. Root evolution at the base of the lycophyte clade: insights from an Early Devonian lycophyte. *Annals of Botany*. **117**(4), pp.585–598.

McArthur, J.M., Howarth, R.J. and Shields, G.A. 2012. Strontium Isotope Stratigraphy *In*: *The Geologic Time Scale* [Online]. Elsevier, pp.127–144. [Accessed 7 January 2022]. Available from: https://linkinghub.elsevier.com/retrieve/pii/B978044459425900007X.

McElwain, J.C. and Punyasena, S.W. 2007. Mass extinction events and the plant fossil record. *Trends in Ecology & Evolution*. **22**(10), pp.548–557.

McKenzie, N.R., Horton, B.K., Loomis, S.E., Stockli, D.F., Planavsky, N.J. and Lee, C.-T.A. 2016. Continental arc volcanism as the principal driver of icehouse-greenhouse variability. *Science (New York, N.Y.)*. **352**(6284), pp.444–7.

Meek, D.W., Hatfield, J.L., Howell, T.A., Idso, S.B. and Reginato, R.J. 1984. A Generalized Relationship between Photosynthetically Active Radiation and Solar Radiation1. *Agronomy Journal*. **76**(6), pp.939–945.

Miller, H.A. 1982. Bryophyte evolution and geography. *Biological Journal of the Linnean Society*. **18**(2), pp.145–196.

Mills, B., Daines, S.J. and Lenton, T.M. 2014. Changing tectonic controls on the long-term carbon cycle from Mesozoic to present. *Geochemistry, Geophysics, Geosystems*. **15**(12), pp.4866–4884.

Mills, B.J.W., Batterman, S.A. and Field, K.J. 2018. Nutrient acquisition by symbiotic fungi governs Palaeozoic climate transition. *Philosophical transactions of the Royal Society of London. Series B, Biological sciences*. **373**(1739).

Mills, B.J.W., Donnadieu, Y. and Goddéris, Y. 2021. Spatial continuous integration of Phanerozoic global biogeochemistry and climate. *Gondwana Research*.

Mills, B.J.W., Krause, A.J., Scotese, C.R., Hill, D.J., Shields, G.A. and Lenton, T.M. 2019. Modelling the long-term carbon cycle, atmospheric CO2, and Earth surface temperature from late Neoproterozoic to present day. *Gondwana Research*. **67**, pp.172–186.

Mitchell, T.D. and Jones, P.D. 2005. An improved method of constructing a database of monthly climate observations and associated high-resolution grids. *International Journal of Climatology*. **25**(6), pp.693–712.

Montañez, I.P., McElwain, J.C., Poulsen, C.J., White, J.D., DiMichele, W.A., Wilson, J.P., Griggs, G. and Hren, M.T. 2016. Climate, pCO2 and terrestrial carbon cycle linkages during late Palaeozoic glacial–interglacial cycles. *Nature Geoscience*. **9**(11), pp.824–828.

Montañez, I.P. and Poulsen, C.J. 2013. The Late Paleozoic Ice Age: An Evolving Paradigm. *Annual Review of Earth and Planetary Sciences*. **41**(1), pp.629–656.

Moore, P.D. 1989. The ecology of peat-forming processes: a review. *International Journal of Coal Geology*. **12**(1–4), pp.89–103.

Morris, J.L., Leake, J.R., Stein, W.E., Berry, C.M., Marshall, J.E.A., Wellman, C.H., Milton, J.A., Hillier, S., Mannolini, F., Quirk, J. and Beerling, D.J. 2015. Investigating Devonian trees as geo-engineers of past climates: linking palaeosols to palaeobotany and experimental geobiology B. Lomax, ed. *Palaeontology*. **58**(5), pp.787–801.

Morris, J.L., Puttick, M.N., Clark, J.W., Edwards, D., Kenrick, P., Pressel, S., Wellman, C.H., Yang, Z., Schneider, H. and Donoghue, P.C.J. 2018. The timescale of early land plant evolution. *Proceedings of the National Academy of Sciences of the United States of America*. **115**(10), pp.2274–2283.

Mu, Q., Heinsch, F.A., Zhao, M. and Running, S.W. 2007. Development of a global evapotranspiration algorithm based on MODIS and global meteorology data. *Remote Sensing of Environment*. **111**(4), pp.519–536.

Mucina, L. 2019. Biome: evolution of a crucial ecological and biogeographical concept. *New Phytologist*. **222**(1), pp.97–114.

Nelsen, M.P., DiMichele, W.A., Peters, S.E. and Boyce, C.K. 2016. Delayed fungal evolution did not cause the Paleozoic peak in coal production. *Proceedings of the National Academy of Sciences of the United States of America*. **113**(9), pp.2442–2447.

Nilson, S.E. and Assmann, S.M. 2007. The Control of Transpiration. Insights from Arabidopsis. *Plant Physiology*. **143**(1), pp.19–27.

Oeser, R.A. and Von Blanckenburg, F. 2020. Do degree and rate of silicate weathering depend on plant productivity? *Biogeosciences*. **17**(19), pp.4883–4917.

Oliver, M.J., Velten, J. and Mishler, B.D. 2005. Desiccation Tolerance in Bryophytes: A Reflection of the Primitive Strategy for Plant Survival in Dehydrating Habitats? *Integrative and Comparative Biology*. **45**(5), pp.788–799.

Or, D. and Lehmann, P. 2019. Surface Evaporative Capacitance: How Soil Type and Rainfall Characteristics Affect Global-Scale Surface Evaporation. *Water Resources Research*. **55**, pp.519–539.

Otto-Bliesner, B.L. 1995. Continental drift, runoff, and weathering feedbacks: Implications from climate model experiments. *Journal of Geophysical Research: Atmospheres*. **100**(D6), pp.11537–11548.

Pärtel, M., Laanisto, L. and Zobel, M. 2007. Constrasting plant productivity-relationships across latitude: the role of evolutinary history. *Ecology*. **88**(5), pp.1091–1097.

Pirozynski, K.A. and Malloch, D.W. 1975. The origin of land plants: A matter of mycotrophism. *Biosystems*. **6**(3), pp.153–164.

Plank, T. and Manning, C.E. 2019. Subducting carbon. *Nature 2019 574:7778*. **574**(7778), pp.343–352.

Pohl, A., Donnadieu, Y., Le Hir, G., Buoncristiani, J.F. and Vennin, E. 2014. Effect of the Ordovician paleogeography on the (in)stability of the climate. *Climate of the Past*. **10**(6), pp.2053–2066.

Poorter, H., Niklas, K.J., Reich, P.B., Oleksyn, J., Poot, P. and Mommer, L. 2012. Biomass allocation to leaves, stems and roots: meta-analyses of interspecific variation and environmental control. *New Phytologist*. **193**(1), pp.30–50.

Porada, P., Lenton, T.M., Pohl, A., Weber, B., Mander, L., Donnadieu, Y., Beer, C., Pöschl, U. and Kleidon, A. 2016. High potential for weathering and climate effects of non-vascular vegetation in the Late Ordovician. *Nature Communications*. **7**(1), pp.1–13.

Porada, P., Van Stan, J.T. and Kleidon, A. 2018. Significant contribution of non-vascular vegetation to global rainfall interception. *Nature Geoscience 2018 11:8*. **11**(8), pp.563–567.

Porada, P., Weber, B., Elbert, W., Pöschl, U. and Kleidon, A. 2013. Estimating global carbon uptake by lichens and bryophytes with a process-based model. *Biogeosciences*. **10**, pp.6989–7033.

Porder, S. 2019. How Plants Enhance Weathering and How Weathering is Important to Plants. *Elements*. **15**(4), pp.241–246.

Post, W.M., Peng, T.-H., Emanuel, W.R., King, A.W., Dale, V.H. and DeAngelis, D.L. 1990. The global carbon cycle. *American Scientist*. **78**, pp.310–326.

Proctor, M.C.F. and Tuba, Z. 2002. Poikilohydry and homoihydry: antithesis or spectrum of possibilities? *New Phytologist*. **156**(3), pp.327–349.

Puttick, M.N., Morris, J.L., Williams, T.A., Cox, C.J., Edwards, D., Kenrick, P., Pressel, S., Wellman, C.H., Schneider, H., Pisani, D. and Donoghue, P.C.J. 2018. The Interrelationships of Land Plants and the Nature of the Ancestral

Embryophyte. *Current Biology*. **28**(5), pp.733-745.e2.

Raven, J.A. 2003. Long-distance transport in non-vascular plants. *Plant, Cell & Environment*. **26**(1), pp.73–85.

Raven, J.A. and Edwards, D. 2001. Roots: evolutionary origins and biogeochemical significance. *Journal of Experimental Botany*. **52**(suppl 1), pp.381–401.

Raymo, M.E. and Ruddiman, W.F. 1992. Tectonic forcing of late Cenozoic climate. *Nature 1992 359:6391*. **359**(6391), pp.117–122.

Read, D.J. and Perez-Moreno, J. 2003. Mycorrhizas and nutrient cycling in ecosystems – a journey towards relevance? *New Phytologist*. **157**(3), pp.475–492.

Rensing, S.A. 2018. Plant Evolution: Phylogenetic Relationships between the Earliest Land Plants. *Current Biology*. **28**(5), pp.R210–R213.

Retallack, G.J. 2001. Cenozoic Expansion of Grasslands and Climatic Cooling. *The Journal of Geology*. **109**(4), pp.407–426.

Rillig, M.C. and Mummey, D.L. 2006. Mycorrhizas and soil structure. *New Phytologist*. **171**(1), pp.41–53.

Rimington, W.R., Pressel, S., Duckett, J.G., Field, K.J., Read, D.J. and Bidartondo, M.I. 2018. Ancient plants with ancient fungi: liverworts associate with early-diverging arbuscular mycorrhizal fungi. *Proceedings of the Royal Society B: Biological Sciences*. **285**(1888), p.20181600.

Ripperdan, R.L. 2001. Stratigraphic variation in marine carbonate carbon isotope ratios. *Reviews in Mineralogy and Geochemistry*. **43**, pp.637–662.

Robinson, J.M. 1990a. Lignin, land plants, and fungi: Biological evolution affecting Phanerozoic oxygen balance | Geology | GeoScienceWorld. *Geology*. **18**(7), pp.607–610.

Robinson, J.M. 1990b. The burial of organic carbon as affected by the evolution of land plants. *Historical Biology*. **3**(3), pp.189–201.

Royer, D.L. 2006. CO2-forced climate thresholds during the Phanerozoic. *Geochimica et Cosmochimica Acta*. **70**(23), pp.5665–5675.

Ruddiman, W.F., Fuller, D.Q., Kutzbach, J.E., Tzedakis, P.C., Kaplan, J.O., Ellis, E.C., Vavrus, S.J., Roberts, C.N., Fyfe, R., He, F., Lemmen, C. and Woodbridge, J. 2016. Late Holocene climate: Natural or anthropogenic? *Reviews of Geophysics*. **54**(1), pp.93–118.

Ruddiman, W.F. and Prell, W.L. 1997. Introduction to the Uplift-Climate Connection *In*: *Tectonic Uplift and Climate Change* [Online]. Boston, MA: Springer US, pp.3–15. [Accessed 15 November 2021]. Available from: http://link.springer.com/10.1007/978-1-4615-5935-1_1.

Ruesch, A. and Holly, K.G. 2008. New IPCC Tier-1 Global Biomass Carbon Map For the Year 2000.

Ruszala, E.M., Beerling, D.J., Franks, P.J., Chater, C., Casson, S.A., Gray, J.E. and Hetherington, A.M. 2011. Land Plants Acquired Active Stomatal Control Early in Their Evolutionary History. *Current Biology*. **21**(12), pp.1030–1035.

Saltzman, M.R. and Thomas, E. 2012. Carbon isotope stratigraphy. *The Geologic Time Scale 2012*. (Dic), pp.207–232.

Sauquet, H., Von Balthazar, M., Magallón, S., Doyle, J.A., Endress, P.K., Bailes, E.J., Barroso De Morais, E., Bull-Hereñu, K., Carrive, L., Chartier, M., Chomicki, G., Coiro, M., Cornette, R., El Ottra, J.H.L., Epicoco, C., Foster, C.S.P., Jabbour, F., Haevermans, A., Haevermans, T., Hernández, R., Little, S.A., Löfstrand, S., Luna, J.A., Massoni, J., Nadot, S., Pamperl, S., Prieu, C., Reyes, E., Dos Santos, P., Schoonderwoerd, K.M., Sontag, S., Soulebeau, A., Staedler, Y., Tschan, G.F., Wing-Sze Leung, A. and Schönenberger, J. 2017. The ancestral flower of angiosperms and its early diversification. *Nature*

Communications. **8**(1), pp.1–10.

Schaphoff, S., Von Bloh, W., Rammig, A., Thonicke, K., Biemans, H., Forkel, M., Gerten, D., Heinke, J., Jägermeyr, J., Knauer, J., Langerwisch, F., Lucht, W., Müller, C., Rolinski, S. and Waha, K. 2018. LPJmL4-a dynamic global vegetation model with managed land-Part 1: Model description. *Geosci. Model Dev*. **11**, pp.1343–1375.

Scheffler, K., Hoernes, S. and Schwark, L. 2003. *Global changes during Carboniferous-Permian glaciation of Gondwana: Linking polar and equatorial climate evolution by geochemical proxies* [Online]. [Accessed 27 June 2019]. Available from: https://web.viu.ca/earle/geol305/labs/carb-perm-glaciation1.pdf.

Scheiter, S., Langan, L. and Higgins, S.I. 2013. Next-generation dynamic global vegetation models: learning from community ecology. *New Phytologist*. **198**(3), pp.957–969.

Schlesinger, W.H. and Jasechko, S. 2014. Transpiration in the global water cycle. *Agricultural and Forest Meteorology*. **189–190**, pp.115–117.

Schnepf, A. and Roose, T. 2006. Modelling the contribution of arbuscular mycorrhizal fungi to plant phosphate uptake. *New Phytologist*. **171**(3), pp.669–682.

Scotese, C.R. 2021. An Atlas of Phanerozoic Paleogeographic Maps: The Seas Come In and the Seas Go Out. *https://doi.org/10.1146/annurev-earth-081320-064052*. **49**, pp.679–728.

Scotese, C.R. and Langford, R.P. 1995. Pangea and the Paleogeography of the Permian *In*: *The Permian of Northern Pangea* [Online]. Berlin, Heidelberg: Springer Berlin Heidelberg, pp.3–19. [Accessed 16 November 2021]. Available from: https://link.springer.com/chapter/10.1007/978-3-642-78593-1_1.

Scotese, C.R., Song, H., Mills, B.J.W. and van der Meer, D.G. 2021. Phanerozoic paleotemperatures: The earth's changing climate during the last 540 million years. *Earth-Science Reviews*. **215**.

Scott, A.C. and Glasspool, I.J. 2006. The diversification of Paleozoic fire systems and fluctuations in atmospheric oxygen concentration. *PNAS July*. **18**, pp.10861–10865.

Sheehan, P.M. 2001. The Late Ordovician Mass Extinction. *Annual Review of Earth and Planetary Sciences*. **29**(1), pp.331–364.

Sheil, D. 2018. Forests, atmospheric water and an uncertain future: the new biology of the global water cycle. *Forest Ecosystems 2018 5:1*. **5**(1), pp.1–22.

Simard, S.W., Beiler, K.J., Bingham, M.A., Deslippe, J.R., Philip, L.J. and Teste, F.P. 2012. Mycorrhizal networks: Mechanisms, ecology and modelling. *Fungal Biology Reviews*. **26**(1), pp.39–60.

Sitch, S., Smith, B., Prentice, I.C., Arneth, A., Bondeau, A., Cramer, W., Kaplan, J.O., Levis, S., Lucht, W., Sykes, M.T., Thonicke, K. and Venevsky, S. 2003. Evaluation of ecosystem dynamics, plant geography and terrestrial carbon cycling in the LPJ dynamic global vegetation model. *Global Change Biology*. **9**(2), pp.161–185.

Smith, S.E., Jakobsen, I., Grønlund, M. and Smith, F.A. 2011. Roles of arbuscular mycorrhizas in plant phosphorus nutrition: interactions between pathways of phosphorus uptake in arbuscular mycorrhizal roots have important implications for understanding and manipulating plant phosphorus acquisition. *Plant physiology*. **156**(3), pp.1050–7.

Smith, T.M., Shugart, H.H., Bonan, G.B. and Smith, J.B. 1992. Modeling the Potential Response of Vegetation to Global Climate Change. *Advances in Ecological Research*. **22**(C), pp.93–116.

Song, Z., Liu, H., Strömberg, C.A.E., Wang, H., Strong, P.J., Yang, X. and Wu, Y. 2018. Contribution of forests to the carbon sink via biologically-mediated silicate weathering: A case study of China. *Science of The Total Environment*. **615**, pp.1–8.

Soudzilovskaia, N.A., van Bodegom, P.M., Terrer, C., van't Zelfde, M., McCallum, I., McCormack, M.L., Fisher, J.B., Brundrett, M., de Sá, N.C. and Tedersoo, L. 2018. Human-induced decrease of ectomycorrhizal vegetation led to loss in global soil carbon content. *bioRxiv*., p.331884.

Sperry, J.S. 2003. Evolution of Water Transport and Xylem Structure. *Source: International Journal of Plant Sciences*. **164**(S3), pp.115–127.

Steemans, P., Hérissé, A. Le, Melvin, J., Miller, M.A., Paris, F., Verniers, J. and Wellman, C.H. 2009. Origin and Radiation of the Earliest Vascular Land Plants. *Science*. **324**(5925), pp.353–353.

Stirbet, A., Lazár, D., Guo, Y. and Govindjee, G. 2020. Photosynthesis: basics, history and modelling. *Annals of Botany*. **126**(4), pp.511–537.

Strullu-Derrien, C., Kenrick, P. and Knoll, A.H. 2019. The Rhynie chert. *Current Biology*. **29**(23), pp.R1218–R1223.

Strullu-Derrien, C., Selosse, M.A., Kenrick, P. and Martin, F.M. 2018. The origin and evolution of mycorrhizal symbioses: from palaeomycology to phylogenomics. *New Phytologist*. **220**(4), pp.1012–1030.

Sulman, B.N., Shevliakova, E., Brzostek, E.R., Kivlin, S.N., Malyshev, S., Menge, D.N.L. and Zhang, X. 2019. Diverse Mycorrhizal Associations Enhance Terrestrial C Storage in a Global Model. *Global Biogeochemical Cycles*. **33**(4), pp.501–523.

Tabor, C.R., Feng, R. and Otto-Bliesner, B.L. 2019. Climate Responses to the Splitting of a Supercontinent: Implications for the Breakup of Pangea. *Geophysical Research Letters*. **46**(11), pp.6059–6068.

Tan, Z.-H., Zeng, J., Zhang, Y.-J., Slot, M., Gamo, M., Hirano, T., Kosugi, Y., Rocha, H.R. da, Saleska, S.R., Goulden, M.L., Wofsy, S.C., Miller, S.D., Manzi, A.O., Nobre, A.D., Camargo, P.B. de and Restrepo-Coupe, N. 2017. Optimum air temperature for tropical forest photosynthesis: mechanisms involved and implications for climate warming. *Environmental Research Letters*. **12**.

Taylor, L.L., Banwart, S.A., Valdes, P.J., Leake, J.R. and Beerling, D.J. 2012. Evaluating the effects of terrestrial ecosystems, climate and carbon dioxide on weathering over geological time: A global-scale process-based approach. *Philosophical Transactions of the Royal Society B: Biological Sciences*. **367**(1588), pp.565–582.

Taylor, L.L., Leake, J.R., Quirk, J., Hardy, K., Banwart, S.A. and Beerling, D.J. 2009. Biological weathering and the long-term carbon cycle: Integrating mycorrhizal evolution and function into the current paradigm. *Geobiology*. **7**(2), pp.171–191.

Taylor, T.N., Kerp, H. and Hass, H. 2005. Life history biology of early land plants: Deciphering the gametophyte phase. *Proceedings of the National Academy of Sciences*. **102**(16), pp.5892–5897.

Tedersoo, L., Bahram, M. and Zobel, M. 2020. How mycorrhizal associations drive plant population and community biology. *Science*. **367**(6480).

Tobis, M., Schafer, C., Foster, I., Jacob, R. and Anderson, J. 1997. FOAM *In*: *Proceedings of the 1997 ACM/IEEE conference on Supercomputing (CDROM) - Supercomputing '97* [Online]. New York, New York, USA: ACM Press, pp.1–15. [Accessed 26 October 2021]. Available from: http://portal.acm.org/citation.cfm?doid=509593.509620.

Trimble, M.J. and Aarde, R.J. van 2012. Geographical and taxonomic biases in research on biodiversity in human-modified landscapes. *Ecosphere*. **3**(12), pp.1–16.

Trotter, J.A., Williams, I.S., Barnes, C.R., Männik, P. and Simpson, A. 2016. New conodont δ18O records of Silurian climate change: Implications for environmental and biological events. *Palaeogeography, Palaeoclimatology, Palaeoecology*. **443**, pp.34–48.

Trotter, J.A., Williams, I.S., Nicora, A., Mazza, M. and Rigo, M. 2015. Long-term cycles of Triassic climate change: a new δ18O record from conodont apatite. *Earth and Planetary Science Letters*. **415**, pp.165–174.

de Vries, J. and Archibald, J.M. 2018. Plant evolution: landmarks on the path to terrestrial life. *New Phytologist*. **217**(4), pp.1428–1434.

Walker, J.C.G., Hays, P.B. and Kasting, J.F. 1981. A negative feedback mechanism for the long-term stabilization of Earth’s surface temperature. *Journal of Geophysical Research: Oceans*. **86**(C10), pp.9776–9782.

Wang, G., Jia, Y. and Li, W. 2015. Effects of environmental and biotic factors on carbon isotopic fractionation during decomposition of soil organic matter. *Scientific Reports 2015 5:1*. **5**(1), pp.1–11.

Wang, J., Bao, Q., Zeng, N., Liu, Y., Wu, G. and Ji, D. 2013. Earth System Model FGOALS-s2: Coupling a dynamic global vegetation and terrestrial carbon model with the physical climate system model. *Advances in Atmospheric Sciences 2013 30:6*. **30**(6), pp.1549–1559.

Waters, E.R. 2003. Molecular adaptation and the origin of land plants. *Molecular Phylogenetics and Evolution*. **29**(3), pp.456–463.

Wellman, C.H., Steemans, P. and Vecoli, M. 2013. Chapter 29 Palaeophytogeography of Ordovician–Silurian land plants. *Geological Society, London, Memoirs*. **38**(1), pp.461–476.

Weng, J.K. and Chapple, C. 2010. The origin and evolution of lignin biosynthesis. *New Phytologist*. **187**(2), pp.273–285.

West, A., Galy, A. and Bickle, M. 2005. Tectonic and climatic controls on silicate weathering. *Earth and Planetary Science Letters*. **235**(1–2), pp.211–228.

Witkowski, C.R., Weijers, J.W.H., Blais, B., Schouten, S. and Sinninghe Damsté, J.S. 2018. Molecular fossils from phytoplankton reveal secular PCO2 trend over the phanerozoic. *Science Advances*. **4**(11).

Wu, D., Zhao, X., Liang, S., Zhou, T., Huang, K., Tang, B. and Zhao, W. 2015. Time-lag effects of global vegetation responses to climate change. *Global Change Biology*. **21**(9), pp.3520–3531.

Xu, J., Lv, Y., Liu, X., Wei, Q., Qi, Z., Yang, S. and Liao, L. 2019. A general non-rectangular hyperbola equation for photosynthetic light response curve of rice at various leaf ages. *Scientific Reports 2019 9:1*. **9**(1), pp.1–8.

Yang, J., Xia, D., Gao, F., Wang, S., Li, D., Fan, Y., Chen, Z., Tian, W., Liu, X., Sun, X., Wang, Z. and Wang, F. 2021. Holocene moisture evolution and its response to atmospheric circulation recorded by aeolian deposits in the southern Tibetan Plateau. *Quaternary Science Reviews*. **270**, p.107169.

Zeng, Z., Zhu, H., Yang, X., Zeng, H., Hu, X. and Xia, C. 2019. The Pangaea Megamonsoon records: Evidence from the Triassic Mungaroo Formation, Northwest Shelf of Australia. *Gondwana Research*. **69**, pp.1–24.

Zeppel, M.J.B., Wilks, J. V. and Lewis, J.D. 2014. Impacts of extreme precipitation and seasonal changes in precipitation on plants. *Biogeosciences*. **11**(11), pp.3083–3093.

Zhang, Y., Xu, M., Chen, H. and Adams, J. 2009. Global pattern of NPP to GPP ratio derived from MODIS data: effects of ecosystem type, geographical location and climate. *Global Ecology and Biogeography*. **18**(3), pp.280–290.

Ziegler, A.M., Scotese, C.R., McKerrow, W.S., Johnson, M.E. and Bambach, R.K. 1979. Paleozoic Paleogeography. *Annual Review of Earth and Planetary Sciences*. **7**(1), pp.473–502.